LIGHT SCATTERING BY ICE CRYSTALS AND MINERAL DUST AEROSOLS IN THE ATMOSPHERE

A Dissertation

by

LEI BI

Submitted to the Office of Graduate Studies of
Texas A&M University
in partial fulfillment of the requirements for the degree of

DOCTOR OF PHILOSOPHY

May 2011

Major Subject: Physics

LIGHT SCATTERING BY ICE CRYSTALS AND MINERAL DUST AEROSOLS IN THE ATMOSPHERE

A Dissertation

by

LEI BI

Submitted to the Office of Graduate Studies of
Texas A&M University
in partial fulfillment of the requirements for the degree of

DOCTOR OF PHILOSOPHY

Approved by:

Co-Chairs of Committee,	George W. Kattawar
	Ping Yang
Committee Members,	Chia-Ren Hu
	Che-Ming Ko
Head of Department,	Edward S. Fry

May 2011

Major Subject: Physics

ABSTRACT

Light Scattering by Ice Crystals and Mineral Dust Aerosols in the Atmosphere.

(May 2011)

Lei Bi, B. S., Anhui Normal University;

M. S., Beijing Normal University

Co–Chairs of Advisory Committee: Dr. George W. Kattawar
Dr. Ping Yang

Modeling the single-scattering properties of nonspherical particles in the atmosphere (in particular, ice crystals and dust aerosols) has important applications to climate and remote sensing studies. The first part of the dissertation (Chapters II-V) reports a combination of exact numerical methods, including the finite-difference time-domain (FDTD), the discrete-dipole-approximation (DDA), and the T-matrix methods, and an approximate method-the physical-geometric optics hybrid (PGOH) method- in the computation of the optical properties of the non-spherical particles in a complete range of size parameters. The major advancements are made on the modeling capabilities of the PGOH method, and the knowledge of the electromagnetic tunneling effect – a semi-classical scattering effect. This research is important to obtain reliable optical properties of nonspherical particles in a complete range of size parameters with satisfactory accuracy and computational efficiency.

The second part (Chapters VI-VII) of the dissertation is to investigate the dependence of the optical properties of ice crystals and mineral dust aerosols in the atmosphere on the spectrum, the particle size and the morphology based on computational models. Ice crystals in the atmosphere can be classified to be simple regular faceted particles (such as hexagon columns, plates, etc.) and imperfect ice crystals. Modeling of the scattering by regular ice crystals is straightforward, as their mor-

phologies can be easily defined. For imperfect ice crystals, the morphology is quite diverse, which complicates the modeling process. We present an effective approach of using irregular faceted particle to characterize the imperfectness of ice crystals. As an example of application, less-than-unity backscattering color ratio of cirrus clouds is demonstrated and explained theoretically, which provides guidance in the calibration algorithm for 1.064-μm channel on the Calipso lidar. Dust aerosols have no particular morphology. To develop an approach to modeling the optical properties of realistic dust particles, the principle of using simple shapes (triaxial ellipsoids and nonsymmetric hexahedra) to represent irregular dust particles is explored. Simulated results have been compared with those measured in laboratory for several realistic aerosol samples. Agreement between simulated results and measurement suggests the potential applicability of the two aforementioned aerosol models. We also show the potential impact of the present study to passive and active atmospheric remote sensing and future research works.

to my parents and to Lynne Zheng

ACKNOWLEDGMENTS

I would like to express my sincere gratitude to my academic advisors, Dr. George Kattawar and Dr. Ping Yang, for their insightful guidance and encouragement to pursue active research topics in electromagnetic scattering and its applications. Dr. George Kattawar's research is supported by Office of Naval Research under contract N00014-06-1-0069, and Dr. Ping Yang's research is supported by National Science Foundation (ATM-0803779), and NASA grants (NNX08AI94G and NNX08AF68G). Additional thanks are extended to the other committee members, Dr. Hu and Dr. Ko, for their careful review of my proposal and dissertation. Their comments and suggestions on improving the dissertation are very helpful.

I also appreciate discussions with my group members, Pengwang Zhai, Yu You, Ben Striker, Zhibo Zhang, Gang Hong, Yu Xie, Meng Gao, Bingqi Yi, Shuoguo Ding, Qian Feng, Bingqiang Sun, and Xin Huang. It is such an enjoyable experience to work with them. It was Pengwang who met me at George Bush airport, and helped me settle down. I can always get my satisfactory answers from Yu You by stepping in his office. Ben Striker helped me a lot to improve my English and I highly appreciate his friendship as well.

Special thanks are given to my brother-in-law Lisen Xu. We shared our joys and pains in the past eight years since I was pursuing my master degree in China. Finally, I am thankful to my parents, sisters, brothers, and to my wife, Lynne Zheng, for their support and love.

TABLE OF CONTENTS

CHAPTER Page

CHAPTER Page

LIST OF TABLES

LIST OF FIGURES

FIGURE Page

FIGURE Page

FIGURE Page

FIGURE Page

FIGURE Page

CHAPTER I

INTRODUCTION AND BACKGROUND

The major objective of this dissertation is to enhance the existing modeling capabilities, and develop new techniques in the simulation of the scattering and the absorption of light by nonspherical particles in the atmosphere. For simplicity, model particles are assumed to be homogenous, dielectric, and isotropic, although some realistic atmospheric particles, such as ice crystals, and mineral dust aerosols, may be inhomogeneous and anisotropic. We focus on investigating the effects associated with the nonsphericity and the orientation of nonspherical particles on their optical properties. In Section A of this chapter, we provide the background information, summarize the current modeling capabilities, and propose specific research subjects. Section B is a brief introduction of basic concepts and quantities of the scattering and the absorption of light by an individual particle. The organization of this dissertation is described in Section C.

A. Light Scattering in the Atmosphere

Atmosphere is a large scale physical system consisting of various types of gases (e.g.,N_2, O_2, CO_2, H_2O, etc.), and small suspended particles, such as water droplets, ice crystals, and aerosols. These air molecules and particulate matters play an important role in regulating the radiation field in the atmosphere by interacting with the solar radiation and the thermal emissions from the earth. The theory of light scattering, which quantifies the radiation interaction involved in such a complex system, is fundamental to understanding atmospherical optical phenomena and climate

---

This dissertation follows the style of Applied Optics.

change, and to atmospheric remote sensing applications [1]. Table I shows the major types of light scattering in the atmosphere and associated theoretical treatments. The scattering of light by molecules is well descried by Rayleigh-Brillouin and rotational Raman scattering. The scattering of light by water droplets can be quantified with high accuracy within the context of Lorenz-Mie theory based on electronic computers. However, the modeling of the absorption and scattering by ice crystals and dust aerosols is still a quite challenging research problem, although diverse treatments of their "nonsphericity" are proposed in quantifying their radiative impacts. The major difficulties are associated with the computational capability in solving macroscopic Maxwell equations for nonspherical particles of large size parameter (a ratio between the characteristic size of the particle and the wavelength) and an effective characterization of diverse particle shapes.

One short cut to avoid the aforementioned difficulties in modeling the optical properties of nonspherical particles is "spherical approximation". In "spherical approximation", a nonspherical particle is represented by a spherical particle of equivalent volume, surface area, or effective size (the ratio of volume over area). More and more evidences show that the method based on "spherical approximation" for nonspherical particles is questionable and leads to large errors for most concerned cases in climate and remote sensing studies. More reliable modeling of the optical properties of nonsphercial particle is required to be developed.

Optical properties of nonspherical particles are more difficult to obtain than those of spheres. It is not easy to identify the earliest efforts to investigate the single-scattering properties of nonspherical particles, but significant advancements were made in the second half of the last century stimulated by an increasing development of electronic computers. Existing scattering methods including exact and approximate techniques were reviewed in several published books [2–5] and jour-

Table I. Types of light scattering in the atmosphere

Particle Type	Dimension (μm)	Method of Solution	Optical Phenomenon
Air Molecules	$1.0^{-4}, 1.0^{-3}$	Rayleigh-Brillouin, Rotational Raman	Blue Sky, Filling-in
Water Droplets	10 - 100	Lorenz-Mie theory	Rainbow
Ice Crystals	1-several thousands	Nonsphericity	Various Halos
Dust Aerosols	1-several hundreds	Nonsphericity	Brownish smog

nal articles [6–8]. Three robust exact methods are the finite-difference time-domain (FDTD) method [9–11] , the discrete-dipole-approximation*(DDA) method [12–15], and the T-matrix method (the extended-boundary-condition method (EBCM) or null field method [16–18], in particular). The FDTD method is to solve Maxwell equations in time domain, while the DDA method is to solve an electromagnetic integral equation in frequency domain. In both methods of DDA and FDTD, it is required to discretize the scattering particle into sub volumes. Due to the limitation of computer memory and CPU time, the two numerical methods (i.e., the FDTD and DDA) are restricted to small or moderate size-parameters. The T-matrix method based on the extended-boundary-condition technique is of a semi-analytical nature, however, this method lends itself more easily to axially symmetric particles and moderate aspect ratios. Furthermore, the upper-limit of the size parameter of this method is sensitive to the morphology of the particle and computer precision. As a result, the methods intending to exactly solve equations in the context of Maxwell theory for scatter-

*The "approximation" in the DDA indicates the existing numerical errors. We say the DDA to be a rigorous method as it solves Maxwell equations in full electrodynamics and the numerical errors can be reduced in a manner so that the true solution is approached.

ing by nonspherical particles are limited to small (or moderate) size parameters. At present, there is still no single method, which can be employed to calculate the single-scattering properties of non-spherical particles in a complete range of size parameters from Raleigh* to geometric optics regimes. It seems that this situation is unlikely or not easily to change in the near future. As a matter of fact, nonspherical particles in the atmosphere always have a large range of sizes from submicron to thousands of microns (see Table 1) and the wavelength of involved radiation is from UV to microwave spectral regions. The range of size parameter is so broad that various efforts are devoted to developing approximate methods for large size parameters, such as anomalous diffraction theory [2, 19–22] and geometric optics method [23–31]. In this dissertation, our final aim is to obtain reliable data set of the single-scattering properties of ice crystals and mineral dust aerosols of arbitrary size parameters, which will be used in the forward radiative transfer simulation and remote sensing applications. The most practical approach may be the unification of rigorous methods and methods of approximate solution. For particles with large size parameters, an approximate method usually employed is based on geometric optics. The major impetus of the present research is associated with increasing development of Earth observing system (A-train satellites). A wealth of data from observations using optical instruments in conjunction with micro-physical modeling will provide unprecedented human ability to understand the earth atmosphere.

The methodology based on the unification of rigorous methods and method of geometric-optics approximation avoids the difficulty in developing a single exact method for a defined nonspherical particle. However, it is found to be not straight-

*"Rayleigh regime" here indicates the elastic scattering of light by particles much smaller than the incident wavelength (the size parameter is very small). It does not necessarily mean that the scatterer is an atom or a molecule.

forward. The essential problems are the efficiency and validity of geometric optics approximation and incorporation of semi-classical scattering effects [32–34], which are the main issues we shall investigate in this dissertation. To be more specific, we devote our efforts to studying the following three research topics: (1) mutual verification of existing numerical methods; (2) develop a more accurate and yet efficient geometric optics method; (3) justify and quantify electromagnetic tunneling effect.

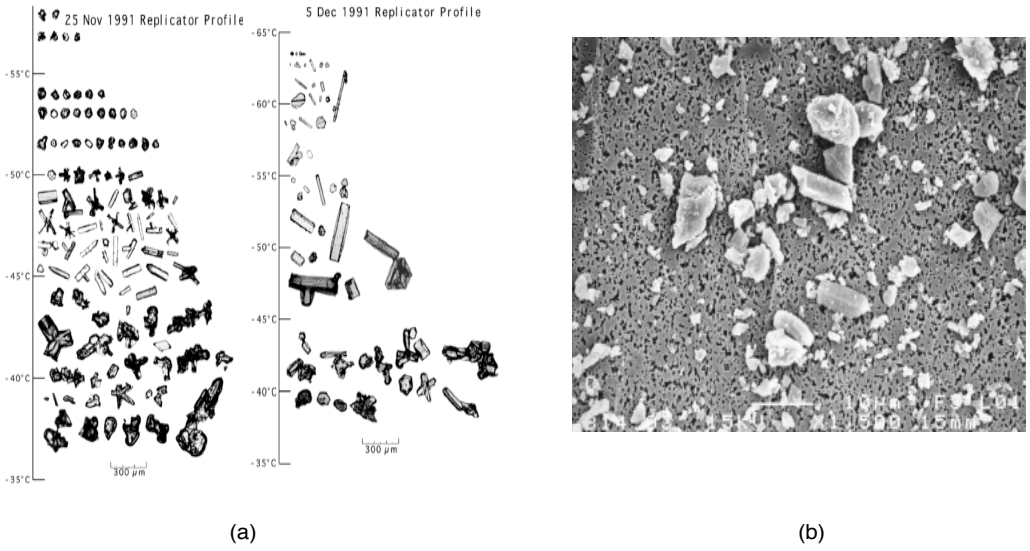

Fig. 1. (a) Morphology of ice crystals at different temperature indicated along the ordinate. (From Heymsfield and Iaquinta [35]). (b) Feldspar aerosols (From Volten et al. [36])

Besides the computational difficulties, the modeling of the scattering by nonspherical particles meets additional issues arising from the diversity of nonsphericity, as shown in Fig. 1. The characterization of the nonsphericity of realistic irregular particles is quite challenging. For ice crystals, the basic shape is hexagonal column or plate. Due to complex atmospheric environment during the growth of ice crystals, ice crystals may be hollow, rough, or quite irregular and even tend to aggregate. For dust

aerosols, there is no particular morphology. Therefore, the parameterization of the nonsphericity of ice crystals and aerosols proposes new research issues for the theory of scattering by nonspherical particles. The effective treatment of this issue would be the use of simple nonspherical shapes to represent realistic irregular particles under the guidance of observed optical phenomenon in the atmosphere, data from airborn instruments and measurements from experiments in the laboratories. We report the present efforts to develop optical models for ice crystals and mineral dust aerosols in the atmosphere.

Before we study the two classes of aforementioned issues, in Section B in this chapter, we introduce the basic concepts of the scattering of light by an individual particle, and commonly defined single-scattering quantities.

B. Basic Concepts and Quantities

In three dimensional free space (or homogenous non-absorbing medium), the basic solution to the macroscopic Maxwell equations is a plane wave without change of its direction of propagation, its magnitude and its polorization. When particles exist in the space (hence, inhomogeneity is introduced), the solution to Maxwell equations is no longer the original plane wave field, and usually termed as the total field. The difference between the total field and the original plane wave (incident field) is called the scattered field. Physically, a radiation condition (the scattered field at infinity should behave like outgoing spherical waves) should be imposed to guarantee the uniqueness of the solutions. From an experimental perspective, the angular information of electromagnetic waves can be detected beyond the direction of original propagating wave. This phenomenon is termed as "electromagnetic wave/light scattering".

In general, electromagnetic wave scattering can be classified into two types; elas-

tic and inelastic. In "elastic scattering", the frequency of scattered field is the same as that of incident field. From a micro-physical perspective, the electromagnetic scattering is due to electric dipoles that oscillat with the same frequency as the incident field. In "inelastic scattering"*, frequency shift happens in the scattering process, such as Raman and Brillouin scattering, in which the incident radiation field will also interact with phonons, magons as well as electronic excitation. The present dissertation is to study "elastic scattering of electromagnetic plane wave by small particles in the atmosphere".

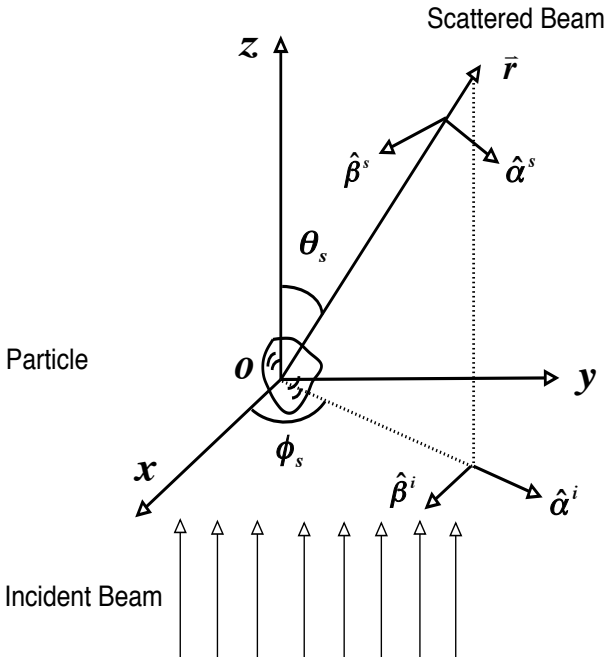

Fig. 2. Definition of scattering geometry by an arbitrary particle

In most situations, the detector/observer is far away from the particles. The observed scattered field in this region also contains the information of micro-physical properties of the particles such as size, morphology and composition. The unique

*This definition has nothing to do with the absorption of light.

behavior of the far scattered field is that the radial components of the electric and magnetic fields are zero. Hence, locally, it is a transverse plane wave. To describe the scattering process, for convenience, a scattering plane is defined as the plane composed of the direction of incident plane wave and the scattering direction, as shown in Fig. 2. With respect to each scattering plane, an amplitude scattering matrix transforms the incident parallel and perpendicular electric field components to their counterparts in the scattered field as follows [3],

$$\begin{bmatrix} E_\alpha^s \\ E_\beta^s \end{bmatrix} = \frac{\exp\left[ik(r-z)\right]}{-ikr} \begin{bmatrix} S_2 & S_3 \\ S_4 & S_1 \end{bmatrix} \begin{bmatrix} E_\alpha^i \\ E_\beta^i \end{bmatrix}, \tag{1.1}$$

where four elements of the amplitude scattering matrix $S_i (i = 1, 4)$ are complex numbers and contain the information of how the particle scatters and absorbs the incident light. As measured quantities have a dimension of "energy", the intensity and polarization characteristics are usually described through Stokes parameters (I, Q, U, V), which are defined in terms of scattering plane as follows [3]

$$I = E_\alpha E_\alpha^* + E_\beta E_\beta^*, \tag{1.2}$$

$$Q = E_\alpha E_\alpha^* - E_\beta E_\beta^*, \tag{1.3}$$

$$U = E_\alpha E_\beta^* + E_\beta E_\alpha^*, \tag{1.4}$$

$$V = i(E_\alpha E_\beta^* - E_\beta E_\alpha^*). \tag{1.5}$$

The phase matrix P is to transform the Stokes vectors of incident light to those of scattered light, and can be derived from the four elements of amplitude scattering matrix. Let's start with four defined quantities:

$$a = E_\alpha {E_\alpha}^*, \quad b = E_\beta {E_\beta}^*, \tag{1.6}$$

$$c = E_\alpha {E_\beta}^*, \quad d = {E_\alpha}^* E_\beta. \tag{1.7}$$

Then $[I, Q, U, V]$ and $[a, b, c, d]$ are related by a linear transformation,

$$\begin{bmatrix} I \\ Q \\ U \\ V \end{bmatrix}^{inc/sca} = L \begin{bmatrix} a \\ b \\ c \\ d \end{bmatrix}^{inc/sca}, \tag{1.8}$$

where the superscripts *inc* and *sca* denote that the quantities are associated with incident field and scattered field, respectively, and L is a 4×4 matrix given by

$$L = \begin{pmatrix} 1 & 1 & 0 & 0 \\ 1 & -1 & 0 & 0 \\ 0 & 0 & 1 & 1 \\ 0 & 0 & i & -i \end{pmatrix}. \tag{1.9}$$

Starting from the amplitude scattering matrix, after some algebraic malipulations, we get

$$\begin{bmatrix} a \\ b \\ c \\ d \end{bmatrix}^{sca} = T \begin{bmatrix} a \\ b \\ c \\ d \end{bmatrix}^{inc}, \tag{1.10}$$

where T is

$$T = \begin{pmatrix} S_2 {S_2}^* & S_3 {S_3}^* & S_2 {S_3}^* & S_3 {S_2}^* \\ S_4 {S_4}^* & S_1 {S_1}^* & S_4 {S_1}^* & S_1 {S_4}^* \\ S_2 {S_4}^* & S_3 {S_1}^* & S_2 {S_1}^* & S_3 {S_4}^* \\ S_4 {S_2}^* & S_1 {S_3}^* & S_4 {S_3}^* & S_1 {S_2}^* \end{pmatrix}. \tag{1.11}$$

Combining Eq. (1.8) and Eq. (1.10) yields the scattering phase matrix

$$P = LTL^{-1}, \tag{1.12}$$

which can be further written in an explicit form of

$$P = \begin{pmatrix} P_{11} & P_{12} & P_{13} & P_{14} \\ P_{21} & P_{22} & P_{23} & P_{24} \\ P_{31} & P_{32} & P_{33} & P_{34} \\ P_{41} & P_{42} & P_{43} & P_{44} \end{pmatrix} \tag{1.13}$$

with elements given by [3]

$$P_{11} = \frac{1}{2}(S_2{S_2}^* + S_4{S_4}^* + S_3{S_3}^* + S_1{S_1}^*), \tag{1.14}$$

$$P_{12} = \frac{1}{2}(S_2{S_2}^* + S_4{S_4}^* - S_3{S_3}^* - S_1{S_1}^*), \tag{1.15}$$

$$P_{13} = \frac{1}{2}(S_2{S_3}^* + S_4{S_1}^* + S_3{S_2}^* + S_1{S_4}^*), \tag{1.16}$$

$$P_{14} = \frac{1}{2i}(S_2{S_3}^* + S_4{S_1}^* - S_3{S_2}^* - S_1{S_4}^*), \tag{1.17}$$

$$P_{21} = \frac{1}{2}(S_2{S_2}^* - S_4{S_4}^* + S_3{S_3}^* - S_1{S_1}^*), \tag{1.18}$$

$$P_{22} = \frac{1}{2}(S_2{S_2}^* - S_4{S_4}^* - S_3{S_3}^* + S_1{S_1}^*), \tag{1.19}$$

$$P_{23} = \frac{1}{2}(S_2{S_3}^* - S_4{S_1}^* + S_3{S_2}^* - S_1{S_4}^*), \tag{1.20}$$

$$P_{24} = \frac{1}{2i}(S_2{S_3}^* + S_4{S_1}^* - S_3{S_2}^* - S_1{S_4}^*), \tag{1.21}$$

$$P_{31} = \frac{1}{2}(S_2{S_4}^* + S_4{S_2}^* + S_3{S_1}^* + S_1{S_3}^*), \tag{1.22}$$

$$P_{32} = \frac{1}{2}(S_2{S_4}^* + S_4{S_2}^* - S_3{S_1}^* - S_1{S_3}^*), \tag{1.23}$$

$$P_{33} = \frac{1}{2}(S_2{S_1}^* + S_4{S_3}^* + S_3{S_4}^* + S_1{S_2}^*), \tag{1.24}$$

$$P_{34} = \frac{1}{2i}(S_2{S_1}^* + S_4{S_3}^* - S_3{S_4}^* - S_1{S_2}^*), \tag{1.25}$$

$$P_{41} = \frac{i}{2}(S_2 {S_4}^* - S_4 {S_2}^* + S_3 {S_1}^* - S_1 {S_3}^*), \tag{1.26}$$

$$P_{42} = \frac{i}{2}(S_2 {S_4}^* - S_4 {S_2}^* - S_3 {S_1}^* + S_1 {S_3}^*), \tag{1.27}$$

$$P_{43} = \frac{i}{2}(S_2 {S_1}^* - S_4 {S_3}^* + S_3 {S_4}^* - S_1 {S_2}^*), \tag{1.28}$$

$$P_{44} = \frac{1}{2}(S_2 {S_1}^* - S_4 {S_3}^* - S_3 {S_4}^* + S_1 {S_2}^*). \tag{1.29}$$

In addition to the description of the angular distribution of scattered light, the integrated scattering properties associated with the extinction, the scattering, and the absorption of light are essentially required in understanding radiative transfer. According to the optical theorem, the total extinction cross section of incident light is given by

$$C_{ext} = \frac{2\pi}{k^2}\{[S_1(0^0) + S_2(0^0)] + [S_2(0^0) - S_1(0^0)](Q_{inc}/I_{inc}) \\ +[S_3(0^0) + S_4(0^0)](U_{inc}/I_{inc}) + i[S_3(0^0) - S_4(0^0)](V_{inc}/I_{inc})\}. \tag{1.30}$$

C_{ext} depends on the particle orientation and polarization state of incident light. Straightforwardly, the scattering cross section is the integration of intensity of outgoing scattered waves

$$C_{sca} = \frac{1}{k^2}\int_0^{\pi}\int_0^{2\pi}(P_{11} + P_{12}Q_{inc}/I_{inc} \\ +P_{13}U_{inc}/I_{inc} + P_{14}V_{inc}/I_{inc})\sin\theta d\theta d\phi. \tag{1.31}$$

Note that two components of Stokes vector (Q_{inc} and U_{inc}) in Eq. (1.31) is a function of azimuthal angle ϕ for a specific incident light. According to the conservation of energy, the absorption cross section is given by

$$C_{abs} = C_{ext} - C_{sca}. \tag{1.32}$$

Single-scattering albedo is a quantity defined as

$$\omega = \frac{C_{sca}}{C_{ext}} = 1 - \frac{C_{abs}}{C_{ext}}. \tag{1.33}$$

A complete set of the single-scattering properties includes the phase matrix, the extinction efficiency (C_{ext} divided by the projected area of particle), and the absorption efficiency (C_{abs} divided by the projected area of particle), which contain microphysical information of particles, such as size, morphology and composition. Asymmetry factor to characterize the angular distribution of scattered intensity is usually defined as

$$\begin{aligned} g =< \cos\theta >= \frac{1}{k^2 C_{sca}} \int_0^{\pi} \int_0^{2\pi} (P_{11} + P_{12} Q_{inc}/I_{inc} \\ + P_{13} U_{inc}/I_{inc} + P_{14} V_{inc}/I_{inc}) \cos\theta \sin\theta d\theta d\phi \end{aligned} \tag{1.34}$$

The extinction efficiency, the single-scattering albedo and the asymmetry factor are important optical parameters in many climate models.

C. Organization of the Dissertation

The remainder of the dissertation is organized as follows. The first part (Chapters II-V) is on the methods for the solution of light scattering by nonspherical particles. The second part (Chapters VI-VII) presents the approach of optical modeling of ice crystals and mineral dust aerosols. Specifically, in Chapter II, we outline the basic mathematical relations to formulate the solution of light scattering. In Chapter III, the general theoretical framework of three rigorous methods (i.e., the FDTD, the DDA and the EBCM) are summarized. We carry out some comparison study for mutual verification. Chapter IV begins with some general physical consideration of geometric optics method, and then presents essential components of a new physical-

geometric optics hybrid (PGOH) method. In Chapter V, we present some studies on electromagnetic edge effect involved in light scattering by nonspherical particles. In Chapter VI, the optical modeling approach for ice crystals is discussed. Numerical results are demonstrated for randomly oriented ice crystals, oriented ice crystals, and imperfect ice crystals. Particular attention is paid to the color ratio (ratio of backscattering coefficients of ice particles at different wavelengths) study. In Chapter VII, we discuss the new exploration of the use of simple geometries to model realistic mineral dust aerosols. We investigate two model shapes: triaxial ellipsoids and nonsymmetric hexahedra. Comparisons of simulated results and measurement data are given. Finally, in Chapter VIII, we conclude the present research and suggest some future studies in this field.

CHAPTER II

FORMAL SOLUTION OF SCATTERING

The scattered field in radiation region can be related to the near-field exactly through the dyadic Green's function. The basic idea is to transform differential Maxwell equations to integral equations. The near-field can be either the internal field within the particle or the field on the surface enclosing the particle. Once the near-field is obtained, the extinction, the scattering and the absorption cross sections can be obtained based on Poyting's theorem. These relationships are fundamental to the methods of FDTD, DDA, and PGOH.

Different from the FDTD, DDA, and PGOH, whose solution of scattering of light are based on the near-field, the T-matrix formulation of the solution of scattering is to relate the expansion coefficients of scattered field and those of incident field in a functional space through a matrix as called T-matrix. Once the T-matrix is obtained, the basic quantities of light scattering can be calculated.

In this Chapter, we summarize the near- to far-field transformation, and the definition of T-matrix. The basic quantities of light scattering are represented based on the near-field, and the T-matrix. As near-field and T-matrix are still unknown, the solution of scattering of light is called formal solution. Three rigorous techniques (the FDTD, DDA, and EBCM) are introduced in Chapter III to calculate the near-field and the T-matrix. An approximate method based on geometric optics is developed to calculate the near-field in Chapter IV.

In principle, the T-matrix can be computed from the FDTD or the DDA; however, it is not necessary to do this to obtain optical quantities of concern. Therefore, the EBCM is called the T-matrix method in most literature. To be more rigorous, T-matrix is not a method but a formulation of the solution of light scattering.

A. Maxwell Equations

Maxwell equations in Gaussian unit system are written as [37]

$$\vec{\nabla} \cdot \vec{D}(\vec{r},t) = 4\pi\rho(\vec{r},t), \qquad \vec{\nabla} \times \vec{H}(\vec{r},t) - \frac{1}{c}\frac{\partial \vec{D}(\vec{r},t)}{\partial t} = \frac{4\pi}{c}\vec{J}(\vec{r},t), \tag{2.1}$$

$$\vec{\nabla} \cdot \vec{B}(\vec{r},t) = 0, \qquad \vec{\nabla} \times \vec{E}(\vec{r},t) + \frac{1}{c}\frac{\partial \vec{B}(\vec{r},t)}{\partial t} = 0, \tag{2.2}$$

where $\vec{D}$ is the electric displacement, $\vec{B}$ is the magnetic flux density, $\vec{H}$ is the magnetic field, $\vec{E}$ is electric field, ρ is free electric charge density, c is the speed of light in vacuum, and $\vec{J}$ is electric current density. $\vec{D}$ is related to $\vec{E}$ through $\vec{D} = \epsilon(\vec{r})\vec{E}$, where ϵ is the permittivity and $\vec{B}$ is related to $\vec{H}$ through $\vec{B} = \mu(\vec{r})\vec{H}$, where μ is the permeability. Here we consider the scattering of a polarized plane wave with the time dependence of $\exp(-i\omega t)$, or $\exp(-ikct)$ by a particle. The active sources of incident plane wave is at infinity, and will not be affected by particles as the sources of passive radiation. The electric charge density and electric current density in the finite regime are zero. Therefore, the two curl equations in (2.1) and (2.2) are written as

$$\vec{\nabla} \times \vec{H}(\vec{r}) + ik\epsilon(\vec{r})\vec{E}(\vec{r}) = 0, \tag{2.3}$$

$$\vec{\nabla} \times \vec{E}(\vec{r}) - ik\mu(\vec{r})\vec{H}(\vec{r}) = 0, \tag{2.4}$$

where, for convenience without of loss of clarity, we use the same symbols of quantities in both the time and frequency domain. The solution to Eqs. (2.3) and (2.4) can be determined by giving the following particle boundary conditions,

$$\hat{n} \times (\vec{H}_1 - \vec{H}_2) = 0, \hat{n} \times (\vec{E}_1 - \vec{E}_2) = 0 \tag{2.5}$$

and radiation conditions,

$$\vec{H} = \hat{k} \times \vec{E}, E_\theta/\phi \rightarrow \frac{\exp(ikr)}{kr}. \tag{2.6}$$

In Eq. (2.5), $\vec{H}_1$ and $\vec{E}_1$ are the fields on the internal surface of the particle and $\vec{H}_2$ and $\vec{E}_2$ are the fields on the external surface of the particle, and $\hat{n}$ is the local outward normal direction.

B. Dyadic Green's Function

For convenience, we rewrite Eqs.(2.3) and (2.4) in the following form,

$$\vec{\nabla} \times \vec{H}(\vec{r}) + ik\vec{E}(\vec{r}) = \frac{4\pi}{c}\vec{J}(\vec{r}), \tag{2.7}$$

$$\vec{\nabla} \times \vec{E}(\vec{r}) - ik\vec{H}(\vec{r}) = -\frac{4\pi}{c}\vec{M}(\vec{r}), \tag{2.8}$$

where $\vec{J}$ and $\vec{M}$ are called equivalent volume sources in free space, given by

$$\vec{J}(\vec{r}) = -i\frac{kc}{4\pi}\left[\epsilon(\vec{r}) - 1\right]\vec{E}(\vec{r}), \quad \vec{M}(\vec{r}) = -i\frac{kc}{4\pi}\left[\mu(\vec{r}) - 1\right]\vec{H}(\vec{r}). \tag{2.9}$$

Taking cross product $\vec{\nabla}\times$ at both sides of Eqs. (2.7) and (2.8) yields,

$$\vec{\nabla} \times \vec{\nabla} \times \vec{E}(\vec{r}) - k^2\vec{E}(\vec{r}) = ik\frac{4\pi}{c}\vec{J}(\vec{r}) - \frac{4\pi}{c}\vec{\nabla} \times \vec{M}(\vec{r}), \tag{2.10}$$

$$\vec{\nabla} \times \vec{\nabla} \times \vec{H}(\vec{r}) - k^2\vec{H}(\vec{r}) = ik\frac{4\pi}{c}\vec{M}(\vec{r}) + \frac{4\pi}{c}\vec{\nabla} \times \vec{J}(\vec{r}). \tag{2.11}$$

To solve Eqs.(2.10) and (2.11), dyadic Green's function $\overleftrightarrow{G}(\vec{r} - \vec{r}')$ is defined to be the solution of [38]

$$\vec{\nabla} \times \vec{\nabla} \times \overleftrightarrow{G}(\vec{r} - \vec{r}') \quad -k^2\overleftrightarrow{G}(\vec{r} - \vec{r}') = \overleftrightarrow{I}\,\delta(\vec{r} - \vec{r}'). \tag{2.12}$$

where $\overleftrightarrow{I}$ is a unit dyadic, and δ is Dirac delta function.

Once dyadic Green's function is obtained, then solution to Eqs. (2.10) and (2.11)

can be represented as,

$$\begin{aligned}\vec{E}(\vec{r}) = \vec{E}^{inc}(\vec{r}) &+ ik\frac{4\pi}{c}\int \overleftrightarrow{G}(\vec{r}-\vec{r}')\cdot\vec{J}(\vec{r}')d^3\vec{r}' \\ &- \frac{4\pi}{c}\int \overleftrightarrow{G}(\vec{r}-\vec{r}')\cdot\vec{\nabla}\times\vec{M}(\vec{r}')d^3\vec{r}', \qquad (2.13)\\ \vec{H}(\vec{r}) = \vec{H}^{inc}(\vec{r}) &+ ik\frac{4\pi}{c}\int \overleftrightarrow{G}(\vec{r}-\vec{r}')\cdot\vec{M}(\vec{r}')d^3\vec{r}' \\ &+ \frac{4\pi}{c}\int \overleftrightarrow{G}(\vec{r}-\vec{r}')\cdot\vec{\nabla}\times\vec{J}(\vec{r}')d^3\vec{r}', \qquad (2.14)\end{aligned}$$

where $\vec{E}^{inc}$ and $\vec{H}^{inc}$ are incident electric and magnetic field in the absence of particles. If $\mu = 1$ (i.e., the particle is dielectric and nonmagnetic), Eqs.(2.13) and (2.14) are written in a simpler form of,

$$\begin{aligned}\vec{E}(\vec{r}) &= \vec{E}^{inc}(\vec{r}) + k^2\int(\epsilon-1)\overleftrightarrow{G}(\vec{r}-\vec{r}')\cdot\vec{E}(\vec{r}')d^3\vec{r}', \qquad (2.15)\\ \vec{H}(\vec{r}) &= \vec{H}^{inc}(\vec{r}) - ik\int(\epsilon-1)\vec{\nabla}G(\vec{r}-\vec{r}')\times\vec{E}(\vec{r}')d^3\vec{r}'. \qquad (2.16)\end{aligned}$$

At this point, we turn to solve the dyadic equation (2.12). Taking dot product $\vec{\nabla}\cdot$ on both sides of Eq. (2.12), we obtain

$$\vec{\nabla}\cdot\overleftrightarrow{G}(\vec{r}-\vec{r}') = -\frac{1}{k^2}\vec{\nabla}\cdot\overleftrightarrow{I}\,\delta(\vec{r}-\vec{r'}) = -\frac{1}{k^2}\vec{\nabla}\delta(\vec{r}-\vec{r'}) \qquad (2.17)$$

By using $\vec{\nabla}\times\vec{\nabla}\times = \vec{\nabla}\vec{\nabla}\cdot - \vec{\nabla}^2$, we write Eq. (2.12) as follows,

$$(\vec{\nabla}^2 + k^2)\overleftrightarrow{G}(\vec{r}-\vec{r}') = \vec{\nabla}\vec{\nabla}\cdot\overleftrightarrow{G}(\vec{r}-\vec{r}') - \overleftrightarrow{I}\,\delta(\vec{r}-\vec{r'}). \qquad (2.18)$$

Substituting Eq.(2.17) into Eq.(2.18) yields

$$(\vec{\nabla}^2 + k^2)\overleftrightarrow{G}(\vec{r}-\vec{r}') = -\left[\overleftrightarrow{I} + \frac{\vec{\nabla}\vec{\nabla}}{k^2}\right]\delta(\vec{r}-\vec{r'}). \qquad (2.19)$$

One can find that the solution to Eq.(2.19) can be

$$\overleftrightarrow{G}(\vec{r}-\vec{r'}) = \left[\overleftrightarrow{I} + \frac{\vec{\nabla}\vec{\nabla}}{k^2}\right] G(\vec{r}-\vec{r'}) \tag{2.20}$$

where G is the free space Green's function defined by

$$(\vec{\nabla}^2 + k^2)G(\vec{r}-\vec{r'}) = -\delta(\vec{r}-\vec{r'}), \tag{2.21}$$

of which one of the solutions that satisfy the radiation condition,

$$\lim_{r\to\infty} r\left[ikG(\vec{r}-\vec{r'}) + \frac{\partial G(\vec{r}-\vec{r'})}{\partial r}\right] = 0 \tag{2.22}$$

is

$$G(\vec{r},\vec{r'}) = \frac{e^{ik|\vec{r}-\vec{r'}|}}{4\pi|\vec{r}-\vec{r'}|}. \tag{2.23}$$

To derive the explicit expression of dyadic Green's function (2.20), we let $R = |\vec{r}-\vec{r'}|$, use the following operations,

$$\vec{\nabla}G(\vec{r}-\vec{r'}) = (ik - \frac{1}{R})G(\vec{r}-\vec{r'})\hat{R}, \tag{2.24}$$

$$\vec{\nabla}\vec{\nabla}G(\vec{r}-\vec{r'}) = \vec{\nabla}\left[(ik-\frac{1}{R})G(\vec{r}-\vec{r'})\right]\hat{R} + (ik-\frac{1}{R})G(\vec{r}-\vec{r'})\vec{\nabla}\hat{R}, \tag{2.25}$$

$$\vec{\nabla}\hat{R} = \frac{\vec{\nabla}\vec{r}}{R} - \frac{\vec{R}\hat{R}}{R^2}, \tag{2.26}$$

$$\vec{\nabla}\vec{r} = \overleftrightarrow{I}, \tag{2.27}$$

and then obtain

$$\overleftrightarrow{G}(\vec{r}-\vec{r'}) = G(\vec{r}-\vec{r'})\left[(\overleftrightarrow{I} - \frac{\vec{R}\vec{R}}{R^2}) - \frac{1-ikR}{(kR)^2}(\overleftrightarrow{I} - \frac{3\vec{R}\vec{R}}{(kR)^2})\right]. \tag{2.28}$$

For later usage, we list other useful properties of dyadic Green's function as follows,

$$\vec{\nabla} \times \overleftrightarrow{G}(\vec{r} - \vec{r'}) = \vec{\nabla} \times (\overleftrightarrow{I} G) = \vec{\nabla} G \times \overleftrightarrow{I} = (ik - \frac{1}{R}) G(R) \hat{R} \times \overleftrightarrow{I}, \quad (2.29)$$

$$G(\vec{r} - \vec{r'})|_{R \to \infty} = \frac{e^{ikr}}{4\pi r} e^{-ik\vec{r'} \cdot \hat{r}}, \quad (2.30)$$

$$\vec{\nabla} G(\vec{r} - \vec{r'})|_{R \to \infty} = ik \frac{e^{ikr}}{4\pi r} e^{-ik\vec{r'} \cdot \hat{r}} \hat{r}, \quad (2.31)$$

$$\overleftrightarrow{G}|_{R \to \infty} = [\overleftrightarrow{I} - \hat{r}\hat{r}] \frac{e^{ikr}}{4\pi r} e^{-ik\vec{r'} \cdot \hat{r}}, \quad (2.32)$$

$$\vec{\nabla} \times \overleftrightarrow{G}|_{R \to \infty} = ik \frac{e^{ikr}}{4\pi r} e^{-ik\vec{r'} \cdot \hat{r}} \hat{r} \times \overleftrightarrow{I}. \quad (2.33)$$

C. Near-to-far-field Transformation

Based on Eq. (2.15) and Eq. (2.32), the scattered field in the radiation zone [39] is

$$\vec{E}^s(\vec{r}) = \frac{k^2 \exp(ikr)}{4\pi r} (\epsilon - 1) \int \left\{ \vec{E}(\vec{r'}) - \hat{r} \left[\hat{r} \cdot \vec{E}(\vec{r'}) \right] \exp\left(-i\vec{k} \cdot \vec{r'} \right) \right\} d^3 r', \quad (2.34)$$

where $\vec{E}(\vec{r'})$ is the total field inside of the particle. One can also express the electric field in the radiation zone through surface integral equation. To do this, the starting point is Greens' theorem:

$$\int \vec{\nabla} \cdot \vec{A} dv = \int \vec{A} \cdot \hat{n}_s ds \quad (2.35)$$

where $\hat{n}_s$ is a unit vector pointing outward the volume and $\vec{A}$ is an arbitrary vector field. Let $\vec{A}$ be in the form of

$$\vec{A} = \vec{b} \times (\vec{\nabla} \times \vec{a}) - \vec{a} \times (\vec{\nabla} \times \vec{b}). \quad (2.36)$$

Here $\vec{a}$ and $\vec{b}$ are given by

$$\vec{a} = \vec{E}(\vec{r'}), \quad \vec{b} = \overleftrightarrow{G}(\vec{r} - \vec{r'}) \cdot \vec{c}. \quad (2.37)$$

By using the following identity

$$\vec{\nabla}\cdot\vec{A}=\vec{a}\cdot\vec{\nabla}\times(\vec{\nabla}\times\vec{b})-\vec{b}\cdot\vec{\nabla}\times(\vec{\nabla}\times\vec{a}), \tag{2.38}$$

one find

$$\begin{aligned}\vec{\nabla}\cdot\vec{A} &= k^2\vec{E}\cdot[\overleftrightarrow{G}\cdot\vec{c}]+\vec{E}\cdot\vec{c}\delta(\vec{r}-\vec{r}')-k^2\vec{E}\cdot[\overleftrightarrow{G}\cdot\vec{c}]=\vec{E}\cdot\vec{c}\delta(\vec{r}-\vec{r}'), \quad (2.39)\\ \vec{A} &= [\overleftrightarrow{G}(\vec{r}-\vec{r}')\cdot\vec{c}]\times\vec{\nabla}\times\vec{E}-\vec{E}\times[\vec{\nabla}\times\overleftrightarrow{G}(\vec{r}-\vec{r}')\cdot\vec{c}]. \quad (2.40)\end{aligned}$$

Substituting Eqs. (2.39) and (2.40) into Eq. (2.35) yields

$$\vec{E}(\vec{r})=\left[-\int_{s_\infty}+\int_s\right]ds\hat{n}\cdot\left\{ik\vec{H}(\vec{r'})\times\overleftrightarrow{G}(\vec{r}-\vec{r}')+\vec{E}(\vec{r'})\times\left[\vec{\nabla}\times\overleftrightarrow{G}(\vec{r}-\vec{r}')\right]\right\} \tag{2.41}$$

Take into account the radiation condition [40],

$$\lim_{r\to\infty}r\left[ik\hat{r}\times\overleftrightarrow{G}(\vec{r}-\vec{r}')+\vec{\nabla}\times\overleftrightarrow{G}(\vec{r}-\vec{r}')\right]=0, \tag{2.42}$$

the integral over the surface at infinity in Eq.(2.41) vanishes. Therefore, one obtain

$$\vec{E}=\int_s ds\hat{n}_s\cdot\left\{ik\vec{H}\times\overleftrightarrow{G}(\vec{r}-\vec{r}')+\vec{E}\times[\vec{\nabla}\times\overleftrightarrow{G}(\vec{r}-\vec{r}')]\right\}. \tag{2.43}$$

In the radiation zone, by using Eqs. (2.30) − (2.33), we further obtain,

$$\vec{E}^s(\vec{r})=\frac{\exp(ikr)}{-ikr}\frac{k^2}{4\pi}\iint\left\{\hat{r}\times\left[\hat{n}_s\times\vec{E}(\vec{r}')\right]-\hat{r}\times\hat{r}\times\left[\hat{n}_s\times\vec{H}(\vec{r}')\right]\right\}\exp(-ik\hat{r}\cdot\vec{r}')d^2\vec{r}'. \tag{2.44}$$

If starting from Green's theorem,

$$\int(\phi\vec{\nabla}^2\psi-\psi\vec{\nabla}^2\phi)dv=\int_s\left[\phi\frac{\partial\psi}{\partial n}-\psi\frac{\partial\phi}{\partial n}\right] \tag{2.45}$$

and letting

$$\phi=E_i,\quad \psi=G(\vec{r}-\vec{r}'), \tag{2.46}$$

we have,

$$\vec{E} = \int_s \left[\vec{E} \frac{\partial G}{\partial n} - G \frac{\partial \vec{E}}{\partial n} \right] d^2\vec{r}'. \tag{2.47}$$

In the radiation zone, Eq. (2.47) is in the form of [28]

$$\vec{E}^s = \frac{\exp(ikr)}{-ikr} \frac{-k^2}{4\pi} \int \left[\hat{n}_s \cdot \hat{r} \vec{E}(\vec{r}') + \frac{1}{ik} \frac{\partial \vec{E}(\vec{r}')}{\partial n_s} \right] \exp(-ik\hat{r} \cdot \vec{r}') d^2\vec{r}'. \tag{2.48}$$

At this point, there are three equations (2.34),(2.44), and(2.48) that establish the relationship between the near-field and the far-field.

D. Equivalence Principle

In a space with active sources, the solution to Maxwell equations can be represented in terms of Hertz potentials. Equivalent principle states that the scattered field outside the particle is the same as the activated field of "equivalent sources" [41]. Therefore, the solution of scattering problem can be written in terms of Hertz potentials associated with "equivalent sources". For example, let the permittivity and permeability of the equivalent system are unity, and equivalent currents in the volume of the particle are,

$$\vec{J}(\vec{r}) = -ik \left[\epsilon(\vec{r}) - 1 \right] \vec{E}(\vec{r}), \quad \vec{M}(\vec{r}) = -ik \left[\mu(\vec{r}) - 1 \right] \vec{H}(\vec{r}) \tag{2.49}$$

For dielectric particles, $\vec{M} = 0$, so the electrical and magnetic Hertz potentials are given by

$$A(\vec{r}) = \iint G(\vec{r}, \vec{r}') \vec{J}(\vec{r}') d^2\vec{r}', \quad F(\vec{r}') = 0 \tag{2.50}$$

Therefore [42]

$$\vec{E}^s(\vec{r}) = \frac{i}{k} \vec{\nabla} \times \vec{\nabla} \times \vec{A}(\vec{r}) \tag{2.51}$$

It can be found that the solution from Eq. (2.51) is equal to Eq. (2.15) obtained from dyadic Green's function.

According to boundary conditions, equivalent surface currents can be given in the form of [4, 41],

$$\vec{M} = \vec{E} \times \hat{n}_s, \quad \vec{J} = \hat{n}_s \times \vec{H}. \tag{2.52}$$

Hertz potentials are given by

$$\vec{A}(\vec{r}) = \int_s G(\vec{r} - \vec{r}')(\hat{n}_s \times \vec{H}(\vec{r}'))dS, \tag{2.53}$$

$$\vec{F}(\vec{r}) = \int_s G(\vec{r} - \vec{r}')(\vec{E}(\vec{r}') \times \hat{n}_s)dS. \tag{2.54}$$

Therefore, the scattered field outside of the volume enclosing the particle is given by [42]

$$\vec{E}_s(\vec{r}) = \frac{i}{k}\vec{\nabla} \times \vec{\nabla} \times \vec{A}(\vec{r}) - \vec{\nabla} \times \vec{F}(\vec{r}). \tag{2.55}$$

Note that,

$$\begin{aligned} \vec{\nabla}\left\{\vec{\nabla} \cdot \left[G(\vec{r} - \vec{r}')[\hat{n}_s \times \vec{H}(\vec{r}')]\right]\right\} &= \left[\hat{n}_s \times \vec{H}(\vec{r}')\right] \cdot \vec{\nabla}\vec{\nabla}G(\vec{r} - \vec{r}') \\ &= \hat{n}_s \cdot \vec{H}(\vec{r}') \times \vec{\nabla}\vec{\nabla}G(\vec{r} - \vec{r}'), \end{aligned} \tag{2.56}$$

$$\begin{aligned} \vec{\nabla}^2\left[G(\vec{r} - \vec{r}')\hat{n}_s \times \vec{H}(\vec{r}')\right] &= -k^2 G(\vec{r} - \vec{r}')\hat{n}_s \times \vec{H}(\vec{r}') \\ &= -k^2 \hat{n}_s \cdot \vec{H}(\vec{r}') \times \left[\overleftrightarrow{I}\, G(\vec{r} - \vec{r}')\right], \end{aligned} \tag{2.57}$$

$$\begin{aligned} \vec{\nabla} \times \left[G(\vec{r} - \vec{r}')\vec{E}(\vec{r}') \times \hat{n}_s\right] &= \vec{\nabla} \times \left[G(\vec{r} - \vec{r}')\overleftrightarrow{I} \cdot (\vec{E}(\vec{r}') \times \hat{n}_s)\right] \\ &= \vec{\nabla} \times \overleftrightarrow{G}(\vec{r} - \vec{r}') \cdot \left[\vec{E}(\vec{r}') \times \hat{n}_s\right] \\ &= -\hat{n}_s \cdot \vec{E}(\vec{r}') \times \vec{\nabla} \times \overleftrightarrow{G}(\vec{r} - \vec{r}'), \end{aligned} \tag{2.58}$$

and

$$\vec{\nabla} \times \overleftrightarrow{G} = \vec{\nabla} \times (\overleftrightarrow{I} G). \tag{2.59}$$

We can obtain,

$$\vec{E}_s(\vec{r}) = \int_s \hat{n}_s \cdot \left\{ ik\vec{H}(\vec{r}') \times \overleftrightarrow{G}(\vec{r} - \vec{r}') + \vec{E}(\vec{r}') \times (\vec{\nabla} \times \overleftrightarrow{G}(\vec{r} - \vec{r}')) \right\}, \tag{2.60}$$

which is the same as Eq. (2.43) derived from vector identity using dyadic Green's function.

E. T-matrix Formulation

The T-matrix is to relate the scattered field and the incident field. Specifically, the incident field and the scattered field are expanded in terms of basis in a functional space. Commonly, vector spheric functions are employed as basis of expansion. Mathematically [5],

$$\vec{E}^{inc} = \sum_{n=1}^{\infty} \sum_{m=-n}^{n} \left[a_{mn} \mathrm{Rg}\vec{M}_{mn}(k\vec{r}) + b_{mn} \mathrm{Rg}\vec{N}_{mn}(k\vec{r}) \right], \tag{2.61}$$

$$\vec{E}^{sca} = \sum_{n=1}^{\infty} \sum_{m=-n}^{n} \left[p_{mn}\vec{M}_{mn}(k\vec{r}) + q_{mn}\vec{N}_{mn}(k\vec{r}) \right], \tag{2.62}$$

where $\mathrm{Rg}\vec{M}_{mn}$, $\mathrm{Rg}\vec{N}_{mn}$,$\vec{M}_{mn}$, and $\vec{N}_{mn}$ are vector spherical functions as defined in Appendix A, and a_{mn}, b_{mn}, p_{mn}, and q_{mn} are corresponding expansion coefficients. The so-called T-matrix is defined as follows,

$$\begin{bmatrix} \vec{p} \\ \vec{q} \end{bmatrix} = \begin{bmatrix} T_{11} & T_{12} \\ T_{21} & T_{22} \end{bmatrix} \begin{bmatrix} \vec{a} \\ \vec{b} \end{bmatrix}, \tag{2.63}$$

where $\vec{p}$ (or $\vec{a}/\vec{b}/\vec{q}$) is a vector whose components are p_{mn} (or $a_{mn}/b_{mn}/q_{mn}$) listed sequentially according to $n(n+1)+m$. For a polarized plane wave propogating in

a direction specified through polar angles(θ', ϕ'), the expansion coefficients a_{mn} and b_{mn} are readily known [5], given by,

$$a_{mn} = 4\pi i^n \gamma_{mn} \vec{E}_0 \cdot \vec{C}^*_{mn}(\theta', \phi') \tag{2.64}$$

$$b_{mn} = 4\pi i^{n-1} \gamma_{mn} \vec{E}_0 \cdot \vec{B}^*_{mn}(\theta', \phi'). \tag{2.65}$$

where $\vec{E}_0$ is the vector amplitude. Constants γ_{mn} and vector spherical harmonics $\vec{C}_{mn}$ and $\vec{B}_{mn}$ are given in Appendix A. Therefore, once T-matrix is obtained, $\vec{E}^{sca}$ is determined by Eqs. (2.62) and (2.63). As we take interest in the far scattered field, $\vec{E}^{sca}|_{r\to\infty}$ can be obtained by using the asymptotic formula of $\vec{M}_{mn}$ and $\vec{N}_{mn}$ or through Kirhoff surface integral equations (Appendix B), given by

$$\vec{E}^{sca}(r\hat{n}^{sca}) = \frac{1}{k} \sum_{n=1}^{\infty} \sum_{m=-n}^{n} i^{-n} \gamma_{mn} \left[-ip_{mn} \vec{C}_{mn}(\theta^s, \phi^s) + q_{mn} \vec{B}_{mn}(\theta^s, \phi^s) \right], \tag{2.66}$$

The solution of scattered electric field can be written in terms of T-matrix as follows,

$$\begin{aligned} \vec{E}^{sca}(r\hat{n}^{sca}) &= \frac{1}{k} \sum_{n=1}^{\infty} \sum_{m=-n}^{n} \sum_{n'=1}^{\infty} \sum_{m'=-n'}^{n'} i^{-n} \gamma_{mn} \\ &\times \Big[-i \left(T^{11}_{mnm'n'} a_{m'n'} + T^{12}_{mnm'n'} b_{m'n'} \right) \vec{C}_{mn}(\theta^s, \phi^s) \\ &+ \left(T^{21}_{mnm'n'} a_{m'n'} + T^{22}_{mnm'n'} b_{m'n'} \right) \vec{B}_{mn}(\theta^s, \phi^s) \Big]. \end{aligned} \tag{2.67}$$

Substituting Eqs (2.64) and (2.65) into Eq. (2.67) yields

$$\begin{aligned}
\vec{E}^{sca}(r\hat{n}^{sca}) = & \frac{\exp(ikr)}{kr}\sum_{n=1}^{\infty}\sum_{m=-n}^{n}\sum_{n'=1}^{\infty}\sum_{m'=-n'}^{n'} i^{-n}\gamma_{mn} \\
\times & \left[\left(-iT^{11}_{mnm'n'}\vec{C}_{mn}(\theta^s,\phi^s) + T^{21}_{mnm'n'}\vec{B}_{mn}(\theta^s,\phi^s)\right) a_{m'n'}\right. \\
+ & \left.\left(-iT^{12}_{mnm'n'}\vec{C}_{mn}(\theta^s,\phi^s) + T^{22}_{mnm'n'}\vec{B}_{mn}(\theta^s,\phi^s)\right) b_{m'n'}\right] \\
= & \frac{\exp(ikr)}{kr}\sum_{n=1}^{\infty}\sum_{m=-n}^{n}\sum_{n'=1}^{\infty}\sum_{m'=-n'}^{n'} i^{-n}\gamma_{mn}4\pi i^{n'}\gamma_{m'n'} \\
\times & \left[\left(-iT^{11}_{mnm'n'}\vec{C}_{mn}(\theta^s,\phi^s) + T^{21}_{mnm'n'}\vec{B}_{mn}(\theta^s,\phi^s)\right)\vec{C}^{*}_{mn}(\theta^i,\phi^i)\cdot\vec{E}_0\right. \\
+ & \left.\left(-T^{12}_{mnm'n'}\vec{C}_{mn}(\theta^s,\phi^s) - iT^{22}_{mnm'n'}\vec{B}_{mn}(\theta^s,\phi^s)\right)\vec{B}^{*}_{mn}(\theta^i,\phi^i)\cdot\vec{E}_0\right] \quad (2.68)
\end{aligned}$$

The scattering dyad is defined through [5],

$$\vec{E}^{sca}(r\hat{n}^{sca}) = \frac{e^{ikr}}{-ikr}\overleftrightarrow{A}(\hat{n}^{sca},\hat{n}^{inc})\cdot\vec{E}_0. \quad (2.69)$$

Comparison of Eq. (2.68) and (2.69) yields

$$\begin{aligned}
\overleftrightarrow{A}(\hat{n}^{sca},\hat{n}^{inc}) = & \sum_{n=1}^{\infty}\sum_{m=-n}^{n}\sum_{n'=1}^{\infty}\sum_{m'=-n'}^{n'} 4\pi i^{n'-n-1}\gamma_{mn}\gamma_{m'n'} \\
\times & \left[\left(-iT^{11}_{mnm'n'}\vec{C}_{mn}(\theta^s,\phi^s) + T^{21}_{mnm'n'}\vec{B}_{mn}(\theta^s,\phi^s)\right)\vec{C}^{*}_{mn}(\theta^i,\phi^i)\right. \\
+ & \left.\left(-T^{12}_{mnm'n'}\vec{C}_{mn}(\theta^s,\phi^s) - iT^{22}_{mnm'n'}.\vec{B}_{mn}(\theta^s,\phi^s)\right)\vec{B}^{*}_{mn}(\theta^i,\phi^i)\right] \quad (2.70)
\end{aligned}$$

The amplitude scattering matrix elements can be obtained straightforwardly, given by

$$S_{11} = \hat{\theta}^s\cdot\overleftrightarrow{A}\cdot\hat{\theta}^i, \quad (2.71)$$

$$S_{12} = -\hat{\theta}^s\cdot\overleftrightarrow{A}\cdot\hat{\phi}^i, \quad (2.72)$$

$$S_{21} = -\hat{\phi}^s\cdot\overleftrightarrow{A}\cdot\hat{\theta}^i, \quad (2.73)$$

$$S_{22} = \hat{\phi}^s\cdot\overleftrightarrow{A}\cdot\hat{\phi}^i. \quad (2.74)$$

For example [5],

$$
\begin{aligned}
S_{11} = & \sum_{n=1}^{\infty} \sum_{m=-n}^{n} \sum_{n'=1}^{\infty} \sum_{m'=-n'}^{n'} 4\pi i^{n'-n-1} \gamma_{mn} \gamma_{m'n'} \\
& \times \Big[\Big(-iT^{11}_{mnm'n'} \hat{\theta}^s \cdot \vec{C}_{mn}(\theta^s, \phi^s) + T^{21}_{mnm'n'} \hat{\theta}^s \cdot \vec{B}_{mn}(\theta^s, \phi^s) \Big) \vec{C}^*_{mn}(\theta', \phi') \cdot \hat{\theta}^i \\
& + \Big(-T^{12}_{mnm'n'} \hat{\theta}^s \cdot \vec{C}_{mn}(\theta^s, \phi^s) - iT^{22}_{mnm'n'} \hat{\theta}^s \cdot \vec{B}_{mn}(\theta^s, \phi^s) \Big) \vec{B}^*_{mn}(\theta', \phi') \cdot \hat{\theta}^i \Big] \quad (2.75)
\end{aligned}
$$

Note that $\hat{\theta}^i = \hat{\phi}^s \times \hat{z}$, and $\phi_i = \phi_s$.

F. Extinction, Scattering, and Absorption

The cross sections associated with the extinction, the scattering and the absorption of light, as discussed in Chapter I, can be obtained starting from the amplitude scattering matrix. Meanwhile, the amplitude scattering matrix is related to near-field or T-matrix, as already known. This section presents the formulation of the defined three cross sections in terms of the near-field or the T-matrix. Let's start from the complex poynting vector, which is defined as [37]

$$\vec{S} = \frac{c}{4\pi} \vec{E} \times \vec{H}^*. \quad (2.76)$$

Here, c is the speed of light, and $\vec{E}$ and $\vec{H}$ are total fields. By cosidering the total field as the superposition of the scattered field and the incident field, the complex poynting vector can be written as the summation of three parts [3]

$$\vec{S} = \vec{S}_e + \vec{S}_s + \vec{S}_i, \quad (2.77)$$

where each part is given by

$$\vec{S}_e = \frac{c}{4\pi}(\vec{E}^{inc} \times \vec{H}^* + \vec{E} \times \vec{H}^{inc*}), \tag{2.78}$$

$$\vec{S}_s = \frac{c}{4\pi}\vec{E}^{sca} \times \vec{H}^{sca}, \tag{2.79}$$

$$\vec{S}_i = \frac{c}{4\pi}\vec{E}^{inc} \times \vec{H}^{inc*}. \tag{2.80}$$

The extinction, scattering, and absorption cross sections can be defined as

$$C_{ext} = -\frac{1}{F_0}\mathrm{Re}\left[\iint \vec{S}_e \cdot \hat{n} d^2\vec{\xi}\right], \tag{2.81}$$

$$C_{sca} = -\frac{1}{F_0}\mathrm{Re}\left[\iint \vec{S}_s \cdot \hat{n} d^2\vec{\xi}\right], \tag{2.82}$$

$$C_{abs} = -\frac{1}{F_0}\mathrm{Re}\left[\iint \vec{S} \cdot \hat{n} d^2\vec{\xi}\right], \tag{2.83}$$

where $\vec{F}_0$ is the flux density of the incident plane wave, given by

$$\vec{F}_0 = \frac{c}{4\pi}\vec{E}^{inc} \cdot \vec{E}^{inc\ *}. \tag{2.84}$$

Based on Gaussian theorm, the above mentioned surface integral equation can be transformed to volume integral equations,

$$C_{ext} = \frac{k}{|E^{inc}|^2}\mathrm{Im}\left[\int_v (\epsilon - 1)\vec{E} \cdot \vec{E}^* d^3\vec{\xi}\right], \tag{2.85}$$

$$C_{sca} = C_{ext} - C_{abs}, \tag{2.86}$$

$$C_{abs} = \frac{k}{|E^{inc}|^2}\int_v \epsilon^i \vec{E}\vec{E}^* d^3\vec{\xi}. \tag{2.87}$$

These equations are valid for arbitrary sources. For an incident plane wave, the extinction cross section can be related to the amplitude scattering matrix at the direct forward direction, as called the optical theorem.

In the T-matrix formulation, one is not required to calculate the internal field. The extinction cross section can be obtained from optical theorem, and the scattering

cross section can be obtained by integrating the scattered intensities in the whole solid angle:

$$C_{ext} = \frac{4\pi}{k|E^{inc}|^2}\mathrm{Im}[\vec{E}^{sca}(\hat{n}^{inc})\cdot\vec{E}^{inc\ *}], \tag{2.88}$$

$$C_{sca} = \frac{1}{|\vec{E}^{inc}|^2}\int_{4\pi} d\hat{r}|\vec{E}^{s}|^2. \tag{2.89}$$

After some mathematical manipulations [5], we have

$$C_{ext} = -\frac{1}{k^2|\vec{E}^{inc}|^2}\mathrm{Re}\sum_{n=1}^{\infty}\sum_{m=-n}^{n}\left[a_{mn}(p_{mn})^* + b_{mn}(q_{mn})^*\right], \tag{2.90}$$

$$C_{sca} = \frac{1}{k^2|\vec{E}^{inc}|^2}\sum_{n=1}^{\infty}\sum_{m=-n}^{n}\left[|p_{mn}|^2 + |q_{mn}|^2\right]. \tag{2.91}$$

where p_{mn} and q_{mn} can be computed from the T-matrix.

CHAPTER III

RIGOROUS NUMERICAL METHODS

As discussed by van de Hulst as a strategy for studies of light scattering by nonspherical particles in the foreword to the monograph "Light Scattering by Nonspherical Particles: Theory, Measurements, and Applications" [4], mutual verification of the results obtained by different persons and particularly by different methods remains strongly advisable. In this chapter, several popular numerical methods mentioned in Chapter I are reviewed at a methodology level. A comparison study between exact methods (the FDTD, DDA, and T-matrix) is carried out to ensure the reliability of simulated results, as numerical errors cannot be avoided in the FDTD and DDA methods, and pre-assumed computational parameter are required. Typical comparison of the single-scattering properties of ice model particles are presented. Applicability of each method in terms of efficiency and accuracy is addressed. We will show the necessity of aforementioned studies and summarize useful standards to ensure the correctness of simulated optical properties.

A. Finite-Difference Time-Domain (FDTD) Method

The FDTD method is an efficient time domain method for the solution of light scattering. The major steps of the FDTD method to solve light scattering problem by nonspherical particles involve the simulation of the Maxwell equations to get the near-field in time domain, the transformation of the near-field from time domain to frequency domain, and obtaining the single-scattering properties through electromagnetic integral equations.

To obtain the near-field, FDTD simulates the propagation of the source by solving

Maxwell curl equations as follows,

$$\vec{\nabla} \times \vec{H}(\vec{r},t) = \frac{\epsilon(\vec{r})}{c}\frac{\partial \vec{E}(\vec{r},t)}{\partial t}, \tag{3.1}$$

$$\vec{\nabla} \times \vec{E}(\vec{r},t) = -\frac{\mu(\vec{r})}{c}\frac{\partial \vec{H}(\vec{r},t)}{\partial t}, \tag{3.2}$$

where $\epsilon(\vec{r})$ is the permittivity of the dielectric particle and c is the speed of light in the vacuum; $\mu(\vec{r})$ is the permeability and always assumed to be unit for nonferromagnetic cloud and aerosol particles. To take the consideration the absorption of the particle, ϵ is complex. Following the Ref. [43], Eq. (3.1) can also be expressed equivalently as follows to avoid complex refractive index in calculation

$$\vec{\nabla} \times \vec{H}(\vec{r},t) = \frac{\epsilon_r(\vec{r})}{c}\frac{\partial \vec{E}(\vec{r},t)}{\partial t} + k\epsilon_i(\vec{r})\vec{E}(\vec{r},t). \tag{3.3}$$

The two equations (3.1) and (3.3) are mathematically equivalent in frequency domain. For numerical calculation, either the total field algorithm or the pure scattered field algorithm can be employed to simulate the propagating of electromagnetic wave in the computational domain. For pure scattering field algorithm, we need to decompose the total field as the superposition of incident field (with superindex i) and scattering field (with superindex s). We get

$$\vec{\nabla} \times \vec{E}^{sca}(\vec{r},t) = -\frac{1}{c}\frac{\partial \vec{H}^{sca}(\vec{r},t)}{\partial t}, \tag{3.4}$$

$$\vec{\nabla} \times \vec{H}^{sca}(\vec{r},t) = \frac{\epsilon_r(\vec{r})}{c}\frac{\partial \vec{E}^{sca}(\vec{r},t)}{\partial t} + k\epsilon_i(\vec{r})\vec{E}^{sca}(\vec{r},t) + \vec{M}^{inc}(\vec{r},t), \tag{3.5}$$

where the source term of the scattered field $\vec{M}^{inc}(\vec{r},t)$ is given by

$$\vec{M}^{inc}(\vec{r},t) = [1-\epsilon_r(\vec{r})]\frac{\partial \vec{E}^{inc}(\vec{r},t)}{\partial(ct)} - k\epsilon_i(\vec{r})\vec{E}^{inc}(\vec{r},t). \tag{3.6}$$

One can see that M^{inc} properly equals to zero in vacuum space. From Eqs. (3.4) and (3.5), we get the time-marching equations using the central difference approximation

in terms of time derivative

$$\vec{H}^{sca}(\vec{r}, t_{n+\frac{1}{2}}) = \vec{H}^{sca}(\vec{r}, t_{n-\frac{1}{2}}) - c\delta t\vec{\nabla} \times \vec{E}^{sca}(\vec{r}, t_n), \tag{3.7}$$

$$\begin{aligned}\vec{E}^{sca}(\vec{r}, t_{n+1}) &= \exp(-\tau\delta t)\vec{E}^{sca}(\vec{r}, t_n) \\ &+ \frac{c\delta t \exp(-\tau\delta t/2)}{\epsilon_r(\vec{r})}\left[\vec{\nabla} \times \vec{H}^{sca}(\vec{r}, t_{n+\frac{1}{2}}) + \vec{M}^{inc}(\vec{r}, t_{n+\frac{1}{2}})\right],\end{aligned} \tag{3.8}$$

where $\tau = kc\epsilon_i/\epsilon_r$. The next step is calculate the derivative of $\vec{E}^{sca}$ and $\vec{H}^{sca}$ in space associated with nabla ($\vec{\nabla}$) operator. According to Yee grids as shown in Fig. 3, for an example, we calculate the x component of $\vec{\nabla} \times \vec{E}^{sca}$ and of $\vec{\nabla} \times \vec{H}^{sca}$ at grid points $\vec{r}_{i+\frac{1}{2},j,k}$ at time t_n and $\vec{r}_{i,j+\frac{1}{2},k+\frac{1}{2}}$ at time $t_{n+\frac{1}{2}}$, respectively. By using the method of central difference approximation, we have

$$\begin{aligned}\left[\vec{\nabla} \times \vec{E}^{sca}(\vec{r}_{i+\frac{1}{2},j,k}, t_n)\right]_x &= \frac{\partial E_y^{sca}(\vec{r}, t_n)}{\partial z} - \frac{\partial E_z^{sca}(\vec{r}, t_n)}{\partial y} \\ &= \frac{1}{\triangle_z}\left[E_y^{sca}(\vec{r}_{i+\frac{1}{2},j,k+\frac{1}{2}}, t_n) - E_y^{sca}(\vec{r}_{i+\frac{1}{2},j,k-\frac{1}{2}}, t_n)\right] \\ &+ \frac{1}{\triangle_y}\left[E_z^{sca}(\vec{r}_{i+\frac{1}{2},j+\frac{1}{2},k}, t_n) - E_z^{sca}(\vec{r}_{i+\frac{1}{2},j-\frac{1}{2},k}, t_n)\right],\end{aligned} \tag{3.9}$$

$$\begin{aligned}\left[\vec{\nabla} \times \vec{H}^{sca}(\vec{r}_{i,j+\frac{1}{2},k+\frac{1}{2}}, t_{n+\frac{1}{2}})\right]_x &= \frac{\partial H_y^{sca}(\vec{r}, t_{n+\frac{1}{2}})}{\partial z} - \frac{\partial H_z^{sca}(\vec{r}, t_{n+\frac{1}{2}})}{\partial y} \\ &= \frac{1}{\triangle_z}\left[H_y^{sca}(\vec{r}_{i,j+\frac{1}{2},k+1}, t_{n+\frac{1}{2}}) - H_y^{sca}(\vec{r}_{i,j+\frac{1}{2},k}, t_{n+\frac{1}{2}})\right] \\ &+ \frac{1}{\triangle_y}\left[H_z^{sca}(\vec{r}_{i,j+1,k+\frac{1}{2}}, t_{n+\frac{1}{2}}) - H_z^{sca}(\vec{r}_{i,j,k+\frac{1}{2}}, t_{n+\frac{1}{2}})\right]\end{aligned} \tag{3.10}$$

The pseudo-spectral time-domain (PSTD) [44, 45] technique embodies its feature in performing the spatial derivative of $\vec{E}$ field and $\vec{H}$ field in the above equation with

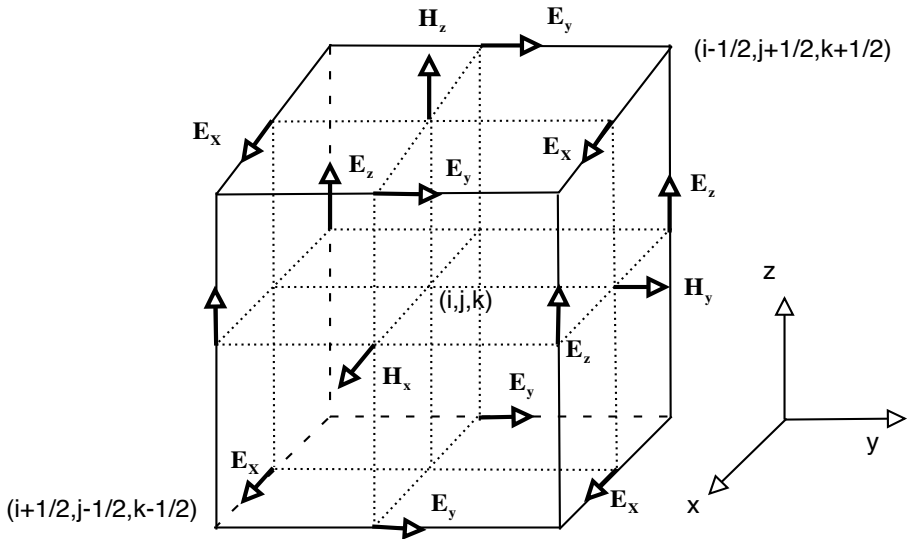

Fig. 3. Three dimensional Yee grid.

spectral methods in the following way,

$$\left[\vec{\nabla}\times\vec{E}^{sca}(\vec{r},t_n)\right]_x = \frac{\partial E_y^{sca}(\vec{r},t_n)}{\partial z} - \frac{\partial E_z^{sca}(\vec{r},t_n)}{\partial y}$$
$$= F^{-1}\{-ik_zF[E_y^{sca}(\vec{r},t_n)]\} - F^{-1}\{-ik_yF[E_z^{sca}(\vec{r},t_n)]\}, \quad (3.11)$$
$$\left[\vec{\nabla}\times\vec{H}^{sca}(\vec{r},t_{n+\frac{1}{2}})\right]_x = \frac{\partial H_y^{sca}(\vec{r},t_{n+\frac{1}{2}})}{\partial z} - \frac{\partial H_z^{sca}(\vec{r},t_{n+\frac{1}{2}})}{\partial y}$$
$$= F^{-1}\{-ik_zF[H_y^{sca}(\vec{r},t_{n+\frac{1}{2}})]\} - F^{-1}\{-ik_yF[H_z^{sca}(\vec{r},t_{n+\frac{1}{2}})]\}, \quad (3.12)$$

where F and F^{-1} stand for the forward and inverse Fourier transformation. Note that the source term $\vec{M}^{inc}$ needs to be specified in advance at every grid point within the particle, which is different from the total field algorithm which introduce the source at the Huygens surface. Either a sinusoidal source or a pulsed source can be employed for simulation. The second method is more popular for its wide frequency range. For pulsed source, the time-stepping process is terminated when the incident and scattered fields are significantly small. The absorbing boundary condition is essential in a time domain method for the light scattering problem. Various versions

of absorbing boundary condition are reviewed in [43] and can be found references therein. In the PSTD method, its importance is not only to truncate the open space, but also eliminate the "wraparound effect" due to the inner periodicity of the discrete Fourier transformation. The uniaxial perfectly matched layer (UPML) boundary condition, due to its simplicity to be numerically implemented, is widely employed currently. The governing equations, given as follows, in the UPML region are different from that in particle and the "white" space between the boundary and the particle surface:

$$(\vec{\nabla} \times \vec{H}^{sca})_x = \frac{\exp[-\tau_2(y)t]}{c} \frac{\partial}{\partial t} \{\exp[\tau_2(y)t] D_x\}, \tag{3.13}$$

$$(\vec{\nabla} \times \vec{H}^{sca})_y = \frac{\exp[-\tau_3(z)t]}{c} \frac{\partial}{\partial t} \{\exp[\tau_3(z)t] D_y\}, \tag{3.14}$$

$$(\vec{\nabla} \times \vec{H}^{sca})_z = \frac{\exp[-\tau_1(x)t]}{c} \frac{\partial}{\partial t} \{\exp[\tau_1(x)t] D_z\}, \tag{3.15}$$

$$(\vec{\nabla} \times \vec{E}^{sca})_x = \frac{\exp[-\tau_2(y)t]}{c} \frac{\partial}{\partial t} \{\exp[\tau_2(y)t] B_x\}, \tag{3.16}$$

$$(\vec{\nabla} \times \vec{E}^{sca})_y = \frac{\exp[-\tau_3(z)t]}{c} \frac{\partial}{\partial t} \{\exp[\tau_3(z)t] B_y\}, \tag{3.17}$$

$$(\vec{\nabla} \times \vec{E}^{sca})_z = \frac{\exp[-\tau_1(x)t]}{c} \frac{\partial}{\partial t} \{\exp[\tau_1(x)t] B_z\}, \tag{3.18}$$

$$\exp[-\tau_1(x)t] \frac{\partial}{\partial t} \{\exp[\tau_1(x)t] D_x\} = \exp[-\tau_3(z)t] \frac{\partial}{\partial t} \{\exp[\tau_3(z)t] E_x^{sca}\}, \tag{3.19}$$

$$\exp[-\tau_2(y)t] \frac{\partial}{\partial t} \{\exp[\tau_2(y)t] D_y\} = \exp[-\tau_1(x)t] \frac{\partial}{\partial t} \{\exp[\tau_1(x)t] E_y^{sca}\}, \tag{3.20}$$

$$\exp[-\tau_3(z)t] \frac{\partial}{\partial t} \{\exp[\tau_3(z)t] D_z\} = \exp[-\tau_2(y)t] \frac{\partial}{\partial t} \{\exp[\tau_2(y)t] E_z^{sca}\}, \tag{3.21}$$

$$\exp[-\tau_1(x)t] \frac{\partial}{\partial t} \{\exp[\tau_1(x)t] B_x\} = \exp[-\tau_3(z)t] \frac{\partial}{\partial t} \{\exp[\tau_3(z)t] H_x^{sca}\}, \tag{3.22}$$

$$\exp[-\tau_2(y)t] \frac{\partial}{\partial t} \{\exp[\tau_2(y)t] B_y\} = \exp[-\tau_1(x)t] \frac{\partial}{\partial t} \{\exp[\tau_1(x)t] H_y^{sca}\}, \tag{3.23}$$

$$\exp[-\tau_3(z)t] \frac{\partial}{\partial t} \{\exp[\tau_3(z)t] B_z\} = \exp[-\tau_2(y)t] \frac{\partial}{\partial t} \{\exp[\tau_2(y)t] H_z^{sca}\}, \tag{3.24}$$

where $\vec{D}$ and $\vec{B}$ are transition variables for $\vec{E}$ and $\vec{H}$, and $\tau_1(x)$, $\tau_2(y)$ and $\tau_3(z)$ are zero except in boundary layer perpendicular to the x, y and z axes. In practical

calculation, we need to specify $\tau_1(x)$, $\tau_2(y)$ and $\tau_3(z)$ in a manner to guarantee that the field varies slowly in space. For example,

$$\tau(x) = -\frac{p+1}{2L^{p+1}} \ln[R(0)] c (N_x - N_{x_0})^p \tag{3.25}$$

where L is the total number of UPML layers perpendicular to x direction; N_x and N_{x_0} is layer index of position x and the interface between boundary and the free space along the x direction, respectively; $R(0)$ is boundary reflection factor; p is a numerical factor and usually selected between 3 and 4. It is easy to get their time-stepping expressions. Take Eqs. (3.13) and (3.19) as example

$$\begin{aligned} D_x(\vec{r}, t_{n+1}) &= \exp[-\tau_2(y)\delta t] D_x(\vec{r}, t_n) \\ &+ c\delta t \exp\left[-\tau_2(y)\frac{\delta t}{2}\right] (\vec{\nabla} \times \vec{H}^{sca})_x(\vec{r}, t_{n+\frac{1}{2}}), \end{aligned} \tag{3.26}$$

$$\begin{aligned} E_x(\vec{r}, t_{n+1}) &= \exp[-\tau_3(z)\delta t] E_x(\vec{r}, t_n) \\ &+ \exp\left[-(\tau_1(x) + \tau_3(z))\frac{\delta t}{2}\right] \\ &\times \left\{D_x(\vec{r}, t_{n+1}) \exp[\tau_1(x)\delta t] - D_x(\vec{r}, t_n)\right\}. \end{aligned} \tag{3.27}$$

The discretization of other equations can be carried out in a similar way.

B. Discrete-Dipole-Approximation (DDA) Method

The DDA is one of several popular numerical methods for computing the scattering properties of an arbitrarily shaped particle with a small/moderate size parameter [6]. In the DDA, an particle is discretized into an array of small volumes. Each small volume is approximated as an electric dipole [12]. Figure 4 shows an example of representing a cube through dipoles. When an electromagnetic wave is incident on the particle, each dipole oscillates in response to the incident field and the induced field associated with all other dipoles. Mathematically, the basic DDA equation is in

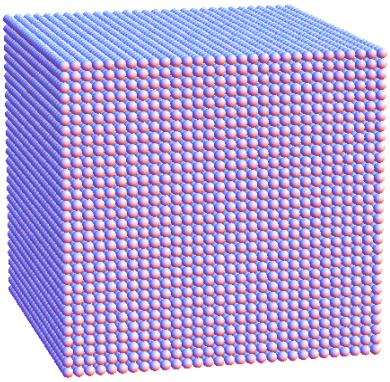

Fig. 4. Schematic geometry of a cube for the DDA method.

the form of

$$\vec{E}_i^{inc} = \alpha_i^{-1}\vec{P}_i - \sum_{j\neq i} G_{ij}\vec{P}_j, \tag{3.28}$$

where $\vec{E}_i^{inc}$ is the incident electric field, $\vec{P}_i$ is the polarizaton of each dipole, α_i is the polarizability, and G_{ij} is the discretized Green's function. When a self-consistent solution to the DDA equation is obtained, it is straightforward to calculate the scattering properties of the particle on the basis of a volume-integral electromagnetic relation that maps the near-field to the far-field [13]. The formulation of the DDA equation as derived from the basic volume integral equation can also be found in [14]. Various numerical aspects of this method such as iterative methods and convergence analysis have been recently reviewed by Yurkin and Hoekstra [15]. Note that the DDA method has been extensively employed by other researchers (e.g., [46, 47]) to investigate the optical properties of dust particles. In the conventional DDA method, the magnetic permeability is assumed to be unity and the near-field around the particle is not computed. As the near-field inside of the particle can be readily obtained, the field outside of the particle can be computed based on volume integral equations.

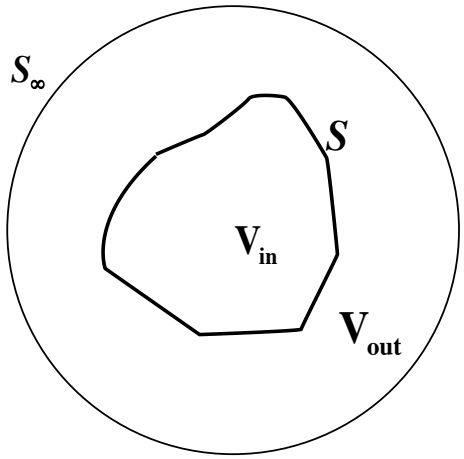

Fig. 5. 2-D view of an arbitrarily shaped object bounded by a closed surface S

C. Extended Boundary Condition Method (EBCM)

The EBCM is first proposed by Waterman [16] to calculate the T-matrix. The basic equations of the EBCM are

$$\begin{aligned}\vec{E}^{sca}(\vec{r}) &= \iint ik(\hat{n}_s \times \vec{H}_+) \cdot \overleftrightarrow{G}(\vec{r}-\vec{r}') + (\hat{n}_s \times \vec{E}_+) \cdot (\vec{\nabla} \times \overleftrightarrow{G}(\vec{r}-\vec{r}'))ds \\ &= \iint \hat{n}_s \cdot \left\{ ik\vec{H}_- \times \overleftrightarrow{G}(\vec{r}-\vec{r}') + \vec{E}_- \times [\vec{\nabla} \times \overleftrightarrow{G}(\vec{r}-\vec{r}')]ds \right\}, \ \vec{r} \in V_{out}, \end{aligned} \tag{3.29}$$

and

$$\begin{aligned}-\vec{E}^{inc}(\vec{r}) &= \iint ik(\hat{n}_s \times \vec{H}_+) \cdot \overleftrightarrow{G}(\vec{r}-\vec{r}') + (\hat{n}_s \times \vec{E}_+) \cdot [\vec{\nabla} \times \overleftrightarrow{G}(\vec{r}-\vec{r}')]ds \\ &= \iint \hat{n}_s \cdot \left\{ ik\vec{H}_- \times \overleftrightarrow{G}(\vec{r}-\vec{r}') + \vec{E}_- \times [\vec{\nabla} \times \overleftrightarrow{G}(\vec{r}-\vec{r}')]ds \right\}. \ \vec{r} \in V_{in} \end{aligned} \tag{3.30}$$

and boundary conditions,

$$\hat{n}_s \times \vec{H}_+ = \hat{n}_s \times \vec{H}_-, \tag{3.31}$$

$$\hat{n}_s \times \vec{E}_+ = \hat{n}_s \times \vec{E}_-. \tag{3.32}$$

where vector fields with subscript + are fields on the external surface, while those with subscript − are fields on the internal surface, and V_{in} and V_{out} are indicated in Fig. 5. It is necessary to point it out that an infinite number of solutions to the two equations (3.29 and 3.30) exist. The solution is pinned down through the boundary conditions, where the refractive index comes in.

Eq. (3.30) and the boundary conditions (3.31 and 3.32) will determine the surface field. By substituting the obtained surface field into the Eq. (3.29), we obtain the scattering solution. Let's start from Eq. (3.30). The internal electrical field is expanded in terms of regular vector spherical functions as follows

$$\vec{E}_{-}(\vec{r}') = \sum_{n'=1}^{\infty} \sum_{m'=-n'}^{n'} \left[c_{m'n'} \mathrm{Rg} \vec{M}_{m'n'}(k_2 r') + d_{m'n'} \mathrm{Rg} \vec{N}_{m'n'}(k_2 r') \right], \tag{3.33}$$

where k_2 is the wavenumber within the particle. Recalling

$$\vec{H}(\vec{r}') = \frac{1}{ik} \vec{\nabla} \times \vec{E}(\vec{r}') = \frac{k_2}{ik} \frac{1}{k_2} \vec{\nabla} \times \vec{E}(\vec{r}'), \tag{3.34}$$

we obtain magnetic field, given by

$$\vec{H}_{-}(\vec{r}') = \frac{k_2}{ik} \sum_{n'=1}^{\infty} \sum_{m'=-n'}^{n'} \left[d_{m'n'} \mathrm{Rg} \vec{M}_{m'n'}(k_2 r') + c_{m'n'} \mathrm{Rg} \vec{N}_{m'n'}(k_2 r') \right]. \tag{3.35}$$

By using Eqs. (3.33), (3.35), (3.31) and (3.32), and expanding dyadic Green's function

in Eq. (3.30) in terms of vector spherical functions, Eq. (3.30) is in the form of

$$
\begin{aligned}
-\vec{E}^{inc}(\vec{r}) = & \sum_{n,m,n',m'} ik(-1)^m \int \hat{n}_s \cdot \Big\{ k_2 \mathrm{Rg}\vec{M}_{mn}(kr) \\
& \times \Big[d_{m'n'} \mathrm{Rg}\vec{M}_{m'n'}(k_2 r') + c_{m'n'} \mathrm{Rg}\vec{N}_{m'n'}(k_2 r') \Big] \times \vec{M}_{-mn}(kr') \\
& + k_2 \mathrm{Rg}\vec{N}_{mn}(kr) \\
& \times \Big[d_{m'n'} \mathrm{Rg}\vec{M}_{m'n'}(k_2 r') + c_{m'n'} \mathrm{Rg}\vec{N}_{m'n'}(k_2 r') \Big] \times \vec{N}_{-mn}(kr') \\
& + k \mathrm{Rg}\vec{N}_{mn}(kr) \\
& \times \Big[c_{m'n'} \mathrm{Rg}\vec{M}_{m'n'}(k_2 r') + d_{m'n'} \mathrm{Rg}\vec{N}_{m'n'}(k_2 r') \Big] \times \vec{M}_{-mn}(kr') \\
& + k \mathrm{Rg}\vec{M}_{mn}(kr) \\
& \times \Big[c_{m'n'} \mathrm{Rg}\vec{M}_{m'n'}(k_2 r') + d_{m'n'} \mathrm{Rg}\vec{N}_{m'n'}(k_2 r') \Big] \times \vec{N}_{-mn}(kr') \Big\} \, ds. \quad (3.36)
\end{aligned}
$$

Recall Eq. (2.61), we can establish the relationship between the coefficients (c_{mn}, d_{mn}) of the internal field and the coefficients (a_{mn}, b_{mn}) of the incident field. The mathematical relations are given by

$$
\begin{aligned}
a_{mn} = & \sum_{n'm'} (-1)^m \int \hat{n}_s \cdot \{ -ikc_{m'n'} \\
& \Big[k_2 \mathrm{Rg}\vec{N}_{m'n'}(k_2 r') \times \vec{M}_{-mn}(kr') + k \mathrm{Rg}\vec{M}_{m'n'}(k_2 r') \times \vec{N}_{-mn}(kr') \Big] \\
& -ikd_{m'n'} \\
& \Big[k_2 \mathrm{Rg}\vec{M}_{m'n'}(k_2 r') \times \vec{M}_{-mn}(kr') + k \mathrm{Rg}\vec{N}_{m'n'}(k_2 r') \times \vec{N}_{-mn}(kr') \Big] \, ds, \quad (3.37)
\end{aligned}
$$

and

$$
\begin{aligned}
b_{mn} = & \sum_{n'm'} (-1)^m \int \hat{n}_s \cdot \{ -ikc_{m'n'} \\
& \Big[k_2 \mathrm{Rg}\vec{N}_{m'n'}(k_2 r') \times \vec{N}_{-mn}(kr') + k \mathrm{Rg}\vec{M}_{m'n'}(k_2 r') \times \vec{M}_{-mn}(kr') \Big] \\
& -ikd_{m'n'} \\
& \Big[k_2 \mathrm{Rg}\vec{M}_{m'n'}(k_2 r') \times \vec{N}_{-mn}(kr') + k \mathrm{Rg}\vec{N}_{m'n'}(k_2 r') \times \vec{M}_{-mn}(kr') \Big] \, ds. \quad (3.38)
\end{aligned}
$$

One usually write Eqs. (3.37) and (3.38) in a matrix form as follows,

$$\begin{bmatrix} \vec{a} \\ \vec{b} \end{bmatrix} = \begin{bmatrix} Q^{11} & Q^{12} \\ Q^{21} & Q^{22} \end{bmatrix} \begin{bmatrix} \vec{c} \\ \vec{d} \end{bmatrix} \tag{3.39}$$

where [5].

$$Q^{11}_{mnm'n'} = -ikk_2 J^{21}_{mnm'n'} - ik^2 J^{12}_{mnm'n'}, \tag{3.40}$$

$$Q^{12}_{mnm'n'} = -ikk_2 J^{11}_{mnm'n'} - ik^2 J^{22}_{mnm'n'}, \tag{3.41}$$

$$Q^{21}_{mnm'n'} = -ikk_2 J^{22}_{mnm'n'} - ik^2 J^{11}_{mnm'n'}, \tag{3.42}$$

$$Q^{22}_{mnm'n'} = -ikk_2 J^{12}_{mnm'n'} - ik^2 J^{21}_{mnm'n'}. \tag{3.43}$$

and

$$\begin{bmatrix} J^{11}_{mnm'n'} \\ J^{12}_{mnm'n'} \\ J^{21}_{mnm'n'} \\ J^{22}_{mnm'n'} \end{bmatrix} = (-1)^m \int dS\hat{n} \cdot \begin{bmatrix} \mathrm{Rg}\vec{M}_{m'n'}(k_2\vec{r}) \times \vec{M}_{-mn}(k\vec{r}) \\ \mathrm{Rg}\vec{M}_{m'n'}(k_2\vec{r}) \times \vec{N}_{-mn}(k\vec{r}) \\ \mathrm{Rg}\vec{N}_{m'n'}(k_2\vec{r}) \times \vec{M}_{-mn}(k\vec{r}) \\ \mathrm{Rg}\vec{N}_{m'n'}(k_2\vec{r}) \times \vec{N}_{-mn}(k\vec{r}) \end{bmatrix}. \tag{3.44}$$

Similarly, starting from Eq. (3.29), one can obtain [5],

$$\begin{bmatrix} \vec{p} \\ \vec{q} \end{bmatrix} = - \begin{bmatrix} \mathrm{Rg}Q^{11} & \mathrm{Rg}Q^{12} \\ \mathrm{Rg}Q^{21} & \mathrm{Rg}Q^{22} \end{bmatrix} \begin{bmatrix} \vec{c} \\ \vec{d} \end{bmatrix} \tag{3.45}$$

where

$$\mathrm{Rg}Q^{11}_{mnm'n'} = -ikk_2 \mathrm{Rg}J^{21}_{mnm'n'} - ik^2 \mathrm{Rg}J^{12}_{mnm'n'}, \tag{3.46}$$

$$\mathrm{Rg}Q^{12}_{mnm'n'} = -ikk_2 \mathrm{Rg}J^{11}_{mnm'n'} - ik^2 \mathrm{Rg}J^{22}_{mnm'n'}, \tag{3.47}$$

$$\mathrm{Rg}Q^{21}_{mnm'n'} = -ikk_2 \mathrm{Rg}J^{22}_{mnm'n'} - ik^2 \mathrm{Rg}J^{11}_{mnm'n'}, \tag{3.48}$$

$$\mathrm{Rg}Q^{22}_{mnm'n'} = -ikk_2 \mathrm{Rg}J^{12}_{mnm'n'} - ik^2 \mathrm{Rg}J^{21}_{mnm'n'}. \tag{3.49}$$

and

$$\begin{bmatrix} \mathrm{Rg}J^{11}_{mnm'n'} \\ \mathrm{Rg}J^{12}_{mnm'n'} \\ \mathrm{Rg}J^{21}_{mnm'n'} \\ \mathrm{Rg}J^{22}_{mnm'n'} \end{bmatrix} = (-1)^m \int dS\hat{n} \cdot \begin{bmatrix} \mathrm{Rg}\vec{M}_{m'n'}(k_2\vec{r}) \times \mathrm{Rg}\vec{M}_{-mn}(k\vec{r}) \\ \mathrm{Rg}\vec{M}_{m'n'}(k_2\vec{r}) \times \mathrm{Rg}\vec{N}_{-mn}(k\vec{r}) \\ \mathrm{Rg}\vec{N}_{m'n'}(k_2\vec{r}) \times \mathrm{Rg}\vec{M}_{-mn}(k\vec{r}) \\ \mathrm{Rg}\vec{N}_{m'n'}(k_2\vec{r}) \times \mathrm{Rg}\vec{N}_{-mn}(k\vec{r}) \end{bmatrix}. \quad (3.50)$$

Finally, the T-matrix defined in Eq. (2.63) is given by

$$\vec{T} = -\mathrm{Rg}\vec{Q}\vec{Q}^{-1}. \quad (3.51)$$

Further technical details associated with T-matrix can be found in [5].

D. Mutual Verification and Comparison Study

Mutual verification of different numerical methods for the solution of light scattering and the comparison study in terms of the accuracy and the computational efficiency for each method are important to obtain reliable data in relevant research work, and, in particular, to develop optical property database of various nonspherical particles. Some previous studies such as [48–51] are carried out to compare the FDTD, the DDA and the EBCM for spheres and some nonspherical particles (such as cube, spheroid, cylinder, etc.).

In general, the EBCM is preferably selected in the simulation of axially symmetric particles (e.g., cylinders and spheroids) with moderate aspect ratios (i.e., the ratio of the dimension along the symmetric axis over that along the horizontal axis), because the EBCM is most fast and accurate in these cases. For axially symmetric particles with extreme aspect rations, and other nonspherical particles, the FDTD and DDA methods come to play an important role.

The FDTD and DDA methods have comparable computational efficiency and

accuracy. The speed difference of the two methods depends on the the shape of the particle, the orientation and refractive index. Some criteria are helpful to select a preferable method for the simulation. First, the computational domain for the FDTD method is larger than that of the DDA method, as the former requires layers of absorbing boundary condition, and a white space. In practical calculations, the difference between the computational domain does not bring large difference of computational efficiency for compact particles (e.g., spheres, cubes, droxtals, etc.), but does for sparse particles, such as bullet rosette. For compact particles, the advantage of larger computational domain for the FDTD method is that the FDTD can employ a surface integral to transform the near-field to the far-field. The mapping algorithm based on a surface-integral is faster than that based on a volume-integral. The efficiency difference of different mapping algorithms is obvious for randomly oriented particles. Second, the applicable range of refractive index of the DDA method is $|m-1|<2$; however, the FDTD method is applicable to much larger refractive indices. In Yurkin's study [50], the FDTD method is generally faster than the DDA method when the refractive index is larger than 1.4 for spheres.

We are concerned with randomly oriented nonspherical particles in most cases. To obtain the optical properties of randomly oriented nonspherical particles, the FDTD or the DDA method computes the optical properties for each single orientation and then performs the numerical integral in terms of results for all the orientations. The EBCM based T-matrix formulation is of analytical nature and obtains the averaged optical properties analytically. An important question involved is that how many orientations of the particle is sufficient to obtain converged results of the averaged optical properties. The number of orientations in general depends on the size parameter, the refractive index, and the particle shape. In this section, we study this issue to obtain a general picture of the number of orientations of spheroidal,

Table II. Error of scattering solution calculated by the DDA in the case of spheroid. The size parameter is 30 and the aspect ratio is 0.7.

$m\|k\|d$	N_β	$P_{11}(\%)$	P_{22}/P_{11}	P_{33}/P_{11}	P_{44}/P_{11}	P_{12}/P_{11}	P_{34}/P_{11}
0.4904	9	0.71420	0.021604	0.010595	0.016547	0.0093813	0.011544
0.4904	12	0.70711	0.017606	0.011916	0.017893	0.0078377	0.011551
0.4904	15	0.61589	0.016576	0.010918	0.016294	0.0078807	0.011346
0.4904	21	0.61118	0.016772	0.010801	0.016277	0.0077997	0.011397

cylindrical, and hexagonal particles.

We first study the optical properties of randomly oriented spheroids and circular cylinders. Spheroid and circular cylinder are of axial-rotational symmetry. The angle β between the direction of incident light and the symmetric axis specifies the orientation of the particle. Due to the mirror symmetry of the spheroid, the range of β is assumed to be from 0^o to 90^o. We use the PSTD code instead of FDTD code as the former is faster and requires smaller resolution of space grids. The refractive index is assumed to be $1.3078 + i1.66 \times 10^{-8}$. The size parameter is defined in terms of the longer axis of spheroid, and the height of the cylinder.

Table II shows the differences of phase matrix elements of spheroids simulated from the DDA results and the T-matrix results by changing the number of β. $m|k|d$ is a computational parameter to control the accuracy of the DDA method, and usually should be less than 0.5. To quantify the difference between the DDA results and the T-matrix counterparts. The following formulae are employed:

$$\text{error} = \frac{|P_{11,dda} - P_{11,T-matrix}|}{|P_{11,T-matrix}|} \times 100\%, \tag{3.52}$$

$$\text{error} = |P_{ij,dda}/P_{11,dda} - P_{ij,T-matrix}/P_{11,T-matrix}|, ij \neq 11. \tag{3.53}$$

We compute Eqs. (3.52) and (3.53) for each scattering angle and then take the

averaged value. When N_β is larger than 15, the differences do not change significantly. Table III is for the PSTD method. The number of ratio indicates the number of grid points per wavelength. When the ratio is set as 15, the difference do not change much when N_β is larger than 15. But, when the ratio is set to be 20, the differences will be reduced as expected. Similar to Tables II and III, Tables IV and V are for circular cylinders.

Table III. Error of scattering solution calculated by the PSTD in the case of spheroid. The size parameter is 30 and the aspect ratio is 0.7

Ratio	N_β	$P_{11}(\%)$	P_{22}/P_{11}	P_{33}/P_{11}	P_{44}/P_{11}	P_{12}/P_{11}	P_{34}/P_{11}
15	7	1.4364	0.036527	0.024500	0.035815	0.014349	0.024424
15	9	1.0013	0.039544	0.026484	0.038881	0.013013	0.022559
15	11	0.9075	0.037130	0.027760	0.040292	0.012789	0.022353
15	13	0.8878	0.035805	0.027716	0.040030	0.012992	0.022318
15	15	0.8684	0.035347	0.027649	0.039873	0.013112	0.022367
15	17	0.8681	0.035471	0.027614	0.039833	0.013189	0.022361
20	11	0.5679	0.027556	0.021311	0.030580	0.011397	0.016556

Table IV. Error of scattering solution calculated by the DDA in the case of cylinder. The size parameter is 30 and the aspect ratio is 0.7

$m\|k\|d$	N_β	$P_{11}(\%)$	P_{22}/P_{11}	P_{33}/P_{11}	P_{44}/P_{11}	P_{12}/P_{11}	P_{34}/P_{11}
0.4898	9	3.56770	0.0180570	0.0141370	0.019194	0.0137200	0.019131
0.4898	12	1.27330	0.0059055	0.0065773	0.008898	0.0083951	0.0113000
0.4898	15	0.91270	0.0072213	0.0078248	0.012404	0.0094639	0.0847210
0.4898	17	0.71122	0.0070595	0.0073248	0.011643	0.0089888	0.0096355
0.4898	21	0.85163	0.0064063	0.0067273	0.010728	0.0087018	0.0101100

Table V. Error of the scattering solution calculated by the PSTD in the case of cylinder. The size parameter is 30 and the aspect ratio is 0.7.

Ratio	N_β	$P_{11}(\%)$	P_{22}/P_{11}	P_{33}/P_{11}	P_{44}/P_{11}	P_{12}/P_{11}	P_{34}/P_{11}
15	9	3.5926	0.023821	0.020411	0.03103	0.013322	0.027035
15	11	2.4431	0.016484	0.015649	0.022164	0.011017	0.027654
15	15	1.8403	0.014947	0.014337	0.021549	0.010211	0.026388
15	17	1.8352	0.015239	0.014432	0.021917	0.0095719	0.027049
15	21	1.8368	0.016048	0.015478	0.023311	0.0091813	0.026759
17	13	1.5181	0.013524	0.012026	0.017403	0.0096900	0.018033
17	15	1.1059	0.010785	0.009828	0.014528	0.0090706	0.017906
17	17	1.0002	0.010538	0.009318	0.013967	0.0085153	0.018603
17	21	1.0844	0.011533	0.010132	0.015510	0.0078135	0.018265
20	21	1.0005	0.010689	0.009265	0.014228	0.0078477	0.017474

Figure 6 shows the comparison of six phase matrix elements for randomly oriented spheroids simulated from the DDA, PSTD and T-matrix methods. 15 zenith angles between 0^o and 90^o are set up for the DDA and PSTD simulations. The results from the three methods agree very well, although some differences are still observable for the P_{44} element. Figure 7 is similar to Fig. 6, but for randomly oriented cylinders.

Based on the aforementioned numerical study, we simulated the optical properties of randomly oriented hexagonal ice crystals. Consider the symmetry of the geometry of hexagonal ice crystals, we select 15 values of β from 0 to 90 degrees and 3 values of ϕ from 0 to 30 degrees. The T-matrix method is not efficient for this geometry. Figure 8 shows the comparison of six non-zero elements of the phase matrix simulated from the DDA, the PSTD, and the FDTD method. The computational parameters are indicated in the figure. Generaly, the results simulated from different numerical methods agree well.

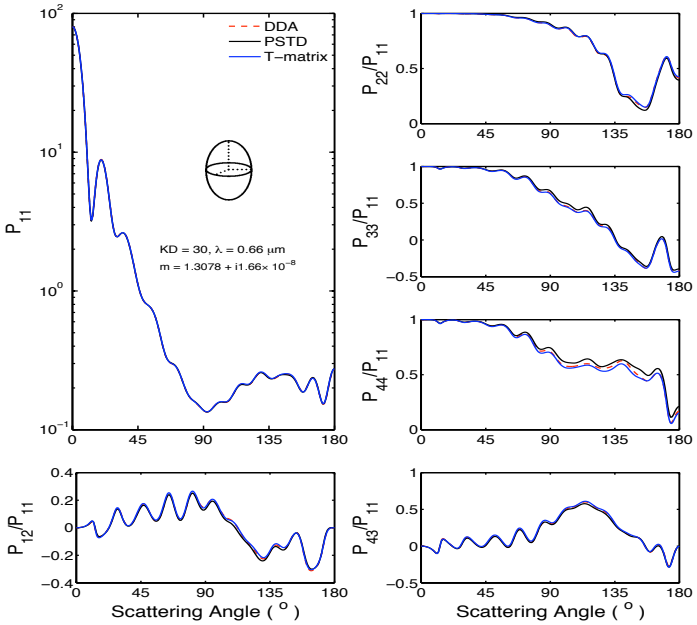

Fig. 6. Comparison of six elements of the phase matrix of randomly oriented spheroids computed from the DDA, PSTD, and T-matrix methods.

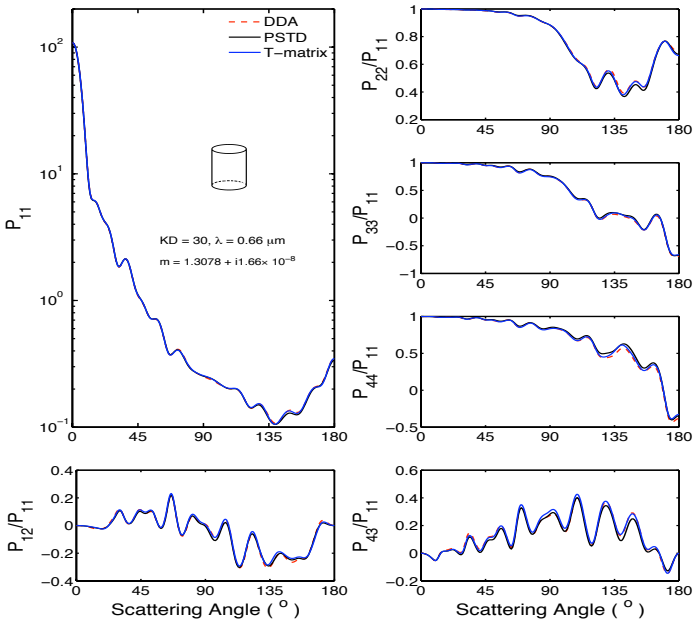

Fig. 7. Comparison of six elements of the phase matrix of randomly oriented cylinders computed from the DDA, PSTD, and T-matrix methods.

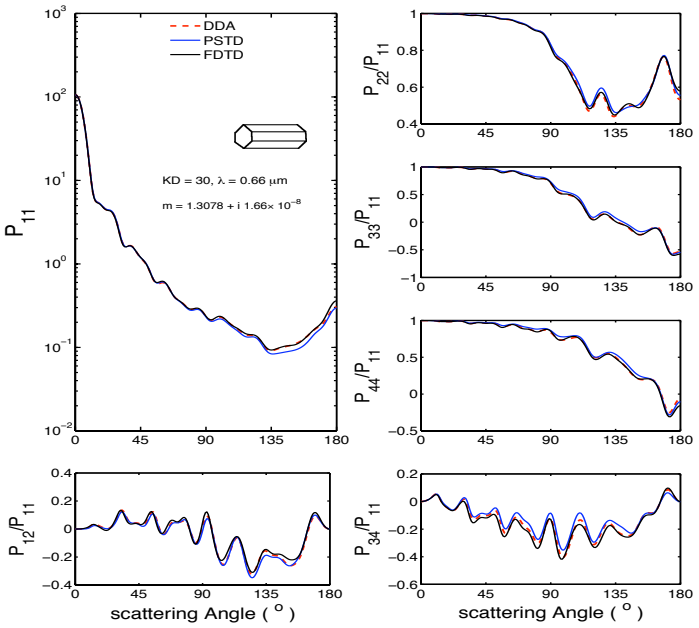

Fig. 8. Comparison of six elements of the phase matrix of hexagonal ice crystals computed from the DDA, PSTD, and FDTD methods.

CHAPTER IV

GEOMETRIC OPTICS APPROXIMATION *

A. Introduction

According to the characteristics of light scattering with respect to particle size parameter, a complete region of size parameter is usually divided into three regions: classical region, semiclassical region, and Rayleigh region. Characteristics of light scattering in the classical region (wavelength λ tends to 0 by comparing it with the size) is the subject of geometric optics or ray optics. The theory of light scattering in the geometric optics domain is quite often called "short-wavelength scattering" or "high frequency scattering" in the literature. Similar divisions are common in the scattering theory of elementary particles (e.g., electrons) by potential. The theory of quantum scattering transits to that of classical scattering as Plank parameter h tends to zero as compared with the classical action S.

The motivation to develop the method based on geometric optics are in several aspects. When the size of particle is about 20 times more than the wavelength of incident light, the method based on geometric optics provides estimation of optical properties of particles before refined calculations in full electrodynamics. In addition and most importantly, in the region of very large size parameters beyond the current capabilities of exact techniques discussed in Chapter II, the geometric optics method is a very valuable method, which provides approximate numbers and curves. Further-

*Part of this chapter is reprinted with permission from "Diffraction and external reflection by dielectric faceted particles" by L. Bi, P. Yang, G. W. Kattawar, Y. Hu and B. A. Baum, J. Quant. Spectrosc. Radiat. Transfer, **112**, 163-173 (2011), and "Scattering and absorption of light by ice particles: solution by a new physical-geometric optics hybrid method" L. Bi, P. Yang, G. W. Kattawar, Y. Hu, and B. A. Baum J. Quant. Spectrosc. Radiat. Transfer, **112**, 1492-1508 (2011)

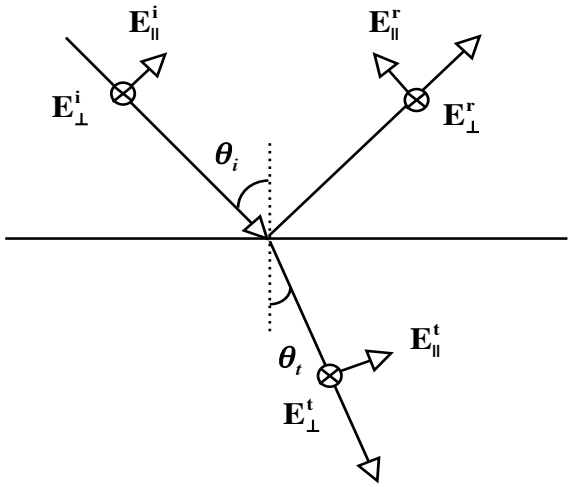

Fig. 9. Schematic geometry of reflection and refraction.

more, the methods based on geometric optics provides some insights in the physical process which determines the behavior of optical properties of particles.

In this chapter, we first outline basic components of geometric optics method, and then introduce the PGOH method. Several versions of the PGOH algorithms are developed and some important improvements made on the PGOH method are specifically discussed. Generally, it is believed that the method based on geometric optics is more accurate when the particle size becomes larger; however, the accuracy and reliability of the method still remain to be examined in details. Some comparison studies of geometric-optics approximation method and exact methods are carried out to understand the accuracy and reliability of the PGOH.

B. General Considerations

1. Snell's Law and Fresnel Formulas

The basic and central concept of geometric optics is a ray of light, which is associated with the intensity of field and the variation of phase, and the state of polarization. When a ray is impinging on an interface between two medium, events of reflection and refraction take place. A conceptual geometry of reflection and refraction is shown in Fig. 9. The electric fields associated with the reflected ray and the refracted ray is determined through the reflection and refraction matrices, given as follows [37, 52],

$$\begin{bmatrix} E_{\parallel}^{r} \\ E_{\perp}^{r} \end{bmatrix} = \begin{bmatrix} R_a & 0 \\ 0 & R_b \end{bmatrix} \begin{bmatrix} E_{\parallel}^{i} \\ E_{\perp}^{i} \end{bmatrix}, \tag{4.1}$$

$$\begin{bmatrix} E_{\parallel}^{t} \\ E_{\perp}^{t} \end{bmatrix} = \begin{bmatrix} T_a & 0 \\ 0 & T_b \end{bmatrix} \begin{bmatrix} E_{\parallel}^{i} \\ E_{\perp}^{i} \end{bmatrix}, \tag{4.2}$$

where the four diagonal elements are given through Fresnel formulas,

$$R_a = \frac{m\cos\theta^i - \cos\theta^t}{m\cos\theta^i + \cos\theta^t}, \qquad R_b = \frac{\cos\theta^i - m\cos\theta^t}{\cos\theta^i + m\cos\theta^t}. \tag{4.3}$$

$$T_a = \frac{2\cos\theta_i}{m\cos\theta_i + \cos\theta_t}, \qquad T_b = \frac{2\cos\theta_i}{\cos\theta_i + m\cos\theta_t}. \tag{4.4}$$

Here θ^i is the incident angle, θ^t is the angle of refraction and m is relative refractive index, which can be complex. θ^t is related to θ^i through Snell's law,

$$\sin\theta^i = m\sin\theta^t. \tag{4.5}$$

Snell's law and Fresnel formulae are derived from Maxwell boundary conditions in the case of infinite planar surface [37, 52]. These formula are still valid approximately for curved surfaces provided that the radius of curvature is much larger than the incident wavelength.

2. Fraunhofer Diffraction

Geometric optics is invalid in the range of small scattering angles. A straightforward example is Fraunhofer diffraction of a plane wave by an aperture. When the distance is close to the aperture, geometric optics is valid (more or less). As the distance between the aperture and observer is increasing, a pattern of oscillating intensity of field is observed and geometric optics is no longer valid. In this case, the forward direction in the far-field is caustic, where the radius of curvature of wavefront is infinite. This feature termed as Fraunhofer differaction can only be explained through wave optics. The diffraction is induced due to an incomplete wavefront. The fundamental theory is Huygens-Fresnel principle, and Kirchhoff theory in electrodynamics.

In the scattering of light by a solid particle, in the radiation zone, the geometric optics is also invalid for small scattering angles. The reason is that an incomplete wave front due to the existence of the particle will contribute to the scattering near forward directions, which is the same as that of Fraunhofer diffraction, based on Babinet's principle [2]. Therefore, as a rough estimation, a geometric optics ray-tracing technique combined with Fraunhofer diffraction provides an approach to calculating the optical properties of large particles. This is indeed the picture of a conventional geometric optics method (CGOM). The advantages of CGOM are simplicity, fastness, and successful explanation of natural optics phenomena such as glory, rainbow, halo, parhelion, sun pillars, and etc. The flaws of CGOM are associated with caustics which leads to singular points, and neglecting of semi-classical scattering effects.

The method of combining geometric optics and Fraunhofer diffraction to describe the scattering of light is mostly based physical considerations. A more rigorous approach is based on Kirchhoff theory, i.e., the hybrid of geometric-optics and electromagnetic integral equations.

3. Physical-geometric Optics Hybrid

The basic principle of the PGOH is to calculate the electromagnetic field on the surface or inside of the particle by using a ray-tracing technique. The corresponding far-field is obtained by mapping the near-field to its counterpart in the radiation (or, far-field) zone either through a volume integral equation (2.34) or a surface integral equation (2.44). The magnitude and phase of each ray is calculated based on the localized-plane-wave approximation by using the Fresnel formulas. The directions of external reflection, internal reflection and refraction are determined by Snell's law. In the context of this method, the inaccuracy of solutions is due to the approximation of near optical field, especially field near the boundary (vertex, edge, and surface) of particle, focus and caustics, where the law of geometric optics breaks down. Furthermore, the interaction between tunneling rays and particle is inherently neglected.

The introduction of near- to far-field mapping concept into the geometric optics method essentially brings out two new outcomes in comparison with CGOM: a new diffraction formula [30] and ray-spreading effect [27, 28] of outgoing rays. For randomly oriented particles, the interference among outgoing rays are usually omitted. This is a not proper assumption for oriented particles. In this chapter, we intend to refine various aspects of the PGOH both theoretically and numerically so that the PGOH produces an efficient and satisfied estimation of the solution to light scattering by arbitrarily shaped nonspherical particles.

C. Beam-tracing Technique

When a plane wave of light is incident on a faceted particle, the portion of the wave-front of the incident electromagnetic wave, intercepted by the projected geometric cross section of the particle, splits into several parts according to the facets on the

illuminated side of the particle. Each part of the wave front (or localized wave) impinges on a single facet, and, after electromagnetic interaction with the facet, leads to outgoing reflected and inwardly propagating refracted beams. Subsequently, the refracted beams undergo multiple internal reflections within the particle, leading to various higher-order outgoing refracted beams. The first-order refracted beams and higher order internally reflected beams may split during their propagation within the particle. In this study a beam-splitting algorithm is developed to describe how the internal beams split and is aimed at specifying the geometries of internal ray tubes. Because the geometry of the scattering particle is assumed to be convex, any externally reflected beams and higher-order refracted beams cannot be blocked by the particle itself. Therefore, the beam-splitting algorithm is irrelevant to beams propagating outside the particle.

An internal beam is specified by its propagating direction and initial cross section. Let the subscript index $p(= 1, 2, 3...)$ indicate the pth order reflection/refraction event. The direction of one internal beam leaving some interface of the pth order reflection/refraction is specified by $\hat{e}_p$, and the vertices of the beam cross section on the interface of electromagnetic interaction are denoted as $\vec{r}_{p,i}(i = 1, N_v)$, where N_v is the number of vertices. When $p = 1$ (i.e., external reflection and refraction), $\vec{r}_{1,i}(i = 1, N_v)$ are the straightforward coordinates of the vertices of the corresponding facet where external reflection takes place.

To describe the splitting of an internal beam (specified by $\hat{e}_p$ and $\vec{r}_{p,i}$), the first step is to determine the intercepting particle facets. We assume N_v to be the number of straight-line rays (with no cross section) starting from the positions of N_v vertices and propagating in the direction $\hat{e}_p$. The facets of the particle surface are convex shapes, and if, for example, the N_v number of rays strike M_v number of different facets, the beam cross-section is divided into M_v parts at least. We first separate

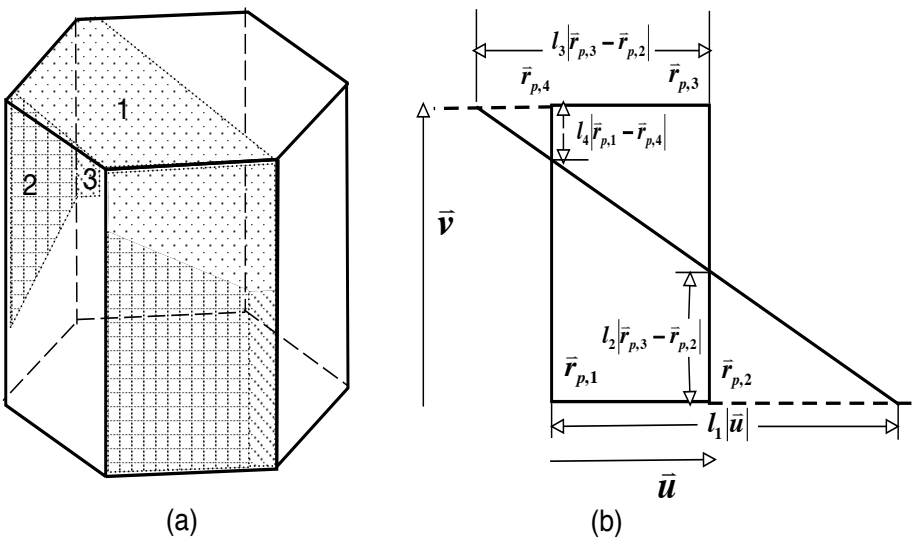

Fig. 10. (a) The first order refracted beam is divided into three sub-beams with each impinging on a single facet. (b) An example of splitting a rectangular beam cross section into two parts.

the beam into M_v parts. The process goes on for each sub beam cross-section so that each part of the original cross section impinges on a single facet of the particle. $\hat{\tau}_i (i = 1, M_v)$ are assigned to denote the normal directions of the facets. Figure 10(a) shows an example of a first-order refracted beam split into three sub-beams (four vertices incident on three different facets) leading to three first-order ray tubes.

We must mathematically separate the initial beam cross section of the internal beam into M_v parts. To this end, we let an arbitrary position within the initial cross section be written as,

$$\vec{r} = c_u \vec{u} + c_v \vec{v}, \tag{4.6}$$

where c_u and c_v are two arbitrary coefficients. Vectors $\vec{u}$ and $\vec{v}$ are defined by

$$\vec{u} = \vec{r}_{p,2} - \vec{r}_{p,1}, \vec{v} = \vec{r}_{p,N} - \vec{r}_{p,1}. \tag{4.7}$$

The coordinates (c_u, c_v) of those points on the initial beam cross section are along the common edge of two facets (outward normal directions are $\vec{\tau}_1$ and $\vec{\tau}_2$) and satisfy the following condition,

$$c_u \frac{w_u}{d_1 - d_2} + c_v \frac{w_v}{d_1 - d_2} = 1, \tag{4.8}$$

where d_1 and d_2 represent the distances from $\vec{r}_{p,1}$ to the planes of two aforementioned facets, respectively, and w_u and w_v are given by

$$w_u = \left(\frac{\vec{u} \cdot \vec{\tau}_1}{\vec{e}_p \cdot \vec{\tau}_1} - \frac{\vec{u} \cdot \vec{\tau}_2}{\vec{e}_p \cdot \vec{\tau}_2} \right), w_v = \left(\frac{\vec{v} \cdot \vec{\tau}_1}{\vec{e}_p \cdot \vec{\tau}_1} - \frac{\vec{v} \cdot \vec{\tau}_2}{\vec{e}_p \cdot \vec{\tau}_2} \right). \tag{4.9}$$

Eq. (4.8) defines a straight line which splits the original beam cross section into two sub-beams. After mathematical manipulation, the intersection points between the straight line given by Eq. (4.8) and the polygon-shaped boundary can be written in the form of

$$\vec{r} = \vec{r}_{p,j} + (\vec{r}_{p,j+1} - \vec{r}_{p,j}) l_j, \text{if } \ l_j \in [0, 1], \tag{4.10}$$

where $l_j (j = 1, N_v)$ are defined as follows:

$$l_1 = \frac{d_1 - d_2}{w_u}, l_N = 1 - \frac{d_1 - d_2}{w_v}, \tag{4.11}$$

$$l_j = \begin{cases} \frac{\hat{n}_p \cdot [(\vec{r}_{p,1} + l_1 \vec{u} - \vec{r}_{p,j}) \times \vec{q}]}{\hat{n}_p \cdot [(\vec{r}_{p,j+1} - \vec{r}_{p,j}) \times \vec{q}]}, & |w_v| \leq |w_u| \\ \frac{\hat{n}_p \cdot [(\vec{r}_{p,1} + (1 - l_N) \vec{v} - \vec{r}_{p,j}) \times \vec{q}]}{\hat{n}_p \cdot [(\vec{r}_{p,j+1} - \vec{r}_{p,j}) \times \vec{q}]}, & |w_v| > |w_u|. \end{cases}, j = 2, N_v - 1 \tag{4.12}$$

where

$$\vec{q} = \begin{cases} \vec{v} - \frac{w_v}{w_u}\vec{u}, & |w_v| \leq |w_u| \\ \frac{w_u}{w_v}\vec{v} - \vec{u}, & |w_v| > |w_u|. \end{cases} \tag{4.13}$$

In Eq. (4.12), $\hat{n}_p$ is the normal direction of the initial beam cross section. As the beam cross section is convex, there are only two l_j in the 0 to 1 range, for example see the case shown in Fig. 10 (b). At this point, it is straightforward to split the original beam into two sub-beams by regrouping the vertices of the original beam cross section and two intersection points. When $M_v > 2$, each sub-beam may impinge on multiple facets, and, thus, the process is repeated for each sub-beam until each next-order sub-beam impinges on a single facet. After the initial beam cross section is divided, the vertex coordinates of the end cross section of each sub-beam can be obtained in a straightforward manner. All sub-beams undergo internal reflections at different facets, corresponding to the emergence of the next order reflected beams.

Similar to a data family tree, all the internal beams are revealed in a recursive data structure. For the *pth* order refraction/reflection, there are a number of the *pth* order internal beams, fundamentally determined by the particle orientation and refractive index. Each *pth* order internal beam would generate several next order internal beams. As the computer program allows for tracing a single beam at each step, a recursive subroutine is most appropriate to implement the beam-splitting algorithm. The recursive subroutine contains the algorithm of splitting the input beam and a loop defined in terms of calling the recursive subroutine itself with each next-order reflected beam as the input. The programming feature based on recursive subroutines requires more computer memory and is unnecessary in the traditional ray-tracing algorithm, where, for one incident ray, only one internal ray emerges at each subsequent reflection and refraction event. To terminate the beam-tracing process, a

necessary condition is required in the recursive subroutine and is addressed in Section C.

D. Geometric-optics Near-field

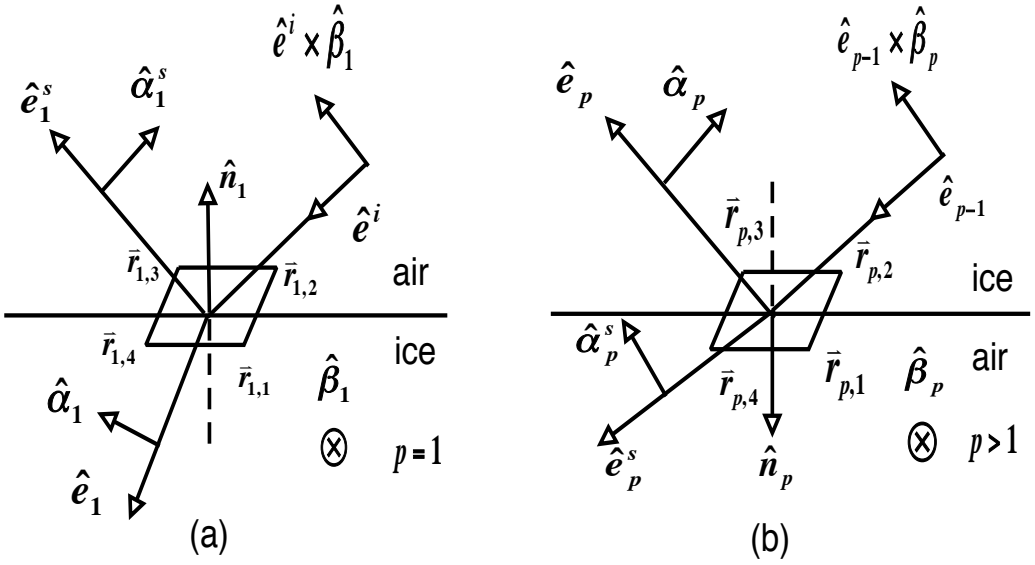

Fig. 11. Coordinate systems defined in the ray-tracing process. (a) external reflection (p=1); (b) internal reflection (p>1).

To calculate the electric field within the particle through a beam-tracing process, we define $(\hat{\beta}^i, \hat{\alpha}^i, \hat{e}^i)$, $(\hat{\beta}_p, \hat{\alpha}_p, \hat{e}_p)$ and $(\hat{\beta}^s_p, \hat{\alpha}^s_p, \hat{e}^s_p)$, as shown in Fig. 11, to specify three local coordinate systems associated with the incident light, the *pth* order inwardly propagating beam, and the *pth* order outwardly propagating beam. Based on defined local coordinated systems, Snell's law, and Fresnel formulas, the geometric-optics near-field within the particle can be expressed as the superposition of electromagnetic fields in conjunction with various internal ray tubes.

We find that for each ray tube, after the electric field at a specific point (e.g., the

first vertex) in the initial beam cross section is known, the electric field at an arbitrary position in the ray tube can be obtained by taking into account the variation of the phase and the amplitude. For one of the *pth* order ray tubes, the two components of the electric field associated with the first vertex of the initial cross section is given by,

$$\begin{bmatrix} E_{p,\alpha}(\vec{r}_{p,1}) \\ E_{p,\beta}(\vec{r}_{p,1}) \end{bmatrix} = U_p \begin{bmatrix} E^i_{p,\alpha} \\ E^i_{p,\beta} \end{bmatrix} \exp\left(ik\delta_{p,1}\right) \exp\left(-kN_i d_{p,1}\right), \tag{4.14}$$

where E^i_α and E^i_β are two components of the incident field along two polarization vectors $\hat{\alpha}^i$ and $\hat{\beta}^i$; U_p is a matrix associated with Snell's law, Fresnel formulas, and necessary coordinate transformations; k is the wave number; N_i is the imaginary part of the effective refractive index [53]; and $\delta_{p,1}$ and $d_{p,1}$ account for the phase delay and the decrease in the amplitude of the electric field due to absorption. When $p = 1$, it can be verified that

$$\delta_{1,1} = \vec{e}^{\,i} \cdot \vec{r}_{1,1}, \quad d_{1,1} = 0. \tag{4.15}$$

At the position denoted by $\vec{r}_{p,1} + \vec{w}_p$, where $\vec{w}_p$ indicates the position in the beam cross section, the two components of the electric field $\vec{E}_p$ are given by

$$\begin{bmatrix} E_{p,\alpha}(\vec{r}_{p,1} + \vec{w}_p) \\ E_{p,\beta}(\vec{r}_{p,1} + \vec{w}_p) \end{bmatrix} = U_p \begin{bmatrix} E^i_{p,\alpha} \\ E^i_{p,\beta} \end{bmatrix} \exp[ik(N_r \hat{e}_p \cdot \vec{w}_p + \delta_{p,1})] \exp\Big[-kN_i(\vec{A}_p \cdot \vec{w}_p + d_{p,1})\Big], \tag{4.16}$$

where $N_r \hat{e}_p \cdot \vec{w}_p$ is associated with the variation of the phase, and $\vec{A}_p$ is a vector defined to account for the variation of the amplitude in the beam cross section. $\vec{A}_p$ is found to be determined by an iterative formula:

$$\vec{A}_1 = 0, \vec{A}_p = \vec{A}_{p-1} + (1 - \hat{e}_{p-1} \cdot \vec{A}_{p-1}) \frac{\hat{n}_{p-1}}{\hat{e}_{p-1} \cdot \hat{n}_{p-1}}. \tag{4.17}$$

$\vec{A}_1 = 0$ if the field has a phase variance but no amplitude variance on the external

reflection interface. $\vec{A}_p(p>1)$ is obtained by considering the differences in total path lengths associated with the first vertex and any other beam cross section position.

At an arbitrary position $\vec{r}'$ in the ray tube, we have

$$\vec{r}' = \vec{r}_{p,1} + \vec{w}_p + l\vec{e}_p, \tag{4.18}$$

where l is a variable associated with the propagating distance from the position $\vec{r}_{p,1} + \vec{w}_p$. Therefore, after considering the phase variation and the decrease of the amplitude along the propagation direction $\vec{e}_p$, the electric field at any position within the ray tube can be written as

$$\begin{bmatrix} E_{p,\alpha}(\vec{r}') \\ E_{p,\beta}(\vec{r}') \end{bmatrix} = \begin{bmatrix} E_{p,\alpha}(\vec{r}_{p,1} + \vec{w}_p) \\ E_{p,\beta}(\vec{r}_{p,1} + \vec{w}_p) \end{bmatrix} \exp(ikNl), \tag{4.19}$$

and at the specific position of $\vec{r}_{p+1,1}$, is given by

$$\begin{bmatrix} E_{p,\alpha}(\vec{r}_{p+1,1}) \\ E_{p,\beta}(\vec{r}_{p+1,1} \end{bmatrix} = U_p \begin{bmatrix} E^i_{p,\alpha} \\ E^i_{p,\beta} \end{bmatrix} \exp\left(ik\delta_{p+1,1}\right) \exp\left(-kN_i d_{p+1,1}\right) \tag{4.20}$$

where

$$\delta_{p+1,1} = \delta_{p,1} + N_r|\vec{r}_{p+1,1} - \vec{r}_{p,|}, \tag{4.21}$$

$$d_{p+1,1} = d_{p,1} + |\vec{r}_{p+1,1} - \vec{r}_{p,|}. \tag{4.22}$$

Thus far, the information of the electric field in the considered ray tube is completely specified.

After the reflection of the pth order ray tube, depending upon the beam splitting, several next-order ray tubes may exist. We let the position vectors of one of the sub-beam cross sections be $\vec{r}'_{p+1,i}(i=1,2,...)$ to be distinguished with the notations of the original beam cross section. Obtaining the electric field in the corresponding next-

order ray tube requires the information of the electric field associated with $\vec{r}'_{p+1,1}$, which is represented in a similar form to Eq. (4.14) and given by

$$\begin{bmatrix} E_{p,\alpha}(\vec{r}'_{p+1,1}) \\ E_{p,\beta}(\vec{r}'_{p+1,1} \end{bmatrix} = U_{p+1} \begin{bmatrix} E^i_{p,\alpha} \\ E^i_{p,\beta} \end{bmatrix} \exp\left(ik\delta'_{p+1,1}\right) \exp\left(-kN_i d'_{p+1,1}\right), \tag{4.23}$$

where U_{p+1} is calculated from U_p and the Fresnel reflection matrix, and $\delta'_{p+1,1}$ and $d'_{p+1,1}$ are given by

$$\delta'_{p+1,1} = \delta_{p+1,1} + N_r \vec{e}_{p+1} \cdot (\vec{r}'_{p+1,1} - \vec{r}_{p+1,1}), \tag{4.24}$$

$$d'_{p+1,1} = d_{p+1,1} + \vec{A}_{p+1} \cdot (\vec{r}'_{p+1,1} - \vec{r}_{p+1,1}). \tag{4.25}$$

Up to this point, the electric field information in the next-order ray tube can be obtained by applying a similar procedure described for the *pth* order ray tube. The internal electric field in all the ray tubes can be determined with the help of the beam-tracing technique.

In principle, each beam propagating within the particle undergoes an infinite number of internal reflections, and the electric field beams amplitude decreases during the interactions with a particle. Therefore, the ray tubes contribution, after a number of internal reflections to the total radiation scattering and absorption by a particle, can be neglected. In the numerical algorithm, the beam-tracing process is terminated when the energy associated with the internal reflected beam is smaller than a user-defined number (e.g., less than 10^{-5}). The energy of the pth order internal reflected beam is given by

$$F = \frac{1}{2}\left(|U_p^{11}|^2 + |U_p^{12}|^2 + |U_p^{21}|^2 + |U_p^{22}|^2\right) \exp\left(-2kN_i d_p\right) \tilde{D}_p |\hat{e}_p \cdot \hat{n}_p|, \tag{4.26}$$

where $\tilde{D}_p$ is an integral over the beam cross section and given as follows:

$$\begin{aligned}\tilde{D}_p &= \int \exp(-2kN_i\vec{w}_p\cdot\vec{A}_p)d^2\vec{w}_p \\ &= \frac{1}{2kN_i}\sum_{j=1}^{N}\frac{(\vec{r}_{p,j+1}-\vec{r}_{p,j})\cdot(\vec{A}_p\times\hat{n}_p)}{|\vec{A}_p|^2-(\vec{A}_p\cdot\hat{n}_p)^2}\frac{\sin[ikN_i\vec{A}_p\cdot(\vec{r}_{p,j+1}-\vec{r}_{p,j})]}{ikN_i\vec{A}_p\cdot(\vec{r}_{p,j+1}-\vec{r}_{p,j})} \\ &\times \exp[-kN_i\vec{A}_p\cdot(\vec{r}_{p,j+1}+\vec{r}_{p,j}-2\vec{r}_{p,1})]. \qquad (4.27)\end{aligned}$$

The calculation of the integral in Eq. (4.27) is based on the Stokes theorem.

The present algorithm of the near-field calculation based on the beam-splitting technique can be applied to arbitrary convex faceted particles. For non-absorbing particles, the efficiency of the algorithm depends on the orientation and shape of the particle and is essentially independent of the particle size. For absorptive particles, large size parameters make the algorithm faster because the higher order beams can be neglected within the limits of acceptable accuracy. Thus, this algorithm can be applied to very large size parameters. The computational time necessary is found to be on the order of seconds for a simulation involving a single particle orientation.

E. Scattering Phase Matrix

Once the electric field within the particle is known, the single-scattering properties of the dielectric particle can be obtained based on fundamental electromagnetic theory. The procedure is similar to those in the DDA and FDTD methods, but the PGOH allows the amplitude scattering matrix to be in analytical form with respect to each reflection/refraction event.

1. Surface Integral Method

On the basis of the electromagnetic equivalence theorem, the electric scattered field $\vec{E}^s(\vec{r})$ in the radiation zone can be formulated as a surface integral (2.44) over the

near electromagnetic field. In a simpler form, the relationship between asymptotic far scattered electric field and near electromagnetic field can be represented through a defined operator as follows,

$$\vec{E}^s(\vec{r})|_{kr\to\infty} = O(\vec{E}, \vec{H}). \tag{4.28}$$

Note that the operator O is linear since

$$O(\vec{E}_1 + \vec{E}_2, \vec{H}_1 + \vec{H}_2) = O(\vec{E}_1, \vec{H}_1) + O(\vec{E}_2, \vec{H}_2). \tag{4.29}$$

Due to the nature of linear operator O, ($\vec{E}$, $\vec{H}$) in Eq. (2.44) can be replaced with the scattered field ($\vec{E}^s$, $\vec{H}^s$) on the surface as $O(\vec{E}^i, \vec{H}^i) = 0$. In the PGOH, the near-field is approximately calculated in successive order by using the ray optics,

$$\vec{E} = \vec{E}^i + \vec{E}^r + \sum_{p=1}^{\infty} \vec{E}_p^t, \quad \vec{H} = \vec{H}^i + \vec{H}^r + \sum_{p=1}^{\infty} \vec{H}_p^t, \tag{4.30}$$

where $\vec{E}^i$ is the incident electric field, $\vec{E}^r$ is the electric field associated with reflected ray, and $\vec{E}_p^t$ is the electric field of pth order outgoing refracted rays. Therefore, the contribution of diffraction and external reflection to the far-field can be calculated separately by mapping the incident field and reflected field on the illuminated side of the particle through Eq. (2.44). Contribution from various refracted waves can be obtained through mapping outgoing refracted waves at various local surface elements.

Let's start to derive the amplitude scattering matrix associated with diffraction, reflection, and outgoing refracted rays. In a vector form, the electric field in the radiation zone is given by

$$\begin{bmatrix} E_\alpha^s \\ E_\beta^s \end{bmatrix} = \frac{e^{ikr}}{-ikr}\frac{k^2}{4\pi} \iint \begin{bmatrix} \hat{\alpha}^s \cdot \vec{Z} \\ \hat{\beta}^s \cdot \vec{Z} \end{bmatrix} e^{-ik\hat{r}\cdot\vec{r}'} d^2\vec{r}', \tag{4.31}$$

where

$$\vec{Z} = \left\{ \hat{r} \times [\hat{n}_s \times \vec{E}(\vec{r}')] - \hat{r} \times \hat{r} \times [\hat{n}_s \times \vec{H}(\vec{r}')] \right\}, \tag{4.32}$$

and

$$\begin{aligned} \hat{\alpha}^s \cdot \vec{Z} &= \left[\hat{\beta}^s \cdot (\hat{n}_s \times \vec{E}) + \hat{\alpha}^s \cdot (\hat{n}_s \times \vec{H}) \right] \\ &= \hat{n}_s \cdot (\vec{E} \times \hat{\beta}^s + \vec{H} \times \hat{\alpha}^s), \end{aligned} \tag{4.33}$$

$$\begin{aligned} \hat{\beta}^s \cdot \vec{Z} &= \left[-\hat{\alpha}^s \cdot (\hat{n}_s \times \vec{E}) + \hat{\beta}^s \cdot (\hat{n}_s \times \vec{H}) \right] \\ &= \hat{n}_s \cdot (-\vec{E} \times \hat{\alpha}^s + \vec{H} \times \hat{\beta}^s). \end{aligned} \tag{4.34}$$

Let's first consider diffraction. Electric and magnetic field associated with incident plane waves are represented as follows,

$$\vec{E}^i = (E^i_\alpha \hat{\alpha}^i + E^i_\beta \hat{\beta}^i) \exp\left(ik\hat{e}^i \cdot \vec{r}' \right), \tag{4.35}$$

$$\vec{H}^i = (E^i_\beta \hat{\alpha}^i - E^i_\alpha \hat{\beta}^i) \exp\left(ik\hat{e}^i \cdot \vec{r}' \right). \tag{4.36}$$

On the local planar surface, the incident field has only phase variation with equal amplitude. Therefore, we have

$$\begin{bmatrix} E^s_{d,l} \\ E^s_{d,r} \end{bmatrix} = \frac{e^{ikr}}{-ikr} D\hat{n} \cdot \begin{bmatrix} \hat{\alpha}^i \times \hat{\beta}^s - \hat{\beta}^i \times \hat{\alpha}^s & \hat{\beta}^i \times \hat{\beta}^s + \hat{\alpha}^i \times \hat{\alpha}^s \\ -(\hat{\beta}^i \times \hat{\beta}^s + \hat{\alpha}^i \times \hat{\alpha}^s) & \hat{\alpha}^i \times \hat{\beta}^s - \hat{\beta}^i \times \hat{\alpha}^s \end{bmatrix} \begin{bmatrix} E^i_\alpha \\ E^i_\beta \end{bmatrix} \tag{4.37}$$

where D is an integral over the local surface and reads,

$$D = \frac{k^2}{4\pi} \int_s \exp\{ik(\hat{e}^i - \hat{r}) \cdot \vec{r}'\} d^2\vec{r}'. \tag{4.38}$$

The expression of four elements of S^d can be further explicitly written as follows

$$S_{11}^d = -D\left[(1+\cos\theta)\hat{e}^i\cdot\hat{n} + \sin\theta\sin\phi\hat{\alpha}^i\cdot\hat{n} + \sin\theta\cos\phi\hat{\beta}^i\cdot\hat{n}\right], \quad (4.39)$$

$$S_{12}^d = D\left[\sin\theta\cos\phi\hat{\alpha}^i\cdot\hat{n} - \sin\theta\sin\phi\hat{\beta}^i\cdot\hat{n}\right], \quad (4.40)$$

$$S_{21}^d = -S_{12}^d, \quad (4.41)$$

$$S_{22}^d = S_{11}^d. \quad (4.42)$$

As of the external reflection, we have

$$\vec{E}^r = (E_\alpha^r\hat{\alpha}^r + E_\beta^r\hat{\beta}^r)\exp\left(ik\hat{e}^i\cdot\vec{r}'\right), \quad (4.43)$$

$$\vec{H}^r = (E_\beta^r\hat{\alpha}^r - E_\alpha^r\hat{\beta}^r)\exp\left(ik\hat{e}^i\cdot\vec{r}'\right), \quad (4.44)$$

and

$$\begin{bmatrix} E_{r,l}^s \\ E_{r,r}^s \end{bmatrix} = \frac{e^{ikr}}{-ikr}D\hat{n}\cdot\begin{bmatrix} \hat{\alpha}^r\times\hat{\beta}^s - \hat{\beta}^r\times\hat{\alpha}^s & \hat{\beta}^r\times\hat{\beta}^s + \hat{\alpha}^r\times\hat{\alpha}^s \\ -(\hat{\beta}^r\times\hat{\beta}^s + \hat{\alpha}^r\times\hat{\alpha}^s) & \hat{\alpha}^r\times\hat{\beta}^s - \hat{\beta}^r\times\hat{\alpha}^s \end{bmatrix}\begin{bmatrix} E_\alpha^r \\ E_\beta^r \end{bmatrix} \quad (4.45)$$

The amplitude scattering matrix associated with external reflection is

$$\begin{aligned}\begin{bmatrix} S_{11}^r & S_{12}^r \\ S_{21}^r & S_{22}^r \end{bmatrix} &= D\begin{bmatrix} \hat{n}\cdot(\hat{\alpha}^r\times\hat{\beta}^s - \hat{\beta}^r\times\hat{\alpha}^s) & \hat{n}\cdot(\hat{\beta}^r\times\hat{\beta}^s + \hat{\alpha}^r\times\hat{\alpha}^s) \\ -\hat{n}\cdot(\hat{\beta}^r\times\hat{\beta}^s + \hat{\alpha}^r\times\hat{\alpha}^s) & \hat{n}\cdot(\hat{\alpha}^r\times\hat{\beta}^s - \hat{\beta}^r\times\hat{\alpha}^s) \end{bmatrix} \\ &\times \begin{bmatrix} R_\alpha & 0 \\ 0 & R_\beta \end{bmatrix}\begin{bmatrix} \sin\phi_0 & -\cos\phi_0 \\ \cos\phi_0 & \sin\phi_0 \end{bmatrix}. \end{aligned} \quad (4.46)$$

Using

$$\hat{\alpha}^r = -\hat{\alpha}^i\cos(2\theta_i) - \hat{e}^i\sin(2\theta_i), \quad \hat{\beta}^r = \hat{\beta}^i, \quad (4.47)$$

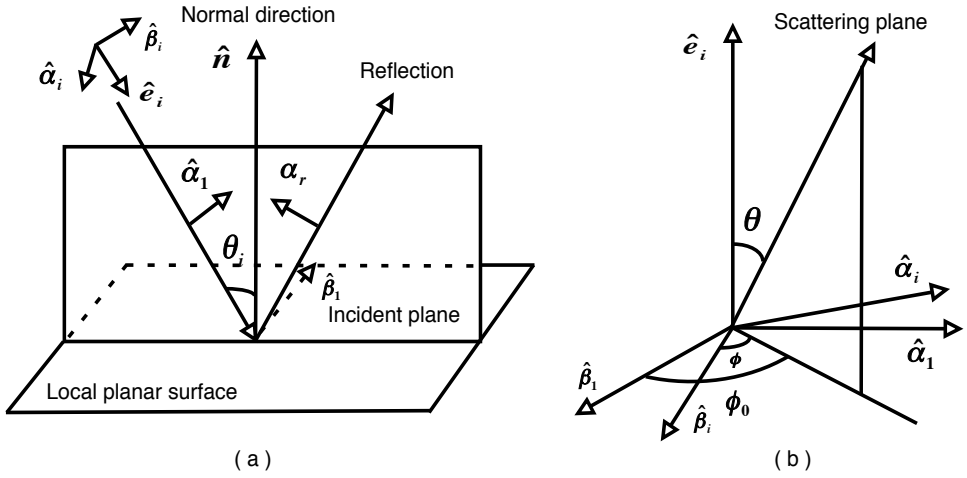

Fig. 12. Illustration of coordinate systems associated with reflection. (a) the local coordinate system $(\hat{\beta}_i, \hat{\alpha}_i, \hat{e}_i)$ of the incident ray is rotated to $(\hat{\beta}_1, \hat{\alpha}_1, \hat{e}_i)$ in order that the Fresnel coefficients can be employed to calculate the reflected electric-magnetic field vectors parallel and perpendicular to the incident plane. (b) θ is the scattering angle, ϕ is the azimuthal angle of scattering plane, and ϕ_0 is the angle between $\vec{\beta}_1$ and the scattering plane.

and

$$\hat{n} \cdot (\hat{\alpha}^r \times \hat{\beta}^s - \hat{\beta}^r \times \hat{\alpha}^s) = -(1 - \cos\theta)\cos\theta_i \sin\phi_0 - \sin\theta \sin\theta_i, \quad (4.48)$$

$$\hat{n} \cdot (\hat{\beta}^r \times \hat{\beta}^s + \hat{\alpha}^r \times \hat{\alpha}^s) = (1 - \cos\theta)\cos\theta_i \cos\phi_0, \quad (4.49)$$

we obtain explicit expressions of four elements,

$$S_{11}^r = D\left[(1 - \cos\theta)\cos\theta_i(R_\beta \cos^2\phi_0 - R_\alpha \sin^2\phi_0) - R_\alpha \sin\theta \sin\theta_i \sin\phi_0\right], \quad (4.50)$$

$$S_{12}^r = D\left[(1 - \cos\theta)\cos\theta_i(R_\alpha + R_\beta)\sin\phi_0 \cos\phi_0 + R_\alpha \sin\theta \sin\theta_i \cos\phi_0\right], \quad (4.51)$$

$$S_{21}^r = D\left[-(1 - \cos\theta)\cos\theta_i(R_\alpha + R_\beta)\sin\phi_0 \cos\phi_0 - R_\beta \sin\theta \sin\theta_i \cos\phi_0\right], \quad (4.52)$$

$$S_{22}^r = D\left[(1 - \cos\theta)\cos\theta_i(R_\alpha \cos^2\phi_0 - R_\beta \sin^2\phi_0) - R_\beta \sin\theta \sin\theta_i \sin\phi_0\right], \quad (4.53)$$

where θ_i is the incident angle, θ is the scattering angle, ϕ_0 is the angle between the scattering plane and $\vec{\beta}_1$ as shown in Fig.12. R_α and R_β are two components of Fresnel reflection coefficient corresponding to parallel and perpendicular components in the incident plane. It is required to be pointed out that D in Eq. (4.38) tends to the largest when the observational direction is along the reflected ray or the incident direction, which will explain peaks associated with reflection and diffraction in the phase function. For a three dimensional particle, the illuminated side of which is composed of N local planar surfaces, the amplitude scattering matrix is represented as the summation in terms of N local surfaces as follows,

$$S = \sum_{i=1}^{N} (S_i^d + S_i^r). \tag{4.54}$$

It should be pointed out that although the amplitude scattering matrix associated with diffraction and external reflection are semi-analytically derived, the formula are not exact due to the approximation of reflected field near the edges of planar surfaces. It is expected that the inaccuracy of reflected field near the edge tends to be very small when the size of the particle is very large, as the ray-optics is exact when the plane of surface is infinity.

For transparent or semi-transparent particles, each outgoing refracted ray contribute to the total amplitude scattering matrix. For each impinging ray, fields associated with outgoing refracted rays of different orders are given by

$$\vec{E}_p^t = (E_{p,\alpha}^t \hat{\alpha}_p^t + E_{p,\beta}^t \hat{\beta}_p^t) \exp(ik\delta_p),$$
$$\vec{H}_p^t = (E_{p,\beta}^t \hat{\alpha}_p^t - E_{p,\alpha}^t \hat{\beta}_p^t) \exp(ik\delta_p).$$

Counterparts in the radiation zone are

$$\begin{bmatrix} E^s_{t,l} \\ E^s_{t,r} \end{bmatrix} = \frac{e^{ikr}}{-ikr} D_p \hat{n} \cdot \begin{bmatrix} \hat{\alpha}^t_p \times \hat{\beta}^s - \hat{\beta}^t_p \times \hat{\alpha}^s & \hat{\beta}^t_p \times \hat{\beta}^s + \hat{\alpha}^t_p \times \hat{\alpha}^s \\ -(\hat{\beta}^t_p \times \hat{\beta}^s + \hat{\alpha}^t_p \times \hat{\alpha}^s) & \hat{\alpha}^t_p \times \hat{\beta}^s - \hat{\beta}^t_p \times \hat{\alpha}^s \end{bmatrix} \begin{bmatrix} E^t_{p,\alpha} \\ E^t_{p,\beta} \end{bmatrix}, \quad (4.55)$$

where (also see 4.71)

$$D_p = \frac{k^2}{4\pi} \int e^{ik\delta_p} d\sigma_p. \quad (4.56)$$

Let

$$\begin{bmatrix} E^t_{p,\alpha} \\ E^t_{p,\beta} \end{bmatrix} = \begin{bmatrix} M_{11} & M_{12} \\ M_{21} & M_{22} \end{bmatrix} \begin{bmatrix} E^i_l \\ E^i_r \end{bmatrix}. \quad (4.57)$$

Then

$$\begin{bmatrix} S^t_{11} & S^t_{12} \\ S^t_{21} & S^t_{22} \end{bmatrix} = D_p \begin{bmatrix} \hat{n} \cdot (\hat{\alpha}^t_p \times \hat{\beta}^s - \hat{\beta}^t_p \times \hat{\alpha}^s) & \hat{n} \cdot (\hat{\beta}^t_p \times \hat{\beta}^s + \hat{\alpha}^t_p \times \hat{\alpha}^s) \\ -\hat{n} \cdot (\hat{\beta}^t_p \times \hat{\beta}^s + \hat{\alpha}^t_p \times \hat{\alpha}^s) & \hat{n} \cdot (\hat{\alpha}^t_p \times \hat{\beta}^s - \hat{\beta}^t_p \times \hat{\alpha}^s) \end{bmatrix} \times \begin{bmatrix} M_{11} & M_{12} \\ M_{21} & M_{22} \end{bmatrix}. \quad (4.58)$$

Four elements of the matrix M are computed based on a ray-tracing technique.

2. Volume Integral Method

The far-field can be formulated as a volume integral (2.34) over the internal field within the particle [39]. The scattered field $\vec{E}^s(\vec{r})$ in the radiation region is transverse with respect to the scattering direction $\hat{r}$ and can be decomposed into two components in the form of

$$\vec{E}^s(\vec{r}) = E^s_\alpha(\vec{r})\hat{\alpha}^s + E^s_\beta(\vec{r})\hat{\beta}^s, \quad (4.59)$$

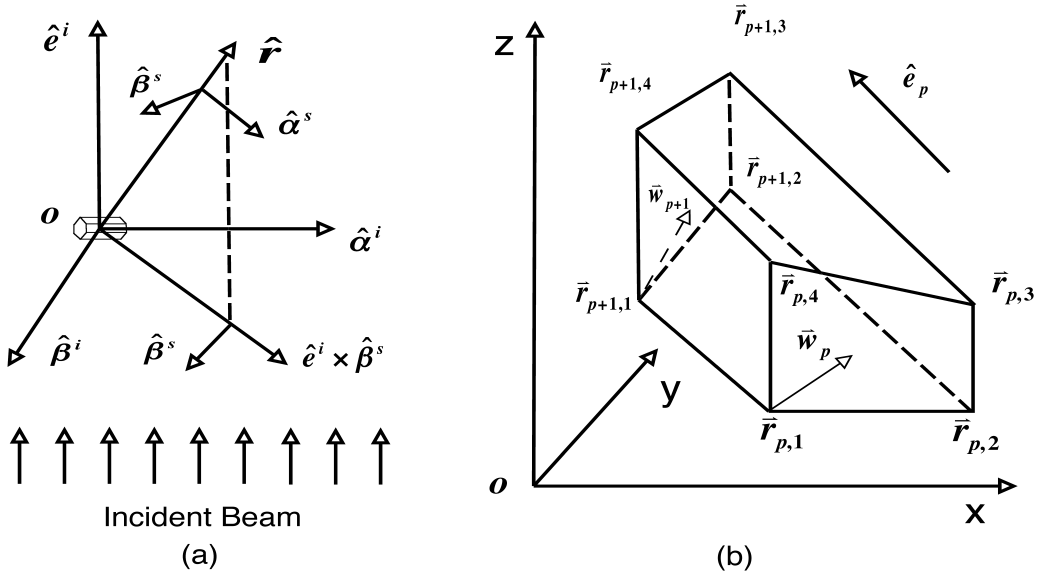

Fig. 13. (a) Scattering coordinate systems; (b) volume associated with a ray tube.

where $\hat{\alpha}^s$ and $\hat{\beta}^s$ are unit vectors parallel and perpendicular to the scattering plane, respectively, as shown in Fig. 13 (a). Taking dot products on both sides of Eq. (2.34) with respect to vectors $\hat{\alpha}^s$ and $\hat{\beta}^s$ yields

$$\begin{bmatrix} E^s_\alpha \\ E^s_\beta \end{bmatrix}_{kr\to\infty} = \frac{k^2 \exp(ikr)}{4\pi r} \iiint_v (m^2-1) \begin{bmatrix} \hat{\alpha}^s \cdot \vec{E}(\vec{r}') \\ \hat{\beta}^s \cdot \vec{E}(\vec{r}') \end{bmatrix} \exp\left(-ik\hat{r}\cdot\vec{r}'\right) d^3\vec{r}'. \quad (4.60)$$

In the geometric optics based PGOH, the internal field in Eq. (4.60) can be formally written as a summation with each term arising from different orders of reflection/refraction events

$$\vec{E}(\vec{r}') = \sum_{p=1}^{\infty} E_{p,\alpha}(\vec{r}')\hat{\alpha}_p + E_{p,\beta}(\vec{r}')\hat{\beta}_p. \quad (4.61)$$

Substituting Eq. (4.61) into Eq. (4.60), we obtain

$$\begin{bmatrix} E^s_\alpha \\ E^s_\beta \end{bmatrix}_{kr\to\infty} = \frac{k^2\exp(ikr)}{4\pi r}\sum_{p=1}^{\infty}\iiint_{v_p}(m^2-1)K_p\begin{bmatrix} E_{p,\alpha}(\vec{r}') \\ E_{p,\beta}(\vec{r}') \end{bmatrix}\exp\left(-ik\hat{r}\cdot\vec{r}'\right)d^3\vec{r}' \quad (4.62)$$

where v_p is the volume associated with the pth order internal ray tube as shown in Fig. 13 (b), and K_p is a matrix given by

$$K_p = \begin{bmatrix} \hat{\alpha}^s\cdot\hat{\alpha}_p & \hat{\alpha}^s\cdot\hat{\beta}_p \\ \hat{\beta}^s\cdot\hat{\alpha}_p & \hat{\beta}^s\cdot\hat{\beta}_p \end{bmatrix}. \quad (4.63)$$

Substituting the geometric-optics near-field given by Eq. (4.19) into Eq. (4.62), we obtain the following equation,

$$\begin{bmatrix} E^s_\alpha \\ E^s_\beta \end{bmatrix}_{kr\to\infty} = \frac{k^2\exp(ikr)}{4\pi r}\sum_{p=1}^{\infty}(m^2-1)K_pU_p\exp(ik\delta_{p,1}-N_ikd_{p,1})I_p\begin{bmatrix} E^i_\alpha \\ E^i_\beta \end{bmatrix}, \quad (4.64)$$

where I_p is an integral defined by

$$I_p = \iiint_{v_p}\exp\left[ik(N_r\vec{e}_p+iN_i\vec{A}_p)\cdot\vec{w}_p\right]\exp(ikNl)\exp(-ik\hat{r}\cdot\vec{r}')d^3\vec{r}'. \quad (4.65)$$

Eq. (4.65) must be analytically solved before additional numerical computations are considered. Recalling Eq. (4.18), we transform Eq. (4.65) into the following form,

$$\begin{aligned} I_p = &\iint_s d^2\vec{w}_p|\hat{e}_p\cdot\hat{n}_p|\exp\left[ik(N_r\vec{e}_p+iN_i\vec{A}_p)\cdot\vec{w}_p\right]\exp\left[-ik\hat{r}\cdot(\vec{r}_{p,1}+\vec{w}_p)\right]d^3\vec{r}' \\ &\times\int_0^{|\vec{r}_{p+1}-\vec{r}_p|+\frac{\vec{w}_{p+1}\cdot\hat{n}_p}{\hat{e}_p\cdot\hat{n}_p}}\exp\left[ik(N-\hat{r}\cdot\hat{e}_p)\right]. \end{aligned} \quad (4.66)$$

After solving the integration in Eq. (4.66) in terms of l and employing the following identities:

$$\vec{w}_{p+1} = \vec{w}_p + \frac{\vec{w}_{p+1}\cdot\hat{n}_p}{\hat{e}_p\cdot\hat{n}_p}\hat{e}_p, \tag{4.67}$$

$$\vec{A}_{p+1}\cdot\vec{w}_{p+1} = \vec{A}_p\cdot\vec{w}_p + \frac{\vec{w}_{p+1}\cdot\hat{n}_p}{\hat{e}_p\cdot\hat{n}_p}, \tag{4.68}$$

$$\hat{e}^s_{p+1}\cdot\vec{w}_{p+1} = \hat{e}^s_p\cdot\vec{w}_p + N_r\frac{\vec{w}_{p+1}\cdot\hat{n}_p}{\hat{e}_p\cdot\hat{n}_p}, \tag{4.69}$$

we obtain an explicit expression for I_p , given as follows,

$$I_p = \frac{4\pi}{k^2}\frac{1}{ik(N-\hat{r}\cdot\hat{e}_p)}\left[|\hat{e}_p\cdot\hat{n}_{p+1}|D_{p+1}\exp\left(ikN|\vec{r}_{p+1}-\vec{r}_p|\right) - |\hat{e}_p\cdot\hat{n}_p|D_p\right], \tag{4.70}$$

where

$$\begin{aligned} D_p &= \frac{k^2}{4\pi}\exp\left(-ik\hat{r}\cdot\vec{r}_{p,1}\right)\int\exp\left\{ik(\hat{e}^s_p-\hat{r}+iN_i\vec{A}_p)\cdot\vec{w}_p\right\}d^2\vec{w}_p \\ &= \frac{ik}{4\pi}\sum_{j=1}^{N}\frac{(\vec{r}_{p,j+1}-\vec{r}_{p,j})\cdot[(\hat{e}^s_p-\hat{r}+iN_i\vec{A}_p)\times\hat{n}_p]}{(\hat{e}^s_p-\hat{r}+iN_i\vec{A}_p)\cdot(\hat{e}^s_p-\hat{r}+iN_i\vec{A}_p)-[(\hat{e}^s_p-\hat{r}+iN_i\vec{A}_p)\cdot\hat{n}_p]^2} \\ &\times \frac{\sin[k(\hat{e}^s_p-\hat{r}+iN_i\vec{A}_p)\cdot(\vec{r}_{p,j+1}-\vec{r}_{p,j})/2]}{k(\hat{e}^s_p-\hat{r}+iN_i\vec{A}_p)\cdot(\vec{r}_{p,j+1}-\vec{r}_{p,j})/2}\exp\left[-ik\hat{r}\cdot(\vec{r}_{p,j+1}+\vec{r}_{p,j})/2\right] \\ &\times \exp\left[ik(\hat{e}^s_p+iN_i\vec{A}_p)\cdot(\vec{r}_{p,j+1}+\vec{r}_{p,j}-2\vec{r}_{p,1})/2\right]. \end{aligned} \tag{4.71}$$

The scattered far-field can be written in an analytical form of

$$\begin{aligned} \begin{bmatrix} E^s_\alpha \\ E^s_\beta \end{bmatrix}_{kr\to\infty} &= \frac{\exp(ikr)}{-ikr}(1-m^2)\sum_{p=1}^{\infty}\frac{K_pU_p}{N-\hat{r}\cdot\hat{e}_p}\begin{bmatrix} E^i_\alpha \\ E^i_\beta \end{bmatrix}[|\hat{e}_{p+1}\cdot\hat{n}_{p+1}| \\ &\times D_{p+1}\exp\left(ik\delta_{p+1}-N_ikd_{p+1}\right) - |\hat{e}_p\cdot\hat{n}_p|D_p\exp\left(ik\delta_p-N_ikd_p\right)]. \end{aligned} \tag{4.72}$$

The amplitude scattering matrix associated with the scattered field in Eq. (4.72) is given by

$$\begin{bmatrix} S_2 & S_3 \\ S_4 & S_1 \end{bmatrix} = (1-m^2)\sum_{p=1}^{\infty} \frac{K_p U_p \Gamma}{N - \hat{r}\cdot\hat{e}_p} \left[|\hat{e}_{p+1}\cdot\hat{n}_{p+1} \right.$$
$$\left. \times \ |D_{p+1}\exp\left(ik\delta_{p+1} - N_i k d_{p+1}\right) - |\hat{e}_p\cdot\hat{n}_p| D_p \exp\left(ik\delta_p - N_i k d_p\right)\right] \qquad (4.73)$$

or

$$\begin{aligned} \begin{bmatrix} S_2 & S_3 \\ S_4 & S_1 \end{bmatrix} &= (m^2-1)\frac{K_1 U_1 \Gamma}{N - \hat{r}\cdot\hat{e}_1} |\hat{e}_1\cdot\hat{n}_1| D_1 \exp(i\delta_{1,1}) \\ &+ (1-m^2)\sum_{p=2}^{\infty}\left[\frac{K_{p-1}U_{p-1}}{N-\hat{r}\cdot\hat{e}_{p-1}} - \frac{K_p U_p}{N-\hat{r}\cdot\hat{e}_p}\right]\Gamma \\ &\times \ |\hat{e}_{p-1}\cdot\hat{n}_p| D_p \exp\left(ik\delta_{p,1}\right)\exp\left(-N_i k d_{p,1}\right). \end{aligned} \qquad (4.74)$$

Γ is a rotational matrix that transforms the two components of the incident field to their counterparts parallel and perpendicular to the scattering plane and given by

$$\Gamma = \begin{bmatrix} \hat{\beta}^i\cdot\hat{\beta}^s & \hat{\alpha}^i\cdot\hat{\beta}^s \\ -\hat{\alpha}^i\cdot\hat{\beta}^s & \hat{\beta}^i\cdot\hat{\beta}^s \end{bmatrix}. \qquad (4.75)$$

Note, a number of beams associated with the *pth* order reflection/refraction are not explicitly indicated in Eq. (4.74), but are actually in the numerical algorithm summation. Once the amplitude scattering matrix is obtained, the phase matrix elements are straightforward to compute [3].

The physical meaning implied in Eq. (4.74) is clearer than in Eq. (4.73). The first term in Eq. (4.74) accounts for the diffraction and external reflection contributions, and the second term arises from higher order outgoing refracted beams. Note the shape factor D is largest when the observation position vector is aligned with the direction of the relevant outgoing beam. This feature partially explains why the

angular scattering pattern is dominant around the scattered beam direction when the size parameter tends to be large. The explicit elements of the amplitude scattering matrix are obtained as follows

$$\begin{bmatrix} S_2 & S_3 \\ S_4 & S_1 \end{bmatrix} = \sum_{i=1}^{N} D_i \frac{(m^2-1)\cos\theta_t}{N_r + iN_i - \hat{r}\cdot\hat{e}_t} \begin{bmatrix} \tilde{S}_2 & \tilde{S}_3 \\ \tilde{S}_4 & \tilde{S}_1 \end{bmatrix}, \tag{4.76}$$

where N_r+iN_i is the effective complex refractive index [53], θ_t is the angle of refraction (different for each local planar surface), and $\hat{e}_t$ is the propagation direction of the first-order refracted wave. Four elements of the matrix $\tilde{S}$ are in the form of

$$\begin{aligned} \tilde{S}_2 &= \left[T_\alpha \cos(\theta_i-\theta_t)\sin^2\phi_0 + T_\beta\cos^2\phi_0 - T_\gamma\sin(\theta_i-\theta_t)\sin^2\phi_0\right]\cos\theta \\ &- \left[T_\alpha\sin(\theta_i-\theta_t) + T_\gamma\cos(\theta_i-\theta_t)\right]\sin\theta\sin\phi_0, \qquad (4.77) \\ \tilde{S}_3 &= \left[-T_\alpha\cos(\theta_i-\theta_t) + T_\beta + T_\gamma\sin(\theta_i-\theta_t)\right]\cos\theta\cos\phi_0\sin\phi_0 \\ &- \left[T_\alpha\sin(\theta_i-\theta_t) + T_\gamma\cos(\theta_i-\theta_t)\right]\sin\theta\cos\phi_0, \qquad (4.78) \\ \tilde{S}_4 &= \left[-T_\alpha\cos(\theta_i-\theta_t) + T_\beta + T_\gamma\sin(\theta_i-\theta_t)\right]\cos\phi_0\sin\phi_0, \qquad (4.79) \\ \tilde{S}_1 &= T_\alpha\cos(\theta_i-\theta_t)\cos^2\phi_0 + T_\beta\sin^2\phi_0 - T_\gamma\sin(\theta_i-\theta_t)\cos^2\phi_0. \qquad (4.80) \end{aligned}$$

where θ_i is the angle of incidence; T_α , T_β, and T_γ are three transmission coefficients [53], given by

$$\begin{aligned} T_\alpha &= \frac{2(N_r+iN_i)\cos\theta_i}{m^2\cos\theta_i + [N_r\cos\theta_t + iN_i/\cos\theta_t]}, \qquad (4.81) \\ T_\beta &= \frac{2\cos\theta_i}{\cos\theta_i + [N_r\cos\theta_t + iN_i/\cos\theta_t]}, \qquad (4.82) \\ T_\gamma &= \frac{i2N_i\tan\theta_t\cos\theta_i}{m^2\cos\theta_i + [N_r\cos\theta_t + iN_i/\cos\theta_t]}. \qquad (4.83) \end{aligned}$$

The formulation of the three transmission coefficients, taking into account the effect of inhomogeneous waves for absorptive particles, has been reported by Yang et al. [53]. Eqs. (2.44) and (2.34) are equivalent when the near-field is exactly known. However,

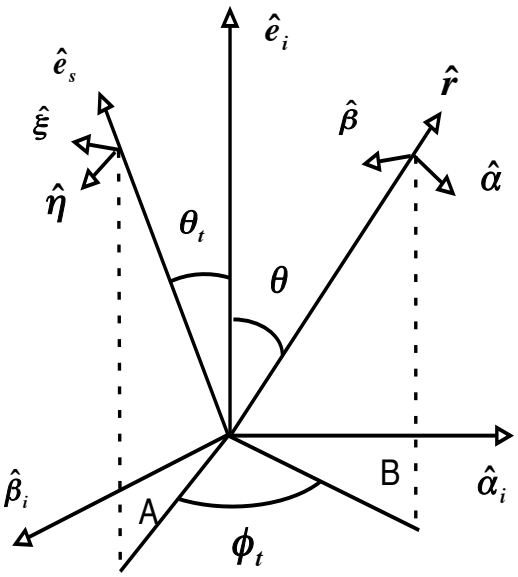

Fig. 14. Rotation of the scattering plane by an angle ϕ_t due to ray spreading.

the amplitude scattering matrices associated with the diffraction and the external reflection derived are not exactly equivalent. Of interest is that the diffraction and the external reflection are inherently combined in Eq. (4.76).

3. Simplified PGOH Algorithm

In the context of CGOM, the direction $\hat{e}_s$ of a outgoing ray and the forward direction $\hat{e}^i$ define a plane (labeled with symbol A as shown in Fig. 14). The amplitude scattering matrix associated with this outgoing ray is defined through

$$\begin{bmatrix} E_\xi^s \\ E_\eta^s \end{bmatrix} = \frac{\exp(ikr)}{-ikr} \begin{bmatrix} \tilde{S}_2 & \tilde{S}_3 \\ \tilde{S}_4 & \tilde{S}_1 \end{bmatrix} \begin{bmatrix} E_\xi^i \\ E_\eta^i \end{bmatrix}, \tag{4.84}$$

where $\hat{\xi}$ and $\hat{\eta}$ are unit vectors, which are perpendicular and parallel to the plane A. In the context of the PGOH, this plane may not be scattering plane when considering

the ray spreading effect. Assume that the scattering plane (labeled with symbol B) makes an angel ϕ with the plane A. Therefore, amplitude scattering matrix in the PGOH is defined in a different way as follows,

$$\begin{bmatrix} E_\beta^s \\ E_\alpha^s \end{bmatrix} = \frac{\exp(ikr)}{-ikr} \begin{bmatrix} S_2 & S_3 \\ S_4 & S_1 \end{bmatrix} \begin{bmatrix} E_\beta^i \\ E_\alpha^i \end{bmatrix}, \tag{4.85}$$

where $\hat{\beta}$ and $\hat{\alpha}$ are unit vectors, which are perpendicular and parallel to the scattering plane, i.e. the plane B , as shown in Fig. 14, respectively. The relation between amplitude scattering matrix $\tilde{S}$ and S is derived through Eq. (2.48) and is given by

$$\begin{bmatrix} S_2 \\ S_3 \\ S_4 \\ S_1 \end{bmatrix} = -\frac{k^2}{4\pi} \exp(ik\zeta) \begin{bmatrix} f_2 & -g_2 & f_3 & -g_3 \\ g_2 & f_2 & g_3 & f_3 \\ f_4 & -g_4 & f_1 & -g_1 \\ g_4 & f_4 & g_1 & f_1 \end{bmatrix} \begin{bmatrix} \tilde{S}_2 \\ \tilde{S}_3 \\ \tilde{S}_4 \\ \tilde{S}_1 \end{bmatrix}. \tag{4.86}$$

In Eq. (4.86), ζ is the phase of the ray, and f_i and g_i are:

$$f_i = \cos\phi_t \Xi_i, \tag{4.87}$$

$$g_i = \sin\phi_t \Xi_i, \quad (i = 1, 4). \tag{4.88}$$

The four elements Ξ_i (i=1, 4) are given by,

$$\Xi_1 = h\cos\phi_t, \tag{4.89}$$

$$\Xi_2 = h\cos\theta\cos\theta_t\cos\phi_t + h\sin\theta\sin\theta_t, \tag{4.90}$$

$$\Xi_3 = -h\cos\theta\sin\phi_t, \tag{4.91}$$

$$\Xi_4 = h\cos\theta_t\sin\phi_t, \tag{4.92}$$

where h is the same as Eq. (46b) in Yang and Liou [28]. Note that the matrix Ξ is different from Eq. (A8) in Yang and Liou [28] by a factor h. By using Eqs. (D.3)

and (D.4), we obtain a very simple and symmetric relation:

$$\begin{bmatrix} S_{11} & S_{12} & S_{13} & S_{14} \\ S_{21} & S_{22} & S_{23} & S_{24} \\ S_{31} & S_{32} & S_{33} & S_{34} \\ S_{41} & S_{42} & S_{43} & S_{44} \end{bmatrix} \propto \begin{bmatrix} \Xi_{11} & \Xi_{12} & \Xi_{13} & 0 \\ \Xi_{21} & \Xi_{22} & \Xi_{23} & 0 \\ \Xi_{31} & \Xi_{32} & \Xi_{33} & 0 \\ 0 & 0 & 0 & \Xi_{44} \end{bmatrix} \times \begin{bmatrix} \tilde{S}_{11} & \tilde{S}_{12} & \tilde{S}_{13} & \tilde{S}_{14} \\ \tilde{S}_{21} & \tilde{S}_{22} & \tilde{S}_{23} & \tilde{S}_{24} \\ \tilde{S}_{31} & \tilde{S}_{32} & \tilde{S}_{33} & \tilde{S}_{34} \\ \tilde{S}_{41} & \tilde{S}_{42} & \tilde{S}_{43} & \tilde{S}_{44} \end{bmatrix}$$
$$\times \begin{bmatrix} 1 & 0 & 0 & 0 \\ 0 & \cos(2\phi_t) & \sin(2\phi_t) & 0 \\ 0 & -\sin(2\phi_t) & \cos(2\phi_t) & 0 \\ 0 & 0 & 0 & 1 \end{bmatrix} \tag{4.93}$$

where the elements of a ray spreading matrix Ξ_{ij} are given in Appendix D. The matrix at right in Eq. (4.93) is associated with rotation of scattering plane A to B. It is required to point out that Eq. (4.93) is only for one outgoing ray. To consider the contribution of all outgoing rays to the scattering direction $\hat{r}$, the final phase matrix in the PGOH is an integral over all scattering directions in the PGOH:

$$S(\theta,\phi) = \int\int \Xi(\theta,\theta_t,\phi,\phi_0)\tilde{S}(\theta_t,\phi_0)L(\phi_t = \phi - \phi_0)\sin\theta_t d\theta_t d\phi_0 \tag{4.94}$$

where S, Ξ, $\tilde{S}$, and L are matrices, and ϕ_0 is the azimuthal angle of scattering planes in the PGOH.

For the diffraction part and the forward scattering, we consider it separately. Forward scattering pattern in the conventional geometric optics is delta functions, but in the context of the PGOH it is angular distributions around the forward directions when the ray spreading effect is considered. For randomly oriented particles, we expect that the interference among forward scattering rays could be properly neglected. In this case, explicit amplitude scattering matrix or phase matrix in terms at forward scattering could be explicitly derived and similar to diffraction pattern.

We notice that the traditional method of using the shadow diffraction theory and the ray-tracing technique to calculate the diffraction and reflection by randomly oriented particles can be improved. van de Hulst [2] suggests that the normalized reflection pattern for randomly oriented convex particles should be the same as that for spheres with the same surface conditions. Therefore, the reflection pattern for a sphere can be used to replace that calculated for general convex particles. This treatment will remove the difficulty in determining the scattered energy within the solid angle elements near the forward and backward directions.

The diffraction plus reflection (DPR) method is only applicable to randomly oriented particles due to singular points existing in the phase function. In the DPR method, the amplitude scattering matrix associated with diffraction is represented in terms of an integral over either the projection or the illuminated side of the particle. The reflection is calculated through geometric optics based on the ray-tracing technique. The energy associated with diffraction is assumed to be one half of the extinction cross section. The final phase matrix is given by

$$P = w_d P^d + w_r P^r, \tag{4.95}$$

where P^d and P^r are normalized phase matrices associated with diffraction and external reflection, respectively. w_d and w_r in Eq. (4.95) are relative weights, given by

$$w_d = \frac{\sigma_e}{\sigma_e + 2\sigma_r}, \tag{4.96}$$

$$w_r = \frac{2\sigma_r}{\sigma_e + 2\sigma_r} \tag{4.97}$$

where σ_r and σ_e are the cross sections associated with the reflection and extinction calculated from the ray-tracing technique. P^d is calculated from the Fraunhofer

diffraction theory as follows:

$$P^d = \begin{bmatrix} |S_{11}^d|^2 + |S_{22}^d|^2 & |S_{22}^d|^2 - |S_{11}^d|^2 & 0 & 0 \\ |S_{22}^d|^2 - |S_{11}^d|^2 & |S_{11}^d|^2 + |S_{22}^d|^2 & 0 & 0 \\ 0 & 0 & 2\mathrm{Re}({S_{11}^d}^* S_{22}^d) & 2\mathrm{Im}(S_{11}^d {S_{22}^d}^*) \\ 0 & 0 & -2\mathrm{Im}(S_{11}^d {S_{22}^d}^*) & 2\mathrm{Re}({S_{11}^d}^* S_{22}^d) \end{bmatrix} \tag{4.98}$$

where the two diagonal elements of the amplitude scattering matrix are given by [30]

$$d_{11}^d = D(1+\cos\theta)\cos\theta, \tag{4.99}$$

$$S_{22}^d = D(1+\cos\theta). \tag{4.100}$$

P^r is related to the Fresnel reflection coefficients, given by

$$P^r = \begin{bmatrix} R_\alpha R_\alpha^* + R_\beta R_\beta^* & R_\alpha R_\alpha^* - R_\beta R_\beta^* & 0 & 0 \\ R_\alpha R_\alpha^* - R_\beta R_\beta^* & R_\alpha R_\alpha^* + R_\beta R_\beta^* & 0 & 0 \\ 0 & 0 & 2\mathrm{Re}(R_\alpha R_\beta^*) & 2\mathrm{Im}(R_\alpha R_\beta^*) \\ 0 & 0 & -2\mathrm{Im}(R_\alpha R_\beta^*) & 2\mathrm{Re}(R_\alpha R_\beta^*) \end{bmatrix} \times \begin{bmatrix} 1 & 0 & 0 & 0 \\ 0 & \cos(\phi_0-\phi) & \sin(\phi_0-\phi) & 0 \\ 0 & -\sin(\phi_0-\phi) & \cos(\phi_0-\phi) & 0 \\ 0 & 0 & 0 & 1 \end{bmatrix}. \tag{4.101}$$

Note that for large randomly oriented convex particles, the reflection pattern is the same as that for spheres with the same surface area and refractive index, as articulated by van de Hulst [2]. Therefore, it is not necessary to compute the reflection pattern by using the ray-tracing technique, but the reflection pattern can be computed with

the analytical solution for spheres [53], given by

$$P_{11}^{r}(\theta) = c\left[\left|R_{\alpha}\left(\frac{\pi-\theta}{2}\right)\right|^{2} + \left|R_{\beta}\left(\frac{\pi-\theta}{2}\right)\right|^{2}\right] \tag{4.102}$$

where c is normalization constant, and $||$ indicates the modulus of a complex quantity.

The simplified PGOH algorithm neglect the phase interference between various outgoing rays for the computation of the phase matrix. In the previous publication, the simplified PGOH algorithm associated with PGOH method in computations of efficiency factors is called improved geometric optics method (IGOM). The applicability of the IGOM is restricted to randomly oriented ice crystals.

F. PGOH Cross Sections

Applying a similar procedure to derive the amplitude scattering matrix based on the beam-splitting algorithm, the extinction cross section obtained from Eq. (41) can be proven to be the same as that derived from an optical theorem given by

$$C_{ext} = \frac{2\pi}{k^{2}}\mathrm{Re}\left[S_{11}(\hat{e}^{i}) + S_{22}(\hat{e}^{i})\right] \tag{4.103}$$

and the absorption cross section is in the form of

$$\begin{aligned} C_{abs} &= \frac{1}{2}\sum_{p=1}^{\infty} N_r \exp\left(-2N_i k d_p\right)\left(|U_p^{11}|^2 + |U_p^{12}|^2 + |U_p^{21}|^2 + |U_p^{22}|^2\right) \\ &\times \left(|\hat{e}_p\cdot\hat{n}_p|\tilde{D}_p - \exp(-2N_i k|\vec{r}_{p+1}-\vec{r}_p|)||\hat{e}_{p+1}\cdot\hat{n}_{p+1}||\tilde{D}_{p+1}\right). \end{aligned} \tag{4.104}$$

The physical process implied in Eq. (4.104) is evident, because each term in the summation represents the energy difference between the energy entering the ray tube and that leaving the ray tube from the absorption of light. The energy entering the ray tube is given by Eq. (4.26). The real part of the effective refractive index in Eq. (4.104) accounts for the difference between the speed of light in the particle and its

surrounding medium.

G. Accuracy of PGOH Simulations

In principle, the PGOH is an approximate method. The accuracy of the PGOH simulations should be estimated by comparing the results with their counterparts simulated from other exact methods. In this study, we select the DDA method as a reference and use the Amsterdam DDA (ADDA) code developed by Yurkin and Hoekstra [15] for benchmark simulations. The DDA method discretizes the volume of the particle into various sub-volumes, termed dipoles, to solve an exact electromagnetic volume integral equation. The numerical accuracy of the DDA method depends on the number of dipoles used to represent the geometry of the particle. The DDA method is essentially an exact method as it directly solves the equations in the context of electrodynamics, and can be employed as a reference to test the accuracy of results computed from the PGOH method. The accuracy of the DDA method has been reported in the literature [50, 51]. When an ice particle is strongly absorptive, the contribution to the scattering matrices from outgoing refracted rays can be neglected. The amplitude scattering matrices associated with the diffraction and external reflection can be semi-analytically derived in the PGOH. Therefore, we can first examine the accuracy of the computation of the PGOH for diffraction and external reflection. There are three versions of PGOH: surface integral method (SIM), volume integral method (VIM), and IGOM.

The SIM and the VIM are applicable to particles with fixed orientations. Figures 15-17 compare the phase functions of compact hexagonal particles (i.e., the aspect ratio is unity) simulated from the SIM, the VIM and the DDA for three representative orientations. For each orientation, simulations were carried out at three size

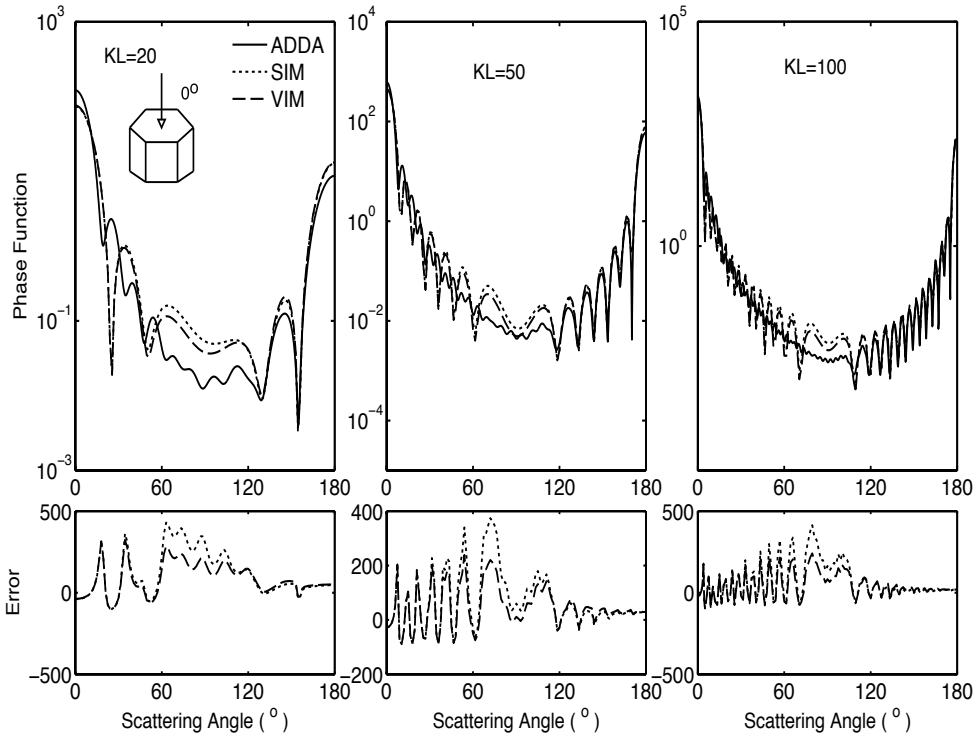

Fig. 15. Phase functions for hexagonal particles. The direction of the incident light is aligned with the axis of six-fold symmetry. The refractive index is 1.3+i1.0. The lower panel shows the relative differences between the results from the SIM and the VIM and that from the ADDA.

parameters: 20, 50 and 100 (i.e., small, moderate, and large values of the size parameter). In Fig. 15, the direction of the incident light is aligned with the axis of six-fold symmetry. A continuous pattern is obtained from the SIM and the VIM. As seen from the figure, the overall pattern of the phase functions from the SIM and the VIM agree with those from the ADDA. Large differences are found at scattering angles less than 90^o. For backscattering angles, the agreement between the methods is better.

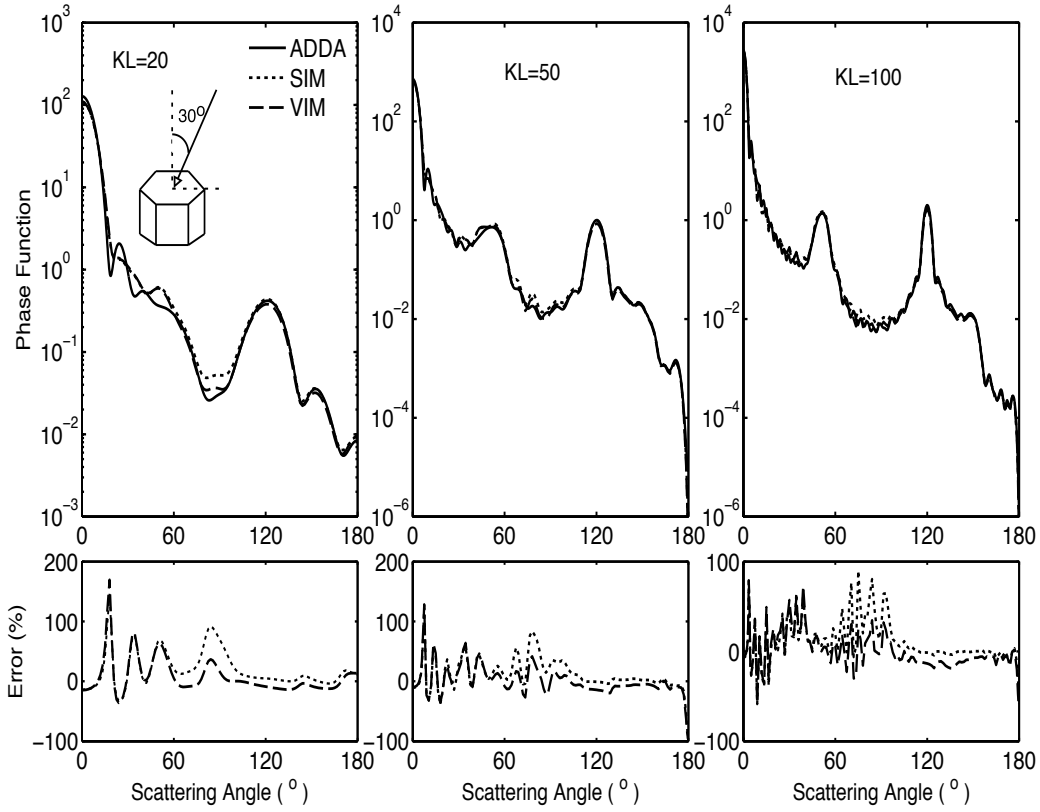

Fig. 16. Same as Fig. 15, except that the incident angle is 30^o. The 120^o peak is from the top reflection. The 51.3^o peak is due to the contributions from two sides.

In Fig. 16, the direction of the incident light makes an angle of 30^o with the axis of the particle and is parallel to one of the mirror planes. Two sharp peaks are found when the size parameter is 100. The 120^o peak is associated with the reflection from the top surface while the 51.3^o peak is from the reflections from two side faces. When the size parameter decreases, the peaks broaden. At a size parameter of 20, the 51.3^o peak is essentially not noticeable. This feature stems from the ray-spreading effect [27, 28]. When the incident light is parallel to the top surface, as seen in Fig. 17, the peak arising from the top reflection disappears and the peak location due to the reflection from two side surfaces is at 120^o. From the comparison of the phase

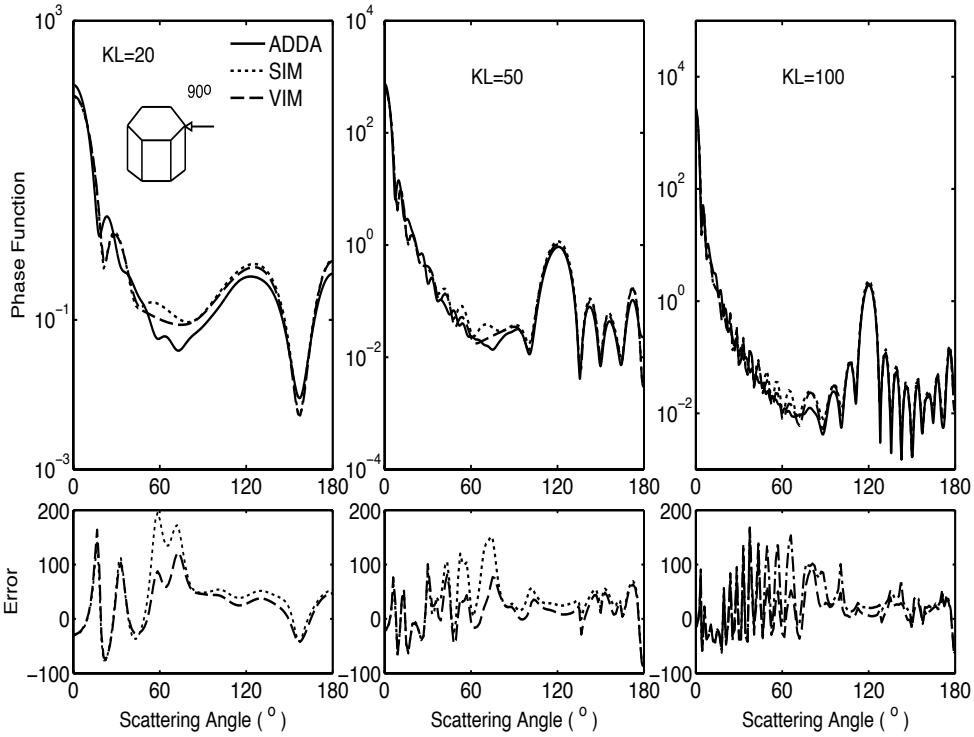

Fig. 17. Same as Fig. 15, except that the incident angle is 90^o. The illuminated side is composed of two local planar surfaces. The two scattering angles predicted from ray optics are the same and equal to 120^o.

functions, the difference between the results from the SIM/VIM and the DDA is pronounced when the incident angle of the incoming light is zero. The phase function values at scattering angles larger than 90^o are more accurate than those between 0^o and 90^o. The SIM and the VIM have comparable accuracy, although the formulae are not exactly equivalent.

The difference between the results calculated from the SIM/VIM and the DDA is due to the inaccuracy of the reflected field near the edges. For simplicity, we demonstrate the intensity of the electric field at the top face when the incident angle

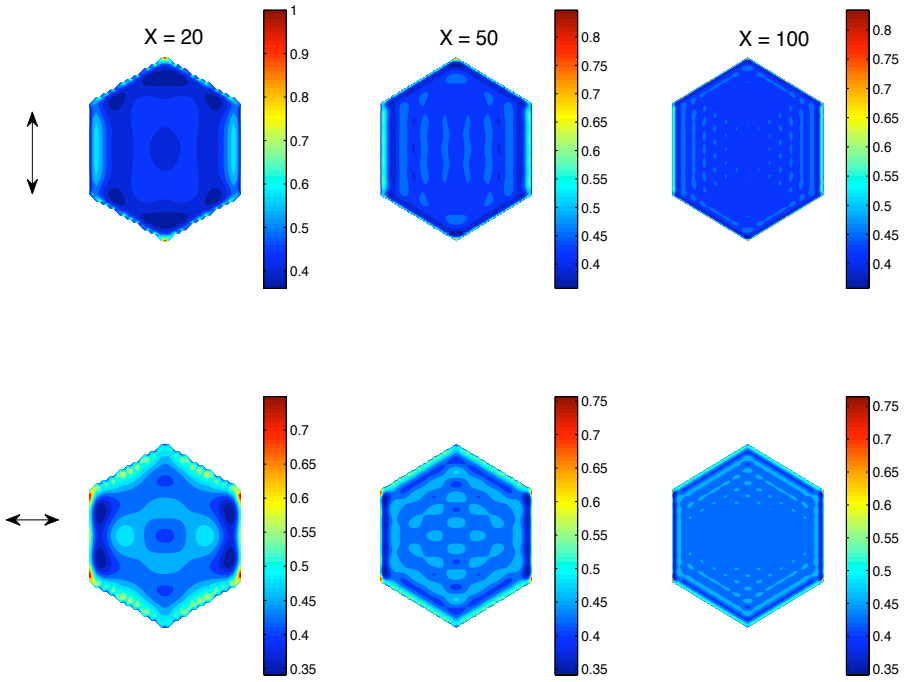

Fig. 18. Intensity of the total field of the first layer of dipoles near the hexagonal top. The direction of incident light is aligned with the axis. The two rows are for different polarization directions of the incident electric field. The three columns correspond to different size parameters.

is 0^o, as shown in Fig. 18. The upper and lower panels correspond to two polarizations of the incident light. In principle, the applicability of ray optics breaks down near the particle edge - the field near the edge is quite different from that within the polygon. At size parameters of 20 and 50, some structures in the intensity pattern may be observed, but these structures become less apparent as the size parameter increases. The comparison shown in Fig. 15 suggests that the edge effect may influence the forward scattering phase function.

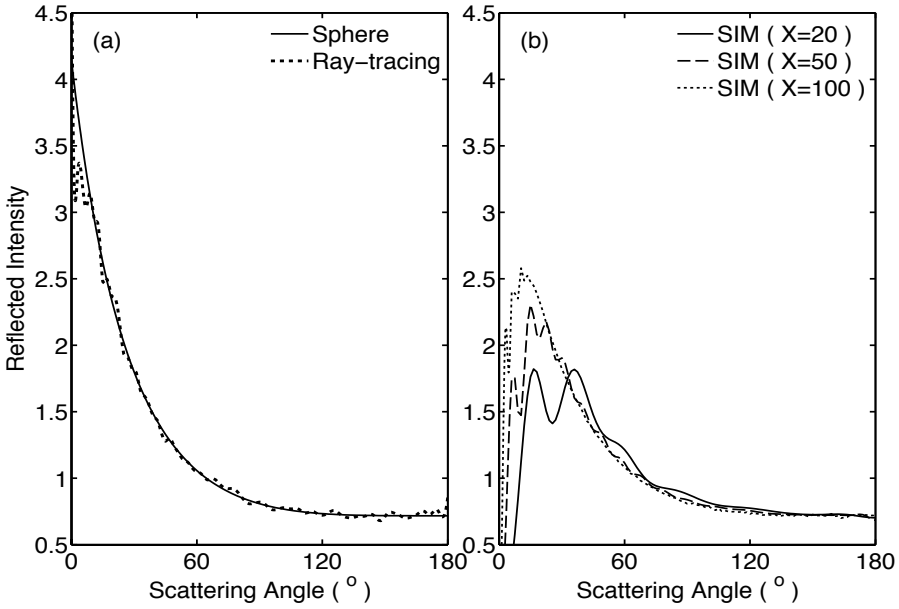

Fig. 19. (a) Comparison of normalized distributions of intensity associated with the external reflection from randomly oriented hexagonal particles calculated from the ray-tracing technique and the analytical solution for spheres with the same refractive index as that of hexagonal particles. (b) Reflection by randomly oriented hexagonal particles calculated from the SIM at three size parameters of 20, 50, and 100.

As discussed in Section D in this chapter, the diffraction and external reflection are separable in the SIM. Figure 19 shows the comparison of the normalized reflection pattern of randomly oriented hexagonal particles from the SIM and the DPR for a sphere with the same refractive index. In the SIM, the reflection pattern depends on the size parameter and is exactly zero in the forward scattering direction. A huge difference between results from the SIM and the DPR method is found near the forward scattering direction. The physical reason for a missing reflection pattern near the forward scattering angle is likely to be associated with the inaccuracy of

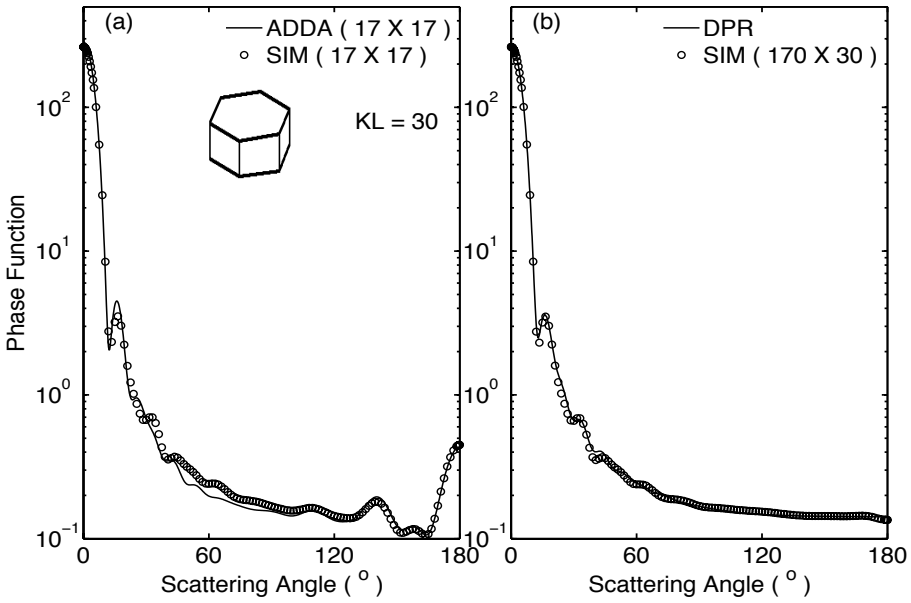

Fig. 20. Comparison of the phase function from the SIM, the ADDA and the DPR for randomly oriented particles. The random orientations in (a) for the ADDA and SIM are set through 17 zenith angles and 17 azimuthal angles. Random orientations in (b) for the SIM are specified through 170 zenith angles and 30 azimuthal angles to produce flat backscattering.

the reflected field near the boundary of the particle. When the size of the particle is large, the results from the SIM tend to match that of a sphere, as the edge effect is negligible. Note that a zero reflection in the forward scattering seems to be an artifact. The general pattern of the external reflection pattern from the ray-tracing technique agrees with that for spheres. However, the ray tracing technique is found to be inaccurate near the forward and the backward directions. From this figure we can see that for randomly oriented hexagonal particles, the DPR method can be employed as an efficient method to calculate the external reflection since it does not require the procedure to perform the average of reflection patterns over orientations.

For the comparison of the phase function of randomly oriented hexagonal particles from the SIM and the ADDA, shown in Fig. 20 (a), the number of orientations was set as 17x17 for the ADDA and SIM simulations. While a close agreement between the SIM and the ADDA is demonstrated, a structure in the backscattering phase function is observed. From the properties of the reflection pattern for randomly oriented particles, the phase function should be flat as illustrated by the DPR method. This is because the number of orientations is insufficient for representing the random orientation condition. Since the ADDA requires more computational time to perform numerical averages over a large number of orientations, we increased the number of orientations for the SIM due to its efficiency. As a result, a flat backscattering feature appears, as shown in Fig. 20 (b). Results from the SIM tended to match that of the DPR method, suggesting that the assumptions in the DPR method are reasonable. Therefore, for randomly oriented particles, the DPR method can be used as an efficient method for the first-order scattering simulation without losing accuracy. Note that the DPR is restricted to randomly oriented particles. For particles with preferred orientations, the SIM/VIM should be chosen. This comparison also indicates that the peak in the phase function around 16, observed in the ADDA calculation, is related to diffraction. For randomly oriented particles with complex shapes, the normalized reflection pattern is not the same as that of a sphere, and then the ray-tracing technique can be used.

In view of the above, the PGOH results from both of the SIM and VIM generally agree with their hexagonal ice particle counterparts computed from the DDA method. In the following part of this section, we present some results for transparent and semi-transparent particles.

Figure 21 shows the phase functions simulated from both the ADDA and PGOH. The aspect ratio of a hexagonal particle is L/D=1.0, where L and D are the length

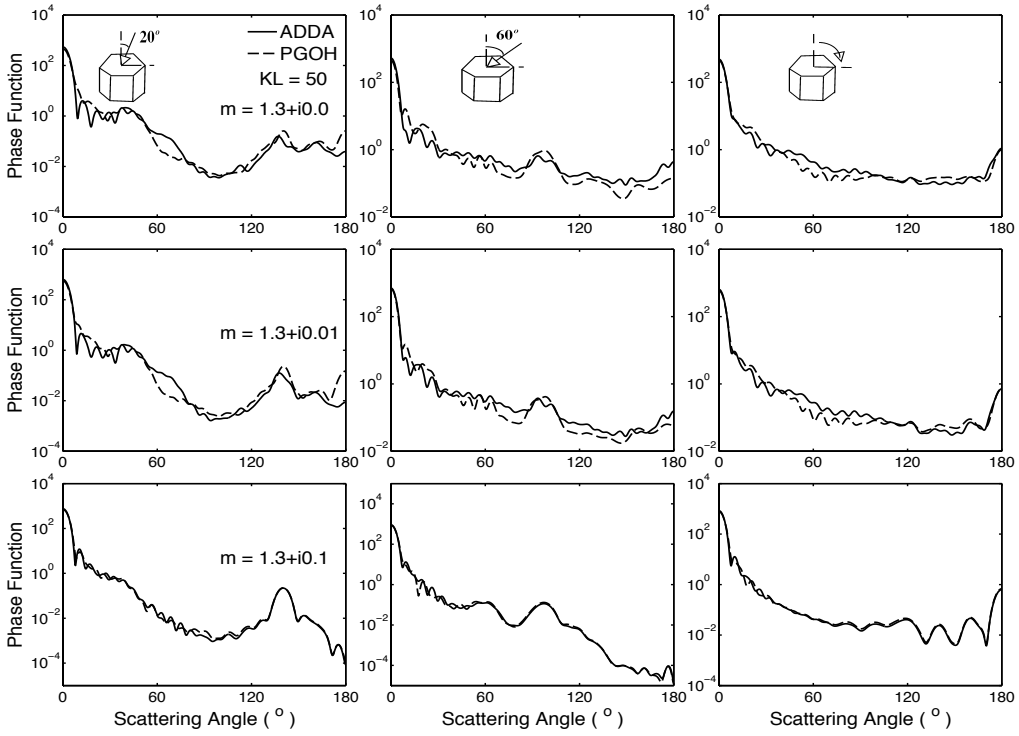

Fig. 21. Comparison of the phase functions computed from the DDA method and the PGOH method for three selected refractive indices. The size parameter defined in terms of the length is 50. The aspect ratio is 1.0.

and width of the particle, and the size parameter, defined in terms of particle length, is 50. The three rows correspond to refractive indices of 1.3, 1.3 + i 0.01, and 1.3 + i 0.1. The first and second columns are for the two fixed orientations indicated in the figure. The third column is the average phase function for 10 orientations with an interval of 10^o between 0^o and 90^o. As illustrated in the figure, the PGOH results and those computed from the ADDA compare well. The agreement is better for the strong absorption case where diffraction and external reflection are dominant. The general agreement between the results computed from the PGOH and the ADDA counterparts suggest that the PGOH provides a reasonably accurate estimation of the

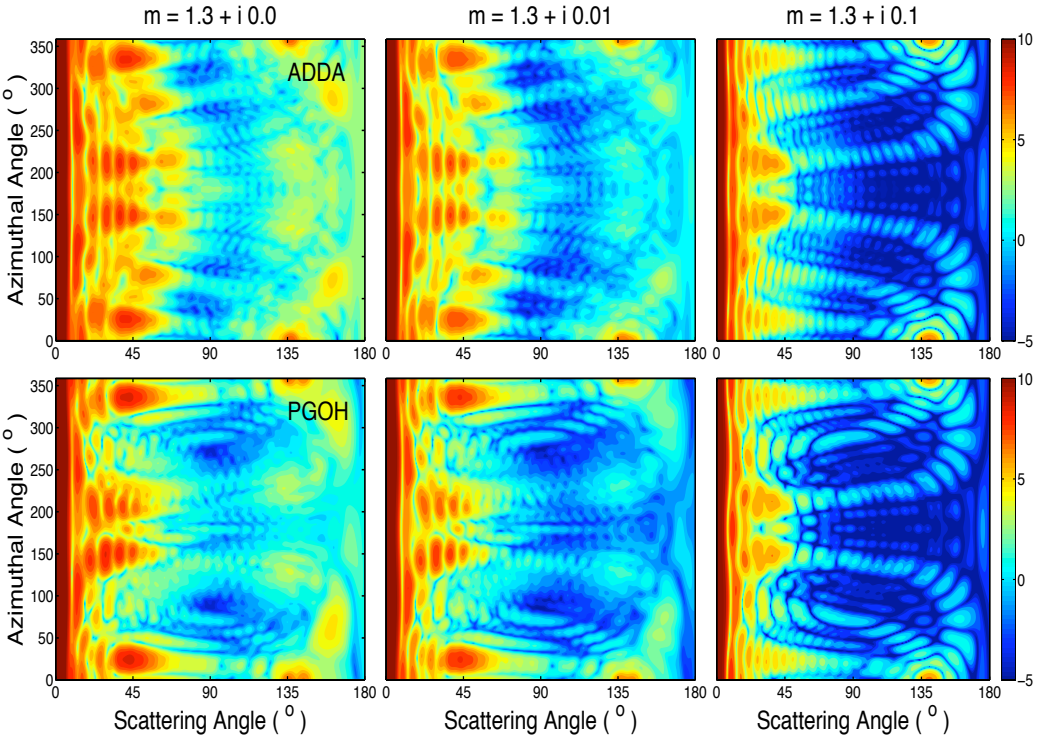

Fig. 22. Comparison of 2-D phase functions computed from the DDA method and the PGOH method for three selected refractive indices. The size parameter defined in terms of the length is 50. The aspect ratio is 1.0.

optical properties of ice particles including moderate sized ones. From the comparison, the averaging process seems to improve the accuracy of the phase function near the backward scattering directions. Note the peak of the phase function due to external reflection is evident for oriented particles.

Figure 22 shows the 2-D phase functions with respect to scattering and azimuthal angles simulated from the ADDA and PGOH. The computational parameters including the shape, the size, and the orientation of the hexagonal particle are the same as those in the first column of Fig. 21. The general angular patterns of PGOH simulated scattering are similar to those for the ADDA for all the selected refractive

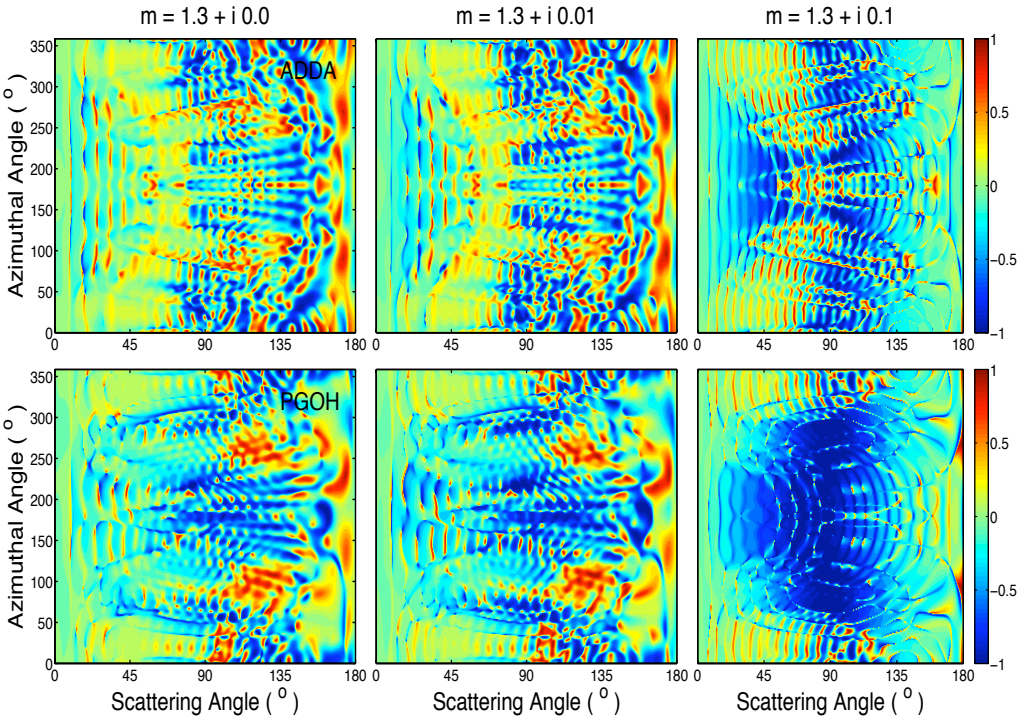

Fig. 23. Comparison of $P12/P11$ computed from the DDA method and the PGOH method for three selected refractive indices. The size parameter defined in terms of the length is 50. The aspect ratio is 1.0.

indices. For stronger absorption cases, the PGOH results are much closer to their ADDA counterparts. Two elements of the phase matrix, P12 and P22, are simulated from the ADDA and PGOH with results shown in Fig. 23 and Fig. 24, respectively. Note the similarity between the PGOH and ADDA results for both the P12 and P22 components.

Figure 25 shows the phase function of ice particles with large size parameters. Figure 25(a) compares the phase functions computed from the ADDA and PGOH. For this case, the DDA code is computationally expensive. Four orientations of an ice particle with respect to the symmetry axis are assumed. The PGOH results have

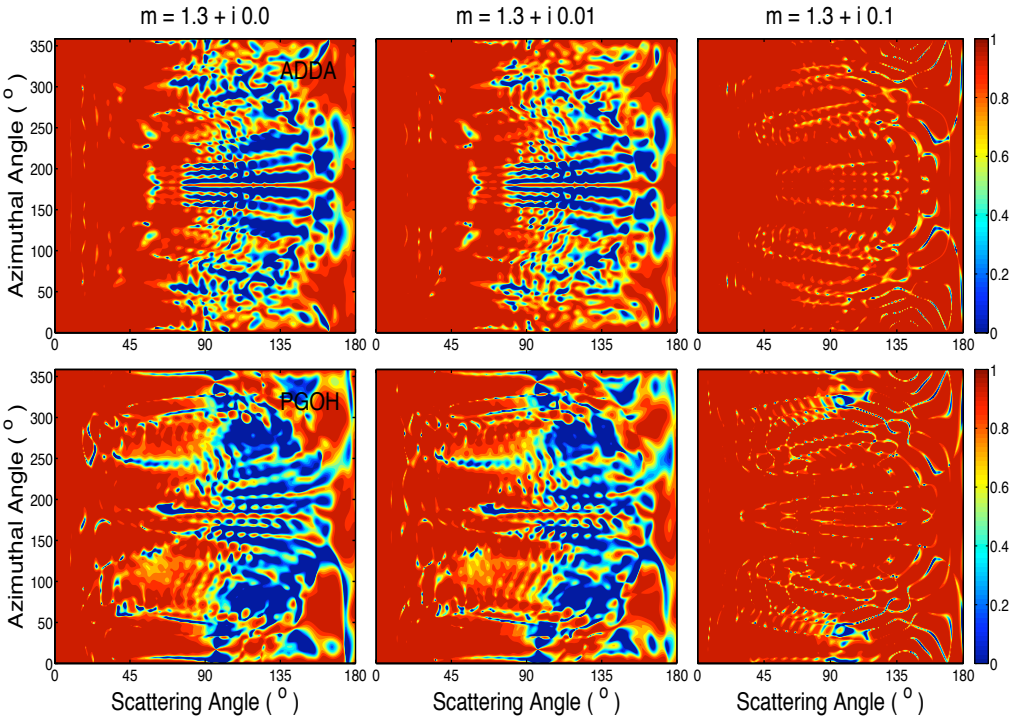

Fig. 24. Comparison of P22/P11 computed from the DDA method and the PGOH method for three selected refractive indices. The size parameter defined in terms of the length is 50. The aspect ratio is 1.0.

similar oscillations to those from the ADDA, but there are some differences noted in the scattering angle range from 90^o to 150^o. The size parameter for a hexagonal particle in Fig. 25((b) is very large, making it beyond the computational capability of the DDA method. As expected, two halos are observed in the phase function computed from the PGOH method. The results are calculated for 1000 different ice particle orientations with respect to the symmetry axis and subsequently averaged. In this simulation, we find that increasing the number of orientations does not diminish the oscillations in the PGOH simulated phase functions. One possible explanation for the oscillation is that it may be caused by interference between the various scattered

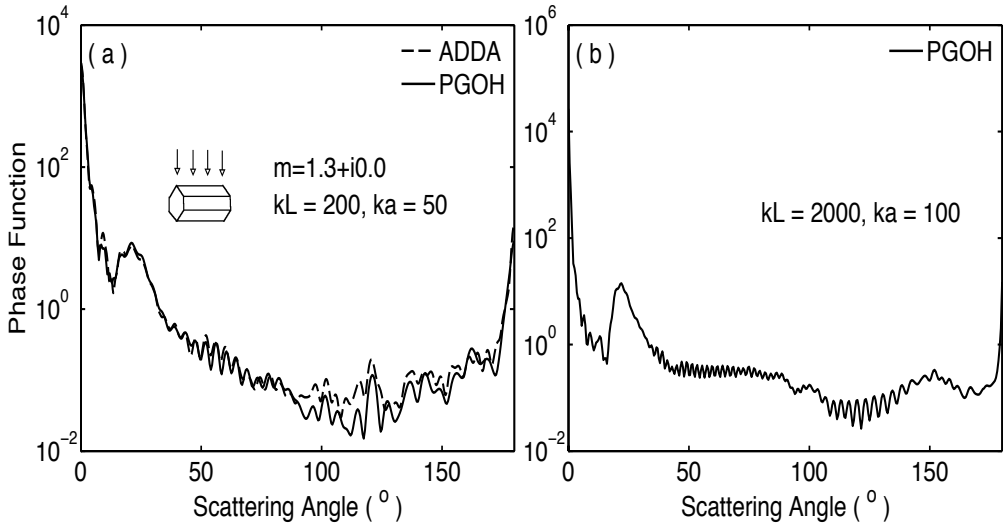

Fig. 25. (a) Comparison of the scattering phase function computed from the ADDA and the PGOH for a size parameter of 200. (b) Phase function computed from the PGOH for hexagonal ice particles randomly oriented with respect to the 6-fold symmetry axis.

beams.

Figure 26 shows the extinction efficiency factor and the absorption efficiency factor simulated from the ADDA and PGOH for three typical refractive indices. The particle orientation has a 20^o incident angle between the 6-fold symmetry axis and the incident direction. The figure shows the extinction efficiency factors computed from the PGOH can be larger than those computed from the ADDA when the size parameter is small. In this size parameter region, the geometric-optics approximation method is expected to fail as the ray is not a proper conceptualization of the process when the particle size is small or comparable with the wavelength of incident light. When the size parameter is larger than 10, the extinction efficiency factors simulated from the PGOH demonstrate similar behavior to their ADDA counterparts; however, the ADDA results are larger than the PGOH results. The physical reason for the

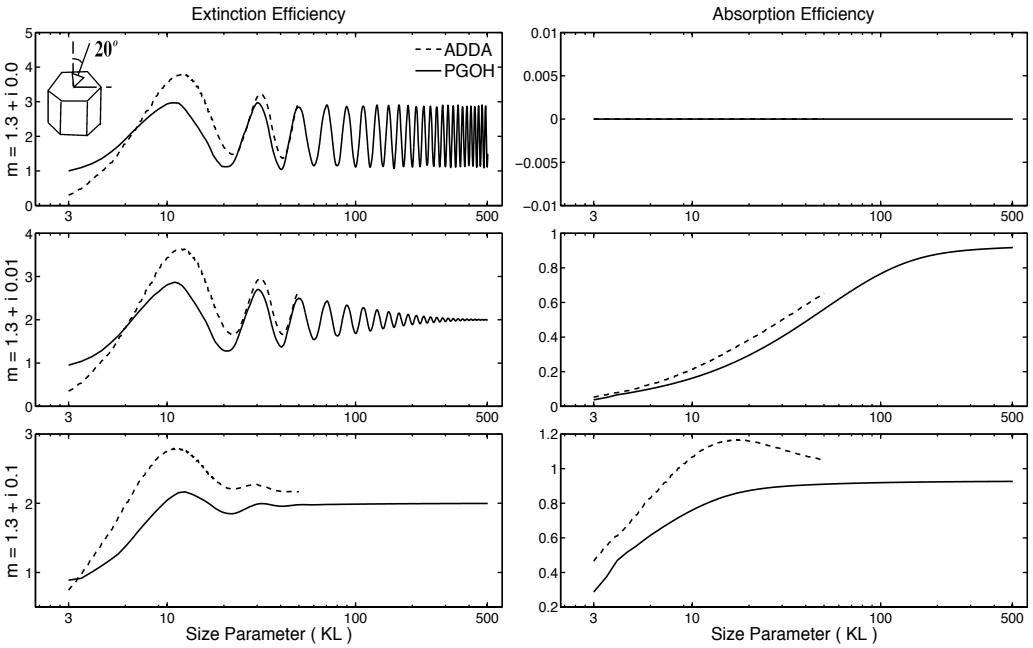

Fig. 26. The extinction and absorption efficiency factors simulated from the ADDA and the PGOH for oriented hexagonal ice particles. These results exclude consideration of the particle edge effect. Three typical refractive indices are selected.

difference is that the edge effect has not been considered. The existence of the edge effect contribution to the extinction of light for particles with no profile curvature are investigated by using the localization principle in Chapter V.

To bridge the gap between the ADDA results and their PGOH counterparts, two semi-empirical formulae to incorporate the edge effect contribution to the extinction and absorption efficiency factors are used in the present study and given by

$$Q_{ext,edge} = \frac{f_e}{(kL)^{2/3}}, \tag{4.105}$$

$$Q_{abs,edge} = \frac{f_a}{(kL)^{2/3}}, \tag{4.106}$$

where the two factors f_e and f_a are determined by the difference between the values of

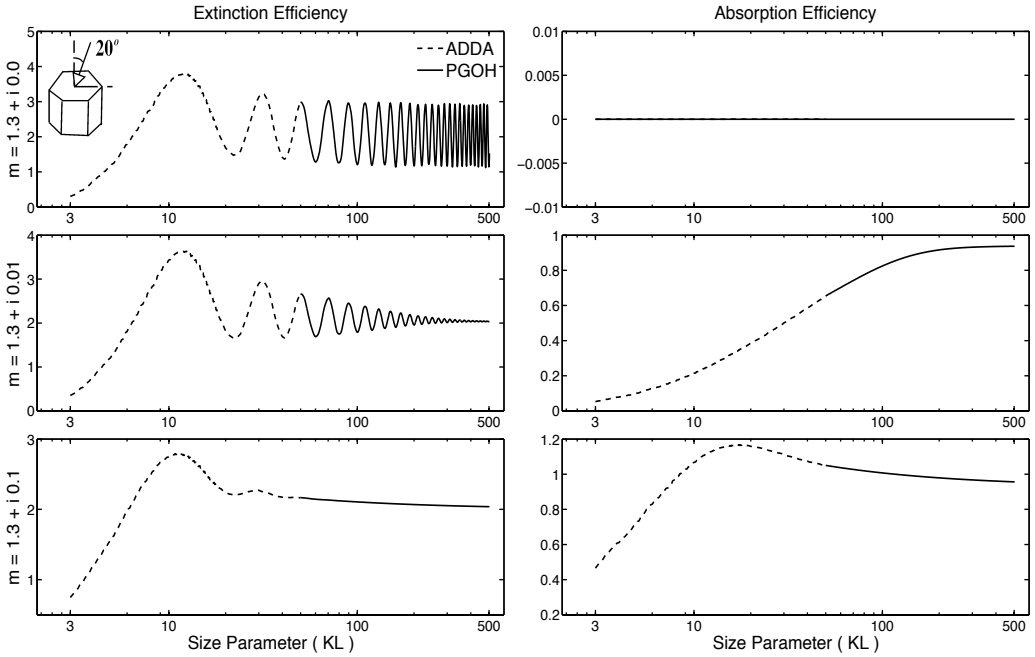

Fig. 27. Similar to Fig. 26, but with the edge effect incorporated in the PGOH method. Note how smoothly the ADDA results transition to those from the PGOH method.

the efficiency factor computed from the ADDA and the PGOH at the size parameter where the two methods are unified.

Figure 27 shows the results of the extinction efficiency factor and the absorption efficiency factor after the incorporation of edge effect contribution given by Eqs. (4.105) and (4.106). As evident from Fig. 27 , the curves of the extinction and absorption efficiency factor are now continuous over the range of size parameters. As a rigorous treatment of the edge effects for ice particles using Maxwells equations is not available at present, the semi-empirical method is essential to obtain the efficiency factors over a complete range of size parameters. The oscillation of the extinction efficiency factors results from interference between the forward transmission and diffraction. For non-absorptive particles, the oscillations do not diminish with

large size parameters. The oscillation phenomenon is not observed for either spheres or randomly oriented nonspherical particles. The non-convergent asymptotic value of the oriented ice particle extinction efficiency factor is demonstrated in the PGOH method results, but to the best of our knowledge, is neither justified through exact methods nor by measurements. Further investigation of this issue is warranted.

CHAPTER V

ELECTROMAGNETIC EDGE EFFECT *

The technical difficulty of the present unified method (i. e., combination of exact method and geometric-optics approximation method) is that the interaction between electromagnetic waves and lateral sides in the penumbra region, separating the illuminated sides and shadow region, cannot be accounted for in the context of geometric optics. Neglecting the contribution of the associated edge effects leads to discontinuities in the extinction efficiency and single-scattering albedo with respect to particle size parameter. A proper incorporation of edge effects is essential to obtain reliable and continuous curves of the extinction efficiency and the absorption efficiency factors.

A. Localization Principle

To introduce the localization principle, we consider the scattering of light by particle of axially rotational symmetry (sphere as a special case). The direction of light is aligned with the symmetry axis. Within the framework of the T-matrix formulation of light scattering, we found that the two off-diagonal elements of the scattering amplitude matrix are zero whereas the two diagonal elements can be written as

$$S_2 = \sum_{n=1}^{\infty} \frac{2n+1}{n(n+1)} \left[a_n \tau_n(\cos(\theta^s)) + b_n \pi_n(\cos(\theta^s)) \right], \tag{5.1}$$

$$S_1 = \sum_{n=1}^{\infty} \frac{2n+1}{n(n+1)} \left[a_n \pi_n(\cos(\theta^s)) + b_n \tau_n(\cos(\theta^s)) \right], \tag{5.2}$$

*Part of this chapter is reprinted with permission from "Edge-effect contribution to the extinction of light by dielectric disks and cylindrical particles" by L. Bi, P. Yang, and G. W. Kattawar, Appl. Opt. **49**, 4641-4616(2010)

where θ^s is the scattering angle, $\pi_n(\cos(\theta^s)) = P_n^1/\sin(\theta^s)$ and $\tau_n(\cos(\theta^s)) = dP_n^1/d\theta^s$. P_n^1 is the associated Legendre function of the first kind of degree n and order 1, and the two coefficients a_n and b_n can be expressed in terms of the T-matrix elements:

$$a_n = -\sum_{n'=1}^{\infty} \sqrt{\frac{2n'+1}{2n+1}} i^{n'-n} \left[T_{1n1n'}^{21} + T_{1n1n'}^{22}\right], \tag{5.3}$$

$$b_n = -\sum_{n'=1}^{\infty} \sqrt{\frac{2n'+1}{2n+1}} i^{n'-n} \left[T_{1n1n'}^{11} + T_{1n1n'}^{12}\right]. \tag{5.4}$$

For a spherical particle, the two coefficients simplify as follows:

$$a_n = -T_{1n1n}^{22}, \tag{5.5}$$

$$b_n = -T_{1n1n}^{11}. \tag{5.6}$$

It has been proven that the two coefficients a_n and b_n for spherical particles given by Eqs. (5.5) and (5.6) in the EBCM are the same as those formulated in the classical Lorenz-Mie theory [5]. By the "localization principle", the term for each n' in Eqs. (5.3) and (5.4) corresponds to a ray that passes the origin at a distance of $(n'+1/2)\lambda/2/\pi$ [2]. In quantum mechanics, this relationship implies that the angular momentum of a classical electron is associated with an eigenvalue of the angular momentum operator. Based on the localization principle, van de Hulst [2] derived the optical properties of large spheres from the exact Lorenz-Mie theory, and the results agree with the geometric-optics results. By using the complex angular momentum theory, Nussenzveig [32] investigated the edge effects implied in the Lorenz-Mie formula with improved accuracy.

To understand the "localization principle", let's start from the interpretation of the angular momentum of a classical particle and a quantum particle. In classical

mechanics, the angular momentum of a free particle is given by

$$L = pd, \tag{5.7}$$

where p is the momentum and d is the distance from the reference point to the trajectory. In quantum mechanics, the momentum is given by

$$p = \hbar k, \tag{5.8}$$

where $\hbar$ is Plank constant, and k is the wavenumber associated with de Broglie wave. Substituting Eq. (5.8) to (5.7), we obtain

$$L = \hbar k d. \tag{5.9}$$

In the quantum scattering of free particles by a potential, particles is described by a scaler plane wave, which is a solution to Schrödinger equation. The wave function of free particles can be expanded in terms of the eigenstates $|n>$ of the operator of angular momentum $\hat{L}^2$. The relation between $\hat{L}^2$ and $|n>$ is given by

$$\hat{L}^2|n>=\hbar^2 n(n+1)|n> . \tag{5.10}$$

Therefore, the angular momentum of the particle described by each term in the summation is

$$L = \hbar\sqrt{n(n+1)} \approx \hbar(n+1/2). \tag{5.11}$$

Comparing Eq.(5.9) and Eq. (5.11), one get the picture to link the description of a classical particle and a quantum particle through

$$d = (n+1/2)\lambda/2\pi. \tag{5.12}$$

Based on the similarity between quantum mechanics and optics, the above formula

(5.12) named "localization principle" is employed to understand the scattering of electromagnetic waves and geometric rays of light by particles. In semi-classical quantum mechanics, 1/2 in Eq. (5.12) is called Langer modification [54].

B. Separation of Edge Effect from Total Extinction

We are concerned with disks and cylinders of various aspect ratios. In the T-matrix formulation, both the incident and scattered fields are expanded in terms of vector spherical functions. According to the theoretical basis, the T-matrix approach may be the most straightforward approach to separate the edge-effect contribution in the total extinction cross section out. However, because the T-matrix method lends itself easier to moderate aspect ratios and moderate sizes in numerical computation, we use the DDA method to separate the extinction of light associated with the edge-effect contribution in calculating the total extinction. Additionally, by unitizing supercomputer, results for particles of much larger size parameters can be obtained. The edge effect is automatically incorporated into the DDA equation, as the source electric field (not including the field induced by the dipoles) inside the particle is a plane wave.

In the expansion of the incident plane wave in terms of multipole fields associated with the index n, the upper limit of n should be sufficiently large to allow the difference between the summation and the value of a plane wave on a spherical surface to be neglected within satisfactory accuracy limits. A mulitipole field with the index n larger than the size parameter of the sphere is required [2], and the number of additional terms is proportional to $(ka)^{1/3}$ where a is the sphere radius. These additional terms are what we associate with the "edge effect" or the "tunneling effect". We consider an incident plane wave propagating along the z-axis with the polarization

vector aligned with the x-axis:

$$\vec{E}^{inc} = \vec{e}_x \exp(ikz), \tag{5.13}$$

where $\vec{e}_x$ is the unit vector along the positive x-axis. By using the multipole expansion, the three components of an electric field in the spherical coordinate system (r, θ, ϕ) can be written as [2, 3]

$$E_r^{inc} = -\frac{1}{k^2 r^2} \cos\phi \sum_{n=1}^{\infty} (2n+1) i^n i \sin\theta \pi_n(\cos\theta) \psi_n(kr), \tag{5.14}$$

$$E_\theta^{inc} = \frac{1}{kr} \cos\phi \sum_{n=1}^{\infty} \frac{2n+1}{n(n+1)} i^n \left[-i\tau_n(\cos\theta)\psi_n'(kr) + \pi_n(\cos\theta)\psi_n(kr) \right], \tag{5.15}$$

$$E_\phi^{inc} = -\frac{1}{kr} \sin\phi \sum_{n=1}^{\infty} \frac{2n+1}{n(n+1)} i^n \left[-i\pi_n(\cos\theta)\psi_n'(kr) + \tau_n(\cos\theta)\psi_n(kr) \right], \tag{5.16}$$

where ψ_n is the Riccati-Bessel function associated with the spherical Bessel function of the first kind j_n [2]. Figure 28 shows the differences between the real part of a plane wave and the values obtained by taking some finite terms in the summation involved in Eqs.(5.14)-(5.16). In Fig. 28, the upper limit of the index n is selected to be 24. It is evident from Fig. 28 that the differences are pronounced near the boundary of a sphere with a size parameter of 25.

To separate out the edge effects inherent in the DDA equations, Eq.(3.28) is decomposed into the two independent sets of equations as follows:

$$\vec{E}_{i,n<[ka-1/2]}^{inc} = \alpha_i^{-1} \vec{P}_i - \sum_{j \neq i} G_{ij} \vec{P}_j, \tag{5.17}$$

$$\vec{E}_i^{inc} - \vec{E}_{i,n<[ka-1/2]}^{inc} = \alpha_i^{-1} \vec{P}_i - \sum_{j \neq i} G_{ij} \vec{P}_j. \tag{5.18}$$

Here, $\vec{E}_{i,n<[ka-1/2]}^{inc}$ is a pseudo plane wave equal to a summation of multipole fields with index $n < [ka - 1/2]$, and the operator $[\cdot]$ indicates the integer part of the argument. The extinction efficiency factor can be straightforwardly calculated from

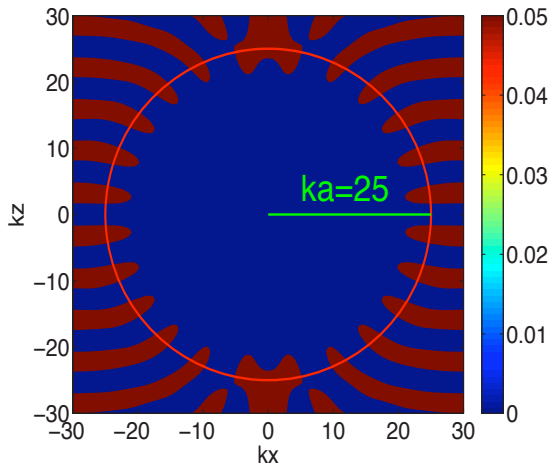

Fig. 28. The difference between the real part of x component of a plane wave and the summation of the multipole fields truncated at n=24.

the solution to Eq.(5.17) and corresponds to the extinction efficiency factor computed from the PGOH method. The extinction efficiency factor calculated from the solution to Eq. (5.18) is the aforementioned edge-effect contribution.

C. Circular Cylinders or Disks

In the case of the scattering of light by a cylinder as shown in Fig. 29, the extinction efficiency factor can be analytically derived by the PGOH method on the basis of the volume integral equation (2.85). Substituting $\vec{E}$ computed from the geometric optics method into Eq. (2.85), we obtain:

$$Q_{ext} = 2\mathrm{Re}\left\{1 - \frac{4m\exp\left[i(m-1)kL\right]}{(m+1)^2 - (m-1)^2\exp(i2mkL)}\right\}, \tag{5.19}$$

where L is the length of the cylinder. Equation (5.19) can also be obtained from the optical theorem by considering the extinction caused by the interference between the transmitted and incident waves. Note there are two features inherent to Eq. (5.19):

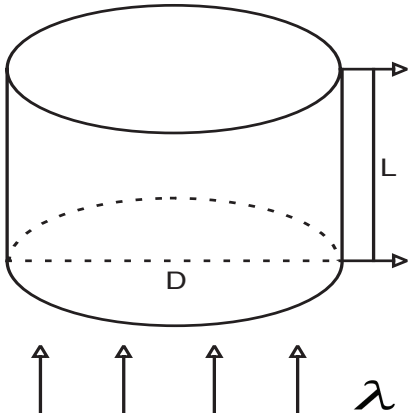

Fig. 29. A plane wave impinging on the basal face of a cylinder. λ is the wavelength.

first, the extinction efficiency factor computed from the PGOH is independent of the shape and size of the geometric cross section; second, when the refractive index is real, i.e., no absorption, Q_{ext} is an oscillating function of L and does not converge to 2 regardless of the size of the scattering particle.

As shown in Figs. 30 and 31, the extinction efficiency factors simulated from the DDA method, excluding the above edge-effect contribution, agree with their counterparts calculated from the PGOH. The saw-like oscillations in the results are evident in Fig. 31. The saw-like curve occurs because the index n is a discrete integer variable, but the diameter of the cylinders is a continuous variable. The relationship associated with the angular momentum implied in the localization principle is only exact provided that the diameter of the cylinder is equal to $2n + 1$. At these values, the extinction efficiency factors excluding the edge effect are very close to those computed from the PGOH. The fact that the extinction efficiency factors excluding the edge-effect contribution agree with their PGOH counterparts suggests that the edge effect is reasonably justified and quantified.

The pronounced edge effect may not be observed for spheres and randomly ori-

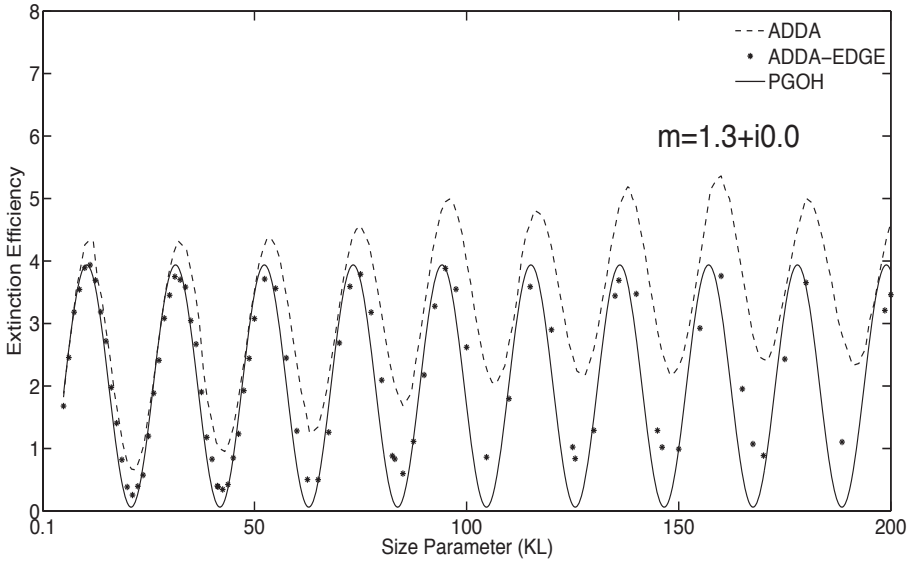

Fig. 30. Extinction efficiency factor of cylinders simulated from the ADDA with the edge effect, the ADDA without the edge effect, and the PGOH. The size parameter defined in terms of the diameter is 50.

ented nonspherical particles when the size parameter is very large. In these cases, the edge effect increases more slowly than the average projected area when the size parameter is increasing. Therefore, the contribution of the edge effect to the extinction efficiency factor can be reasonably neglected when the particle size is very large. But for a particle with fixed orientation, the speed of increase of the edge-effect contribution may be faster than the geometric cross section. As a result, the edge effect is pronounced and cannot be neglected even for quite large particles. For a randomly oriented particle, the phenomenon of oscillation without convergence due to the interference between diffracted light and transmitted light, shown in Fig. 30, is not observed primarily due to reduced interference in the averaging process.

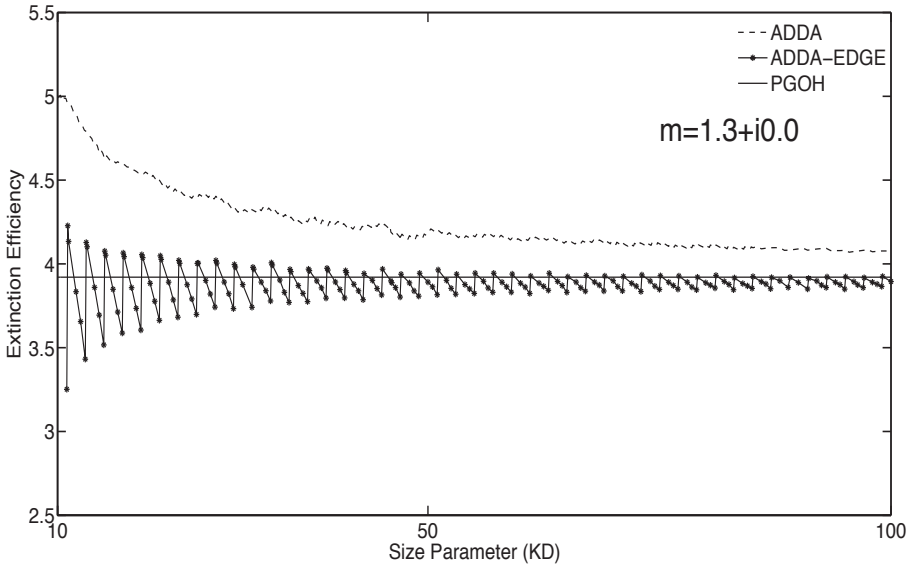

Fig. 31. Extinction efficiency factor of disks simulated with the ADDA with the edge effect, the ADDA without the edge effect, and the PGOH. The size parameter defined in terms of the length is 10.

D. Global Effect or Local Curvature Effect ?

Previous studies of the edge effect on light scattering by spheres and rounded particles suggest that the edge effect is associated with the radius of curvature of the "profile". According to Jones [33, 34], the edge-effect contribution to the extinction efficiency factor is given by

$$Q_{edge} = \frac{c}{S} \int_p R^{1/3} ds, \tag{5.20}$$

where c is a universal constant, S is the projected area of the particle on a plane perpendicular to the direction of the incident light, ds is the arc length along the projection of the illuminated area boundary, and R is the curvature radius of the "profile" along the edge. The theory behind Joness treatment is that the effect due

to the presence of a particle on the extinction process is essentially the same as that of a cylinder with its axis perpendicular to the normal direction at the glancing point and to the direction of the incident wave. For a specifically oriented cylinder, Q_{ext} was derived from Eq. (5.20) by Fournier and Evans [55] and is given by

$$Q_{edge} = \frac{c}{(x \sin\theta)^{2/3}} \tag{5.21}$$

where x is the radius of the circular cross section, and θ is the angle between the direction of the incident light and the symmetry axis. For the present case where $\theta = 0$, Eqs. (5.20) and (5.21) cannot be used to quantify the edge effect, because the curvature radius is infinite and would lead to an infinitely large edge-effect contribution to the extinction efficiency factor. Therefore, the edge-effect contribution to the extinction may be a global effect.

CHAPTER VI

OPTICAL MODELING OF ICE CRYSTALS *

A. Introduction

Solar radiation occurs over a wide range of wavelengths. The main range of solar radiation includes ultraviolet radiation (UV, 0.001-0.4 μm), visible radiation (light, 0.4-0.7 μm), and infrared radiation (IR, 0.7-100 μm). The energy of solar radiation is not divided evenly over all wavelengths but is rather sharply centered on the wavelength band of 0.2-2 μm. The infrared radiation in the atmosphere is mainly from thermal emissions from the earth. The wavelength coverage of interest in this dissertation is chosen as (0.2-15.25 μm). Channels of MODISE and CALIPSO lidar are within the selected range.

B. Randomly Oriented Ice Crystals

We use the updated indices of refraction of ice crystals [56], employ a more accurate version of IGOM code (or called simplified PGOH algorithm), and include three new ice habits (hollow bullet rosette, aggregate of 5 plates, and aggregate of 10 plates). In this study, some new criteria are used to select the wavelengths and size bins in the scattering computation. The database will cover the size range from 2 to 10000 μm and a spectral range from the 0.199 to 15.25 μm. 189 size bins are used

---

*Part of this chapter is reprinted with permission from "Simulation of the color ratio associated with the backscattering of radiation by ice crystals at 0.532 and 1.064-μm wavelengths" by L. Bi, P. Yang, G. W. Kattawar, B. A. Baum, Y. X. Hu, D. M. Winker, R. S. Brock, and J. Q. Lu, J. Geophys. Res. **114**, D00H08, doi:10.1029/2009JD011759, and "Scattering and absorption of light by ice particles: solution by a new physical-geometric optics hybrid method" L. Bi, P. Yang, G. W. Kattawar, Y. Hu, and B. A. Baum, J. Quant. Spectrosc. Radiat. Transfer, **112**, 1492-1508 (2011)

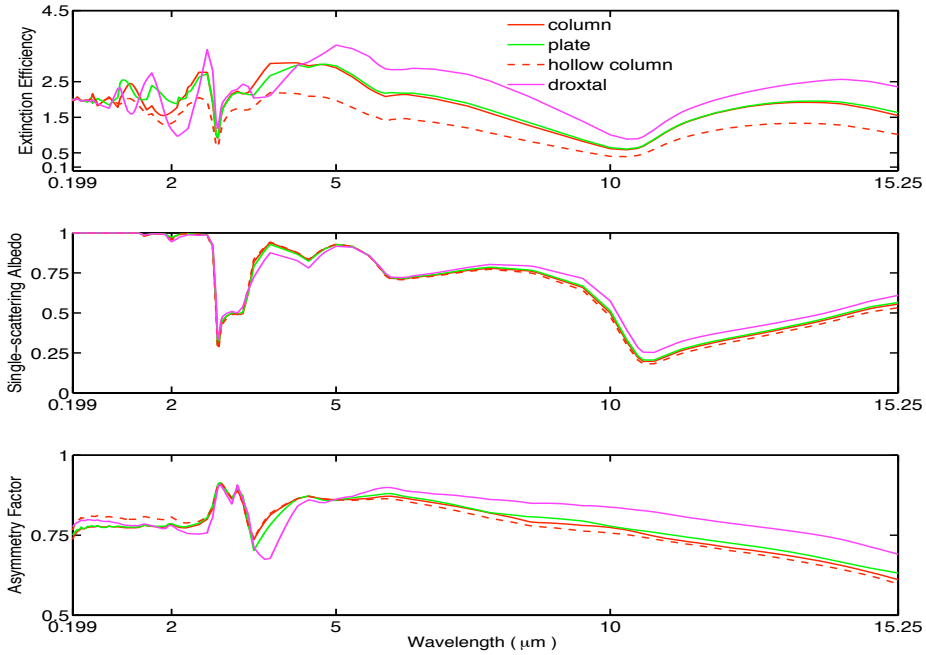

Fig. 32. Extinction efficiency factor, single-scattering albedo and asymmetry factor of ice crystals (hexagonal column, hexagonal plate, hollow hexagonal column, and droxtal) of maximum dimension 10 μm.

instead of 49 size bins in the old database. 101 spectral points are carefully chosen so those sharp gradients of refractive indices with respect to the wavelength are properly taken into account. Data for other unselected wavelengths are obtained through linear interpolation of simulated data in terms of wavelength.

Figure 32 shows the extinction efficiency, the single-scattering albedo and the asymmetry factor of 4 ice habits (hexagonal column, hexagonal plate, hollow hexagonal column, and droxtal ice crystal.). Ice crystals are assumed to be randomly oriented in space. The size defined in terms of maximum dimension is 10 μm. The general trend of curves with respect to the wavelength ranging from 0.199 to 15.25 μm is similar for different habits. The values for column and plate are quite close for the chosen size. At a particular wavelength, the extinction efficiency for droxtal is

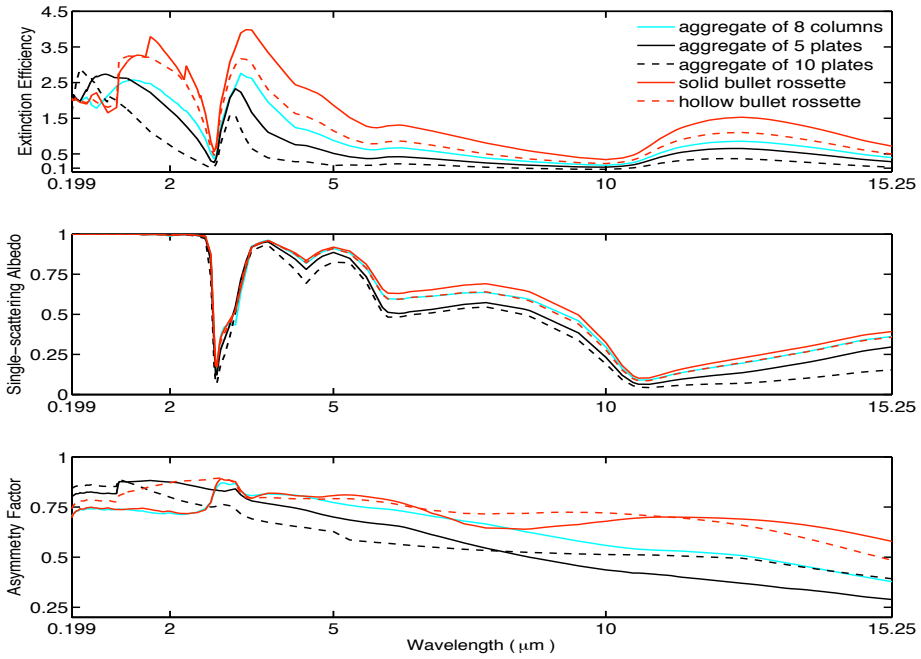

Fig. 33. Similar to Fig. 32, but for complex ice crystals

largest, whereas the counterpart for hollow column is smallest. Figure 33 is similar to Fig. 32, but for 5 complex ice crystals.

C. Oriented Ice Crystals

Large ice particles in the atmosphere may not be randomly oriented in space, but reveal some preferable orientations and flutter relative to a horizontal plane. Straightforward evidence to support the existence of preferably oriented ice particles in the atmosphere is various optical phenomena such as parhelia, sub sun, and sun pillars [57]. Their existence is confirmed based on observations from satellite instruments and groundbased lidar [58–65]. Aerodynamic microphysical processes to determine ice particle orientation and fall characteristics have been investigated [61].

The optical properties of oriented ice particles are quite different from those of

randomly oriented particles, and cause a different radiative impact on the atmosphere. An accurate modeling of the single-scattering properties of oriented ice particles has important implications to climate study and remote sensing applications. As previously stated, the CGOM has inherent flaws, and is thus inappropriate for studying the optical properties of particles with fixed orientations. For example, the phase function of oriented ice particles is not a continuous curve, but a set of singular points. Some attempts to study the optical properties of oriented ice particles based on the PGOH method can be found in [66, 67].

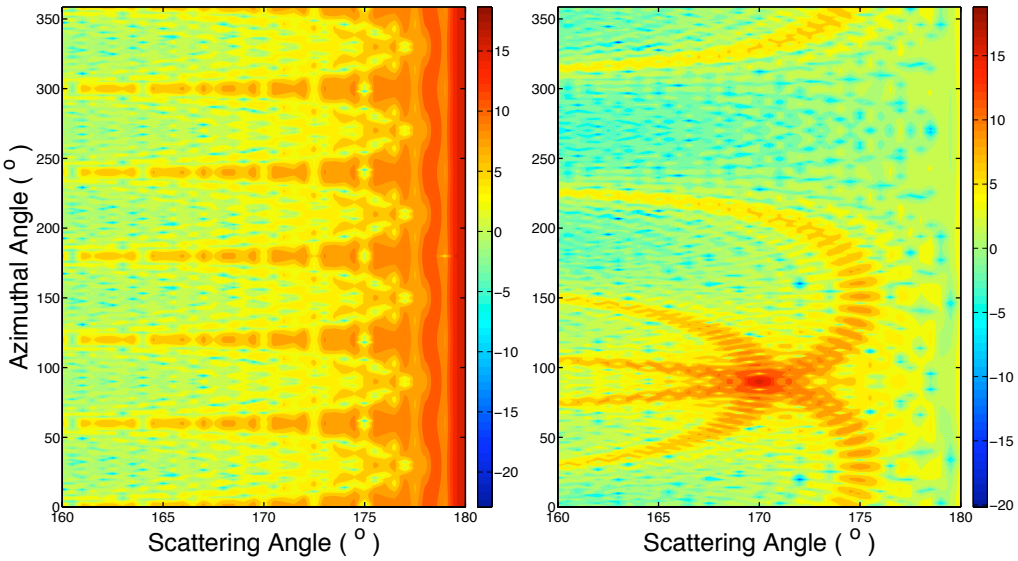

Fig. 34. Display of the phase function as a function of scattering angle and azimuthal angles. The direction of incident light makes a 0^o (left) and 5^o (right) angle with the six-fold symmetry axis.

In the formulation of CGOM, the backscattering radiation is associated with scattered beams propagating in the backscattering direction. Therefore, for a specific orientation with unidentified backscattered beams, the backscattering cross section is zero. However, in the PGOH, the backscattered radiation can still be considered. The

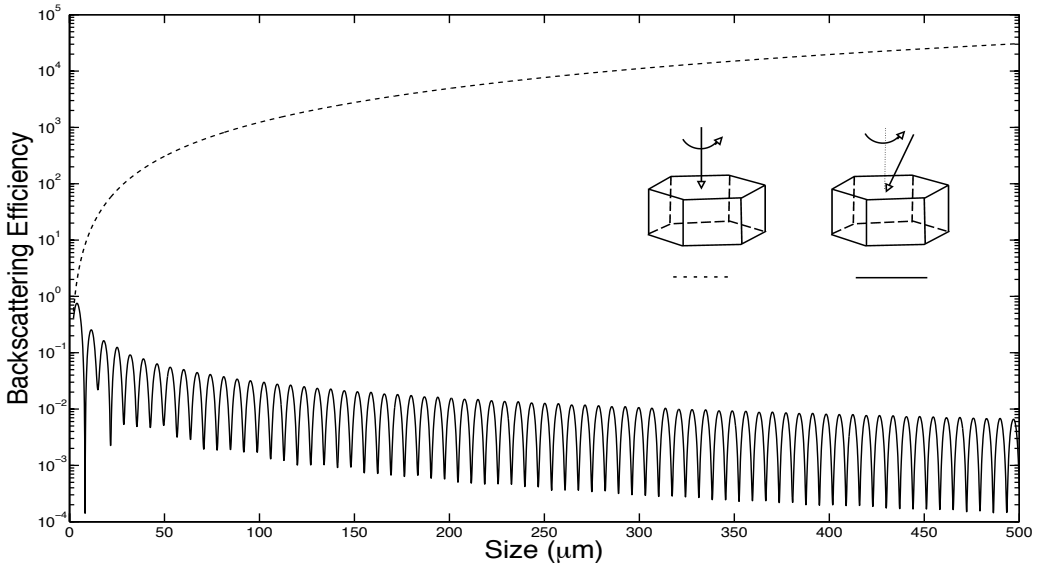

Fig. 35. Backscattering efficiency for diffraction and external reflection.

physical reason is the spreading effect of beams propagating near the backscattered angle. However, backscattered beams in the CGOM could also spread some energy into other directions. In the following discussion, beam spreading and interference are crucial concepts in understanding the properties of backscattered radiation for oriented particles. Two effects associated with the beam spreading and interference can be understood based on Eq. (4.74). For non-absorptive particles with different size parameters, $D_p \exp(ik\delta_{p,1})$ accounts for the beam spreading and phase variance.

To understand the beam spreading effect on the backscattering radiation, we now investigate the diffraction and external reflection by a hexagonal plate. The higher order refraction scattering contribution is separated to avoid interference among scattered beams. Two orientations of a plate are considered, the incident light normal to the top facet and the incident light at a 5^o angle from the symmetry axis. Figure 34 illustrates the 2-D phase functions for the two cases, and the spreading of externally

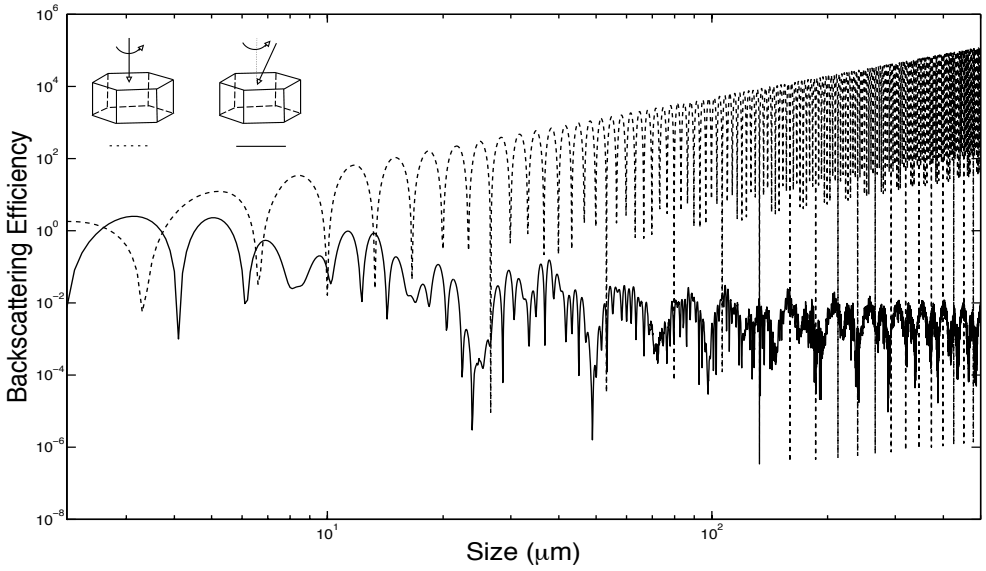

Fig. 36. Backscattering efficiency for all scattered beams.

reflected beams can be observed. Figure 35 shows the backscattering efficiency with respect to the particle size. The reflected beam directly contributes the backscattering when the incident light direction is normal to the basal face. As the size parameter increases, the degree of ray spreading decreases and increased backscatter results. When the incident direction makes a 5^o angle with the six-fold symmetry axis, the scattering angle associated with the reflected beam in the CGOM is 170^o. In this case, the observed backscattering physically begins from the spreading of the reflected beam, as shown in Fig. 34. As the size parameter increases, less energy is spread into the backscattering direction. Similar to the case of Fraunhofer diffraction, the backscattering efficiency generally decreases but oscillates locally. As can be seen in Fig. 35, the backscattering efficiency dependence on the size parameter differs for various plate particle orientations. The results in Fig. 36 are similar to those in Fig. 35 but include consideration of all higher order scattered beams. The interference be-

tween scattered beams depends on the phase delay associated with total path length. As a result, the backscatter cross section oscillates significantly with respect to the particle size. However, the physics of the ray spreading effect determines the behavior of backscatter in terms of the size parameter.

D. Imperfect Ice Crystals

The optical properties of imperfect hexagonal ice particles are investigated to explain why halos are rarely observed. Observed ice particle habits generally reveal various geometric characteristics due to complex temperature and humidity conditions during their growth. Because of complex atmospheric conditions encountered during particle growth, the top or bottom facets of ice particles are not generally regular hexagons [4] and often reveal surface texture. The complexity of ice particle imperfections pose challenges for realistic numerical simulations of optical properties. To simplify the modeling procedure, Macke et al. [26] and Hess et al. [68] developed a method to model ice particle imperfections through statistical ray path deviations in a regular hexagonal particle with the CGOM. To modify the PGOH method to model ice particle imperfections, we distort regular hexagonal ice particles instead of using either the complex polycrystal method [26] or by changing the ray path in the beam-tracing process [68]. The advantages of the present method are simplicity and efficiency, which allow calculating consistent single-scattering properties over a wide range of size parameters.

Figure 37 shows a set of ice particle habits including the basic hexagonal column or plate. To model imperfect ice particles, we distort the regular hexagonal shape using two different procedures. Ice particles are given irregular top and bottom faces but the right angle is kept between the top and six side facets. Specifically, the

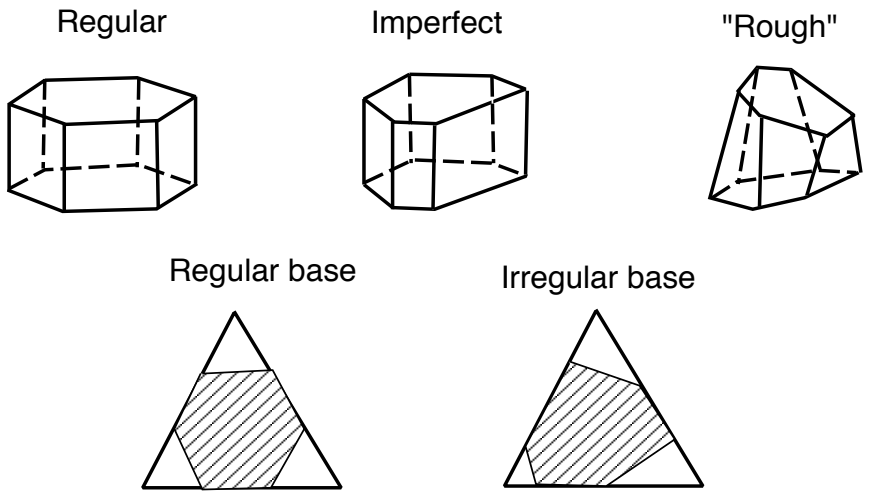

Fig. 37. Model particles chosen to represent both regular and irregular hexagonal ice particles.

shape of the top face is obtained by randomly choosing two points on each side of a right triangle to be vertices of a hexagon. To model ice particles with more complex characteristics such as roughness, we randomly tilt the normal directions of each face of a regular hexagonal prism. Considering the top face as an example, the normal direction could be defined through two random numbers ξ_1 and ξ_2 between 0 and 1 given by,

$$\left(\xi_1\xi_2, \xi_1\sqrt{1-(\xi_2)^2}, \sqrt{1-(\xi_1)^2}\right). \tag{6.1}$$

By using the aforementioned procedure, an ensemble of imperfect ice particles can be generated. The average scattering properties of an ensemble of irregular ice particles might be expected to represent the realistic optical properties of imperfect ice particles, although the morphology of model particles is quite different from that of realistic ice particles. The optical properties of the imperfect model particles can be easily computed using the present PGOH algorithm. As shown in the following

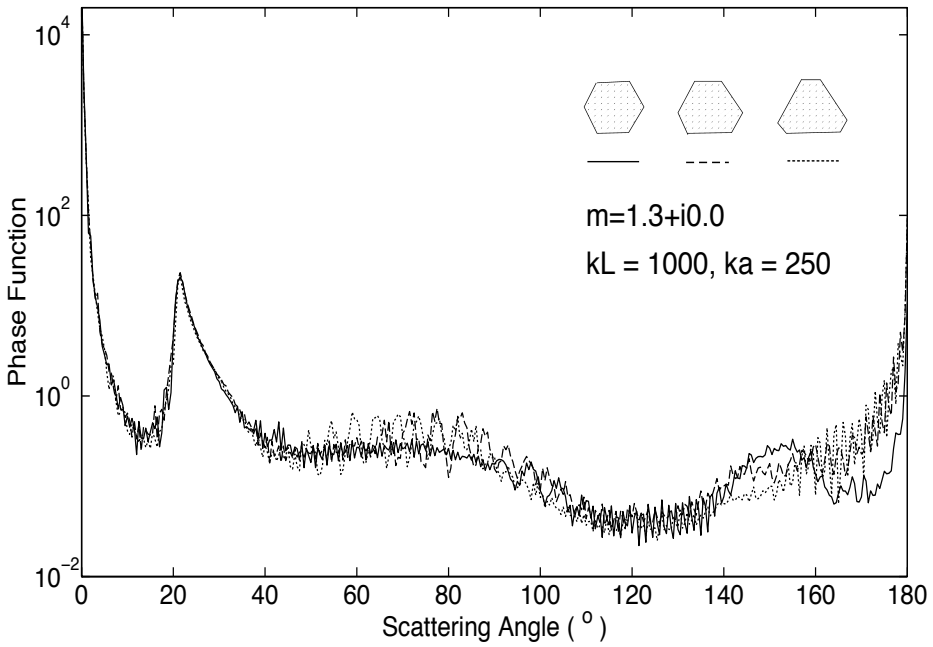

Fig. 38. Phase functions computed from the PGOH method for hexagonal particles with irregular bases.

results, the adoption of irregular habit choices effectively diminishes halo phenomena.

Figure 38 shows the phase functions for hexagonal particles with irregular bases computed from the PGOH method. For convenience, each side is parallel to its facing side and the ratio of its longer side to its shorter side is assumed to 1, 2 or 3. When the ratio is 1, the particle is a regular hexagonal ice particle, the size parameter defined in terms of the length is 500, and the aspect ratio is 0.5 (diameter divided by length). Other assumptions are that the surface area of two particles with irregular bases is the same as for a regular ice particle, the direction of the incident light is normal to the side faces, and the particle is randomly oriented with respect to a symmetric axis. We observe some differences in the phase functions simulated from the PGOH method for the three particles. The irregular base has three 60^o vertex angles, and

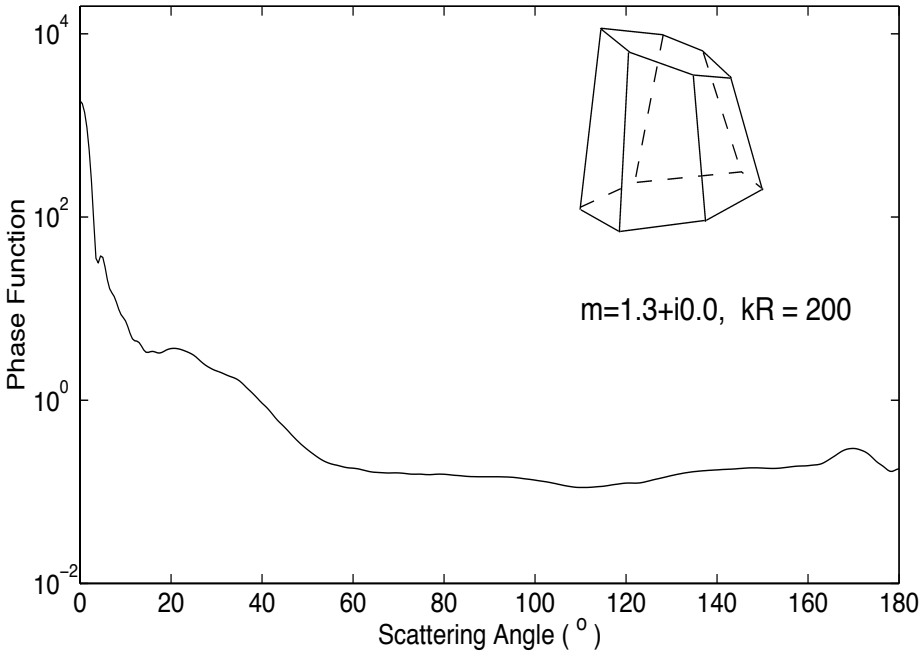

Fig. 39. Phase functions computed from the PGOH method for hexagonal particles with tilted facets.

the 22^o halo can be observed. The 154^o scattering maximum is reduced for the two irregular hexagonal columns. The 154^o scattering maximum for a regular hexagonal particle is due to the refracted beams undergoing several internal reflections [24]. Due to less symmetry associated with the irregular ice particles, the 154^o scattering maximum for an irregular hexagonal particle is not observed. Figure 39 shows the scattering phase function computed from the PGOH for randomly oriented hexagonal particles with tilted facets. As evident in the figure, the halo peaks observed from the regular hexagonal particles are diminished. The present method of tilting the facets of hexagonal ice particles can be employed to simulate the presence of surface roughness.

E. Backscattering Color Ratio

In an application to lidar calibration algorithm, we investigate the cirrus clouds backscattering color ratio, a quantity of the ratio between backscattering cross sections at the two-lidar wavelengths of 1.064 and 0.532 μm. As a rough approximation, the color ratio is assumed to be unity. A more accurate value of color ratio can only be obtained; once more accurate single-scattering properties are provided. A theoretical simulation was carried out, and the simulated results were compared with measurements obtained from ground-based instruments. It is found that the color ratio should be less than unity, and peaks around 0.88. A theoretical explanation in the principle of ray-spreading effects (or, diffraction of localized waves) was explicitly demonstrated to reveal the inherent physical processes leading to less-unity color ratio value.

The CALIPSO (Cloud-Aerosol Lidar and Infrared Pathfinder Satellite Observation) space-based platform includes three co-aligned nadir-viewing instruments. One is the Cloud-Aerosol Lidar with Orthogonal Polarization (CALIOP), a dual-wavelength (0.532 and 1.064 μm) lidar. The primary goal of CALIPSO is to improve the understanding of the role of clouds and aerosols in weather, climate and air quality processes by providing global altitude-resolved optical properties [69]. For CALIOP lidar algorithms [70, 71], the backscatter color ratio χ, a ratio of total backscatter coefficients at 1.064-μm and 0.532-μm channels under ice cloud conditions, is defined as follows:

$$\chi = \frac{\beta_{1.064}}{\beta_{0.532}} = \frac{\int_{D_{min}}^{D_{max}} \sigma_{sca,1.064}(D) P_{11,1.064}(\theta_s = 180^o, D) n(D) dD}{\int_{D_{min}}^{D_{max}} \sigma_{sca,0.532}(D) P_{11,0.532}(\theta_s = 180^o, D) n(D) dD}, \tag{6.2}$$

where D is the characteristic length of an ice particle that is usually specified in terms of its maximum dimension [72]. In Eq. (6.2), n(D) is the particle number density,

σ_{sca} is the scattering cross section and P_{11} is the normalized phase function. The color ratio describes the spectral variations in the optical properties of a scattering medium of interest; the optical properties are based on the microphysical properties of the medium. In the scene classification algorithm [71], the backscatter color ratio is one of the quantities required in the discrimination of aerosols from cloud particles and in the inference of cloud thermodynamic phase.

In the lidar calibration algorithm [70], the 0.532 μm channel is calibrated using the molecular backscattering signal. This method is not applicable to the 1.064 m channel due to quite weak molecular backscattering at this wavelength. In practice, however, when cirrus clouds are selected as calibration targets, the 0.532 μm calibration coefficient can be transferred to the 1.064 μm channel. A prerequisite for this calibration technique is a priori knowledge of the color ratio values associated with ice clouds. Traditionally, it has been assumed that ice clouds are spectrally independent, i.e., $\chi = 1$. Since the color ratio of ice clouds is a critical quantity in the CALIOP calibration algorithm, recent efforts [73, 74] have been made to develop more realistic χ values. Ground-based lidar measurements of χ at Hampton University in Hampton, Virginia, were recorded from June 2006 through July 2007 [74], and provided color ratio values of $\chi = 0.88 \pm 0.12$.

We will focus on direct numerical calculations of χ, and will discuss the physical mechanisms having an influence on χ. We will also provide estimates of χ based on assumed ice particle geometries, including both hexagonal and spherical shapes. The present numerical simulations involve two stages: (1) calculation of ice particle single-scattering properties, and (2) derivation of ice cloud bulk-scattering properties. The bulk-scattering properties are obtained by integrating individual ice particle scattering properties over a particle size distribution.

The single and bulk-scattering properties of ice clouds are calculated for various

aspect ratios and size parameters at 0.532 and 1.064 μm wavelengths. One basic feature of hexagonal ice particles is that they have locally planar surfaces that lead to the enhancement of backscattering. In this study, we are concerned with the ratio of the spectral sensitivity in the direct backscattering direction. The particle sizes in cirrus clouds range from several to thousands of micrometers (μm). Therefore, for the single-scattering calculations, ice particles are assumed to have maximum dimensions that range from 2 to 10000 μm (the maximum dimension for a column, a plate or a sphere is its length, width or diameter, respectively). The value of the size parameter (a quantity proportional to the ratio of the particle maximum dimension to the incident wavelength) for the two wavelengths is quite different. The refractive indices for ice at the two wavelengths are $m_{0.532} = 1.3116 + i1.48243 \times 10^{-9}$, and $m_{1.064} = 1.3004 + i1.89839 \times 10^{-6}$ [56]. Note that the imaginary part of the refractive index at 1.064 μm is larger than that at 0.532 μm by three orders of magnitude, which means that the absorption for large particles is stronger at 1.064 μm than at 0.532 μm. The single-scattering property computations for the nonspherical ice particles are based on a combination of the finite-difference time-domain (FDTD) method [9, 10] and an improved geometric optics method (IGOM) [28, 72]. For comparison, the single-scattering properties of ice spheres are calculated from the Lorenz-Mie theory.

In previous calculations of the bulk-scattering properties [75], the single-scattering properties were calculated for 45 discrete sizes (called size bins). The single-scattering property database included a variety of ice habits including hexagonal plates, solid and hollow columns, 3D bullet rosettes, droxtals, and aggregates. In the intervening years since the formation of the database, a number of improvements have become available for light scattering calculations. For example, following Mishchenko and Macke [76], a new treatment of polarized ray spreading has been incorporated for forward scattering that now makes obsolete the delta-transmission term for rays that pass through

two opposing (flat) facets of a hexagonal ice particle. The IGOM has been improved, especially for the efficiency factors and the phase function at backscattering angles. The present simulations based on the new IGOM code are limited to hexagonal plates and columns. The discretization of the particle size has been enhanced with the new simulations.

Given the individual particle single-scattering properties, the next step is to calculate bulk-scattering properties that are more representative of ice clouds, from which the color ratio values are derived. Bulk-scattering properties, and in particular the backscattering cross section per unit volume, are calculated by integrating individual particle scattering properties over a given set of particle size and habit distributions. For this study, ice habits are assumed to be hexagonal columns, plates or spheres, and a mixture of habits is not considered because a full set of scattering properties is unavailable for a more extensive set of habits. Future work will explore similar color ratio calculations for mixtures of habits.

Integration of ice particle single-scattering properties is based on a set of 1117 particle size distributions (PSDs) from the various field campaigns described in Baum et al. [77]. These campaigns include the First International Satellite Cloud Climatology Project Regional Experiment (FIRE-I), held in 1986 and (FIRE-II), held in 1991; the Atmospheric Radiation Measurement (ARM) Intensive Operation Period (IOP), held in 2000 near Lamont, Oklahoma; the Tropical Rainfall Measuring Mission (TRMM) validation campaign in the Kwajelein Islands, the Kwajalein Experiment (KWAJEX), held in 1999; and the Cirrus Regional Study of Tropical Anvils and Cirrus Layers (CRYSTAL) Florida Area Cirrus Experiment (FACE), held in 2002. The data from the FIRE and ARM IOP campaigns were obtained from mid-latitude, primarily synoptic, cirrus, while the other data were obtained from tropical anvil (TRMM) or tropical tropopause cirrus (CRYSTAL-FACE). The ice water contents

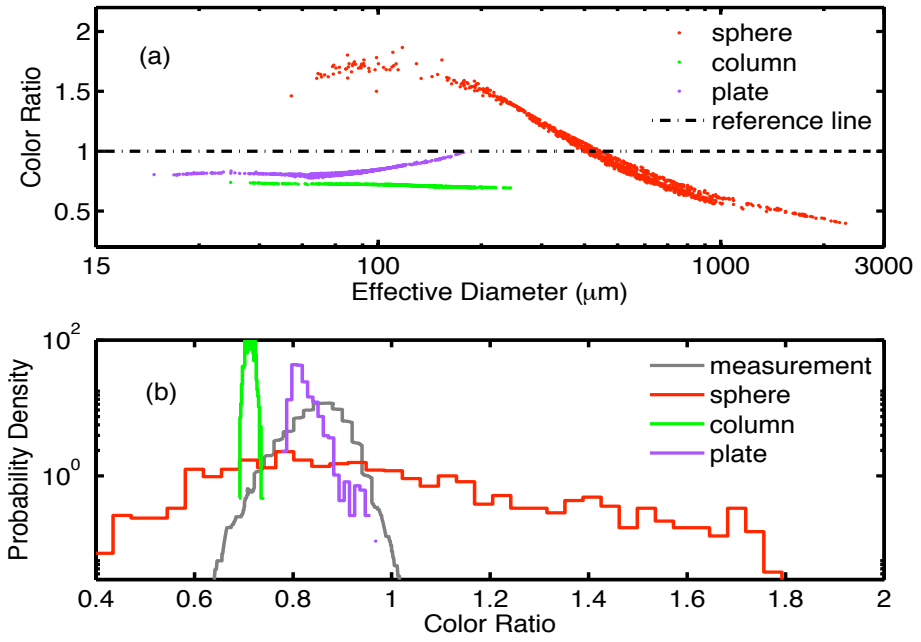

Fig. 40. (a) Color ratio as a function of effective diameter for spheres, columns and plates. (b) Comparison of simulated probability distributions of color ratio with ground-based lidar measurements from Hampton University [74].

for this set of PSDs range from approximately 10^{-3} to 1 g m-3, and the median mass diameters range from 50 to 2000 μm.

Fig. 40 (a) shows the color ratio as a function of effective particle size. The values of the color ratio for spheres can be larger than 1 and may be as large as 2 for smaller effective diameters. The values are smaller than unity when the effective diameter is larger than 400 μm. For plates, the values increase with effective size and approach unity. As noted previously, color ratio values are smaller for columns than those for plates. Fig. 40 (b) shows simulated probability distributions of the color ratio in comparison with that based on ground-based lidar measurements [74]. For both columns and plates, the entire range of color ratio values is consistent with ground-based lidar measurements. As mentioned previously, the color ratio for ice spheres

has a broad range of values ranging from 0.4 to 2. Note that numerical investigations presented here are based on a simple simulation model that captures the main physics of ice particles. In fact, realistic ice particles tend to have more complex shapes and include hollow cavities as well as surface roughening. Furthermore, depending on the updraft velocity in the environment where the ice particles are located, the ice particles may not randomly oriented in the atmosphere.

CHAPTER VII

OPTICAL MODELING OF MINERAL DUST AEROSOLS *

To study the optical properties of aerosol particles, we propose two scattering models based on two different shapes: triaxial ellipsoids and nonsymmetric hexahedra. The former is round and smooth with sphere as its special case. The latter embodies its feature of corners and edges, obtained by titling regular hexahedra/cube. As spheres and cubes fail to reproduce the nonzero elements of phase functions measured in laboratories, the essential idea of the present modeling approach is to explore the applicability of the use of simple nonspherical/nonsymmetric geometries to represent highly irregular aerosol particles in modeling simulation. The reason of doing this is that measured phase matrix for different aerosol samples demonstrates similar behaviors with respect to scattering angles, although morphologies of these samples are quite different. Meanwhile, the essential symmetry of model particles should be reduced so that the angular scattering pattern is featureless.

There are several criteria to judge the appropriateness or merit of the two proposed scattering models. First, is the proposed model able to reproduce the measured scattering phase matrix for some sampled aerosols? Second, how many shapes of model particles are required to reproduce the measured data? Third, how sensitive of the model to shape distributions in mimicking the measurements for the same aerosol sample but at different wavelengths? As significant efforts are required at the present stage to obtain optical property databases of defined nonspherical geometries for var-

---

*Part of this chapter is reprinted with permission from "Single-scattering properties of tri-axial ellipsoidal particles for a size parameter range from the Rayleigh to geometric-optics regimes" by L. Bi, P. Yang, G. W. Kattawar, and R. Kahn, Appl. Opt. **48**, 114-126, and "Modeling optical properties of mineral aerosol particles by using Nonsymmetric hexahedra" by L. Bi, P. Yang, G. W. Kattawar, and R. Khan, Appl. Opt. **49**, 334-342.

ious morphology parameters and refractive indices, it is still difficult to conduct a systematic comparison study of nonspherical geometries published in literature. We report some typical numerical studies and comparisons for the two aforementioned representative nonspherical/nonsymmetric model geometries.

A. Introduction

Mineral dust is a major component of atmospheric aerosols over large areas of the globe, especially near source regions, such as the Sahara and Gobi deserts [78]. These particles exert a significant influence on the terrestrial climate, radiative forcing, and energy budget through direct scattering and absorbing of solar radiation and terrestrial thermal emission and indirect effects through interactions with clouds [79–83]. To quantify the radiative impact of aerosol particles, there has been significant research, both experimentally and theoretically, on the optical properties of realistic dust particles and their consequent effect on the transfer of radiation in the atmosphere [84–91]. The nonsphericity of airborne dust-like particles has been widely recognized as an important factor in remote sensing of the optical and microphysical properties of these particles. Especially, it has been shown that neglecting the nonsphericity of aerosol particles may lead to large errors in aerosol property retrieval [87, 88, 92, 93]. The scanning electron microscope (SEM) images of some sampled aerosol particles [36] show that the morphologies of these irregular particles are very complicated. Specifically, these particles have small-scale structures, but lack well-defined overall shapes. In numerical modeling of the optical properties of dust particles, it is unrealistic to account for the morphological details of these particles. The application of simple geometries to complex particle optical property simulation has been discussed by Macke and Mishchenko [94] and Kahnert et al. [95]. To account for the nonsphericity in many

previous studies reported in the literature, rounded dust particles (for example, Saharan dust) are usually assumed to be spheroids (i.e., ellipsoids of revolution) as a first-order approximation for the overall shapes of these particles [96–99] although some more complicated particle geometries have also been considered (e.g., [46, 100]). Realistic dust aerosols are almost exclusively irregular particles without any particular symmetry. It is shown that retrieving mineral aerosol particle complex refractive index based on the spheroidal model from measured scattering matrices [36] always overestimates the imaginary part. To match theoretical simulations with measurements, one has to use unphysical complex refractive indices and shape distributions [101]. Most recently, Nousiainen [102] summarized the current status of the optical modeling of mineral dust particles.

B. Model Simulations: Triaxial Ellipsoids

It requires one degree of freedom (i.e.,particle size) to specify the geometry of a spherical particle, whereas two degrees of freedom (the particle maximum dimension and aspect ratio) are needed to specify the geometry of a spheroidal particle. The dimensions of an ellipsoid along three orthogonal axes may be different. Thus, ellipsoid geometry has one more degree of freedom than the commonly used spheroid geometry, and the former is a better approximation to the shapes of realistic dust particles. Chobrial and Sharief [103] estimated that the aspect ratios of the three axes (hereafter, indicated by a, b, and c) of sandstorm particles are approximately c:b=1:0.71 and b:a=0.71:0.53. For simplicity, in the following discussions the two aspect ratios, c:b=1:0.71 and b:a=0.71:0.53, are indicated in a concise form given by c:b:a=1:0.71:0.53.

We investigate the single-scattering properties of dielectric and homogeneous

ellipsoidal particles for a complete size parameter spectrum. The analytical solution to the scattering of light by an ellipsoid has been partially solved [104–106]. However, the analytical solution is computationally stable only in the case of quite small particles. To compute the single-scattering properties of ellipsoids with size parameters required for practical remote sensing applications, numerical methods, such as the T-matrix [107–109], DDA [13, 15], FDTD [10, 110], and PSTD methods [44, 45] can be used for small to moderate size parameters.

For large particles, approximate approaches such as the anomalous diffraction theory [19] and the so-called physical optics approximation method [111] have been applied to arbitrarily oriented ellipsoids. However, in both the approximate methods, only the angular patterns of the scattered light associated with oriented ellipsoids have been studied. For many practical applications involved in atmospheric radiative transfer simulation and remote sensing, it is necessary to compute the full scattering matrix, extinction efficiency and single-scattering albedo of randomly oriented particles. In this study, we employ the IGOM algorithm developed by Yang and Liou [28] and a DDA code (ADDA 0.77) developed by Yurkin and Hoekstra [15] to compute a complete set of optical properties for large and small ellipsoidal particles, respectively.

1. Geometry of Ellipsoid

Fig. 41 shows the geometry of an ellipsoid and the configurations of two coordinate systems. The geometry of an ellipsoid centered at the origin can be completely described by its surface equation in the Cartesian coordinate system $oxyz$ as follows:

$$\frac{x^2}{a^2} + \frac{y^2}{b^2} + \frac{z^2}{c^2} = 1, \tag{7.1}$$

where a, b and c are principal radii (or semi axes) along three orthogonal directions. When any two of them, say a and b, are the same, the ellipsoid reduces to a spheroid.

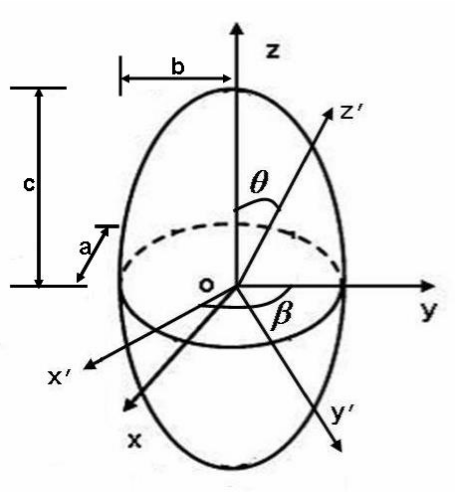

Fig. 41. Geometry of a non-axially-symmetric ellipsoid in $oxyz$ and $ox'y'z'$ coordinate systems.

The $oxyz$ coordinate system is usually called the particle coordinate system, distinguished from the incident ray coordinate system $ox'y'z'$ used for specifying scattering angle and the scattering plane. In this study, the direction of the incident ray is along oz', and the directions of parallel and perpendicular polarizations are specified along the $x'-$ and $y'-$axes, respectively. The coordinate transformation from $ox'y'z'$ to $oxyz$ is given by

$$\begin{aligned}
\begin{pmatrix} x \\ y \\ z \end{pmatrix} &= \begin{pmatrix} \sin\beta & -\cos\beta & 0 \\ \cos\beta & \sin\beta & 0 \\ 0 & 0 & 1 \end{pmatrix} \begin{pmatrix} 1 & 0 & 0 \\ 0 & \cos\theta & \sin\theta \\ 0 & -\sin\theta & \cos\theta \end{pmatrix} \begin{pmatrix} x' \\ y' \\ z' \end{pmatrix} \\
&= \begin{pmatrix} \sin\beta & -\cos\theta\cos\beta & -\sin\theta\cos\beta \\ \cos\beta & \cos\theta\sin\beta & \sin\theta\sin\beta \\ 0 & -\sin\theta & \cos\theta \end{pmatrix} \begin{pmatrix} x' \\ y' \\ z' \end{pmatrix}, \qquad (7.2)
\end{aligned}$$

where θ and β are two angles that specify the direction of incident ray in the particle coordinate system. In the incident ray coordinate system, the surface equation of the ellipsoid is given by

$$Dz' = -E \pm abc\sqrt{D - (Ax'^2 + By'^2 + Cx'y')}, \tag{7.3}$$

where

$$\begin{aligned}
A &= (a^2 - b^2)\cos^2\theta\cos^2\beta + b^2\cos^2\theta + c^2\sin^2\theta, \\
B &= a^2\sin^2\beta + b^2\cos^2\beta, \\
C &= (a^2 - b^2)\sin(2\beta)\cos\theta, \\
D &= c^2\sin^2\theta(a^2\sin^2\beta + b^2\cos^2\beta) + a^2b^2\cos^2\theta, \\
E &= (a^2 - b^2)c^2\sin\beta\cos\beta\sin\theta x' + [a^2(c^2 - b^2) + c^2(b^2 - a^2)\cos^2\beta]\sin\theta\cos\theta y'.
\end{aligned}$$

The plus and minus signs in equation (7.3) describe the illuminated and non-illuminated sides, respectively. The edge (or shadow boundary) that connects the illuminated and non-illuminated sides is determined by the following equation:

$$Ax'^2 + By'^2 + Cx'y' = D; z' = -E/D. \tag{7.4}$$

It can be shown that the interface of the illuminated and non-illuminated sides is an ellipse. If $A = B$, the semi axes of the ellipse is given by

$$\bar{a} = \sqrt{\frac{D}{A - C/2}}, \tag{7.5}$$

$$\bar{b} = \sqrt{\frac{D}{B + C/2}}, \tag{7.6}$$

otherwise ($A \neq B$),

$$\bar{a} = \sqrt{\frac{D(1-\tan^2\omega)}{A - B\tan^2\omega}}, \tag{7.7}$$

$$\bar{b} = \sqrt{\frac{D(1-\tan^2\omega)}{B - A\tan^2\omega}}, \tag{7.8}$$

where ω is given by

$$\omega = \frac{1}{2}\arctan\frac{C}{B-A}. \tag{7.9}$$

Note that the plane containing the ellipse is not perpendicular to the direction of the incident light, and ω is zero for spheroids, i.e. when a is equal to b. It can be proved that the projected area is

$$S = \pi\bar{a}\bar{b} = \pi\sqrt{D}. \tag{7.10}$$

Employing the following transformation

$$x' = \cos\omega\bar{x'} + \sin\omega\bar{y'}, \tag{7.11}$$

$$y' = -\sin\omega\bar{x'} + \cos\omega\bar{y'}, \tag{7.12}$$

which means the rotation from $o - x'y'$ to $o - \bar{x}\bar{y}$ by an angle ω, we obtain a similar ellipse equation for the projection of the particle onto the $ox'y'$ plane, given by

$$\frac{\bar{x'}^2}{\bar{a}^2} + \frac{\bar{y'}^2}{\bar{b}^2} = 1. \tag{7.13}$$

The preceding ellipsoid geometry description in both the particle coordinate system and the incident coordinate system is quite useful in the ray-tracing, diffraction and edge-effect calculations. Similar results can be found in [19], where the differences in formula are due to different coordinate conventions and definitions of the Euler angles.

2. Ray Tracing

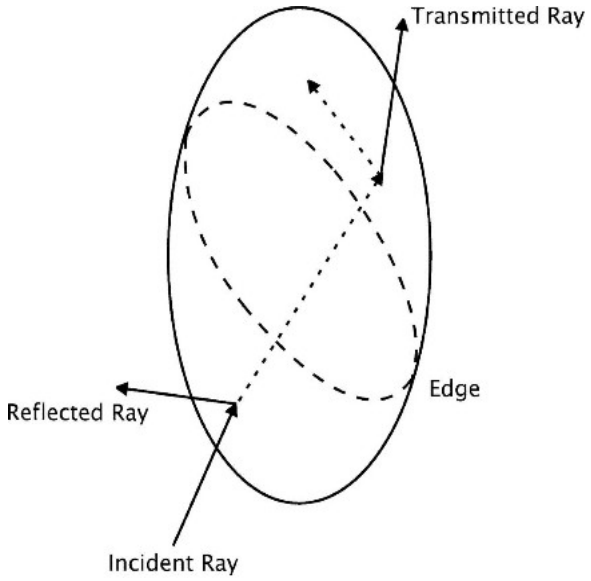

Fig. 42. Schematic geometry for the ray-tracing calculations involving a triaxial ellipsoids.

The basic principle of the IGOM is to calculate the electromagnetic field on the surface of the ellipsoid by using the ray-tracing technique, as illustrated in Fig. 42. The corresponding far-field is obtained by mapping the near-field to its counterpart in the radiation (or, far-field) zone. The magnitude and phase of each ray is calculated based on the localized-plane-wave approximation by using the Fresnel formulas. The directions of external reflection, internal reflection and refraction are determined by Snell's law. The first step for the ray-tracing calculation is to initialize the incident rays and determine the intersection points. The intersection points of the incident rays with the particle are determined by the Monte Carlo method in the incident

coordinate system as follows:

$$x' = \bar{a}\sqrt{\xi}\cos\omega\cos(2\pi\chi) + \bar{b}\sqrt{\xi}\sin\omega\sin(2\pi\chi), \tag{7.14}$$

$$y' = -\bar{a}\sqrt{\xi}\sin\omega\cos(2\pi\chi) + \bar{b}\sqrt{\xi}\cos\omega\sin(2\pi\chi), \tag{7.15}$$

$$z' = [-E - abc\sqrt{D - (Ax'^2 + By'^2 + Cx'y')}]/D, \tag{7.16}$$

where ξ and χ are two random numbers with a uniform probability distribution between 0 and 1. The ray tracing process is carried out in the particle system, in which the incident point coordinates are obtained by the coordinate transformation given by Eq.(7.2). According to Snell's law, the surface normal direction $\hat{n}$ at the incident point (x_1, y_1, z_1) is needed to determine the reflection and refraction directions. Given the surface equation (7.1), we have

$$\hat{n} = (x_1/a^2, y_1/b^2, z_1/c^2)/\sqrt{x_1^2/a^4 + y_1^2/b^4 + z_1^2/c^4}. \tag{7.17}$$

Given the initial point (x_1, y_1, z_1) on the surface and direction of the ray within the particle, the ray tracing process requires the next intersection point (x_2, y_2, z_2), which can be determined by

$$(x_2, y_2, z_2) = (x_1, y_1, z_1) + d(v_1, v_2, v_3), \tag{7.18}$$

$$d = -\frac{2x_1v_1/a^2 + 2y_1v_2/b^2 + 2z_1v_3/c^2}{v_1^2/a^2 + v_2^2/b^2 + v_3^2/c^2}, \tag{7.19}$$

where d is the length of the internal ray and (v_1, v_2, v_3) is the unit vector of its direction. Using Eqs. (7.17)-(7.19), Snell's law, and the Fresnel formulas, the ray-tracing calculation can be carried out until the energy associated with the ray of interest is effectively negligible (say, 10^{-5}). The technical details associated with the electromagnetic field computation in the ray-tracing technique can be found in Yang and Liou [28].

3. Diffraction

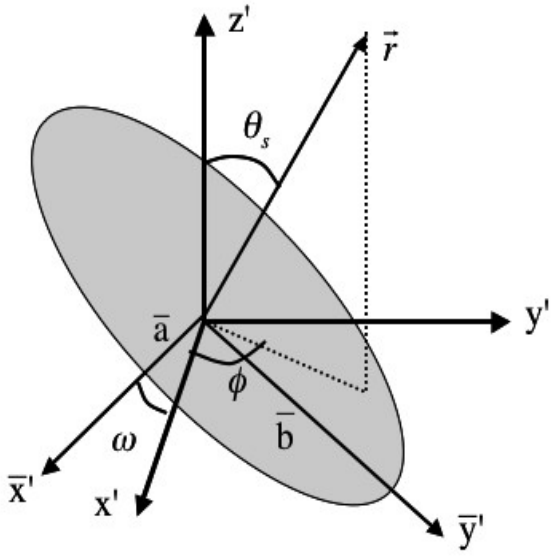

Fig. 43. Diffraction of an ellipsoid with an elliptic projection. Semi axes $\bar{a}$ and $\bar{b}$ and rotation angle ω are defined in Eqs.(7.7)-(7.9).

In addition to the contributions from the reflected and refracted rays involved in the ray-tracing calculation, the diffraction of the incident wave also contributes to the scattered energy. Using the surface mapping technique, Yang and Liou [30] showed that the amplitude scattering matrix for diffraction is given as follows

$$A_{dif} = \frac{k^2}{2\pi} I_s \begin{pmatrix} (\cos\theta_s + \cos^2\theta_s)/2 & 0 \\ 0 & (1+\cos\theta_s)/2 \end{pmatrix}, \tag{7.20}$$

and

$$I_s = \int\int_s \exp(-ik\hat{r}\cdot\vec{\xi}) d^2\xi, \tag{7.21}$$

where θ_s is the scattering angle, s is the projected area, k is the wave number and $\hat{r}$ is a unit vector pointing along the observational direction, as illustrated in Fig. 43.

The explicit form of the integral in Eq. (7.21) for an ellipse can be given in the form of

$$I_s = \pi \bar{a}\bar{b} \frac{2J_1(k \sin\theta_s \sqrt{\bar{a}^2 \cos^2\phi + \bar{b}^2 \sin^2\phi})}{k \sin\theta_s \sqrt{\bar{a}^2 \cos^2\phi + \bar{b}^2 \sin^2\phi}}, \tag{7.22}$$

where J_1 is the first-order Bessel function, and ϕ is the azimuthal angle, which specifies the scattering plane.

4. Integrated Scattering Properties

Fig. 44(a) shows the extinction efficiency, absorption efficiency, single-scattering albedo and asymmetry factor of randomly oriented ellipsoids at 0.66μm wavelength. The refractive index is $1.53 + i0.008$ based on Levoni et al. [112]. The axis ratios are assumed to be $a : b : c = 0.53 : 0.71 : 1$. The size parameter is defined in terms of the radius of equivalent volume spheres. The ADDA code is employed for size parameters ranging from 0.5 to 30. The IGOM code with the inclusion of the edge effect is applied to a size parameter region from 15 to 1000. Agreement is shown for size parameters between 15 and 30, which means that the IGOM method is successfully extended to the small size parameter region (~ 15) by adding the missing physics (i.e. the edge effect contributions). Additionally, the absorption efficiency for size parameters from the Rayleigh to geometric optics regimes can also be effectively computed in the context of a combination of the DDA, IGOM and edge effect contributions. Fig. 44(b) is similar to Fig. 44(a), except that the aspect ratios for Fig. 44(b) are $0.30 : 0.70 : 1.0$. Again, a smooth transition from the DDA solutions to the IGOM results is noticed.

Fig. 45 showes the integrated single-scattering properties at 12.0μm wavelength for two aspect ratios. The refractive index at this wavelength is $1.5502+i0.0916$, which means that ellipsoids are quite absorptive. Similar to the cases shown in Fig.44, the results from the DDA converge to those from IGOM but more smoothly. The results

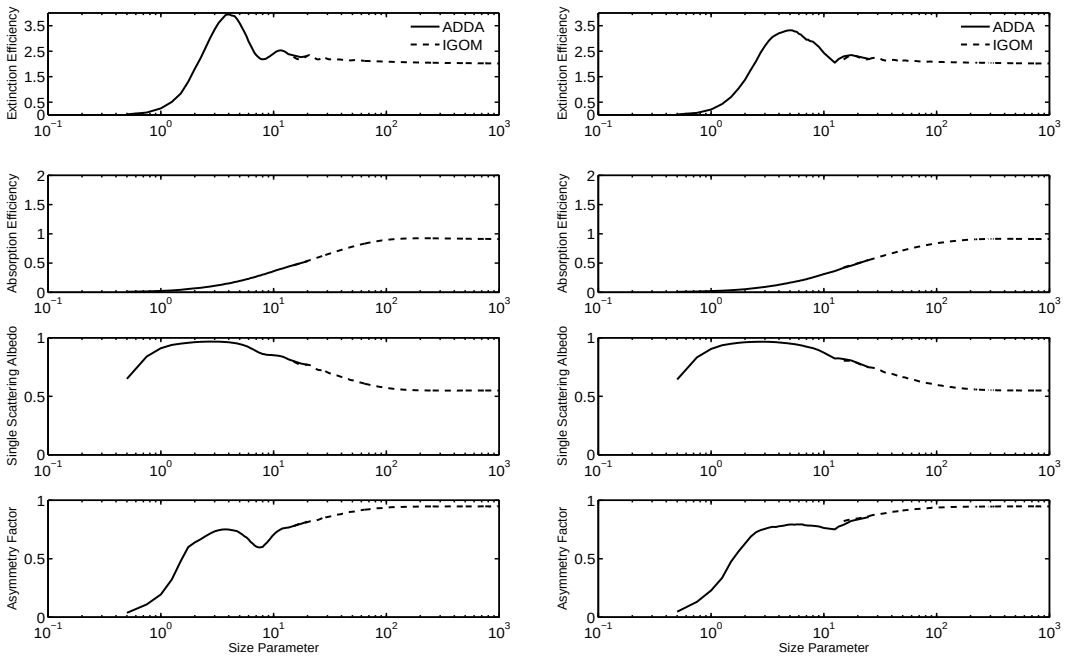

(a) (b)

Fig. 44. Integrated single-scattering properties (extinction efficiency, absorption efficiency, single scattering albedo, and asymmetry factor) of randomly oriented ellipsoids. The wavelength is 0.66 μm, the complex refractive index is $1.53 + 0.008i$, and the aspect ratios are $a : b : c = 0.53 : 0.71 : 1.00$, and $a : b : c = 0.30 : 0.70 : 1.00$ for left and right panels, respectively.

from IGOM are more accurate in those cases having stronger absorption. Note that we did not consider the edge effect contribution in the asymmetry factor computation, but the asymmetry factor calculated from the DDA also converges to that from IGOM. This is due to the fact that diffraction dominates the scattered intensity pattern. The edge effect correction to the phase function should slightly influence the asymmetry factor.

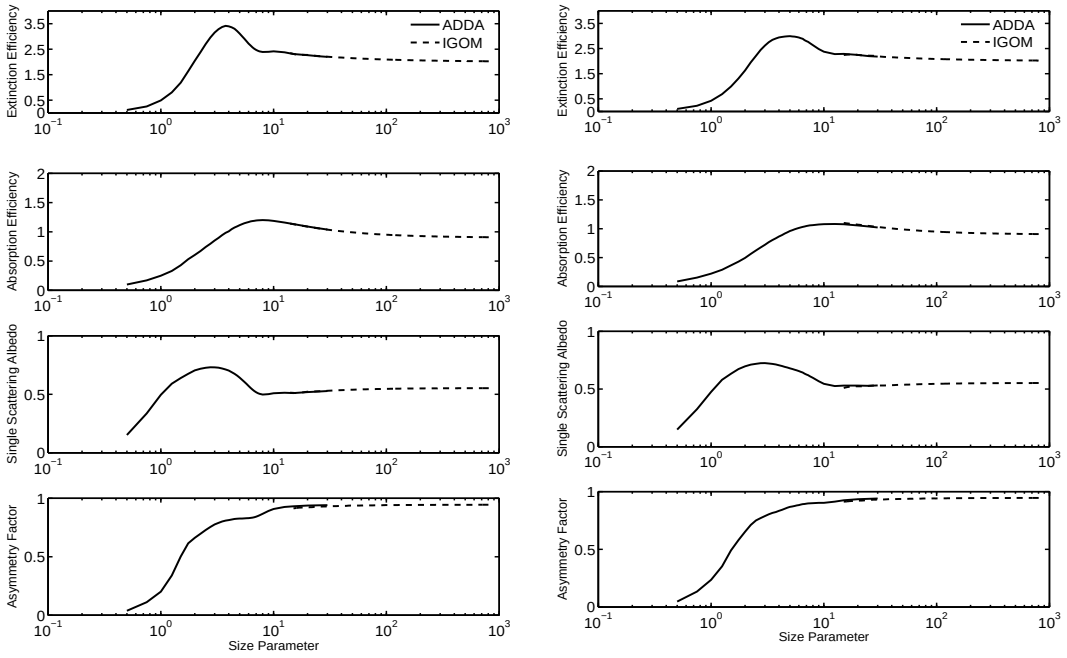

(a) (b)

Fig. 45. Same as Fig. 44 except that the wavelength is 12μm. The complex refractive index is $1.5502 + 0.0916i$. The aspect ratio: $a : b : c = 0.53 : 0.71 : 1.00$ (a), and $a : b : c = 0.30 : 0.70 : 1.00$ (b).

5. Phase Matrix

In this section we compare the nonzero phase matrix elements computed by the DDA and IGOM. We consider two wavelengths corresponding to weak and strong absorption and two axis ratios (0.53 : 0.71 : 1 and 0.30 : 0.70 : 1.0). The size parameter is defined in terms of volume-equivalent sphere and is assumed to be 30 for all the cases.

In Fig. 46, the wavelength we considered is 0.66 μm, and the axis ratios are 0.53 : 0.71 : 1 and 0.30 : 0.70 : 1.0 for the left and right panels, respectively. The excellent agreement between the phase functions (P_{11}) from the two methods is found. For other phase matrix elements, differences are noticeable. Fig. 46(a) and Fig.

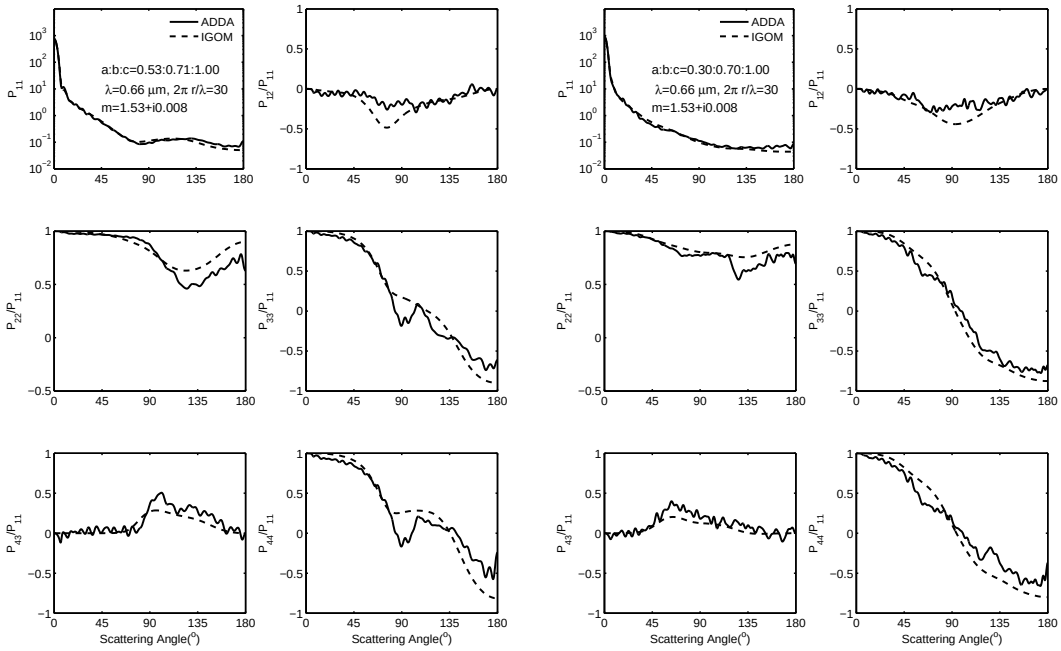

(a) (b)

Fig. 46. Comparison of the phase matrix of an ellipsoid computed from the IGOM and DDA method at a size parameter of 30. The aspect ratio: $0.53 : 0.71 : 1.0$ (a), and $0.30 : 0.70 : 1.0$ (b).

46(b) are quite different for each nonzero element. This means that the phase matrix elements are sensitive to the axis ratios of ellipsoids. For the P_{11} element, the phase function in (b) is quite featureless, whereas the phase function in (a) has some features.

Fig. 47 shows nonzero phase matrix elements at 12μm wavelength. The axis ratios are also assumed to be $0.53 : 0.71 : 1$ and $0.30 : 0.70 : 1.0$ for the left and right panels, respectively. In Fig. 47, the agreement of the phase function (P_{11}) from the two methods is also observed. The differences for other elements are still noticeable; however, the IGOM results turn out to be better for the case with strong absorption. The fact that the accuracy of the IGOM is related to the absorption has also been reported in a previous study [99]. The curves for P_{12} from the DDA and IGOM agree with each other when θ is larger than 90^o. In comparison with weak absorption

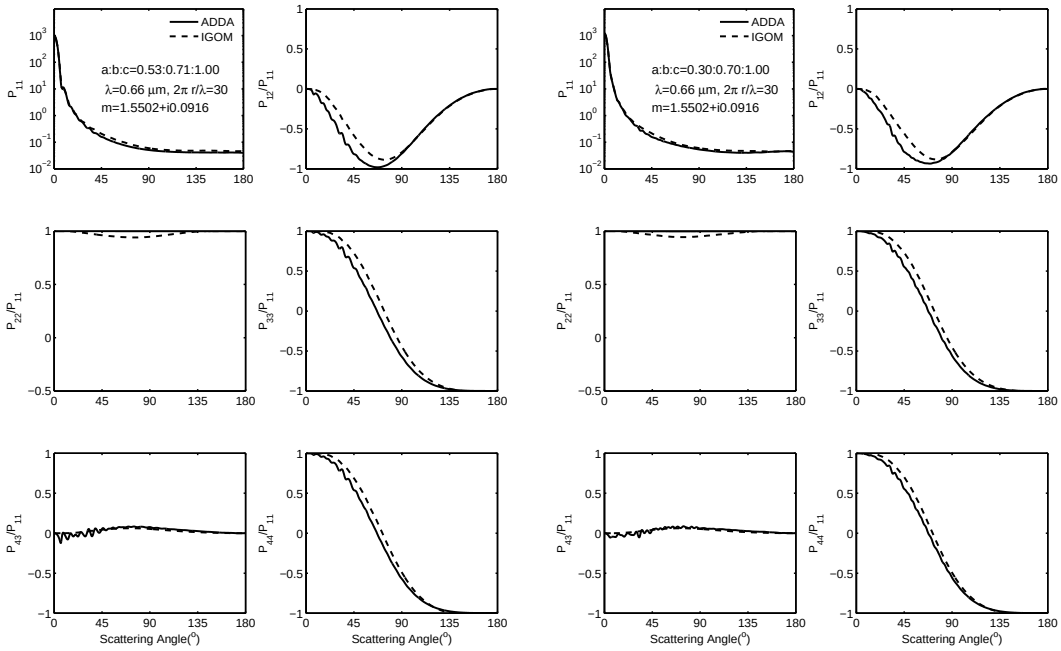

(a) (b)

Fig. 47. Same as Fig. 46 except the wavelength is 12μm. The aspect ratio: 0.53 : 0.71 : 1.0 (a), and 0.30 : 0.70 : 1.0 (b).

cases, the phase matrix elements for 12 μm are quite smooth without pronounced oscillations. Unlike Fig. 46, Fig. 47(a) and (b) are quite similar. The reason is that, in the strong absorption case, external reflection and diffraction dominate the scattering process, and internal reflection and refraction are quite weak. Therefore, the single-scattering quantities are not sensitive to the axis ratios, especially, under random orientation conditions.

6. Simulation and Measurement

To examine the applicability of an ellipsoidal model to realistic dust particle bulk scattering property simulation, we compare the simulated phase function with that from laboratory measurement for feldspar aerosol particles. The full scattering phase matrix was measured by Volten et al [84] at wavelengths 0.442 and 0.633 μm. We

choose the 0.633-μm case for the comparison of the simulations of the phase matrix elements against their experimental counterparts. The measured data of the bulk phase matrix elements are for scattering angle $5^o \sim 173^o$, and the phase function (i.e., P_{11}) is normalized to 1 at 30^o. Measurements near forward and backward scattering were not carried out due to technical difficulties. The size distributions of feldspar samples were provided by Volten et al [84] along with the effective radii. The effective variance was assumed to be 1.0. Nousiainen and Vermeulen [113] employed a lognormal size distribution

$$n(r) = \frac{N_{tot}}{\sqrt{2\pi}\ln(10)\log(\sigma)r}\exp\{-\frac{[\log(r)-\log(R)]^2}{2[\log(\sigma)]^2}\}, \tag{7.23}$$

where R is the mean radius and σ is the geometric standard deviation, which is specified by fitting the formula to the measured size distribution. With $R = 0.167\mu$m and $\sigma = 2.32$ in Eq. (7.23), the effective radius and variance for the fitted size distribution are 0.98μm and 1.02, respectively, when $r \in [0.08, 100]\mu$m.

The measured phase matrix of feldspar particles was compared with theoretical simulation based on spheroidal shapes [113]. It demonstrates that using spheroids was far superior to using spheres for approximating nonspherical feldspar particle shapes in scattering computation. Ellipsoid has one more degree of freedom and lower symmetry than spheroid. Thus, it is expected that ellipsoids offer a better approximation of realistic irregular particles. To test this speculation, we first compute the bulk scattering properties of spheroids from a combination of the T-matrix simulations [107] and the present IGOM for the lognormal size distribution in Eq. (7.23). To match the experimental data, four sets of aspect ratios (0.4583:1, 0.6481:1, 0.5477:1, and 0.4472:1) are assumed for spheroids in the bulk scattering phase matrix computation via the following formula:

$$< P_{ij} >= \frac{\sum_{k=1}^{4} W_k \int P_{ij}^k(r)\sigma_{sca}^k(r)n(r)dr}{\sum_{k=1}^{4} W_k \int \sigma_{sca}^k(r)n(r)dr}, \tag{7.24}$$

where P_{ij}^k is the normalized P_{ij} element for kth axis ratio, σ^k is corresponding scattering cross section, and W_k is corresponding weight. The best agreement between the theoretical and experimental results is achieved when the weights for the four aspect ratios are 0.4444, 0.0525, 0.1676, and 0.3357.

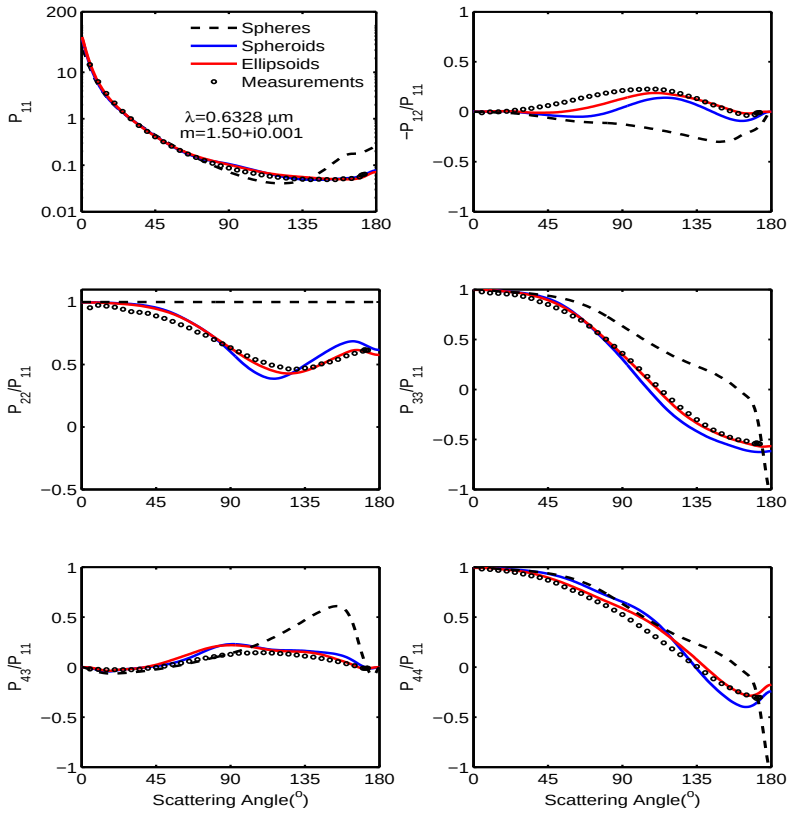

Fig. 48. Comparison of the bulk phase function from laboratory measurement [84] with the present simulations based on spherical, spheroidal, and ellipsoidal models.

Furthermore, we define volume-equivalent ellipsoids, and define the c-axis of an ellipsoid to be the same as that of its volume-equivalent spheroid. However, the lengths of the other two axes of the ellipsoid are different, so a tri-axial ellipsoid

is formed. We select four sets of aspect ratios, which are given by a:b:c= 0.3:0.7:1, 0.6:0.7:1, 0.5:0.6:1, and 0.4:0.5:1. The best agreement between the measurements and theoretical simulations is observed when the weights are selected as 0.3168, 0.0683, 0.1730, and 0.4420 for aspect ratios a:b:c= 0.3:0.7:1, 0.6:0.7:1, 0.5:0.6:1, and 0.4:0.5:1, respectively. Fig. 48 shows the comparison between the measured phase matrix and the theoretical simulations based on spherical, spheroidal, and ellipsoidal shapes. The simulated P_{11} values are normalized to 1 at scattering angle $\theta_s = 30^o$. It is evident that the phase matrix elements simulated on the basis of the ellipsoid model (red lines) agree better with the measured data than those based on the spheroid model (blue lines), whereas the sphere model (dashed black lines) leads to much larger discrepancies, particularly, in backward directions ($> 90^o$). The phase functions (P_{11}) simulated from the spheroid and ellipsoid models are quite similar. However, in terms of agreement with the measurements, the ellipsoid model are more accurate than the spheroid model for simulating the other phase matrix elements associated with polarization, particularly, in the cases of $-P_{12}/P_{11}$, P_{22}/P_{11}, P_{33}/P_{11}, and P_{44}/P_{11} for scattering angles larger than 90^o.

Note that we used only four aspect ratios for spheroids and ellipsoids. This case study demonstrates that the ellipsoid model is better than spheroid model for simulating the polarization characteristics of nonspherical feldspar particles. Selecting an optimized shape (i.e., aspect ratio) distribution of ellipsoids in the optical property computation for realistic dust particles deserves further investigations.

C. Model Simulations: Nonsymmetric Hexahedra

Under the assumption of independent scattering, the optical properties of an ensemble of particles depend on the particle shape mixture, refractive index and size

distribution. Laboratory measurements [84] demonstrate that the scattering matrices of several dust samples have similar patterns over a wide range of scattering angles, although the particle geometries, shown by scanning electron microscope (SEM) images, of these samples are quite different. Quantitative differences of the scattering matrices are mainly attributed to the differences in the complex refractive index and the particle size distribution [84] . Guided by the measurements, a straightforward approach to modeling the single-scattering properties of dust aerosols is to use an ensemble of relatively regular nonspherical geometries to represent realistic dust particles that have complicated morphologies [94–96] by employing estimated refractive indices and measured size distributions.

In some previous studies [96–99], spheroids were assumed to be the first-order approximation to the overall shapes of irregular dust aerosols. A recent study [114] explored the use of tri-axial ellipsoids to improve the spheroid model by adding the degree of freedom in the particle morphology. Gaussian spheres and other much more complicated geometries have also been suggested in several recent studies [46, 115]. Other simplified approaches were investigated to model the scalar optical properties of randomly oriented irregular particles [116–119]. Although the spheroid model is quite successful in modeling the optical properties of mineral particles, it suffers from some shortcomings. For example, the scattering properties of an ensemble of single-shaped (i.e., with a specific aspect ratio) spheroids or even tri-axial ellipsoids have angular features inherent to the specific geometries of these particles. To match the theoretical simulations to laboratory measurements, an artificial shape distribution and a relatively large imaginary part of the refractive index are necessary [101].

Although relatively regular geometries such as cylinders, hexagonal columns/plates, droxtals, platonic particles, and polyhedral prisms have been extensively exploited in optical modeling of particulate matter in the atmosphere [26,100,120–124], this study

is intended to explore the use of nonsymmetric geometries to simulate dust optical properties. To mimic realistic dust particles, the present geometries are defined to have sharp edges and corners without symmetry, aimed at producing a featureless scattering pattern even if a single geometry rather than a mixture of various geometries is used. Guided by the fact that ellipsoids can be regarded as deformed spheres, a straightforward approach to obtaining nonsymmetric geometries possessing sharp edges/corners and planar faces is to deform regular hexahedra. Fig. 49 shows the nonsymmetrical hexahedra produced by deforming a regular hexahedron. The mathematical parameters to define the geometry of a nonsymmetric hexahedron will be given in Subsection 1. The present study is directed toward understanding the characteristics of the optical properties of nonsymmetrical hexahedra, and the applicability of the nonsymmetrical hexahedron model to the simulation of laboratory measurements of the optical properties of realistic dust particles.

We compare theoretical simulations with laboratory measurements of the optical properties of quartz and the dust particles from the Pinatubo eruption. The geometries of these samples are quite different, but they have similar complex refractive indices whose real parts are in the range $1.5 - 1.7$. In the present simulation, the refractive index is assumed to be $1.5 + i0.001$. The experimental data show that the scattering matrix elements for different aerosols have similar patterns over a wide range of scattering angles [84].

1. Nonsymmetric Hexahedron Generator

A hexahedron is a 3D solid with six faces. Topologically, there are seven types of convex hexahedra, corresponding to different arrangements of faces and vertices [125]. For simplicity, we confine this study to irregular hexahedra with topologies similar to that of a cubic particle (i.e. quadrilateral faces, eight vertices and twelve edges). One

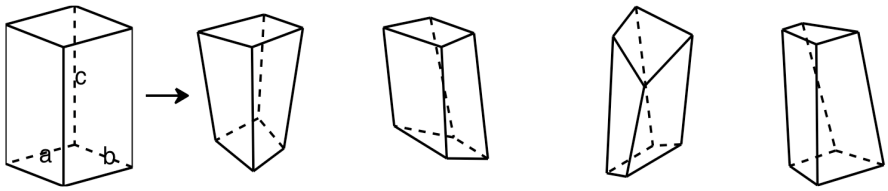

Fig. 49. Symmetric and nonsymmetric hexahedra

degree of morphological freedom (i.e. particle size) is required to specify the geometry of a cube, whereas three parameters are needed to define a regular hexahedron having different side lengths: the particle maximum dimension (c) and two aspect ratios (a/c and b/c), as shown in Fig. 49. To obtain irregular hexahedra, one practical way is to randomly tilt the faces of the corresponding regular hexahedra, whereas the centers of all the faces are fixed. Mathematically, the six faces of a hexahedron can be defined via

$$\vec{n}_i \cdot (\vec{p} - \vec{p}_i^c) = 0, (i = 1, 6), \tag{7.25}$$

where $\vec{p}$ is the position vector, $\hat{n}_i$ denotes the normal direction of a face, and $\vec{p}_i^c$ denotes the corresponding position vector of the center of the face. The solution to Eq. (7.25) gives the coordinates of the eight vertices. Therefore, one hexahedron can be generated by specifying normal directions of six faces. To obtain nonsymmetric hexahedra, the Monte Carlo method can be employed. As an example, the normal direction of the top face can be determined by:

$$\hat{n}_1 = (\sin\theta\cos\phi, \sin\theta\sin\phi, \cos\theta). \tag{7.26}$$

In the preceding expression, θ and ϕ are the zenith and azimuthal angles, respectively, and can be determined in terms of two random numbers, ξ_1 and ξ_2 , uniformly

distributed between 0 and 1, as follows:

$$\theta = \theta_{max}\xi_1, \phi = 2\pi\xi_2 \tag{7.27}$$

where θ_{max} is a parameter introduced to restrict the range of the value of θ. The normal directions of the remaining five faces can be determined in a similar way. To maintain the topology, it is necessary to preserve the relative position of the eight vertices. To this end, we introduced a restriction condition: the smallest z/y/x coordinates of top/left/front vertices should be larger than the largest z/y/x coordinates of the bottom/right/back vertices. If this condition is not satisfied, another set of random numbers will be generated. Once a new nonsymmetric hexahedron is generated, the surface area is normalized to that of a unit sphere by scaling the position of all the vertices $\vec{P}_i (i = 1 - 8)$ as follows:

$$\vec{p}_i' = \vec{p}_i \sqrt{4\pi/S} \tag{7.28}$$

where $\vec{p}_i'$ denotes the coordinates of the corresponding irregular hexahedra with the same surface areas as that of the unit sphere. In this way, the shapes of irregular hexahedra have been completely determined and the size parameter can be quantified in terms of the radii of surface-area equivalent spheres. In the simulation, if the size is defined in terms of the radius (r) of a surface-area equivalent sphere, the vertices of the irregular hexahedron need to be scaled to $r\vec{p}_i'$. One class of irregular hexahedra with the same inscribed sphere is of particular interest, and it can be proven that the effective radius is a constant. Here the definition of the effective radius [119, 126] is given by

$$r_{eff} = \frac{3V}{4A} \tag{7.29}$$

where V is the volume and A is the average projected area. Consider a sphere with a radius r; we randomly select six points on the surface. An irregular hexahedron can be constructed by taking the normal directions on the sphere at the six selected points as those of the six faces of an irregular hexahedron. Therefore, we have,

$$V = \frac{r}{3} \sum_{i=1}^{6} S_i \tag{7.30}$$

where S_i is the area of the ith face. Evidently, the effective radius is equal to r. This result can also be obtained for an arbitrary shape with the same inscribed sphere [127].

2. Typical Numerical Results

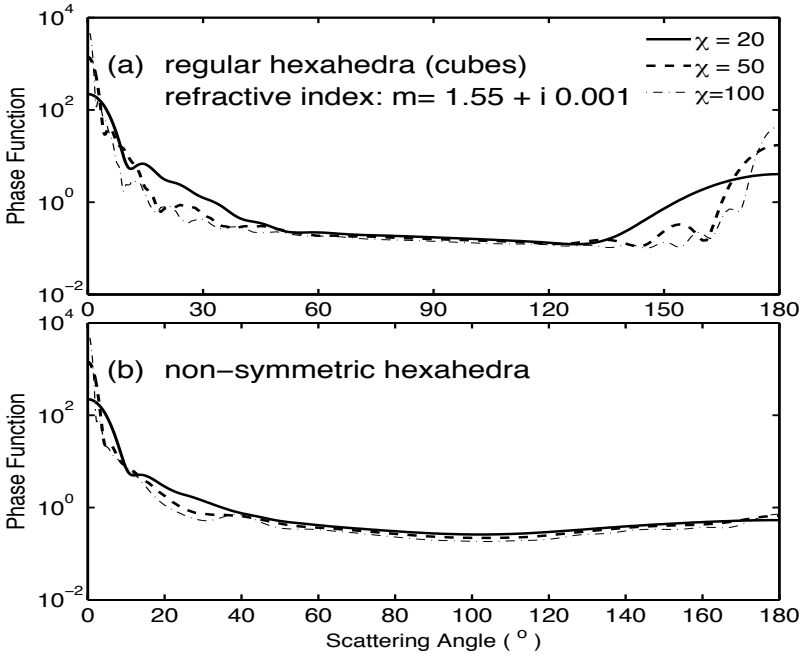

Fig. 50. Phase function of randomly oriented cubes and nonsymmetric hexahedra calculated from the IGOM.

In this section, we present the single-scattering properties of nonsymmetric hexahedra. We also present a comparison between the present simulations and laboratory

measurements. An ensemble of hexahedra with various shapes is generated. The characteristic morphology of this ensemble is specified by two aspect ratios (a/c, and b/c) of the regular hexahedron and the maximum tilting angle θ_{max}. For simplicity, θ_{max} is assumed to be 0.4π, and two aspect ratios are selected to be the same. The single-scattering properties of selected nonsymmetric hexahedra from this ensemble are presented in this section.

Fig. 50(a) shows the phase function computed from IGOM for randomly oriented cubes at a refractive index of m=1.5+i0.001 for three size parameters. It is found that the phase functions have quite large values near the backscattering direction. The phase function of a cube from the conventional geometric optics method has also been investigated in [128]. However, from aerosol measurements, the phase functions for dust analogs are flat near the backscattering direction. Therefore, a regular hexahedron is not a proper shape model for dust aerosols. Fig. 50(b) is similar to Fig. 50(a), except for nonsymmetric hexahedra. It is evident that the magnitude of the backscattering phase function substantially decreases after the particle symmetry is eliminated. As seen in this figure, eliminating the symmetry of a regular hexahedron may be an effective method to more realistically model the phase function of dust. In the geometric optics method, the contributions to the phase function are from the diffraction, external reflection and transmission. The angular distribution of the external reflection feature does not depend on shape for randomly oriented distributions of particles. The diffraction feature associated with the phase function oscillations may be smoothed out through averaging over orientations and sizes. To obtain a featureless phase function, a straightforward method is to make the transmission part featureless. To this end, tilting the normal direction of a regular hexahedron is a simple yet effective approach.

Fig. 51 shows the integrated single-scattering properties (extinction efficiency

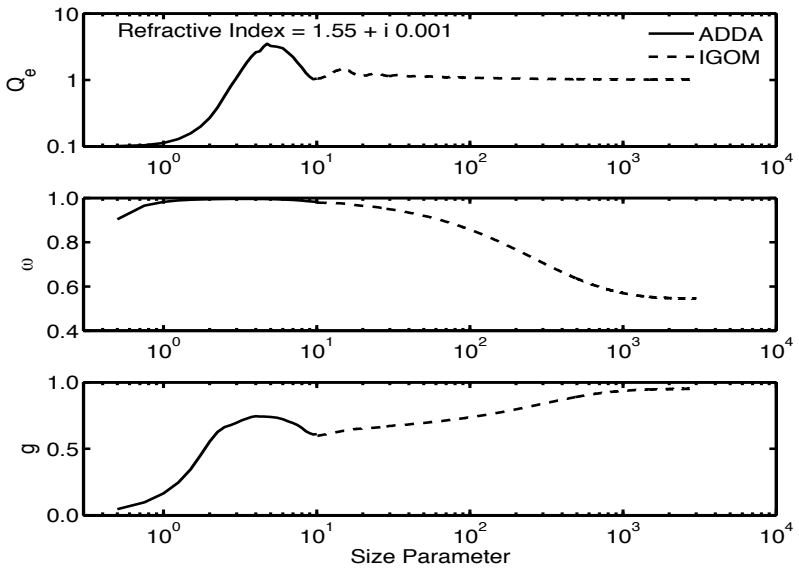

Fig. 51. Integrated scattering properties computed from the DDA method and IGOM for randomly oriented nonsymmetric hexahedra

Q_e, single-scattering albedo ω, and asymmetry factor g) for randomly oriented nonsymmetric hexahedra. We employ the DDA method when the size parameter defined in terms of an equivalent-surface sphere is less than 10. The optical properties from the larger size parameter objects are computed from the IGOM. It is evident from Fig. 51 that a combination of the DDA and IGOM can provide reliable single-scattering properties for a wide range of size parameters, similar to the cases of spheroids and tri-axial ellipsoids [99, 114]. Small inconsistency of efficiency factors from the DDA and the IGOM is removed by adjusting the coefficients of edge effects [99, 114].

To validate the calculation of the IGOM, we compare the phase function of a randomly oriented nonsymmetric hexahedron simulated from the ADDA and IGOM at the size parameter of 10. To examine the diffraction and external calculation, Fig. 52 shows the phase function at the refractive index of 1.55 + i1.0 (i.e. the particle is strongly absorptive). The contribution of outgoing refracted wave to the scattering

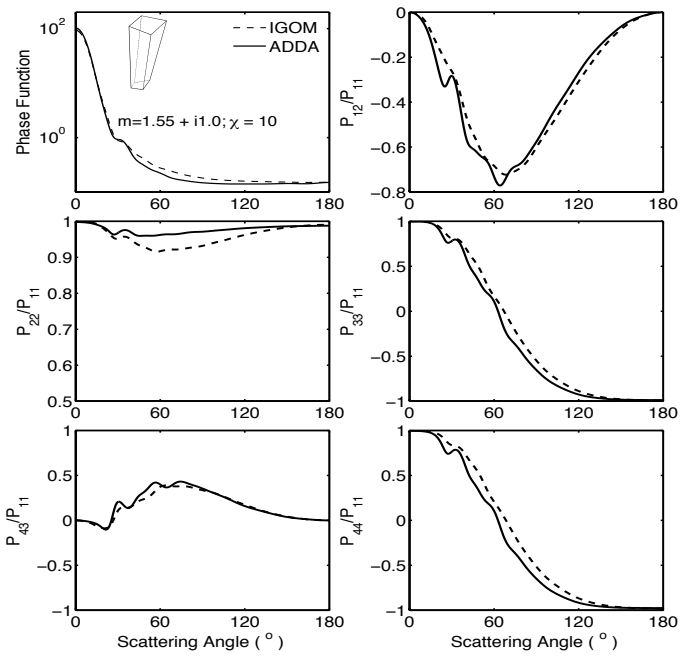

Fig. 52. Comparison of six elements of the phase matrix of a nonsymmetric hexahedron simulated from the IGOM and ADDA. The particle is strongly absorptive. The agreement of results from the IGOM and ADDA indicates the validity of the calculation of the diffraction and external reflection in the IGOM at a size parameter of 10.

pattern can be properly neglected. An excellent agreement of the results from the ADDA and IGOM indicates that the calculation of diffraction and external reflection from the IGOM is properly accounted with a very good accuracy. Fig. 53 is the same as Fig. 52 except that the refractive index is 1.55 + i 0.001. In this case, the accuracy of the IGOM is not as good as that in Fig. 52; however, the IGOM can provide a general profile of six elements of the phase matrix as function of scattering angle. As the ADDA method is extremely time-consuming for randomly oriented nonsymmetric hexahedra, a combination of the ADDA and IGOM is employed to cover a complete range of size parameters with a transitional point of 10.

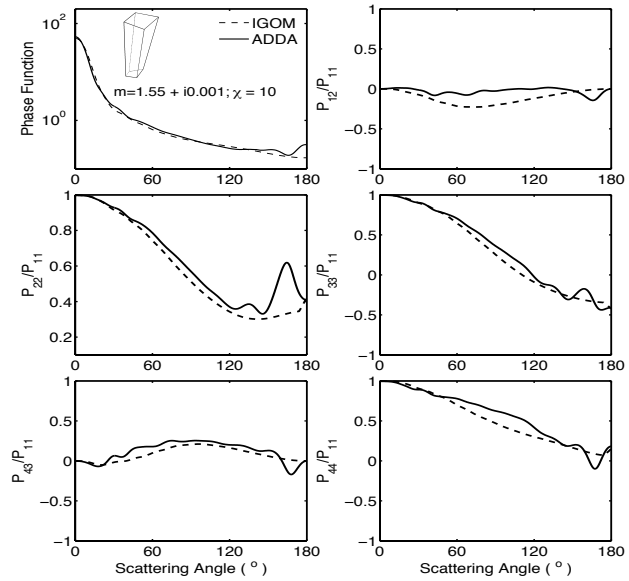

Fig. 53. Same as Fig. 52, except that the nonsymmetric hexahedron is semi-transparent.

3. Simulation and Measurement

We compare theoretical simulations with laboratory measurements of the optical properties of quartz and the dust particles from the Pinatubo eruption. The geometries of these samples are quite different, but they have similar complex refractive indices whose real parts are in the range 1.5 1.7. In the present simulation, the refractive index is assumed to be 1.55+i0.001. The experimental data show that the scattering matrix elements for different aerosols have similar patterns over a wide range of scattering angles [84].

Fig. 54 shows the comparison of six elements of the phase matrix for sampled quartz particles [84]. For the present computation, three nonsymmetric hexahedral shapes are employed. The effective radius is 2.3 μm and the variance is 1.5. Close

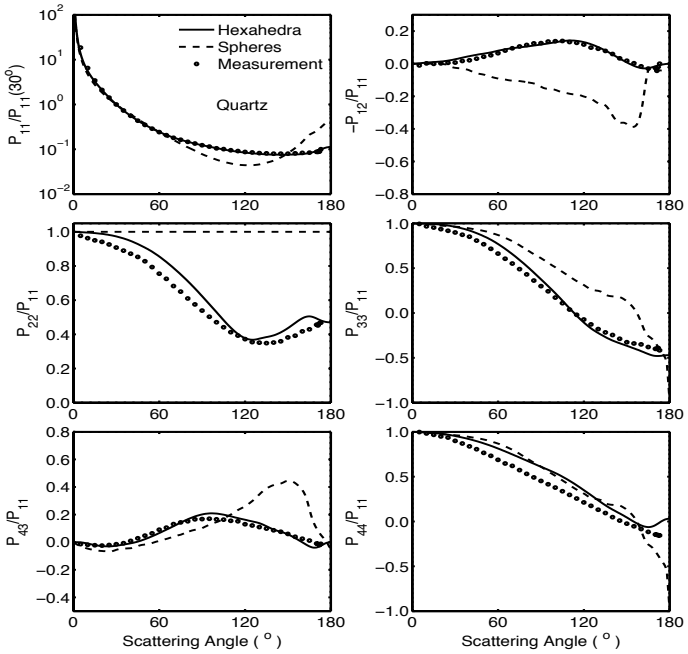

Fig. 54. Comparison of simulated results of hexahedra with measurements for quartz particles at the wavelength of 0.633 μm.

agreement between the simulated results and measurement data is observed. For comparison, the simulated results from the Lorentz-Mie theory are also presented. As expected, the results associated with nonsymmetric hexahedra are significantly better than their spherical counterparts in comparison with the measurements. It should be pointed out that the agreement of the elements obtained with the present model cannot be reproduced by using prisms (i.e., polyhedra with symmetry). The range of variation in the curve produced using the regular prism model is narrow, and the curve of the experimental data is out of the range [129]. Therefore, it is difficult to match the experimental data with simulations based on the prism model, even though an aspect-ratio distribution is employed for the regular prism model.

Fig. 55 shows the characteristics of the single-scattering properties simulated for

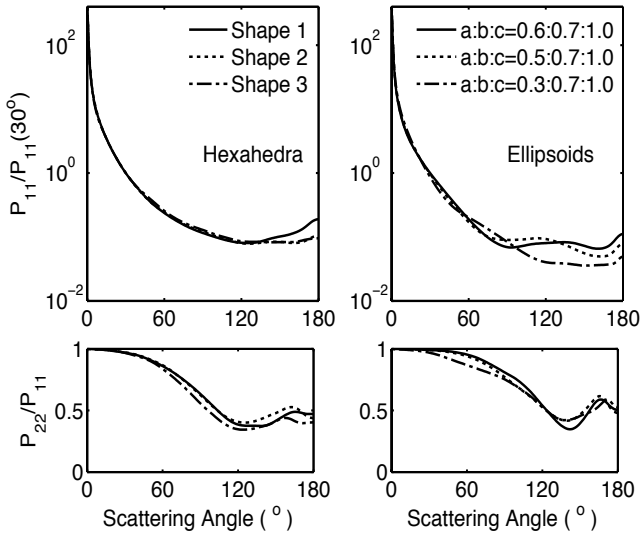

Fig. 55. Simulated bulk-scattering properties from single shape. The left panel is for three nonsymmetric hexahedra. The right panel is for three tri-axial ellipsoids. The size distribution is the same as that employed in Fig. 54.

several shapes. The left panel is for three nonsymmetric hexahedra generated from the Monte Carlo method. The right panel is for three tri-axial ellipsoids. It is demonstrated that the phase functions of the ellipsoids possess features at scattering angles between 60^o and 180^o except in the case of an extreme aspect ratio. This explains the fact that the ellipsoids with extreme aspect ratios usually have a larger weight in the particle aspect ratio distribution to match theoretical results with measurement counterparts. For nonsymmetric hexahedra, the backscattering phase function has no oscillating features. Therefore, it is more appropriate to use nonsymmetric hexahedra to mimic the laboratory measurements. The P22/P11 curves for hexahedra and ellipsoids show the similar behavior.

Similar to Fig. 54, Fig. 56 shows the comparison of the six elements of the phase matrix for sampled Pinatubo particles [84]. The effective radius of the Pinatubo

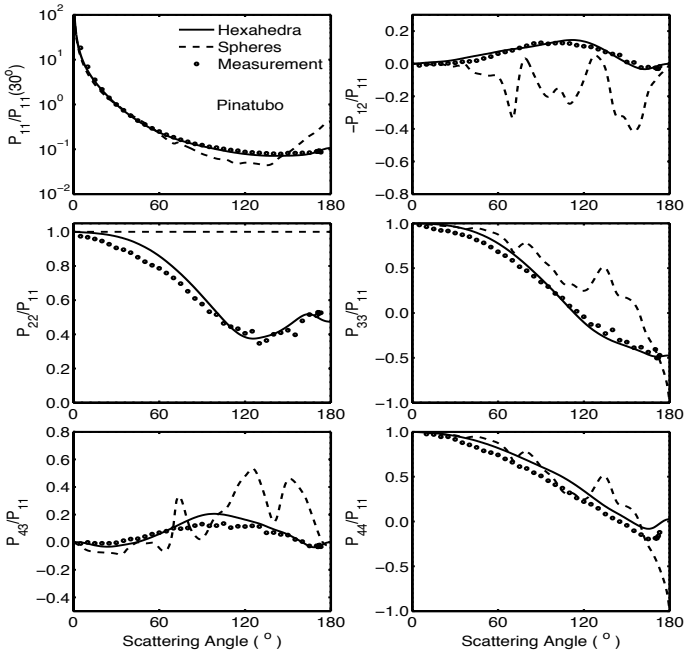

Fig. 56. Same as Fig. 54, but for the pinatubo aerosol sample

sample is 3 μm and the variance of the size distribution is 12.3. We used the same nonsymmetric hexahedra as those for quartz particles. The final results are not sensitive to the weights of the different shapes. Reasonably good agreement is again obtained when the theoretical results are compared with the measurements. It should be pointed out that the geometries of quartz and Pinatubo aerosol samples are quite different and also have different size distributions. However, the same nonsymmetric hexahedron model for particle shape (but with different effective size and variance) can be used to simulate of the phase matrix of these two different aerosol samples, demonstrating that a relatively simple geometry can be used to represent complicated nonspherical aerosols in scattering computation.

This sensitivity study is directed toward answering the question of whether the present model captures the main effects of the nonsphericity and irregularity of real-

istic mineral aerosols in computing their optical properties. In reality, the properties of dust particles are very complicated. For example, dust particles may be inhomogeneous, and the refractive index and shape may be size-dependent. For moderate or even larger particles, the effect of surface texture and roughness may be important. Although the laboratory measurements also have some uncertainties, the comparison between the present simulation and laboratory data suggests that the nonsymmetric hexahedron model is a quite promising for studying dust aerosol optical properties. To further develop this model for application to aerosol study, a systematic and accurate database of the optical properties of individual nonsymmetric hexahedra is required. This database may provide a relatively realistic aerosol model that could be applied to aerosol retrieval studies [130–132].

CHAPTER VIII

SUMMARY AND CONCLUSIONS

In this dissertation, we have systematically developed the current numerical techniques for the solution of light scattering by nonspherical particles in a complete range of size parameters, and have studied the optical properties of ice crystals and mineral dust aerosols in the atmosphere. We have developed a new PGOH method, which is applicable to arbitrary oriented ice crystals with complex refractive indices. With this mew PGOH algorithm, the accuracy of PGOH simulations is much better understood. In addition, the knowledge of electromagnetic tunneling effect involved in scattering is advanced through proposed numerical study, and semi-emprical formulae. The consideration of edge effect is essential to obtain smooth transition from Rayleigh regime to geometric optics regimes.

We have modeled the optical properties of randomly oriented ice crystals, oriented ice crystals and imperfect ice crystals by using the newly developed numerical methods. Particular attention is paid to the computation of the value of color ratio of ice crystals. The value of color ratio is an important parameter in the calibration algorithm of Calipso lidar.

We have proposed two new nonspherical models (i.e., triaxial ellipsoidal model, and nonsymmetric hexahedral model) to model the single-scattering properties of mineral dust aerosols. The two newly defined geometries are employed to explore the use of simple geometries to reproduce the laboratory measurements. The agreement of simulated results with some measurements suggests the reliability/feasibility of this methodology that avoids the definition of the details of rather irregular and complex geometries, but capture the effect arising from the nonsphericity and the lack of symmetry on the basis of model particles.

In a summary, the developed numerical techniques and models of ice crystals and mineral dust aerosols allow the computation of the single-scattering properties of nonspherical ice and mineral dust aerosol particles in the atmosphere with reasonable accuracy and time. In the perspective of applications, the single-scattering properties are fundamentally required to interpret the observations from space-based satellites and ground-based instruments, to assess the radiative impact of cirrus clouds and aerosols in climate study, and to develop a calibration algorithm for space-based lidar. A single-scattering database based on current numerical techniques and models can be employed to link the theory and observations. Furthermore, the developed single-scattering model also includes the polarization characteristics of model particles. The aerosol polarimetry sensor (APS) on the Glory platform will provide an unprecedented opportunity to study the polarization characteristics of realistic dust particles in the atmosphere. Therefore, the developed model will benefit the APS in terms of dust retrieval.

The developed techniques can also find applications in other disciplines, such as astronomy, biophysics, and oceanography, to name a few.

REFERENCES

[1] K. N. Liou, *An Introduction to Atmospheric Radiation* (Academic Press, New York, 1980).

[2] H. C. van de Hulst, *Light Scattering by Small Particles* (Wiley, New York, 1981).

[3] C. F. Bohren and D. R. Huffman, *Absorption and Scattering of Light by Small Particles* (Wiley, New York, 1983).

[4] M. I. Mishchenko, L. D. Travis, and A. A. Lacis, *Light Scattering by Nonspherical Particles: Theory, Measurements, and Applications* (Academic Press, Cambridge, 1999).

[5] M. I. Mishchenko, L. D. Travis, and A. A. Lacis, *Scattering, Absorption and Emission of Light by Small Particles* (Academic Press, Cambridge, 2002).

[6] F. M. Kahnert "Numerical methods in electromagnetic scattering theory," J. Quant. Spectrosc. Radiat. Transfer. **79**, 775-824 (2003).

[7] F. M. Kahnert, "Electromagnetic scattering by nonspherical particles: recent advances," J. Quant. Spectrosc. Radiat. Transfer. **111**, 1788-1790 (2010).

[8] P. Yang and K. N. Liou, "Light scattering and absorption by nonspherical ice crystals," in *Light Scattering Reviews: Single and Multiple Light Scattering,* A. A. Kokhanovsky, ed. (Springer Praxis, Chichester, UK, 2006), pp. 31-71.

[9] S. K. Yee, "Numerical solution of initial boundary value problems involving Maxwells equations in isotropic media,"IEEE Trans. Antennas. Propag. **14**, 302-307 (1966).

[10] P. Yang and K. N. Liou, "Finite-difference time domain method for light scattering by small ice crystals in three-dimensional space," J. Opt. Soc. Am. A **13**, 2072-2085 (1996).

[11] W. Sun, Q. Fu, and Z. Chen, "Finite-difference time-domain solution of light scattering by dielectric particles with perfectly matched layer absorbing boundary conditions," Appl. Opt. **38**, 3141-3151 (1999).

[12] E. M. Purcell and C. R. Pennypacker, "Scattering and absorption of light by nonspherical dielectric grains," Astrophys. J. **186**, 705-714 (1973).

[13] B. T. Draine, "The discrete-dipole approximation and its application to interstellar graphite grains," Astrophys. J. **333**, 848-872 (1988).

[14] G. H. Goedecke and S. G. O'Brien, "Scattering by irregular inhomogeneous particles via the digitized Green's function algorithm," Appl. Opt. **27**, 2431-2438 (1988).

[15] M. A. Yurkin and A. G. Hoekstra, "The discrete dipole approximation: An overview and recent developments," J. Quant. Spectrosc. Radiat. Transfer. **106**, 558-589 (2007).

[16] P. C. Waterman, "Matrix formulation of electromagnetic scattering," Proc. IEEE **53**, 805-812 (1965).

[17] M. I. Mishchenko, L. D. Travis, and D. W Mackowski, "T-matrix computations of light scattering by nonspherical particles: a review," J. Quant. Spectrosc. Radiat. Transfer **55**, 535-575 (1996).

[18] A. Doicu, Y. Eremin, and T. Wriedt. *Acoustic and Electromagnetic Scattering Analysis Using Discrete Sources* (Academic Press, New York, 2000).

[19] G. J. Streekstra, A. G. Hoekstra, and R. M. Heethaar, "Anomalous diffraction by arbitrarily oriented ellipsoids: applications in ektacytometry,"Appl. Opt. **33**, 7288-7296(1994).

[20] Y. Liu, W. P. Arnott, and J. Hallett, "Anomalous diffraction theory for arbitrarily oriented finite circular cylinders and comparison with exact T-matrix results,"Appl. Opt. **37**, 5019-5030 (1998).

[21] P. Yang, Z. Zhang, B. A. Baum, H.-L. Huang, and Y. Hu, "A new look at anomalous diffraction theory (ADT): algorithm in cumulative projected-area distribution domain and modified ADT,"J. Quant. Spectrosc. Radiat. Transfer **89**, 421-442(2004).

[22] X. Sun, H. Tang, and G. Yuan, "Anomalous diffraction approximation method for retrieval of spherical and spheroidal particle size distributions in total light scattering,"J. Quant. Spectrosc. Radiat. Transfer **109**, 89-106 (2008).

[23] P. Wendling, R. Wendling, and H. K. Weickmann, "Scattering of solar radiation by hexagonal ice crystals," Appl. Opt. **18**, 2663-2671 (1979).

[24] Q. M. Cai and K. N. Liou, "Polarized light scattering by hexagonal ice crystals: theory,"Appl. Opt. **32**, 2780-2788 (1993).

[25] Y. Takano and K. N. Liou, "Solar radiative transfer in cirrus clouds. Part I: single-scattering and optical properties of hexagonal ice crystals,"J. Atmos. Sci. **46**, 3-19 (1989).

[26] A. Macke, "Scattering of light by polyhedral ice crystals,"Appl. Opt. **32**, 2780-2788 (1993).

[27] K. Muinonen, "Scattering of light by crystals: a modified Kirchhoff approximation,"Appl. Opt. **28**, 3044-3050 (1989).

[28] P. Yang and K. N. Liou, "Geometric-optics-integral-equation method for light scattering by nonspherical ice crystals,"Appl. Opt., **35**, 6568-6584 (1996).

[29] P. Yang and K. N. Liou, "Light scattering by hexagonal ice crystals: solution by ray-by-ray integration algorithm,"J. Opt. Soc. Am. A., **14**, 2278-2289 (1997).

[30] P. Yang and K. N. Liou, "Single-scattering properties of complex ice crystals in terrestrial atmosphere," Contr. Atmos. Phys., **71**, 223-248,1998.

[31] A. G. Borovoi and I. A. Grishin, "Scattering matrices for large ice crystal particles,"J. Opt. Soc. Am. A. **20**, 2071-2080 (2003).

[32] H. M. Nussenzveig, *Diffraction Effects in Semiclassical Scattering* (Cambridge University Press, New York, 1992).

[33] D. S. Jones, "Approximate methods in high-frequency scattering,"Proc. R. Soc. Lond. A **239**, 338-348 (1957).

[34] D. S. Jones, "High-frequency scattering of electromagnetic waves,"Proc. R. Soc. Lond. A **240**, 206-213 (1957).

[35] A. J. Heymsfield and J. Iaquinta, "Cirrus crystal terminal velocities," J. Atmos. Sci. **57**, 916-938 (2000).

[36] H. Volten, O. Muñoz, E. Rol, J. F. de Haan, W. Vassen, J. W. Hovenier, K. Muinonen, and T. Nousiainen, "Scattering matrices of mineral particles at 441.6 nm and 632.8 nm," J. Geophys. Res. **106**, 17375-17401 (2001).

[37] J. D. Jackson, *Classical Electrodynamics* (John Wiley & Sons, New York, 1981).

[38] C. T. Tai, *Dyadic Green's Function in Electromagnetic Theory* (International Textbook, Scranton, PA, 1971)

[39] D. S. Saxon, *Lectures on the Scattering of Light* (University of California, Los Angeles, 1955).

[40] A. Sommerfeld, *Electrodynamics* (Academic Press, New York, 1952).

[41] S. A. Schelkunoff, *Electromagnetic Waves* (D. Von Nostrand, New York, 1943).

[42] R. F. Harrington, *Time-Harmonic Electromagnetic Fields* (McGraw-Hill, New York, 1961).

[43] P. Yang and K. N. Liou, "Finite difference time domain method for light scattering by nonspherical and inhomogeneous particles," in *Light Scattering by Nonsphercial Particles, Theroy, Measurements, and Applications*, M. I. Mishchenko, J. W. Hovenier, and L. D. Travis, eds. (Academic Press, New York, 2000), pp. 173-221.

[44] Q. H. Liu, "The pseudospectral time-domain(PSTD) algorithm for acoustic waves in absorptive media," IEEE Trans. Ultrason. Ferroelectr. Freq. Control. **45**, 1044-1055 (1998).

[45] G. Chen, P. Yang, and G. W. Kattawar, "Application of the pseudospectral time-domain method to the scattering of light by nonspherical particles," J. Opt. Soc. Am. A **25**, 785-790 (2008).

[46] O. V. Kalashnikova, R. Kahn, I. N. Sokolik, and W.-H Li, "Ability of multiangle remote sensing observations to identify and distiguish mineral dust types: optical models and retrievals of optically thick plumes," J. Geophys. Res. **110**, D18S14, doi:10.1029/2004JD004550 (2005).

[47] G. Hong, P. Yang, F. Z. Weng, and Q. H. Liu, "Microwave scattering properties of sand particles: Application to the simulation of microwave radiances over sandstorms," J. Quant. Spectrosc. Radiat. Transfer. **109**, 684-702 (2008).

[48] T. Wriedt and U. Comberg, "Comparison of computational scattering method," J. Quant. Spectrosc. Radiat. Transfer **60**, 3, 411-423(1998).

[49] M. A. Yurkin, V. P. Maltsev, and A. G. Hoekstra, "The discrete dipole approximation for simulation of light scattering by particles much larger than the wavelength,"J. Quant. Spectrosc. Radiat. Transfer **106**, 546-557 (2007).

[50] M. A. Yurkin, A. G. Hoekstra, R. S. Brock, and J. Q. Lu, "Systematic comparison of the discrete dipole approximation and the finite difference time domain method for large dielectric scatterers," Opt. Express **15**, 17902-17911 (2007)

[51] A. Penttila, E. Zubko, K. Lumme, K. Muinonen, M. A. Yurkin, B. Draine, J. Rahola, A. G. Hoekstra, Y. Shkuratov. "Comparison between discrete dipole implementations and exact techniques," J. Quant. Spectrosc. Radiat. Transfer. **106**, 417-436 (2007).

[52] M. Born and E. Wolf, *Principle of Optics* (Pergamon Press, Oxford, 1975).

[53] P. Yang, B. C. Gao, B. A. Baum, W. J. Wiscombe, M. I. Mischenko, D. M. Winker, S. L. Nasiri. "Asymptotic solutions of optical properties of large particles with strong absorption," Appl. Opt. **40**, 1532-1547(2001).

[54] R. E. Langer, "On the connection formulas and the solutions of the wave equation,"Phys. Rev. **51**, 669-676 (1937).

[55] G. R. Fournier and B. T. Evans, "Approximations to extinction from randomly oriented circular and elliptical cylinders,"Appl. Opt. **35**, 4271-4282 (1996).

[56] S. G. Warren, and R. E. Brandt, "Optical constants of ice from the ultraviolet to the microwave: a revised compilation," J. Geophys. Res., **113**, D14220, doi:10.1029/2007JD009744 (2008).

[57] M. Minnaert, *The Nature of Light and Colour in the Open Air* (New York, Dover, 1954).

[58] C. M. R. Platt, N. L. Abshire, and G. T. McNice, "Some microphysical properties of an ice cloud from lidar observation of horizontally oriented crystals,"J. Appl. Meterorol, **17**, 1220-1224 (1978).

[59] H. Chepfer, G. Brogniez, P. Goloub, F. M. Breon, and P. H. Flamant, "Observations of horizontally oriented ice crystals in cirrus clouds with POLDER-1/ADEOS-1,"J. Quant. Spectrosc. Radiat. Transfer **63**, 521-543 (1999).

[60] V. Noel and H. Chepfer, "Study of ice crystal orientation in cirrus clouds based on satellite polarized radiance measurements,"J. Atmos. Sci. **61**, 2073-2081 (2004).

[61] F. M. Breon and B. Durbulle, "Horizontally oriented plates in clouds," J. Atmos. Sci. **61**, 2888-2898 (2004).

[62] A. Ono, "Shape and riming properties of ice crystals in natural clouds,"J. Atmos. Sci. **26**, 138-147 (1969).

[63] Y. Hu, M. Vaughan, Z. Liu, B. Lin, P. Yang, D. Flittner, B. Hunt, R. Kuehn, J. Huang, D. Wu, S. Rodier, K. Powell, C. Trepte, and D. Winker, "The depolarization-attenuated backscatter relation: CALIPSO lidar measurement vs. theory," Opt. Express **15**, 5327-5332(2007).

[64] C. Lavigne, A. Roblin, and P. Chervet, "Solar glint from oriented crystals in cirrus clouds,"Appl. Opt. **47**, 6266-6276 (2008).

[65] V. N. Marichev, V. P. Galileyskii, D. O. Kuzmenkov, and A. M. Morozov, "Experimental observation of the mirror reflection of laser radiation from oriented particles concentrated in the atmospheric layer," Atmos. Oceanic. Opt. **23**,128-131 (2010).

[66] A. G. Borovoi, N. V. Kustova, and U. G. Oppel, "Light backscattering by hexagonal ice crystal particles in the geometrical optics approximation," Opt. Eng. **44**, 071208 (2005).

[67] A. G. Borovoi and N. V. Kustova, "Specular scattering by preferably oriented ice crystals,"Appl. Opt. **48**, 3878-3885 (2009).

[68] M. Hess, R. B. A. Koelemeijer, and P. Stammes, "Scattering matrices of imperfect hexagonal crystals,"J. Quant. Spectrosc. Radiat. Transfer **60**, 301-308 (1998).

[69] D. M. Winker, J. R. Pelon, and M. P. McCormick,"The CALIPSO mission: spaceborne lidar for observation of aerosols and clouds," Proc. SPIE, **4893**, 1-11 (2003).

[70] J. A. Reagan, X. Wang, and M. T. Osborn, "Spaceborne lidar calibration from cirrus and molecular backscatter returns," IEEE Trans. Geosci. Remote Sens., **40**, 2285-2290(2002).

[71] Z. Liu, M. A. Vaughan, D. M. Winker, C. A. Hostetler, L. R. Poole, D. Hlavka, W. Hart, and M. McGill, "Use of probability distribution functions for discriminating between cloud and aerosol in lidar backscattering data," J. Geophys.

Res., **109**, D15202(2004).

[72] P. Yang, H. L. Wei, H. L. Huang, B. A. Baum, Y. Hu, G. W. Kattawar, M. I. Mishchenko, and Q. Fu, "Scattering and absorption property database for nonspherical ice particles in the near- through far-infrared spectral region," Appl. Opt., **44**, 5512-5523(2005).

[73] M. A. Vaughan, M. J. McGill, Z. Liu, Y. Hu, R. E. Kuehn, and S. D. Rodier, "Backscatter Color Ratios of Cirrus Clouds Measured by the Cloud Physics Lidar, Proceedings of the 15th Conference on Clouds and Precipitation (ICCP2008)," available online at http://convention-center.net/iccp2008/abstracts/Program_on_line/Poster_13/Vaughan_extended.pdf

[74] Z. M. Tao, M. P. McCormick, D. Wu, Z. Y. Liu, and M. A. Vaughan, "Measurements of cirrus cloud backscatter color ratio with a two-wavelength lidar," Appl. Opt., **47**, 1478-1485 (2008).

[75] B. A. Baum, P. Yang, A. J. Heymsfield, S. Platnick, M. D. King, and S. T. Bedka, "Bulk scattering models for the remote sensing of ice clouds. Part 2: Narrowband models," J. Appl. Meteor., **44**, 1896-1911(2005).

[76] M. I. Mishchenko, and A. Macke, "Incorporation of physical optics effects and computation of the Legendre expansion for ray-tracing scattering functions involving δ -function transmission," J. Geophys. Res. **103**, 1799-1805(1998).

[77] B. A. Baum, A. J. Heymsfield, P. Yang, and S. T. Bedka,"Bulk scattering properties for the remote sensing of ice clouds I: Microphysical data and models," J. Appl. Meteor., **44**, 1885-1895(2005).

[78] G. A. d'Almeida, P. Koepke, and E. P. Shettle, *Atmospheric Aerosols: Global Climatology and Radiative Characteristics* (Deepak, Hampton, Va. 1991).

[79] P. Chylek, and J. Coakley, "Aerosols and climate,"Science, **183**, 75-77 (1983).

[80] J. Haywood, and O. Boucher, "Estimates of the direct and indirect radiative forcing due to troposphere aerosols: a review," Rev. Geophys. **38**, 513-543 (2000).

[81] V. Ramanathan, P. J. Crutzen, J. T. Kiehl, and D. Rosenfeld, "Aerosols, climate, and the hydrological cycle,"Science, **294**, 2119-2124 (2001).

[82] I. N. Sokolik, D. Winker, G. Bergametti, D. Gillette, G. Carmichael, Y. J. Kaufman, L. Gomes, L. Schuetz, and J. Penner, "Introduction to special section on mineral dust: outstanding problems in quantifying the radiative impact of mineral dust,"J. Geophys. Res., **106**, 18015-18027 (2001).

[83] Y. J. Kaufman, D. Tanre, and O. Boucher, "A satellite view of aerosols in the climate system,"Nature, **419**, 215-222 (2002).

[84] H. Volten, O. Muoz, J. W. Hovenier, and L. B. F. M. Waters, "An update of the Amsterdam light scattering database,"J. Quant. Spectrosc. Radiat. Transfer **100**, 437-443 (2005).

[85] R. A. West, L. R. Doose, A. M. Eibl, M. G. Tomasko, and M. I. Mishchenko, "Laboratory measurements of mineral dust scattering phase function and linear polarization,"J. Geophys. Res., **102**, 16871-16881 (1997).

[86] D. B. Curtis, B. Meland, M. Aycibin, N. P. Arnold, V. H. Grassian, M. A. Young, and P. D. Kleiber, "A laboratory investigation of light scattering from

representative components of mineral dust aerosols at a wavelength of 550 nm,"J. Geophys. Res., **113**, D08210 (2008).

[87] O. V. Kalashnikova and I. N. Sokolik, "Importance of shapes and compositions of wind-blown dust particles for remote sensing at solar wavelengths,"Geophys. Res. Lett. **29**, doi: 10.1029/2002GL014947 (2002).

[88] M. I. Mishchenko, A. A. Lacis, B. E. Carlson, and L. D. Travis, "Nonsphericity of dust-like tropospheric aerosols: implications for aerosol remote sensing and climate modeling,"Geophys. Res. Lett. **22**, 1077-1080 (1995).

[89] Q. Feng, P. Yang, G. W. Kattawar, C. N. Hsu, S.-C. Tsay and I. Laszlo, "Effects of particle nonsphericity and radiation polarization on retrieving dust properties from MODIS observations,"J. Aerosol Sci., **40**, 776-789 (2009).

[90] M. Kahnert, T. Nousiainen, and B. Veihelmann, "Spherical and spheroidal model particles as an error source in aerosol climate forcing and radiance computations: a case study for feldspar aerosols,"J. Geophys. Res., **110**, D18S13 (2005).

[91] M. Kahnert, T. Nousiainen, and P. Raisanen, "Mie simulations as an error source in mineral aerosol radiative forcing calculations," Q. J. R. Meteorol. Soc. **133**, 299-307 (2007).

[92] Y. Liu, W. P. Arnott, and J. Hallertt, "Particle size distribution retrieval from multispectral optical depth: influences of particle nonsphericity and refractive index," J. Geophys, Res. **104**, 31753-31762 (1999).

[93] R. Kahn, R. West, D. McDonald, B. Rheingans, and M. I. Mishchenko, "Sensitivity of multiangle remote sensing observations to aerosol sphericity," J. Geo-

phys. Res. **102**, 16861-16870 (1997).

[94] A. Macke and M. I. Mishchenko, "Applicability of regular particle shapes in light scattering calculations for atmospheric ice particles," Appl. Opt. **35**, 4291-4296 (1996).

[95] F. M. Kahnert, J. J. Stamnes, and K. Stamnes, "Can simple particle shapes be used to model scalar optical properties of an ensemble of wavelength-sized particles with complex shapes?" J. Opt. Soc. Am. A **19**, 521-531 (2002).

[96] M. I. Mishchenko, L. D. Travis, R. A. Kahn, and R. A. West, "Modeling phase functions for dustlike troposheric aerosols using a shape mixture of randomly oriented polydisperse spheroids," J. Geophys. Res. **102**, 16831-16847 (1997).

[97] O. Dubovik, B. N. Holben, T. Lapyonok, A. Sinyuk, M. I. Mishchenko, P. Yang, and I. Slutsker, "Non-spherical aerosol retrieval method employing light scattering by spheroids," Geophys. Res. Lett. **29**, 014506 (2002).

[98] O. Dubovik, A. Sinyuk, T. Lapyonok, B. N. Holben, M. I. Mishchenko, P. Yang, T. F. Eck, H. Volten, O. Munoz, B. Veihelmann, W. J. van der Zande, J. F. Leon, M. Sorokin, and I. slutsker, "Application of spheroid models to account for aerosol particle nonsphericity in remote sensing of desert dust," J. Geophys. Res. **111**, D11208 (2006).

[99] P. Yang, Q. Feng, G. Hong, G. W. Kattawar, W. J. Wiscombe, M. I. Mishchenko, O. Dubovik, I. Laszlo, and I. N. Sokolik, "Modeling of the scattering and radiative properties of nonspherical dust particles," J. Aerosol. Sci. **38**, 995-1014 (2007).

[100] P. Yang, K. N. Liou, M. I. Mishchenko, and B.-C. Gao, "Efficient finite-difference time domain scheme for light scattering by dielectric particles: application to aerosols," Appl. Opt., **39**, 3727-3737 (2000).

[101] B. Veihelmann, "Sunlight on atmospheric water vapor and mineral aerosol : modeling the link between laboratory data and remote sensing," Doctoral thesis (Radboud University Nijmegen, 2005).

[102] T. Nousiainen, "Optical modeling of mineral dust particles: a review," J. Quant. Spectrosc. Radiat. Transfer, **110**, 1261-1279 (2009).

[103] S. I. Bhobrial and S. M. Sharief, "Microwave attenuation and cross polarization in dust storms," IEEE. Trans. Antennas. Propagat. **35**, 418-425 (1987).

[104] F. Möglich, "Beugungerscheinungen an Körpern von Ellipsoidischer Gestalt," Ann. Phys. **83**, 609 (1927).

[105] B. D. Sleeman, "The scalar scattering of a plane wave by an ellipsoid," J. Inst. Maths Applics. **3**, 4-15 (1967).

[106] A. F. Stevenson, "Solution of electromagnetic scattering problems as power series in the ratio (dimension of scatterer) wavelength," J. Appl. Phys. **24**, 1134-1142 (1953).

[107] M. I. Mishchenko and L. D. Travis, "Light scattering by polydispersions of randomly oriented spheroids with sizes comparable to wavelengths of observations," Appl. Opt. **33**, 7206-7225 (1994).

[108] T. Wriedt, "Using the T-matrix method for light scattering computations by non-axisymmetric particles: Superellipsoids and realistically shaped particles," Part. Part. Syst. Char. **19**, 256-268 (2002).

[109] J. B. Schneider and I. C. Peden, "Differential cross section of a dielectric ellipsoid by the T-matrix extended boundary condition method," IEEE Trans. Antennas. Propag. **36**, 1317-1321 (1988).

[110] A. Taflove and S. C. Hagness, *Advances in Computational Electrodynamics: the Finite-Difference-Time-Domain Method, 3rd ed.* (Artech House, Boston, 2005).

[111] P. Mazeron and S. Muller, "Light scattering by ellipsoids in a physical optics approximation," Appl. Opt. **35**, 3726-3735 (1996).

[112] C. Levoni, M. Cervino, R. Guzzi, and F. Torricella, "Atmospheric aerosol optical properties: A database of radiative characteristics for different components and classes," Appl. Opt. **36**, 8031-8041 (1997).

[113] T. Nousiainen, and K. Vermeulen, "Comparison of measured single-scattering matrix of feldspar particles with T-matrix simulations using spheroids," J. Quant. Spectrosc. Radiat. Transfer. **79**, 1031-1042 (2003).

[114] L. Bi, P. Yang, G. W. Kattawar, and R. Kahn, "Single-scattering properties of tri-axial ellipsoidal particles for a size parameter range from the Rayleigh to geometric-optics regimes,"Appl. Opt. **48**, 114-126 (2009).

[115] A. A. Kokhanovsky, "Optical properties of irregularly shaped particles,"J. Appl. Phys. D **36**, 915-923 (2003).

[116] P. Chylek, G. W. Grams, and R. G. Pinnick, "Light Scattering by Irregular Randomly Oriented Particles,"Science, **193**, 480-482 (1976).

[117] J. B. Pollack and J. N. Cuzzi, "Scattering by nonspherical particles of size comparable to a wavelength: a new semi-empirical theory and its application to tropospheric aerosols,"J. Atmos. Sci. **37**, 868-881 (1980).

[118] P. Drossart, "A statistical model for the scattering by irregular particles," Astrophys. J. **361**, L29-L32 (1990).

[119] T. C. Grenfell and S. G. Warren, "Representation of a nonspherical ice particle by a collection of independent spheres for scattering and absorption of radiation," J. Geophys. Res. **104**, 31697-31709 (1999).

[120] A. Macke, J. Mueller, and E. Raschke, "Single scattering properties of atmospheric ice crystals," J. Atmos. Sci. **53**, 2813-2825 (1996).

[121] M. I. Mishchenko, L. D. Travis, and A. Macke, "Scattering of light by polydisperse, randomly oriented, finite circular cylinders," Appl. Opt. **35**, 4927-4940 (1996).

[122] P. Yang, B. A. Baum, A. J. Heymsfield, Y.-X. Hu, H.-L. Huang, S.-C. Tsay, and S. A. Ackerman, "Single scattering properties of droxtals," J. Quant. Spectrosc. Radiat. Transfer **79/80**, 1159-1169 (2003).

[123] Z. Zhang, P. Yang, G. W. Kattawar, S-C Tsay, B. A. Baum, Y. Hu, A. J. Heymsfield, and J. Reichardt, "Geometrical-optics solution to light scattering by droxtal ice crystals," Appl. Opt. **43**, 2490-2499 (2004).

[124] Z. Zhang, P. Yang, G. W. Kattawar, and W. J. Wiscombe, "Single-scattering properties of platonic solids in geometrical-optics regime," J. Quant. Spectrosc. Radiat. Transfer **106**, 595-603 (2007).

[125] E. W. Weisstein, "Hexahedron," from MathWorld–A Wolfram Web Resource, http://mathworld.wolfram.com/Hexahedron.html

[126] J. S. Foot, "Some observations of the optical properties of clouds: II. Cirrus," Q. J. R. Meteorol. Soc. **114**, 145-164 (1988).

[127] E. S. Fry, J. Musser, G. W. Kattawar, and P. Zhai, "Integrating cavities: temporal response,"Appl. Opt. **45**, 9053-9065 (2006).

[128] K. N. Liou, Q. Cai, J. B. Pollack, and J. N. Cuzzi, "Light scattering by randomly oriented cubes and parallelepipeds,"Appl. Opt. **22**, 3001-3008 (1983).

[129] T. Nousiainen, M. Kahnert, and B. Veihelmann, "Light scattering modeling of small feldspar aerosol particles using polyhedral prisms and spheroids,"J. Quant. Spectrosc. Radiat. Transfer **101**, 471- 484 (2006).

[130] O. V. Kalashnikova and R. A. Kahn, "Mineral dust plume evolution over the Atlantic from combined MISR/MODIS aerosol retrievals,"J. Geophys. Res. **113**, D24204 (2008).

[131] Y. Liu, P. Koutrakis, and R. Kahn, "Estimating fine particulate matter component concentrations and size distributions using satellite-retrieved fractional aerosol optical depth: part 1 - method development," J. Air Waste Manage. Assoc. **57**, 1351-1359 (2007).

[132] Y. Liu, P. Koutrakis, R. Kahn, S. Turquety, and R. M. Yantosca, "Estimating fine particulate matter component concentrations and size distributions using satellite-retrieved fractional aerosol optical depth: part 2 - a case study,"J. Air Waste Manage. Assoc. **57**, 1360-1369 (2007).

[133] P. M. Morse and H. Feshbach, *Methods of Theoretical Physics* (McGraw-Hill, New York, 1953).

[134] F. Borghese, P. Denti and R. Saija, *Scattering from Model Nonspherical Particles: Theory and Applications to Environmental Physics* (Springer, Heidelberg, 2002).

[135] M. I. Mishchenko, "Gustav Mie and the fundamental concept of electromagnetic scattering by particles: a perspective," J. Quant. Spectrosc. Radiat. Transfer **110**,1210-1222(2009).

[136] D. W. Mackowski and M. I. Mishchenko, "Calculation of the T-matrix and the Scattering matrix for ensembles of spheres," J. Opt. Soc. Am. A **13**, 2266-2278(1996).

[137] T. A. Nieminen, D. H. Rubinsztein, and N. R. Heckenberg, "Calculation of the T-matrix: general considerations and application of the point-matching method," J. Quant. Spectrosc. Radiat. Transfer **79/80**, 1019-1029 (2003).

[138] D. W. Mackowski,"Discrete dipole moment method for calculation of the T-matrix for nonspherical particles," J. Opt. Soc. Am. A **19**, 881-893(2002).

[139] F. M. Schulz, K. Stamnes, and J. J. Stamnes "Scattering of electromagnetic waves by spheroidal particles: A novel approach exploiting the T-matrix computed in spheroidal coordinates," Appl. Opt., **37**, 7875-7896 (1998).

[140] V. G. Farafonov and V. B. Il'in, "Single light scattering: computational methods," in *Light Scattering Reviews: Single and Multiple Light Scattering,* A. A. Kokhanovsky, ed. (Springer Praxis, Chichester, UK, 2006), pp. 125-177.

[141] P. Zhai, Y. K. Lee, G. W. Kattawar, and P. Yang, "On the near- to far-field transformation for the finite-difference time-domain (FDTD) application," Appl. Opt. **43**, 3738-3746 (2004).

[142] W. Gordon, "Far-field approximations to the Kirchoff-Helmholtz representations of scattered fields," IEEE Trans. Antennas. Propag. **23**, 590-592 (1975).

APPENDIX A

VECTOR SPHERICAL FUNCTIONS

This appendix presents a brief and consistent summary of vector spherical functions which satisfy the vector Helmholtz equation in the spherical coordinate system.

Scalar Helmholtz Equation

It has been demonstrated (e.g. [133]) that vector spherical functions can be constructed from the solution of the scalar Helmholtz equation in spherical coordinate system (the scalar Helmholtz equation can be solved by using the method of separation of variables in 11 coordinate systems). Let ψ be the solution of the scalar Helmholtz equation,

$$(\vec{\nabla}^2 + k^2)\psi = 0. \tag{A.1}$$

In the spherical coordinate system, Eq. (A.1) is [133]

$$\left[\frac{1}{r^2}\frac{\partial}{\partial r}(r^2\frac{\partial}{\partial r}) + \frac{1}{r^2\sin\theta}\frac{\partial}{\partial\theta}(\sin\theta\frac{\partial}{\partial\theta}) + \frac{1}{r^2\sin^2\theta}\frac{\partial^2}{\partial\phi^2} + k^2\right]\psi(\vec{r}) = 0. \tag{A.2}$$

The general solution to Eq. (A.2) is in the form of

$$\psi_{mn}(kr,\theta,\phi) = f_n(kr)P_n^m(\cos\theta)e^{im\phi}, \tag{A.3}$$

$$n = 0, 1, 2...; \quad m = -n, -n+1, ...n-1, n \tag{A.4}$$

$P_n^m(\cos\theta)$ in Eq. (A.3) are the associated Legendre functions, given by

$$P_n^m(x) = \frac{(-1)^m}{2^n n!}(1-x^2)^{m/2}\frac{d^{n+m}}{dx^{n+m}}(x^2-1)^n. \tag{A.5}$$

Note that (A.5) hods for both positive and negative values of m. The relation between P_n^{-m} and P_n^m is given by

$$P_n^{-m}(x) = (-1)^m \frac{(n-m)!}{(n+m)!} P_n^m(x). \tag{A.6}$$

In some books (e.g. [3]), the definition of associated Legendre function is defined by a difference of a factor $(-1)^m$.

$f_n(kr)$ in Eq. (A.3) is the solution to the following spherical Bessel equation,

$$x^2 \frac{d^2y}{dx^2} + 2x\frac{dy}{dx} + [x^2 - n(n+1))]y = 0. \tag{A.7}$$

If $f_n(kr)$ is the spherical Bessel functions $j_n(kr)$, ψ_{mn} is regular at origin and written as $\mathrm{Rg}\psi_{mn}$. Since a scalar plane wave is also a solution of Helmholz equation and finite at origin, therefore, a relation between a scalar plane wave and $\mathrm{Rg}\psi_{mn}$ can be established, written as follows,

$$\mathrm{Rg}\psi_{mn} = \frac{(-i)^n}{4\pi} \int d\Omega e^{i\vec{k}\cdot\vec{r}} P_n^m(\theta') e^{im\phi'}. \tag{A.8}$$

To obtain Eq. (A.8), the following two equations are used:

$$e^{i\vec{k}\cdot\vec{r}} = 4\pi \sum_{n=0}^{\infty} \sum_{m=-n}^{n} i^n j_n(kr) Y_{mn}^*(\theta', \phi') Y_{mn}(\theta, \phi), \tag{A.9}$$

$$j_n(kr) Y_{mn}(\theta, \phi) = \frac{(-i)^n}{4\pi} \int d\Omega' e^{i\vec{k}\cdot\vec{r}} Y_{mn}(\theta', \phi'). \tag{A.10}$$

Eq. (A.8) is an integral representation of regular solution to Eq. (A.1). It is required to be pointed out that in the literature or books, there are two different definitions of spherical harmonics:

$$Y_{mn}(\theta, \phi) = P_n^m(\theta, \phi) e^{im\phi}, \tag{A.11}$$

$$Y_{mn}(\theta, \phi) = \sqrt{\frac{2n+1}{4\pi} \frac{(n-m)!}{(n+m)!}} P_n^m(\theta, \phi) e^{im\phi}. \tag{A.12}$$

The definition of spherical harmonics in (A.9) is consistent with (A.12) in [37], but Eq. (A.10) is valid for both definitons. The definition of associated Legendre functions is also consistent with that in [37], but different from that in [3] by a facotr $(-1)^m$. Note $Y^*_{mn}(\theta,\phi) = (-1)^m Y_{-mn}(\theta,\phi)$.

Hansen Vectors

As seen from the Eq. (A.1), one method to find solutions of vector Helmherz equation is to find a vector operator $\hat{O}$, which commutes with Laplacian operator $\vec{\nabla}^2$. A vector operator indicates that the result of $\hat{O}\psi_{mn}$ is a vector field. Such operators can be easily found. For example, a constant vector field $\vec{c}$, the momentum operator ($i\vec{\nabla}$), and the angular momentum operator ($\hat{L} = i\vec{r} \times \vec{\nabla}$), etc. Also, note that $\vec{\nabla} \times \vec{F}$ satisfies vector Helmholtz equation if $\vec{F}$ does. In the problem of light scattering, the electric and magnetic fields are divergence free. Therefore, we take most interest in those divergence free bases. Two selectable operators are $\hat{L}$ and $\vec{\nabla} \times \hat{L}$. Note that $\vec{\nabla} \times \vec{\nabla} \times \hat{L}$ cannot obtain a new solution, because

$$\vec{\nabla} \times \vec{\nabla} \times \vec{L} = \vec{\nabla}(\vec{\nabla} \cdot \vec{L}) - \vec{\nabla}^2 \vec{L} = \vec{\nabla}(\vec{\nabla} \cdot \vec{L}) - k^2 \vec{L} = -k^2 \vec{L}. \tag{A.13}$$

Therefore, two bases of divergence free bases can be obtained [5],

$$\vec{M}_{mn} = \gamma_{mn}(i\hat{L})\psi_{mn}(kr,\theta,\phi) = \gamma_{mn} f_n(kr)(i\hat{L})[P_n^m(\cos\theta)e^{im\phi}] \tag{A.14}$$

$$\vec{N}_{mn} = \gamma_{mn}\frac{1}{k}\vec{\nabla} \times (i\hat{L})\psi_{mn}(kr,\theta,\phi) = \frac{1}{k}\vec{\nabla} \times \vec{M}_{mn} \tag{A.15}$$

$$\vec{M}_{mn} = \frac{1}{k}\vec{\nabla} \times \vec{N}_{mn} \tag{A.16}$$

$$\gamma_{mn} = \left[\frac{(2n+1)(n-m)}{4\pi n(n+1)(n+m)}\right]^{1/2} \tag{A.17}$$

The longitudinal vector is given by [5]

$$\vec{L}_{mn} = \frac{\gamma'_{mn}}{k}\vec{\nabla}\psi_{mn}, \quad \gamma'_{mn} = \sqrt{n(n+1)}\gamma. \tag{A.18}$$

Now, let's start to derive explicit expressions of $\vec{L}_{mn}$, $\vec{M}_{mn}$ and $\vec{N}_{mn}$. To obtain explicit expressions of (A.15), we first recall two identities:

$$\vec{\nabla} = \hat{r}\frac{\partial}{\partial r} - \frac{i}{r}\hat{r}\times\hat{L}, \tag{A.19}$$

$$\vec{\nabla}\times i\vec{L} = \vec{r}\vec{\nabla}^2 - \vec{\nabla}(1 + r\frac{\partial}{\partial r}). \tag{A.20}$$

By using Eq. (A.19), we have

$$\vec{\nabla}\psi_{mn} = \hat{r}f'_n(kr)Y_{nm} - \frac{1}{r}(\hat{r}\times i\hat{L}Y_{mn})f_n(kr) \tag{A.21}$$

$$\vec{\nabla}\left[(r\frac{\partial f_n(kr)}{\partial r})Y_{nm}\right] = \hat{r}\frac{\partial}{\partial r}(r\frac{\partial f_n(kr)}{\partial r})Y_{nm} - \frac{1}{r}(\hat{r}\times i\hat{L}Y_{mn})(r\frac{\partial f_n(kr)}{\partial r}) \tag{A.22}$$

$$\begin{aligned}
\vec{\nabla}(1 + r\frac{\partial}{\partial r})\psi_{mn} &= \hat{r}\left[f'_n(kr) + \frac{\partial}{\partial r}(r\frac{\partial f_n(kr)}{\partial r})\right]Y_{nm} \\
&- \frac{1}{r}(\hat{r}\times i\hat{L}Y_{mn})\left[f_n(kr) + r\frac{\partial f_n(kr)}{\partial r}\right] \\
&= k\left[\frac{\partial}{\partial(kr)}f_n(kr) + \frac{\partial}{\partial(kr)}(kr\frac{\partial f_n(kr)}{\partial(kr)})\right]\hat{r}Y_{nm} \\
&- \frac{1}{r}(\hat{r}\times i\hat{L}Y_{mn})\left[f_n(kr) + (kr)\frac{\partial f_n(kr)}{\partial(kr)}\right] \\
&= k\left[2\frac{\partial f_n(kr)}{\partial(kr)} + kr\frac{\partial^2 f_n(kr)}{\partial(kr)^2}\right]\hat{r}Y_{nm} \\
&- \frac{1}{r}(\hat{r}\times i\hat{L}Y_{mn})\left[f_n(kr) + (kr)\frac{\partial f_n(kr)}{\partial(kr)}\right].
\end{aligned} \tag{A.23}$$

By using Eqs. (A.20) and (A.23), and

$$\vec{\nabla}^2\psi_{mn} = -k^2\psi_{mn} \tag{A.24}$$

we obtain

$$
\begin{aligned}
(\vec{\nabla}\times i\vec{L})\psi_{mn} &= -k\left[kf_n(kr)+2\frac{\partial f_n(kr)}{\partial(kr)}+kr\frac{\partial^2 f_n(kr)}{\partial(kr)^2}\right]\hat{r}Y_{nm} && \text{(A.25)}\\
&- \frac{1}{r}(\hat{r}\times i\hat{L}Y_{mn})\left[f_n(kr)+(kr)\frac{\partial f_n(kr)}{\partial(kr)}\right] && \text{(A.26)}\\
&= -k\left[-n(n+1)\frac{f_n(kr)}{kr}\right]\hat{r}Y_{nm} && \text{(A.27)}\\
&+ k(\hat{r}\times i\hat{L}Y_{mn})\left[\frac{f_n(kr)}{kr}+\frac{\partial f_n(kr)}{\partial(kr)}\right] && \text{(A.28)}
\end{aligned}
$$

Define the angular part [5],

$$\vec{P}_{mn}(\theta,\phi)=\hat{r}P_n^m(\cos\theta)e^{im\phi}, \qquad \text{(A.29)}$$

$$\vec{B}_{mn}(\theta,\phi)=\hat{r}\times\hat{L}P_n^m(\cos\theta)e^{im\phi}=\hat{r}\times\vec{C}_{mn}(\theta,\phi), \qquad \text{(A.30)}$$

$$\vec{C}_{mn}(\theta,\phi)=i\hat{L}P_n^m(\cos\theta)e^{im\phi}=\vec{\nabla}(\vec{r}P_n^m(\cos\theta)e^{im\phi})=\vec{B}_{mn}(\theta,\phi)\times\hat{r}. \qquad \text{(A.31)}$$

Here, B and C are called vector spheric harmonics. Then, we have

$$
\begin{aligned}
\vec{L}_{mn}(kr,\theta,\phi) &= \gamma'_{mn}\left[\frac{d}{dkr}f_n(kr)\vec{P}_{mn}(\theta,\phi)+\frac{1}{kr}f_n(kr)\vec{B}_{mn}(\theta,\phi)\right], && \text{(A.32)}\\
\vec{M}_{mn}(kr,\theta,\phi) &= \gamma_{mn}f_n(kr)\vec{C}_{mn}(\theta,\phi), && \text{(A.33)}\\
\vec{N}_{mn}(kr,\theta,\phi) &= \gamma_{mn}\left\{\frac{n(n+1)}{\rho}f_n(kr)\vec{P}_{mn}(\theta,\phi)\right.\\
&+ \left.\frac{1}{kr}\frac{d}{dkr}[krf_n(kr)]\vec{B}_{mn}(\theta,\phi)\right\}. && \text{(A.34)}
\end{aligned}
$$

Explicit expression of vector spherical harmonics are given in the next section.

For regular vector spherical functions, their integral representations can also be constructed. When vector operators act on the scalar solution (A.8) rather than

(A.3), the following relations are obtained,

$$\mathrm{Rg}\vec{L}_{mn}(kr,\theta,\phi) = \frac{(-i)^{n-1}}{4\pi}\gamma'_{mn}\int d\Omega' e^{ikr\hat{r}\cdot\hat{r}'}\vec{P}_{mn}(\theta',\phi'), \tag{A.35}$$

$$\mathrm{Rg}\vec{M}_{mn}(kr,\theta,\phi) = \frac{(-i)^{n}}{4\pi}\gamma_{mn}\int d\Omega' e^{ikr\hat{r}\cdot\hat{r}'}\vec{C}_{mn}(\theta',\phi'), \tag{A.36}$$

$$\mathrm{Rg}\vec{N}_{mn}(kr,\theta,\phi) = \frac{(-i)^{n-1}}{4\pi}\gamma_{mn}\int d\Omega' e^{ikr\hat{r}\cdot\hat{r}'}\vec{B}_{mn}(\theta',\phi'). \tag{A.37}$$

From (A.36) and (A.37) and note $j_n(-kr) = (-1)^n j_n(kr)$, we find

$$\vec{C}_{mn}(\theta,\phi) = \frac{(-i)^{n}}{4\pi j_n(kr)}\int d\Omega' e^{ikr\hat{r}\cdot\hat{r}'}\vec{C}_{mn}(\theta',\phi'), \tag{A.38}$$

$$\vec{e}\cdot\vec{B}_{mn}(\theta,\phi) = \frac{(-i)^{n-1}}{4\pi\frac{1}{kr}\frac{d}{d(kr)}[krj_n(kr)]}\int d\Omega' e^{ikr\hat{r}\cdot\hat{r}'}\vec{e}\cdot\vec{B}_{mn}(\theta',\phi'), \tag{A.39}$$

or

$$\vec{C}^*_{mn}(\theta,\phi) = \frac{(-i)^{n}}{4\pi j_n(kr)}\int d\Omega' e^{ikr\hat{r}\cdot\hat{r}'}\vec{C}^*_{mn}(\theta',\phi'), \tag{A.40}$$

$$\vec{e}\cdot\vec{B}^*_{mn}(\theta,\phi) = \frac{(-i)^{n-1}}{4\pi\frac{1}{kr}\frac{d}{d(kr)}[krj_n(kr)]}\int d\Omega' e^{ikr\hat{r}\cdot\hat{r}'}\vec{e}\cdot\vec{B}^*_{mn}(\theta',\phi'), \tag{A.41}$$

or

$$\vec{C}^*_{mn}(\theta,\phi) = \frac{(i)^{n}}{4\pi j_n(kr)}\int d\Omega' e^{-ikr\hat{r}\cdot\hat{r}'}\vec{C}^*_{mn}(\theta',\phi'), \tag{A.42}$$

$$\vec{e}\cdot\vec{B}^*_{mn}(\theta,\phi) = \frac{(i)^{n-1}}{4\pi\frac{1}{kr}\frac{d}{d(kr)}[krj_n(kr)]}\int d\Omega' e^{-ikr\hat{r}\cdot\hat{r}'}\vec{e}\cdot\vec{B}^*_{mn}(\theta',\phi'), \tag{A.43}$$

or

$$\vec{C}_{mn}(\theta,\phi) = \frac{(i)^{n}}{4\pi j_n(kr)}\int d\Omega' e^{-ikr\hat{r}\cdot\hat{r}'}\vec{C}_{mn}(\theta',\phi'), \tag{A.44}$$

$$\vec{e}\cdot\vec{B}_{mn}(\theta,\phi) = \frac{(i)^{n-1}}{4\pi\frac{1}{kr}\frac{d}{d(kr)}[krj_n(kr)]}\int d\Omega' e^{-ikr\hat{r}\cdot\hat{r}'}\vec{e}\cdot\vec{B}_{mn}(\theta',\phi'), \tag{A.45}$$

where $\vec{e}$ is a constant vector perpendicular to $\vec{r}$. The vector field space constructed by $\vec{L}_{mn}$, $\vec{M}_{mn}$ and $\vec{N}_{mn}$ is complete. The mathematical proof is referred to the book [18].

Any divergence free field can be expanded in the following way,

$$\vec{E}(\rho,\theta,\phi) = \sum_{n=0}^{\infty}\sum_{m=-n}^{n}[a_{mn}\vec{M}_{mn}(\rho,\theta,\phi) + b_{mn}\vec{N}_{mn}(\rho,\theta,\phi)]. \tag{A.46}$$

For incident field and internal field (finite at origion), the vector spherical functions is generated by using spherical bessel function. For scattered field (radiation condition), the Hankel function is utilized. Expansion coefficients can be solved usually by employing orthogonality relations as follows [5],

$$\int d\Omega \vec{B}_{mn}\cdot\vec{C}^{*}_{m'n'} = 0, \tag{A.47}$$

$$\int d\Omega \vec{B}_{mn}\cdot\vec{P}^{*}_{m'n'} = 0, \tag{A.48}$$

$$\int d\Omega \vec{C}_{mn}\cdot\vec{P}^{*}_{m'n'} = 0, \tag{A.49}$$

$$\int d\Omega \vec{B}_{mn}\cdot\vec{B}^{*}_{m'n'} = \frac{1}{(\gamma_{mn})^2}\delta_{mm'}\delta_{nn'}, \tag{A.50}$$

$$\int d\Omega \vec{C}_{mn}\cdot\vec{C}^{*}_{m'n'} = \frac{1}{(\gamma_{mn})^2}\delta_{mm'}\delta_{nn'}, \tag{A.51}$$

$$\int d\Omega \vec{P}_{mn}\cdot\vec{P}^{*}_{m'n'} = \frac{1}{(\gamma'_{mn})^2}\delta_{mm'}\delta_{nn'}. \tag{A.52}$$

At this point, bases of vector fields which satisfy vector Helmholtz equation are obtained. Actually, there are other methods to find the bases (e.g, [134]). The bases described in this section is much more convenient due to separate longitudinal and transverse parts.

Vector Spherical Harmonics

Vector spherical harmonics are related to spherical harmonics. They are defined as [5]

$$\vec{P}_{mn}(\theta,\phi) = (-1)^m \sqrt{\frac{(n+m)!}{(n-m)!}} \vec{P}_{mn}(\theta) e^{im\phi} \tag{A.53}$$

$$\vec{B}_{mn}(\theta,\phi) = (-1)^m \sqrt{\frac{(n+m)!}{(n-m)!}} \vec{B}_{mn}(\theta) e^{im\phi} \tag{A.54}$$

$$\vec{C}_{mn}(\theta,\phi) = (-1)^m \sqrt{\frac{(n+m)!}{(n-m)!}} \vec{C}_{mn}(\theta) e^{im\phi} \tag{A.55}$$

where

$$\vec{P}_{mn}(\theta) = \hat{r} d^n_{0m}(\theta) \tag{A.56}$$

$$\vec{B}_{mn}(\theta) = \hat{\theta}\tau_{mn}(\theta) + \hat{\phi} i\pi_{mn}(\theta) \tag{A.57}$$

$$\vec{C}_{mn}(\theta) = \hat{\theta} i\pi_{mn}(\theta) - \hat{\phi}\tau_{mn}(\theta) \tag{A.58}$$

where

$$\pi_{mn}(\theta) = \frac{m}{\sin\theta} d^n_{0m}(\theta) \tag{A.59}$$

$$\tau_{mn}(\theta) = \frac{d}{d\theta} d^n_{0m}(\theta) \tag{A.60}$$

where d^n_{0m} is Wigner-D function [5], given by,

$$d^n_{0m} = (-1)^m \sqrt{\frac{(n-m)!}{(n+m)!}} P^m_n(\cos\theta) \tag{A.61}$$

When $m = 1$, then

$$\pi_{1n}(\theta) = \frac{1}{\sin\theta}(-1)\frac{1}{\sqrt{n(n+1)}} P^1_n(\cos\theta) = \frac{1}{\sqrt{n(n+1)}}\pi_n(\theta), \tag{A.62}$$

$$\tau_{1n}(\theta) = (-1)\frac{1}{\sqrt{n(n+1)}}\frac{d}{d\theta} P^1_n(\cos\theta) = \frac{1}{\sqrt{n(n+1)}}\tau_n(\theta). \tag{A.63}$$

when $\theta = 0$,

$$\pi_{1n}(0) = \tau_{1n}(0) = \frac{1}{2}\sqrt{n(n+1)}. \tag{A.64}$$

APPENDIX B

FAR-FIELD ASYMPTOTIC: KIRCHHOFF SURFACE INTEGRAL*

The Lorenz-Mie theory [3] and the T-matrix [16] formulation provide exact solutions for the scattering of electromagnetic waves by small particles. It has been demonstrated that the Lorenz-Mie theory is a special case of the T-matrix method when the latter is applied to spheres [5]. In the two methods, the incident, scattered and internal fields are expanded in terms of vector spherical wave functions. A recent paper by Mischenko [135] discussed the fundamental concepts of electromagnetic scattering. The expansion coefficients in the Lorenz-Mie theory and the T-matrix formulation are determined from the boundary condition and extended boundary condition (EBC), respectively. Two aspects associated with the T-matrix should be addressed. First, the method to calculate the T-matrix is not restricted to EBC as other methods can be employed [136–138]. In principle, the T-matrix is another formulation of the scattering solution and contains much more information than the amplitude scattering matrix (e.g., the orientation of the scattering particle). Second, other expansion bases (e.g., vector spheroidal/ellipsoidal wave functions) can be employed to expand the electromagnetic fields [139, 140].

The scattered field is written in the form of

$$\vec{E}^s = \sum_{n=1}^{\infty} \sum_{m=-n}^{n} \left[p_{mn} \vec{M}_{mn}(k\vec{r}) + q_{mn} \vec{N}_{mn}(k\vec{r}) \right] \tag{B.1}$$

where $\vec{M}_{mn}$ and $\vec{N}_{mn}$ are the so-called vector spherical wave functions, which are transverse at infinity [5, 133], k is the wave number, and p_{mn} and q_{mn} are the expan-

*This appendix is reprinted with permission from "On the far field in the Lorenz-Mie theory and T-matrix formulation" by L. Bi, P. Yang, and G. W. Kattawar, J. Quant. Spectrosc. Radiat Transfer, **111**, 515-518(2009)

sion coefficients. The vector spherical wave functions are related to vector spherical harmonics [5] given by

$$\vec{M}_{mn}(kr,\theta,\phi) = \gamma_{mn} h_n^{(1)}(kr)\vec{C}_{mn}(\theta,\phi) \tag{B.2}$$

$$\vec{N}_{mn}(kr,\theta,\phi) = \gamma_{mn}\left\{\frac{n(n+1)}{kr}h_n^{(1)}(kr)\vec{P}_{mn}(\theta,\phi) + \frac{1}{kr}\frac{d}{d(kr)}(krh_n^{(1)}(kr)) + \vec{B}_{mn}(\theta,\phi)\right\} \tag{B.3}$$

where $h_n^{(1)}(kr)$ is the Hankel function of the first kind, $\vec{C}_{mn}$, $\vec{B}_{mn}$, and $\vec{P}_{mn}$ are vector spherical harmonics and γ_{mn} is a defined constant, given by

$$\gamma_{mn} = \sqrt{(2n-1)(n-m)/4\pi(n+1)(n+m)} \tag{B.4}$$

The solution in the radiation zone can be expressed via the asymptotic forms of $\vec{M}_{mn}$ and $\vec{N}_{mn}$ [5] as follows:

$$\vec{M}_{mn}(kr,\theta,\phi) = \frac{(-i)^{n+1}e^{ikr}}{kr}\gamma_{mn}\vec{C}_{mn}(\theta,\phi) \tag{B.5}$$

$$\vec{N}_{mn}(kr,\theta,\phi) = \frac{(-i)^{n}e^{ikr}}{kr}\gamma_{mn}\vec{B}_{mn}(\theta,\phi) \tag{B.6}$$

Note that the expansion of the scattered field in terms of $\vec{M}_{mn}$ and $\vec{N}_{mn}$ in Eq. (B.1) is due to the above asymptotic behaviors, and has taken into account the radiation condition. The preceding asymptotic properties are obtained by analyzing the differential equation satisfied by the Hankel function. Specifically, the scattered far-field is given by

$$\vec{E}^s(\vec{r}) = \frac{e^{ikr}}{-ikr}\sum_{n=1}^{\infty}\sum_{m=-n}^{n} i^{-(n+1)}\gamma_{mn}\left[-ip_{mn}\vec{C}_{mn}(\theta^s,\phi^s) + q_{mn}\vec{B}_{mn}(\theta^s,\phi^s)\right] \tag{B.7}$$

where θ^s and ϕ^s are the polar zenith angle and azimuthal angle of the scattering direction, respectively.

The far field can also be formulated in terms of the so-called Kirchhoff surface integral (2.44). When the refractive index of the particle is equal to one, $\vec{E}$ and $\vec{H}$ are equal to the incident electromagnetic fields and $\vec{E}^s$ in Eq. (2.44) is zero. Therefore, $\vec{E}$ and $\vec{H}$ in Eq. (2.44) can be either the scattered field or the total field. In this method, the radiation condition has been incorporated into the integral (2.44), when it is derived from the Maxwell equations. The Huygens principle is explicit in this formulation.

Fundamentally, the scattered field expressed in formula (B.1) should satisfy the integral (2.44). In appearance, the near field and far field are radially correlated. If we substitute Eq. (B.1) and the associated magnetic field into Eq. (2.44), the same solution given by Eq. (B.7) can be obtained. This process has been performed numerically for the scattering by spheres [141] to validate the implementation of near-to-far field transformation in the Finite-Difference Time-Domain (FDTD) method. In the following discussion, we will show that the same asymptotic formulation can be analytically obtained from Eq. (2.44). To the best of our knowledge, although this relation is implied, it is not explicitly proven in the literature. For convenience, we rewrite Eq. (2.44) as two equations:

$$\hat{\alpha}^s \cdot \vec{E}^s(\vec{r}) = \frac{e^{ikr}}{-ikr}\frac{k^2}{4\pi}\int \left\{\hat{\beta}^s \cdot [\hat{n}_s \times \vec{E}(\vec{r}')] + \hat{\alpha}^s \cdot [\hat{n}_s \times \vec{H}(\vec{r}')]\right\} e^{-ik\hat{r}\cdot\vec{r}'} ds, \quad \text{(B.8)}$$

$$\hat{\beta}^s \cdot \vec{E}^s(\vec{r}) = \frac{e^{ikr}}{-ikr}\frac{k^2}{4\pi}\int \left\{-\hat{\alpha}^s \cdot [\hat{n}_s \times \vec{E}(\vec{r}')] + \hat{\beta}^s \cdot [\hat{n}_s \times \vec{H}(\vec{r}')]\right\} e^{-ik\hat{r}\cdot\vec{r}'} ds, \quad \text{(B.9)}$$

where $\hat{\alpha}^s$ and $\hat{\beta}^s$ are two unit vectors parallel and perpendicular to the plane defined by the z axis and the scattering direction, as illustrated in Fig. 57. In a spherical coordinate system, we have

$$\hat{\alpha}^s = \hat{\theta}^s, \hat{\beta}^s = -\hat{\phi}^s \quad \text{(B.10)}$$

If the incident field is along the z axis, this plane is called the scattering plane and $\hat{\theta}^s$ is the scattering angle.

Expansion of Polarized Plane Wave

To analytically integrate the integrals in Eqs. (B.8) and (B.9), it is important to expand the polarized plane waves $\hat{\beta}^s e^{-ik\hat{r}\cdot\vec{r}'}$ and $\hat{\alpha}^s e^{-ik\hat{r}\cdot\vec{r}'}$ in terms of vector spherical wave functions as follows:

$$\hat{\beta}^s e^{-ik\hat{r}\cdot\vec{r}'} = \sum_{n=1}^{\infty}\sum_{m=-n}^{n}\left[a_{\beta,mn} Rg^*\vec{M}_{mn}(kr,\theta,\phi) + b_{\beta,mn} Rg^*\vec{N}_{mn}(kr,\theta,\phi)\right], \quad \text{(B.11)}$$

$$\hat{\alpha}^s e^{-ik\hat{r}\cdot\vec{r}'} = \sum_{n=1}^{\infty}\sum_{m=-n}^{n}\left[a_{\alpha,mn} Rg^*\vec{M}_{mn}(kr,\theta,\phi) + b_{\alpha,mn} Rg^*\vec{N}_{mn}(kr,\theta,\phi)\right], \quad \text{(B.12)}$$

where $Rg^*\vec{M}_{mn}$ and $Rg^*\vec{N}_{mn}$ are the conjugates of the regular vector spherical functions, which are defined by replacing the Hankel function in Eqs. (B.5) and (B.6) by the spherical Bessel function. To determine the coefficients, we consider $a_{\beta,mn}$ as an example, given by

$$\begin{aligned} a_{\beta,mn} &= \frac{\gamma_{mn}}{j_n(kr)}\int \hat{\beta}^s e^{-ik\hat{r}\cdot\vec{r}'}\cdot\vec{C}_{mn}(\theta,\phi)\sin\theta d\theta d\phi \\ &= 4\pi(-i)^n\gamma_{mn}\hat{\beta}^s\cdot\vec{C}_{mn}(\theta^s,\phi^s) \\ &= 4\pi(-i)^n\gamma_{mn}\tau_{mn}(\theta^s)(-1)^m\sqrt{\frac{(n+m)!}{(n-m)!}}e^{im\phi^s} \end{aligned} \quad \text{(B.13)}$$

The other coefficients can be determined in the same way, given by

$$b_{\beta,mn} = 4\pi(-i)^n\gamma_{mn}\pi_{mn}(\theta^s)(-1)^m\sqrt{\frac{(n+m)!}{(n-m)!}}e^{im\phi^s} \quad \text{(B.14)}$$

$$a_{\alpha,mn} = 4\pi(-i)^{n-1}\gamma_{mn}\pi_{mn}(\theta^s)(-1)^m\sqrt{\frac{(n+m)!}{(n-m)!}}e^{im\phi^s} \quad \text{(B.15)}$$

$$b_{\alpha,mn} = 4\pi(-i)^{n-1}\gamma_{mn}\tau_{mn}(\theta^s)(-1)^m\sqrt{\frac{(n+m)!}{(n-m)!}}e^{im\phi^s} \quad \text{(B.16)}$$

where $j_n(kr)$ is the spherical Bessel function, and $\tau_{mn}(\theta^s)$ and $\pi_{mn}(\theta^s)$ are angular distribution functions [5]. It is evident that $a_{\beta,mn} = -ib_{\alpha,mn}$ and $b_{\beta,mn} = -ia_{\alpha,mn}$.

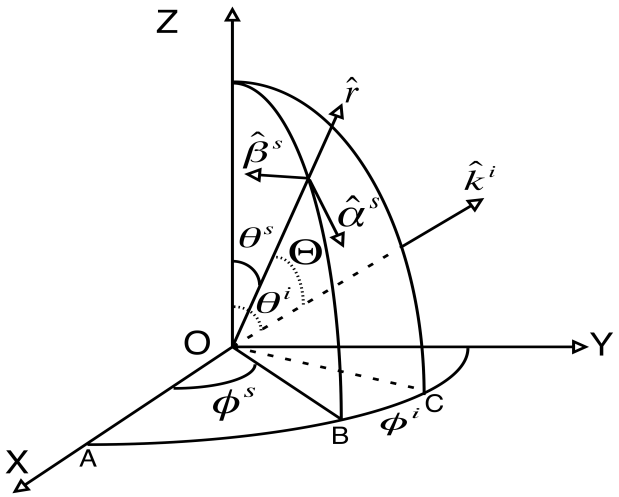

Fig. 57. Illustration of the incident direction $\hat{k}^i$, scattered direction $\hat{r}$ and associated unit vectors. Θ is the scattering angle. When the incident plane wave is along the z axis, θ_s is equal to the scattering angle

Evaluation of Integral

We evaluate the integral in Eq. (B.8) based on an assumption. As the surface enclosing the particle in the integral can be an arbitrary, for simplicity, it is assumed to be a spherical surface with a radius of a. Then, the integral in Eq. (B.8) is written as follows:

$$\hat{\alpha}^s \cdot \vec{E}^s = \frac{e^{ikr}}{-ikr} \frac{\rho^2}{4\pi} \left[I_1 + I_2 \right], \tag{B.17}$$

where $\rho = ka$ and

$$I_1 = \int \left(\hat{\beta}^s e^{-ik\hat{r}\cdot\vec{r}'}\right) \cdot \left(\hat{r}' \times \vec{E}^s(\vec{r}')\right) \sin\theta' d\theta' d\phi', \tag{B.18}$$

$$I_2 = \int \left(\hat{\alpha}^s e^{-ik\hat{r}\cdot\vec{r}'}\right) \cdot \left(\hat{r}' \times \vec{H}^s(\vec{r}')\right) \sin\theta' d\theta' d\phi'. \tag{B.19}$$

The electric scattered field $\vec{E}^s$ and magnetic field $\vec{H}^s$ on the sphere are given as follows

$$\vec{E}^s(a,\theta',\phi') = \sum_{n=1}^{\infty}\sum_{m=-n}^{n}\left[p_{mn}\vec{M}_{mn}(\rho,\theta',\phi') + q_{mn}\vec{N}_{mn}(\rho,\theta',\phi')\right], \tag{B.20}$$

$$\vec{H}^s(a,\theta',\phi') = \sum_{n=1}^{\infty}\sum_{m=-n}^{n}\left[p_{mn}\vec{N}_{mn}(\rho,\theta',\phi') + q_{mn}\vec{M}_{mn}(\rho,\theta',\phi')\right]. \tag{B.21}$$

Note that

$$\hat{r}\times\vec{C}_{mn} = \vec{B}_{mn}, \hat{r}\times\vec{B}_{mn} = -\vec{C}_{mn}, \hat{r}\times\vec{P}_{mn} = 0. \tag{B.22}$$

Then, we have

$$\begin{aligned}\hat{r}'\times\vec{E}^s(\vec{r}) \;=\; & \sum_{n=1}^{\infty}\sum_{m=-n}^{n}\gamma_{mn}\left[p_{mn}h_n^{(1)}(\rho)\vec{B}_{mn}(\theta',\phi')\right. \\ & \left. - q_{mn}\frac{1}{\rho}\frac{d}{d\rho}[\rho h_n^{(1)}(\rho)]\vec{C}_{mn}(\theta',\phi')\right], \end{aligned}\tag{B.23}$$

$$\begin{aligned}\hat{r}'\times\vec{H}^s(\vec{r}) \;=\; & (-i)\sum_{n=1}^{\infty}\sum_{m=-n}^{n}\gamma_{mn}\Big[-p_{mn}h_n^{(1)}(\rho)\vec{C}_{mn}(\theta',\phi') \\ & +q_{mn}\frac{1}{\rho}\frac{d}{d\rho}[\rho h_n^{(1)}(\rho)]\vec{B}_{mn}(\theta',\phi')\Big]. \end{aligned}\tag{B.24}$$

By employing the following identities [5]

$$\vec{B}_{m'n'}\cdot\vec{C}_{mn} = \vec{B}_{m'n'}\cdot\vec{P}_{mn} = \vec{P}_{m'n'}\cdot\vec{C}_{mn} = 0, \tag{B.25}$$

and

$$\int \vec{B}_{mn}(\theta,\phi)\cdot\vec{B}^{*}_{mn}(\theta,\phi)\sin\theta d\theta d\phi = (\gamma_{mn})^{-2}\delta_{mm'}\delta_{nn'}, \tag{B.26}$$

$$\int \vec{C}_{mn}(\theta,\phi)\cdot\vec{C}^{*}_{mn}(\theta,\phi)\sin\theta d\theta d\phi = (\gamma_{mn})^{-2}\delta_{mm'}\delta_{nn'}, \tag{B.27}$$

it is straightforward to show that

$$I_1 = -a_{\beta,mn}q_{mn}j_n(\rho)\frac{1}{\rho}\frac{d}{d\rho}\left(\rho h_n^{(1)}(\rho)\right) + b_{\beta,mn}p_{mn}h_n^{(1)}(\rho)\frac{1}{\rho}\frac{d}{d\rho}\left(\rho j_n(\rho)\right), \tag{B.28}$$

$$I_2 = (-i)\left[-a_{\alpha,mn}p_{mn}j_n(\rho)\frac{1}{\rho}\frac{d}{d\rho}\left(\rho h_n^{(1)}(\rho)\right) + b_{\alpha,mn}q_{mn}h_n^{(1)}(\rho)\frac{1}{\rho}\frac{d}{d\rho}\left(\rho j_n(\rho)\right)\right] \tag{B.29}$$

Therefore, we have

$$\begin{aligned} I_1 + I_2 &= i\left[j_n(\rho)\frac{1}{\rho}\frac{d}{d\rho}(\rho h_n^{(1)}(\rho)) - h_n^{(1)}(\rho)\frac{1}{\rho}\frac{d}{d\rho}(\rho j_n(\rho))\right](b_{\alpha,mn}q_{mn} + a_{\alpha_{mn}}p_{mn}) \\ &= i\left[j_n(\rho)\frac{d}{d\rho}h_n^{(1)}(\rho) - h_n^{(1)}(\rho)\frac{d}{d\rho}j_n(\rho)\right](b_{\alpha,mn}q_{mn} + a_{\alpha,mn}p_{mn}) \\ &= \frac{1}{\rho^2}\left(b_{\alpha,mn}q_{mn} + a_{\alpha,mn}p_{mn}\right). \end{aligned} \tag{B.30}$$

Furthermore, we obtain

$$\begin{aligned} \vec{\alpha}^s\cdot\vec{E}^s &= \frac{e^{ikr}}{-ikr}\frac{1}{4\pi}\left(b_{\alpha,mn}q_{mn} + a_{\alpha,mn}p_{mn}\right) \\ &= \frac{e^{ikr}}{-ikr}\sum_{n=1}^{\infty}\sum_{m=-n}^{n} i^{-(n+1)}\gamma_{mn} \\ &\times \left[-ip_{mn}\hat{\alpha}^s\cdot\vec{C}_{mn}(\theta^s,\phi^s) + q_{mn}\hat{\alpha}^s\cdot\vec{B}_{mn}(\theta^s,\phi^s)\right]. \end{aligned} \tag{B.31}$$

Eq. (B.9) can be integrated in a similar way and given by

$$\begin{aligned} \vec{\beta}^s\cdot\vec{E}^s &= \frac{e^{ikr}}{-ikr}\frac{1}{4\pi}\left(b_{\beta,mn}q_{mn} + a_{\beta,mn}p_{mn}\right) \\ &= \frac{e^{ikr}}{-ikr}\sum_{n=1}^{\infty}\sum_{m=-n}^{n} i^{-(n+1)}\gamma_{mn} \\ &\times \left[-ip_{mn}\hat{\beta}^s\cdot\vec{C}_{mn}(\theta^s,\phi^s) + q_{mn}\hat{\beta}^s\cdot\vec{B}_{mn}(\theta^s,\phi^s)\right]. \end{aligned} \tag{B.32}$$

Note that $\vec{E}^s = (\hat{\alpha}^s \cdot \vec{E}^s)\hat{\alpha}^s + \hat{\beta}^s \cdot \vec{E}^s)\hat{\beta}^s$. Therefore, the same result as Eq. (B.7) is obtained

APPENDIX C

DIFFRACTION-TYPE INTEGRAL AND LINE-INTEGRAL METHOD

A repeated encounter of the integral in the PGOH is of the type:

$$I_s = \int\int_s \exp\left(ik\vec{w}\cdot\vec{r'}\right) d^2\vec{s}, \tag{C.1}$$

where $\vec{r'}$ is the position vector within a planar surface area s, $\vec{w}$ is an arbitrary vector, and k is a constant, which can be complex. The shape of the surface area of concern depends on the geometry of the particle. For example, an ellipse for light scattering by an ellipsoid, and a polygon for light scattering by faceted ice crystals. Figure 58 (a) shows a 4-polygon shaped facet in 3-D space. In this appendix, we develop a systematic algorithm to calculate the above integral for an arbitrary shaped area of the integration.

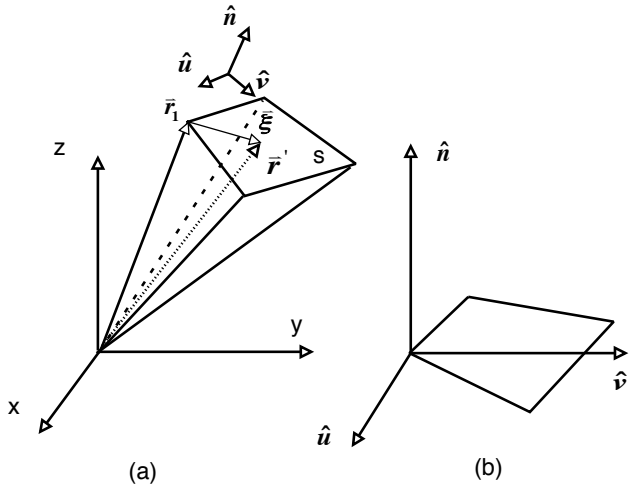

Fig. 58. A facet in 3-D space.

Let's first consider a general polygon shaped boundary. For simplicity, as shown in Fig. 58, a local coordinate system $(\hat{u}, \hat{v}, \hat{n})$ is defined, where $\hat{n}$ is the outward normal direction of the facet, and $\hat{u}$ and $\hat{v}$ are two unit vectors tangent to the surface. In x-y-z coordinate system, the vertices of the N-polygon is denoted as $\vec{r}_j, (j = 1, N+1,$ and $\vec{r}_{N+1} = \vec{r}_N)$. The sequence of vertices is arranged in anti-clock wise direction with respect to $\hat{n}$. By choosing a position of reference in the plane of the facet (e.g., $\vec{r}_1$), the coordinates of vertices of the polygon can be written in the form of

$$\vec{r}_j = \vec{r}_1 + \vec{a}_j. \tag{C.2}$$

Similarly, an arbitrary position vector $\vec{r}'$ in the plane of the facet can be written as

$$\vec{r}' = \vec{r}_1 + \vec{\xi} = \vec{r}_1 + u\hat{u} + v\hat{v}. \tag{C.3}$$

Now, Eq. (C.1) can be transformed to be the integration over u and v as follows,

$$I_s = \exp\left(ik\vec{w} \cdot \vec{r}_1\right) \int\int_s \exp\left[ik(w_u u + w_v v)\right] dudv. \tag{C.4}$$

To evaluate Eq. (C.4), we define a vector field $\vec{F}$ [142], whose components along $\hat{u}$ and $\hat{v}$ are given by

$$\vec{F} \cdot \hat{u} = F_u = -\frac{w_v}{ik(|\vec{w}|^2 - |\vec{w} \cdot \hat{n}|^2)} \exp\left(ik(w_u u + w_v v)\right), \tag{C.5}$$

$$\vec{F} \cdot \hat{v} = F_v = \frac{w_u}{ik(|\vec{w}|^2 - |\vec{w} \cdot \hat{n}|^2)} \exp\left(ikik(w_u u + w_v v)\right). \tag{C.6}$$

Based on the Stokes formula,

$$\int\int_s \left[\frac{\partial F_v}{\partial u} - \frac{\partial F_u}{\partial v}\right] dudv = \int_{\partial S} F_u du + F_v dv, \tag{C.7}$$

we have

$$\int\int_s \exp\left[ik(w_u u + w_v v)\right] = \int_{\partial S} F_u du + F_v dv. \tag{C.8}$$

Therefore,

$$\int\int_s \exp(ik\vec{w}\cdot\vec{\xi})d^2\xi \;=\; \frac{i}{k(|\vec{w}|^2-|\vec{w}\cdot\hat{n}|^2)}\int_{\partial S}\exp[ik\vec{w}\cdot\vec{\xi}](w_v du - w_u dv) \quad \text{(C.9)}$$

For each side of the polygon, on which the position vector can be parameterized in terms of t as follows,

$$\vec{\xi}(t) = \vec{a}_n + t(\vec{a}_{n+1}-\vec{a}_n). \quad \text{(C.10)}$$

By using

$$w_v du - w_u dv = [(\vec{a}_{n+1}-\vec{a}_n)\times\vec{w}]\cdot\hat{n}dt, \quad \text{(C.11)}$$

we have [142]

$$\begin{aligned}
\int_{\partial S}\exp[ik\vec{w}\cdot\vec{\xi}](w_v du - w_u dv) &= \sum_{n=1}^{N}\exp\left(ik\vec{w}\cdot\vec{a}_n\right)[(\vec{a}_{n+1}-\vec{a}_n)\times\vec{w}]\cdot\hat{n} \\
&\times \int_0^1 \exp\left(ik\vec{w}\cdot(\vec{a}_{n+1}-\vec{a}_n)t\right)dt \\
&= \sum_{n=1}^{N}[(\vec{a}_{n+1}-\vec{a}_n)\times\vec{w}]\cdot\hat{n} \\
&\times \frac{\exp\left(ik\vec{w}\cdot\vec{a}_{n+1}\right)-\exp\left(ik\vec{w}\cdot\vec{a}_n\right)}{ik\vec{w}\cdot(\vec{a}_{n+1}-\vec{a}_n)} \\
&= \sum_{n=1}^{N}[(\vec{a}_{n+1}-\vec{a}_n)\times\vec{w}]\cdot\hat{n}\frac{\sin\left(k\vec{w}\cdot(\vec{a}_{n+1}-\vec{a}_n)/2\right)}{k\vec{w}\cdot(\vec{a}_{n+1}-\vec{a}_n)/2} \\
&\times \exp\left\{ik\vec{w}\cdot(\vec{a}_{n+1}+\vec{a}_n)/2\right\} \quad \text{(C.12)}
\end{aligned}$$

Substituting Eq. (C.12) into Eq. (C.4), we obtain

$$\begin{aligned}
I_s \;&=\; \sum_{n=1}^{N}\frac{i\,[(\vec{r}_{n+1}-\vec{r}_n)\times\vec{w}]\cdot\hat{n}}{k(|w|^2-|\vec{w}\cdot\hat{n}|^2)}\frac{\sin\left(k\vec{w}\cdot(\vec{r}_{n+1}-\vec{r}_n)/2\right)}{k\vec{w}\cdot(\vec{r}_{n+1}-\vec{r}_n)/2} \\
&\times\; \exp\left\{ik\vec{w}\cdot(\vec{r}_{n+1}+\vec{r}_n)/2\right\} \quad \text{(C.13)}
\end{aligned}$$

From Eq. (C.13), the final value of the integral can be represented in terms of the position vectors of all the vertices. In principle, an arbitrary boundary can be approximated by a N-polygon. Therefore, the above formula can be employed to calculate the integral for any shaped boundary. In addition, two aspects are required to be pointed out in numerical calculation of Eq. (C.13):

- When $\vec{w}$ is aligned with $\hat{n}$ or $-\hat{n}$ (is normal to the planar surface), the denominators in Eq. (C.13) are zero. In this case, I_s is equal to the area of the facet:

$$I_s = \frac{1}{2}\sum_{j=1}^{N-2}[(\vec{r}_{j+1} - \vec{r}_1) \times (\vec{r}_{j+2} - \vec{r}_1)] \cdot \hat{n}. \tag{C.14}$$

- When $k\vec{w} \cdot (\vec{r}_{n+1} - \vec{r}_n)/2 = 0$,

$$\frac{\sin\left(k\vec{w} \cdot (\vec{r}_{n+1} - \vec{r}_n)/2\right)}{k\vec{w} \cdot (\vec{r}_{n+1} - \vec{r}_n)/2} = 1. \tag{C.15}$$

For an ellipse (circle as a special case), Eq. (C.1) has analytical formula. Let the equation of ellipse in $u - v - n$ coordinate system be

$$\frac{u^2}{a^2} + \frac{v^2}{b^2} = 1 \tag{C.16}$$

An arbitrary point within the ellipse is given by,

$$u = a\rho\cos\phi, v = b\rho\sin\phi, \quad \text{where} \quad \rho \in [0,1] \quad \text{and} \quad \phi \in (0, 2\pi]. \tag{C.17}$$

Then, we have

$$\begin{aligned} I_s &= \exp(ik\vec{w}\cdot\vec{r}_0)\int_0^1\int_0^{2\pi}\exp\left[ik(aw_u\rho\cos\phi + bw_v\rho\sin\phi)\right]\rho d\rho d\phi \\ &= \exp(ik\vec{w}\cdot\vec{r}_0)\int_0^1\int_0^{2\pi}\exp\left[ik\sqrt{a^2w_u^2+b^2w_v^2}\rho\cos(\phi-\phi_0)\right]\rho d\rho d\phi \\ &= \pi ab\frac{2J_1\left(k\sqrt{a^2w_u^2+b^2w_v^2}\right)}{k\sqrt{a^2w_u^2+b^2w_v^2}}\exp\left(ik\vec{w}\cdot\vec{r}_0\right) \end{aligned} \tag{C.18}$$

where $\vec{r}_0$ is the position vector of the ellipse center, and J_1 is the first order Bessel function.

- A computational example: an arbitrarily oriented ellipse

The relation between the coordinates (x,y,z) and (u,v,n) of the same position in the $\{O,\hat{e}_x,\hat{e}_y,\hat{e}_z\}$ and $\{\vec{r}_o,\hat{e}_u,\hat{e}_v,\hat{e}_n\}$ systems is given by

$$\begin{pmatrix} x \\ y \\ z \end{pmatrix} = \begin{pmatrix} r_{o,x} \\ r_{o,y} \\ r_{o,z} \end{pmatrix} + \begin{pmatrix} \hat{e}_x\cdot\hat{e}_u & \hat{e}_x\cdot\hat{e}_v & \hat{e}_x\cdot\hat{e}_n \\ \hat{e}_y\cdot\hat{e}_u & \hat{e}_y\cdot\hat{e}_v & \hat{e}_y\cdot\hat{e}_n \\ \hat{e}_z\cdot\hat{e}_u & \hat{e}_z\cdot\hat{e}_v & \hat{e}_z\cdot\hat{e}_n \end{pmatrix} \begin{pmatrix} u \\ v \\ n \end{pmatrix} \tag{C.19}$$

In the z-y-z convention of Euler rotation, the above matrix can be witten in terms of Euler angles (α,β,γ) as follows,

$$\begin{pmatrix} c_1c_2c_3 - s_1s_3 & -c_2s_3c_1 - c_3s_1 & c_1s_2 \\ c_1s_3 + c_3c_2s_1 & c_1c_3 - c_2s_1s_3 & s_2s_1 \\ -c_3s_2 & s_3s_2 & c_2 \end{pmatrix} \tag{C.20}$$

where c_1 means $\cos\alpha$, c_2 means $\cos\beta$, and c_3 means $\cos\gamma$. The relative position of the two coordinate systems is determined by $\vec{r}_o$ and (α,β,γ). The equation of ellipse

can be paramterized in terms of t,

$$\begin{pmatrix} x(t) \\ y(t) \\ z(t) \end{pmatrix} = \begin{pmatrix} r_{o,x} \\ r_{o,y} \\ r_{o,z} \end{pmatrix} + \begin{pmatrix} c_1c_2c_3 - s_1s_3 & -c_2s_3c_1 - c_3s_1 & c_1s_2 \\ c_1s_3 + c_3c_2s_1 & c_1c_3 - c_2s_1s_3 & s_2s_1 \\ -c_3s_2 & s_3s_2 & c_2 \end{pmatrix} \begin{pmatrix} a\cos t \\ b\sin t \\ 0 \end{pmatrix} \quad \text{(C.21)}$$

where the range of t is $(0, 2\pi]$.

We apply both Eq. (C.13) and Eq. (C.18) to the same problem. In computation, $k = 1$ and $\vec{w} = (\sin\theta, 0, \cos\theta)$, $a = 1, b = 2$, $\vec{r}_0 = (5, 5, 10)$, $(\alpha, \beta, \gamma) = (30^o, 30^o, 30^o)$. Figure 59 shows the value of the integral as a function of θ computed from the method of analytical solution and the method of ling integral.

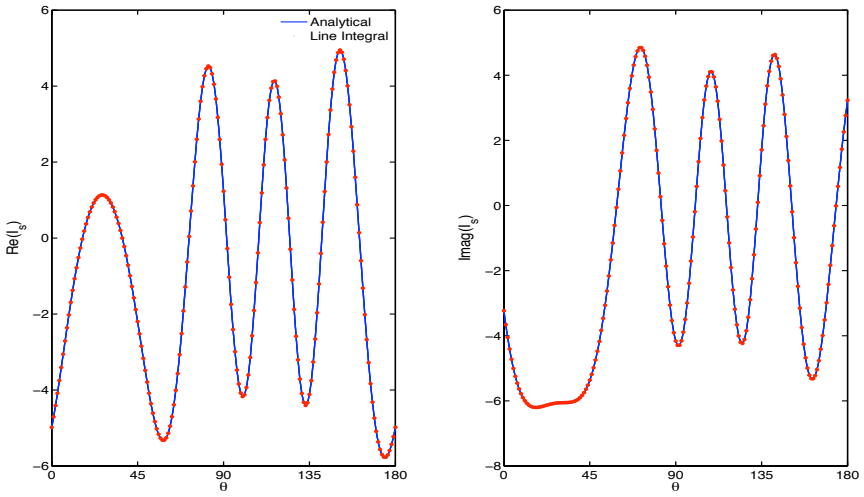

Fig. 59. The value of the integration I_s as a function of the scattering angle θ computed from the method of analytical solution and line integral.

APPENDIX D

RAY-SPREADING MATRIX

For randomly oriented particles, it is assumed that the interference among waves associated with various outgoing rays can be properly neglected. Based on this assumption, the phase matrix can be obtained by incorporating the ray-spreading effect into the phase matrix computed from the CGOM through a ray-spreading matrix. In this appendix, we derive this matrix. For simplicity, we let

$$\begin{bmatrix} S_2 & S_3 \\ S_4 & S_1 \end{bmatrix} = -\frac{k^2}{4\pi} \exp(ik\zeta) \begin{bmatrix} M_2 & M_3 \\ M_4 & M_1 \end{bmatrix}. \tag{D.1}$$

Then, Eq. (4.86) can be rewritten as

$$\begin{bmatrix} M_2 & M_3 \\ M_4 & M_1 \end{bmatrix} = \begin{bmatrix} \Xi_2 & \Xi_3 \\ \Xi_4 & \Xi_1 \end{bmatrix} \times \begin{bmatrix} \tilde{S}_2 & \tilde{S}_3 \\ \tilde{S}_4 & \tilde{S}_1 \end{bmatrix} \times \begin{bmatrix} \cos\phi_t & \sin\phi_t \\ -\sin\phi_t & \cos\phi_t \end{bmatrix}. \tag{D.2}$$

The matrix on the right of $\tilde{S}$ is associated with the rotation of scattering plane. The corresponding matrix that has effect on Stokes vector is

$$\begin{bmatrix} 1 & 0 & 0 & 0 \\ 0 & \cos(2\phi_t) & \sin(2\phi_t) & 0 \\ 0 & -\sin(2\phi_t) & \cos(2\phi_t) & 0 \\ 0 & 0 & 0 & 1 \end{bmatrix}. \tag{D.3}$$

The matrix on the left of $\tilde{S}$ is associated with the ray-spreading of light. The corresponding ray-spreading matrix that has effect on Stokes vector is

$$\begin{bmatrix} \Xi_{11} & \Xi_{12} & \Xi_{13} & 0 \\ \Xi_{21} & \Xi_{22} & \Xi_{23} & 0 \\ \Xi_{31} & \Xi_{32} & \Xi_{33} & 0 \\ 0 & 0 & 0 & \Xi_{44} \end{bmatrix}. \tag{D.4}$$

The first three elements of the fourth column and the fourth row are zero because f_i and g_i (i.e., Ξ_i, i=1,4) are real, and the other elements are given by

$$\Xi_{11} = \frac{1}{2}({\Xi_1}^2 + {\Xi_2}^2 + {\Xi_3}^2 + {\Xi_4}^2), \tag{D.5}$$

$$\Xi_{12} = \frac{1}{2}({\Xi_2}^2 - {\Xi_1}^2 + {\Xi_4}^2 - {\Xi_3}^2), \tag{D.6}$$

$$\Xi_{21} = \frac{1}{2}({\Xi_2}^2 - {\Xi_1}^2 - {\Xi_4}^2 + {\Xi_3}^2), \tag{D.7}$$

$$\Xi_{22} = \frac{1}{2}({\Xi_2}^2 + {\Xi_1}^2 - {\Xi_4}^2 - {\Xi_3}^2), \tag{D.8}$$

$$\Xi_{13} = \Xi_2\Xi_3 + \Xi_1\Xi_4, \tag{D.9}$$

$$\Xi_{23} = \Xi_2\Xi_3 - \Xi_1\Xi_4, \tag{D.10}$$

$$\Xi_{31} = \Xi_2\Xi_4 + \Xi_1\Xi_3, \tag{D.11}$$

$$\Xi_{32} = \Xi_2\Xi_4 - \Xi_1\Xi_3, \tag{D.12}$$

$$\Xi_{33} = \Xi_1\Xi_2 + \Xi_3\Xi_4, \tag{D.13}$$

$$\Xi_{44} = \Xi_1\Xi_2 - \Xi_3\Xi_4, \tag{D.14}$$

The process in deriving the ray-spreading matrix is quite similar to that in deriving the phase matrix from amplitude scattering matrix presented in Chapter I.

VITA

Lei Bi was born in Anhui province, China. Mr. Bi received his Bachelor of Science degree in physics from Anhui Normal University, Wuhu, Anhui, China in July 2003. In 2006, Mr. Bi received a Master of Science degree in physics from Beijing Normal University, Beijing, China. During 2006 − 2011, Mr. Bi was a research assistant in Department of Physics at Texas A&M university. He can be reached by email at bihualei@gmail.com or by contacting Dr. Ping Yang in department of atmospheric sciences at Texas A&M University.

The typist for this dissertation was Lei Bi.